Fabrication and modelling of 3-3 piezoelectric composites

Perry, Andrew John

Award date:
2002

Awarding institution:
University of Bath

FABRICATION AND MODELLING OF 3-3 PIEZOELECTRIC COMPOSITES

submitted by Andrew John Perry

for the degree of Doctor of Philosophy

of the University of Bath

2002

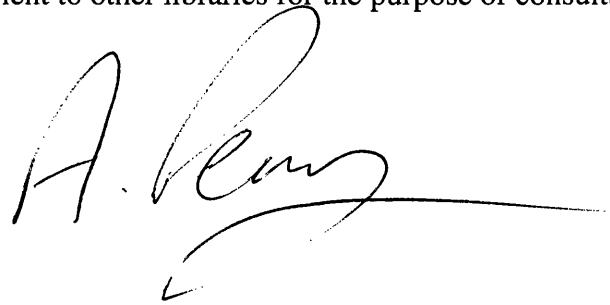

ProQuest LLC
789 East Eisenhower Parkway
P.O. Box 1346
Ann Arbor, MI 48106-1346

Acknowledgements

I would like to take this opportunity to thank everyone who has contributed to the completion of this thesis.

Thanks to my supervisors Dr. Chris Bowen and Prof. Ron Stevens for continued support and guidance throughout this project, and to Steve Mahon, DERA, for support in the early stages of this project.

I am eternally grateful to my colleagues at the University of Bath, namely Brian Casey, Luke Nelson, Hudai Kara and Simon Panteny for their technical support and unrelenting good humour throughout the past 3 years.

Finally, I would like to thank all the technical and administrative staff at the Department of Engineering and Applied Science for their daily assistance, without which, this work would not have been possible.

Abstract

Three-dimensional modelling of a 3-3 piezoelectric structure was carried out using ANSYS finite element modelling software. Hydrophone figures of merit were calculated for structures with increasing amounts of interconnecting porosity. In addition to air being the second phase, polymer fillers were added to the three dimensional model in order to observe the effect of polymer Young's modulus and Poisson's ratio on the piezoelectric response of the composite material. Results show that increasing the porosity has the effect of improving the hydrostatic piezoelectric properties for applications such as low frequency hydrophones. The optimum amount of porosity depends on the figure of merit to be maximised.

In order to validate model predictions, porous piezoelectric structures were fabricated by either the BurPS (Burnt out Polymer Spheres) method or polymer foam reticulation. Corresponding measurements of piezoelectric coefficients were carried out on the porous samples.

Experimental results confirmed finite element modelling predictions. PZT-porosity composites and PZT-polymer composites were produced exhibiting superior hydrostatic strain constant (d_h), hydrostatic voltage constant (g_h) and hydrostatic figure of merit ($d_h g_h$) compared to that of dense PZT.

List of figures.

List of tables

List of Equations

1 Theory and Background

This thesis gives an account of a study into piezocomposites for use in hydrophone applications. This first section will discuss piezoelectric behaviour, hydrophones and their related figures of merit, materials properties and hydrophone performance. Common methods of fabrication of hydrophones will be discussed.

As finite element modelling has been used to investigate the relationship between composite structure and properties, this will also be described.

1.1 Piezoelectric Behaviour

In the following section the background to and history of to piezoelectricity will be examined. The discovery of the piezoelectric phenomenon, crystal structure and properties of the bulk material and the different materials types available will be discussed. In addition, common types of piezoelectric devices will be examined including the operating conditions and possible improvements of devices.

1.1.1 Crystal Structure of Piezoelectrics

Over 120 years has passed since the discovery of piezoelectricity. Although the development of the piezoelectric industry, from discovery to application, has been slow in comparison to other industries, such as the semiconductor industry, significant advances have been made and piezoelectric materials or devices are found in many household items.

1.1.1.1 Discovery of Piezoelectricity

Pierre and Jacques Curie first published the phenomenon of piezoelectricity in 1880. In their work they demonstrated a direct connection between the macroscopic piezoelectric phenomenon and crystallographic structure. The Curie brothers used crystals such as quartz, topaz and Rochelle salt and with limited equipment conclusively measured the development of a surface charge on these crystals when they were subjected to mechanical stress. This was immediately given the name piezoelectricity in order to distinguish it from other effects of interest such as contact electricity and pyroelectricity[1].

The Curie brothers predicted the direct piezoelectric effect, applied mechanical stress induces a surface charge, but did not predict the indirect piezoelectric effect, mechanical strain in response to an applied electric field. It was Lippmann in 1881 who calculated this

effect from thermodynamic principles. This "converse" effect was then immediately experimentally confirmed by the Curie brothers in the same year.

1.1.1.2 Spontaneous Dipole Moment

X-ray studies of crystals found by the Curie brothers to be exhibiting piezoelectricity confirmed that these crystals lacked internal symmetry in their unit cells. Two different cases can exists, the first case is when the centres of the positive and negative charges are non symmetric with the unit cell planes when no pressure is applied. This is the case in barium titanate, a common piezoelectric material. The second case is that exhibited by quartz, where the dipole moments are only induced by application of pressure on the crystal.[1]

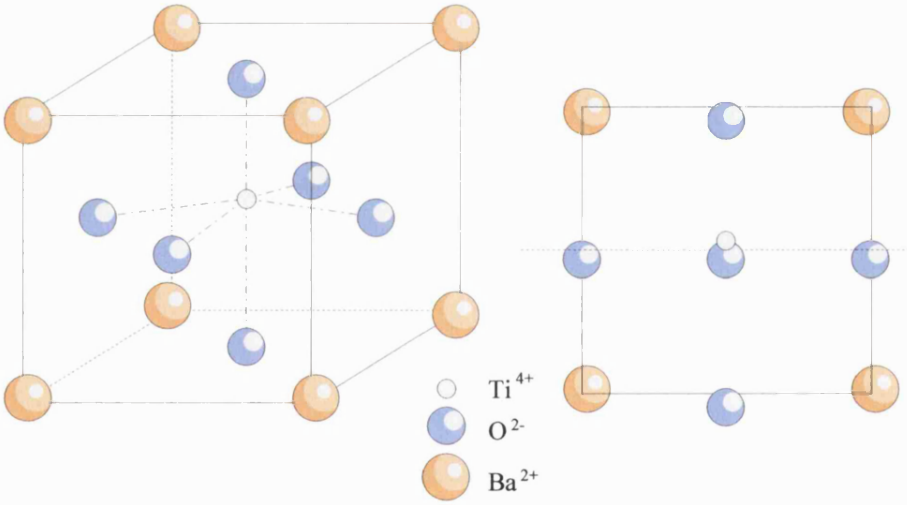

Figure 1-1: Schematic of a unit cell of barium titanate showing the displacement of the titanium ion with respect to the centre of the unit cell.

The dipole moment in a crystal can be calculated by considering the size of the charge and the displacement from the centre of the unit cell. If a positive charge is displaced upwards from the centre of the unit cell and a negative charge is displaced downwards from the centre of the unit cell, both of these cases would contribute positively to the dipole moment, which would be the sum of both values.

The polarisation creates an electric field with internal and surface effects. This surface effect is a charge, which is equal to the internal polarisation.

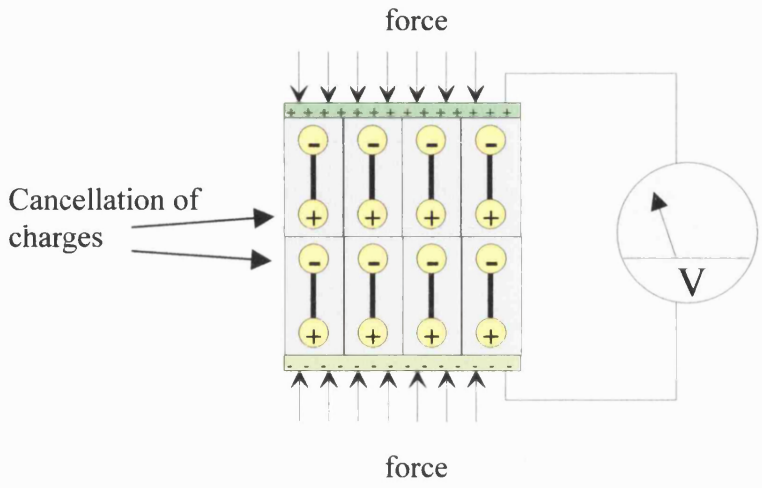

Figure 1-2: Charge manifested on the surface of a bulk piezoelectric sample.

This process can be described as the summation of dipoles stacked on top of each other as shown in Figure 1-2. The charge on the top of each unit cell is cancelled out by the opposite charge on the cell above it. This effect is continuous throughout the crystal with the exception of the two outermost surfaces, where the charges manifest. Thus, it follows that the surface charge per unit area is proportional to the polarisation.

1.1.1.3 Crystal Groups Exhibiting Piezoelectricity

In crystal chemistry, elements of symmetry are used to define different crystal classes and point groups. These elements are centre of symmetry, axes of rotation and mirror planes. Using this system all crystals can be classified into one of 32-point groups, which in turn are subdivisions of 7 crystal systems. Out of the 32 possible point groups, 20 of these groups can exhibit the piezoelectric effect due to their non-centrosymmetric crystal structure.

1.1.1.4 Common Materials

A number of materials that exhibit the piezoelectric effect have been extensively researched and used over the past 100 years. Quartz was the first material discovered to exhibit the

piezoelectric effect and is used extensively in the form of a single crystal. Polycrystalline ceramics such as barium titanate and lead zirconate titanate are also commonly used. Single crystal piezoelectric ceramics can exhibit improved piezoelectric properties than their polycrystalline counterparts and is currently the subject of large amounts of research due to the ability to manufacture and choose the optimum orientation for poling and actuation[2]. However, single crystal ceramics are expensive and time consuming to produce, and can only be manufactured in certain simple geometries. The high cost and simple shapes restrict single crystal piezoelectric ceramics to high value / high performance applications.

Polycrystalline ceramics are, however, relatively cheap to produce as they can be made using conventional ceramics procedures with no specialised equipment. They can also be more readily produced in a variety of shapes and sizes. Despite inferior properties, polycrystalline piezoelectric ceramics are used in the majority of applications due to their ease and cost of manufacture.

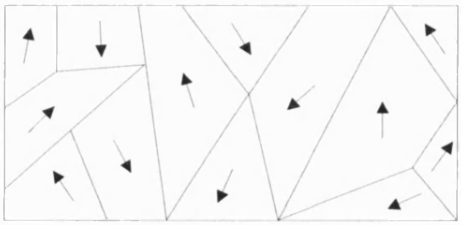

Figure 1-3: Example of unpoled domain configuration in a polycrystalline piezoelectric.

Areas within a material where dipoles have the same orientation are called "domains". Initially most materials exhibit a number of randomly aligned domains as shown in Figure 1-3. In order to take advantage of the piezoelectric effect in polycrystalline ferroelectric materials, they need to be poled. This is the process of aligning all the domains, and hence dipoles, so the piezoelectric properties of each domain will reinforce one another and lead to a net, bulk effect.

1.1.1.5 Poling

The process of poling is to induce, in the piezoelectric material, a net polarisation so that piezoelectric behaviour can be observed under an applied mechanical stress or electric field.

The temperature at which a crystal structure changes from a non-symmetrical (piezoelectric) to a symmetrical (non-piezoelectric) form is called the Curie temperature. Therefore above the Curie temperature no piezoelectric effect is exhibited.

As a piezoelectric ceramic cools from above its Curie point it will contract. Since all the crystallites within the polycrystalline ceramic are randomly oriented this contraction will be isotropic. However, each individual crystal will favour anisotropic contraction according to its orientation. These two systems lead to the piezoelectric material forming many, seemingly randomly, oriented domains in order to minimise the overall elastic strain energy within the ceramic body.

Within a single domain the dipoles are aligned, but since many domains exist in polycrystalline materials any local piezoelectric property is cancelled out in the bulk material due to the random orientation of the domains.

If the application of an electric field to this material is considered, the relationship between applied electric field and polarisation can be seen in Figure 1-4.

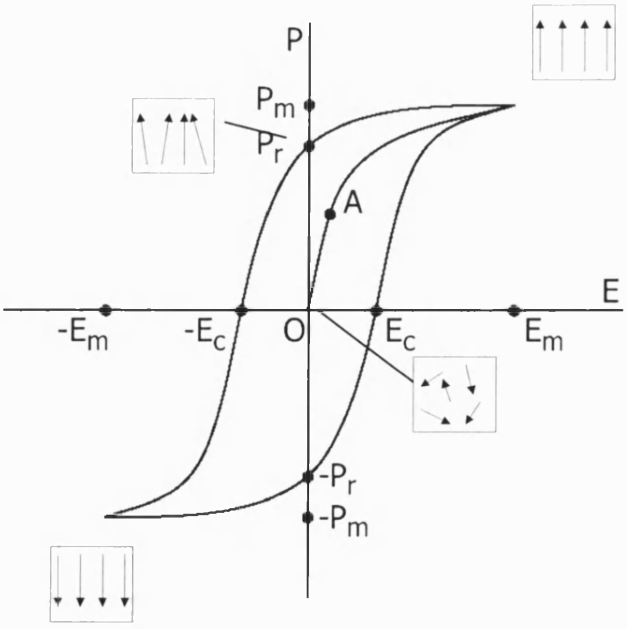

Figure 1-4: Graph showing electric field (E) against polarisation (P).

Initially, under small fields the material behaves as a dielectric, hence there is a linear relationship between electric field (E) and polarisation (P). At these small fields there is insufficient electric field to switch any of the dipole moments to the direction of the electric field. This corresponds to section O-A in Figure 1-4. Further increasing the electric field will eventually switch those domains whose orientation is 180 degrees to the electric field as this requires little energy. Further increases in field strength will continue to align all possible domains until the sample consists of domains which are all oriented in the direction of the applied electric field. This is the saturation point (E_m-P_m), where a further increase in electric field has no effect on the domains in the piezoelectric sample and hence polarisation is at a maximum.

As the field strength is decreased the polarisation will also decrease but when the field strength reaches zero there is remnant polarisation, (P_r) in the ceramic. The ceramic will now exhibit a piezoelectric effect as the majority of the dipoles are aligned. However if the applied electric field is applied in the opposite direction the domains will switch back until there is again no remnant polarisation. The electric field required to produce this effect is called the coercive field (E_c in Figure 1-4). Further reduction in the electric field will align domains in the opposite direction and lead to minima in polarisation ($-P_m$). Increasing the field from the minimum value ($-E_m$) to zero will again produce remnant polarisation ($-P_r$) and will require the coercive field (E_c) to obtain zero polarisation in the sample. Increasing the field strength from E_c will again align the domains until maximum polarisation (P_m) is again reached.

In practice there are two common ways align the dipoles and to pole piezoelectric materials which are termed "oil bath" poling and "corona" poling (Figure 1-5).

In "oil bath" poling a sample of piezoelectric material is firstly heated in an oil bath. As shown in Figure 1-6, a sufficiently high electric field is then applied by directly applying an electric potential difference across the sample to align the domains. The applied field is maintained across the sample whilst the oil bath and sample temperature is reduced to a near ambient value. Alternatively, the electric field can be applied in air in a process called "corona" poling; a schematic of a poling rig is shown in Figure 1-5.

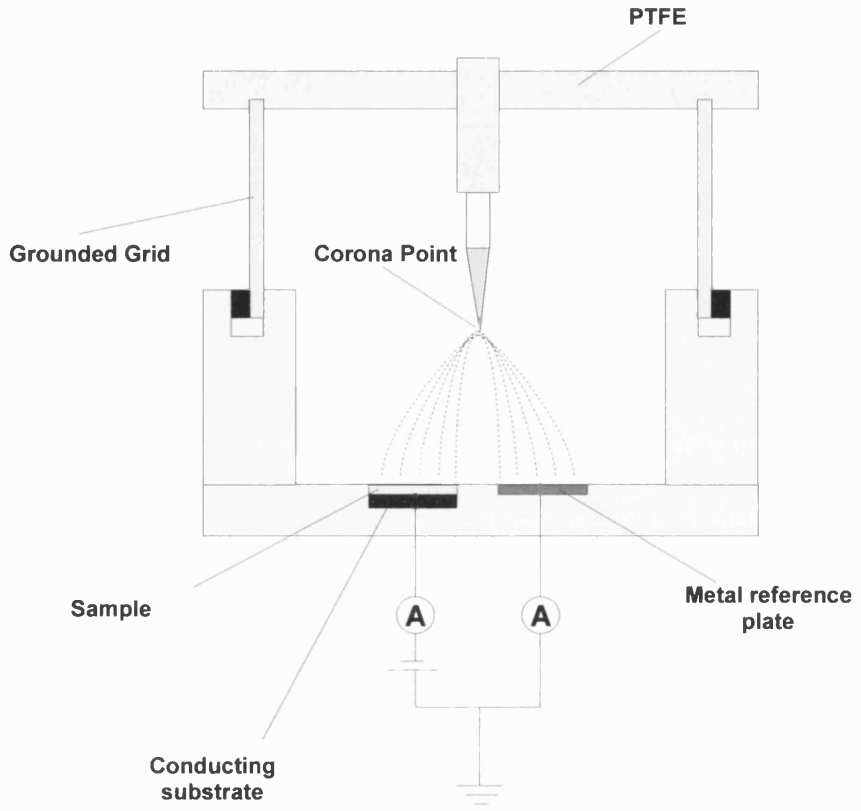

Figure 1-5: Schematic of a corona poling rig, from (3).

A high DC potential is applied between the corona point and the ground plate. At the corona point the air is ionised and attracted to the lower ground plate. This has the effect of "spraying" charged particles onto the surface of the sample. This creates a large electric field between the sample surfaces and thus aligns the domains. Heat is applied during the process and the sample is cooled under the electric field. Once the sample is cooled sufficiently the field can be removed and the material is poled.

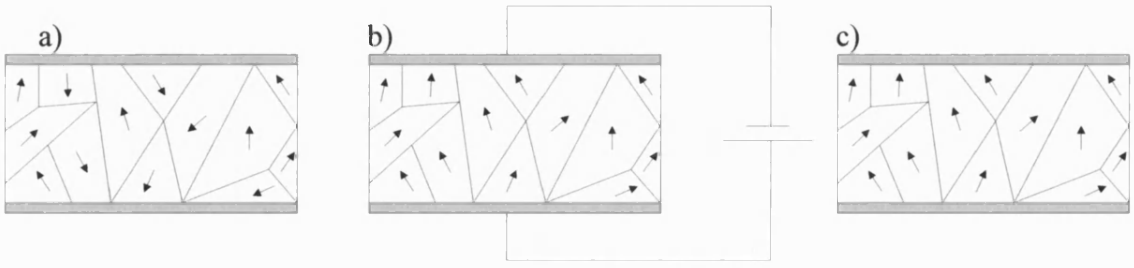

Figure 1-6: The poling process: a) random dipoles, b) heat and electrical field applied and c) once cooled the field is removed leading to a remnant polarisation.

In both types of poling procedure heat is applied in order to reduce the field strength needed to switch the domains by 180° and 90°. Poled ceramics can be depoled by application of high mechanical stress, high electric field or elevated temperatures, or a combination of these.

1.1.1.6 Effect of Composition of Common Materials to Improve Properties

Lead zirconate titanate (PZT) is a widely used piezoelectric material. Figure 1-7 shows the phase diagram of lead zirconate and lead titanate. On cooling the ceramic will either change structure from cubic to rhombohedral (in the case of more than 50% $PbZrO_3$) or tetragonal (in the case of more than 50% $PbTiO_3$).

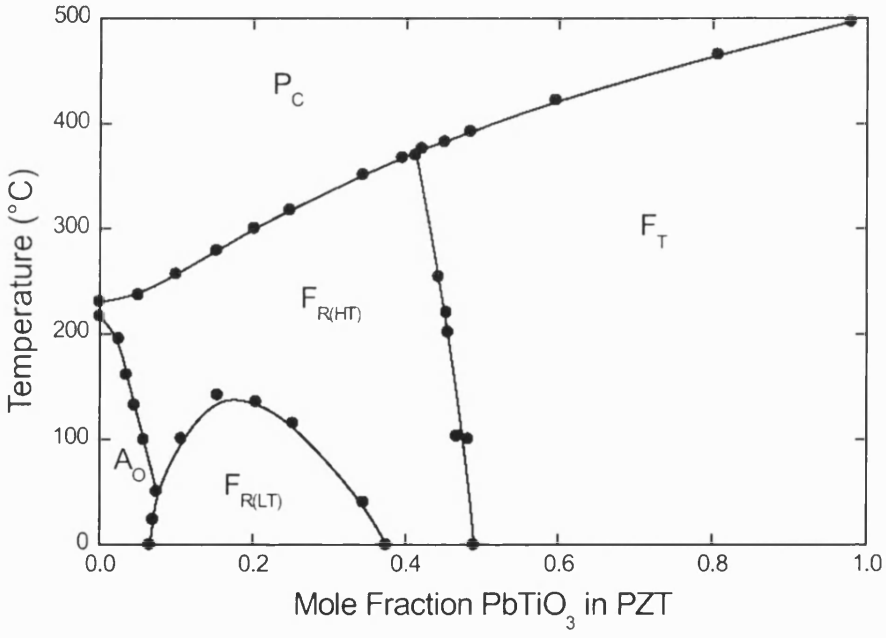

Figure 1-7: Phase diagram for lead zirconate titanate (PZT)[1].

PZT is commonly doped to change and tailor its piezoelectric properties, for specific applications. This doping is often classed either as "soft doping" or "hard doping". As these names suggest, soft doping will lead the ceramic to have softer properties, for example lower elastic coefficients and higher dielectric properties. Hard doping will have the opposite effect.

Soft doping can be achieved by doping PZT with large ions such as La^{3+}, Nd^{3+}, Th^{4+} and Bi^{3+}which are usually added to the raw PZT powder during the mixing process. The ions added in this case sit on the A sites in a solid solution (originally occupied by Pb^{2+} ions) and have a charge associated with them, larger than that of the lead ions. For electro-neutrality to be conserved, the extra positive charges present are counterbalanced with lead ion vacancies (V^{Pb}). For example, in the case of doping PZT with La^{3+} ions, a lead vacancy is created for every 2 La^{3+} ions occupying the lead ion A site as shown in Equation 1-1 below.

$$0.02La_2O_3 + Pb(Ti,Zr)O_3 \longrightarrow (Pb_{0.94}La_{0.04}V_{0.02}^{Pb})(Ti,Zr)O_3 + 0.06PbO$$

Equation 1-1: Pb vacancy creation by La^{3+} addition

If the dopant ion has an associated charge of 4^+ then a lead vacancy is created for every dopant ion in the lattice. Elements with smaller ionic radii such as Nb^{5+} and Ta^{5+} will sit in the B sites (Zr / Ti sites). These ions also have a higher positive charge associated with them than the host site, and this also creates lead ion vacancies[4]. Lattices where lead ion vacancies are present have a lower resistance to the transport of ions; they can "hop" into the vacancy spots. Because of this ease of movement, domain motion can be affected by lower electric fields, thus the coercive field is reduced. Increased energy spent in domain motion leads to high mechanical and electrical losses, but a high piezoelectric coefficient. The increased mobility of domains due to the lead ion vacancies results in a rapid release of internal stresses built up from poling the ceramic and therefore the properties of soft-doped PZT are stable sooner after poling than an under doped or hard-doped PZT.

Lead ion vacancies occur not only in doped PZT but also in pure PZT. During sintering, lead is lost to the atmosphere in the form of lead oxide (PbO). In this case the lead ion vacancy has a relative charge of 2^- (absence of 2^+ ion) and so, to preserve electro-neutrality, two holes (h^+) are created for every vacancy. These holes can combine with electrons attracted by the higher valence dopant resulting in high electrical resistivity.

The two factors of high resistivity and low energy domain wall motion give soft PZT's higher piezoelectric activities than hard PZT's, but also high dielectric losses.

Hard doping can be achieved by adding compounds containing ions such as K^+, Na^+ for A-site occupation and $Fe^{2/3+}$, $Co^{2/3+}$, Ni^{2+} for B-site occupation. Hard doping, as the name suggests, has the tendency to have the reverse effect of soft doping, resulting in lower dielectric loss and lower dielectric constant whilst increasing the coercive field and reducing the bulk resistivity. A hard doping ion will create oxygen vacancies in the lattice. These ions usually have a smaller charge associated with them than the host ion, creating a net negative charge which results in the oxygen vacancies being generated to ensure electroneutrality as shown in Equation 1-2 below.

For example:

$$0.02Fe_2O_3 + Pb(Ti,Zr)O_3 \rightarrow Pb\left(Fe_{0.04}Ti_xZr_{0.96-x}\right)\left(O_{2.98}V_{0.02}^{O}\right) + 0.01O_2$$

Equation 1-2: Oxygen vacancy creation by addition of Fe^{3+}.

The host ion in the lattice, in this case Ti^{4+} or Zr^{4+} has a charge associated with it of 4+; if the dopant ion has a charge of 3+ then one oxygen (O'') vacancy is created for every two dopant ions in the lattice.[4]

There are therefore a wide variety of materials available. In order to determine which material is most suitable for a particular application, such as a hydrophone, materials properties and related figures of merit need to be discussed.

1.1.2 Figures of Merit

A number of figures of merit are quoted when discussing piezoelectric materials and their applications; the following section will discuss them in detail, giving account of their origins and significance as a performance indicator in numerous applications, with particular reference to those applicable under hydrostatic conditions.

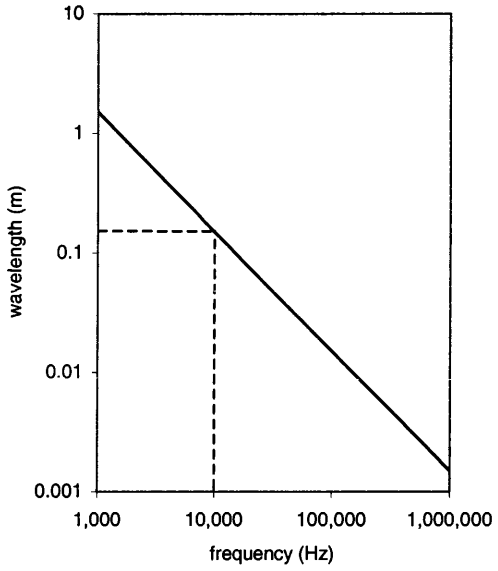

Figure 1-8: Graph showing frequency of acoustic wave against wavelength in water. Speed of sound in water is assumed to be $1500ms^{-1}$.

The graph in Figure 1-8 shows how the wavelength of an acoustic wave varies with frequency in water (speed of sound in water is $1500ms^{-1}$). The hydrophone devices of primary interest in this work are used at low frequency, typically 10kHz or lower. At these frequencies the wavelengths are greater than 15cm, this is larger than the typical active material in a hydrophone device. For this reason mechanical loads on the piezoelectric material under these circumstances are considered to be hydrostatic as the device lies within individual compressions or rare-fractions of an acoustic signal.

It has been stated that in an applied electric field a poled piezoelectric device will strain and when a stress is applied it will produce a charge. For these effects to be quantified certain coefficients need to be defined namely d_h, which is termed the *hydrostatic strain coefficient,* and g_h, which is the *hydrostatic voltage constant.*

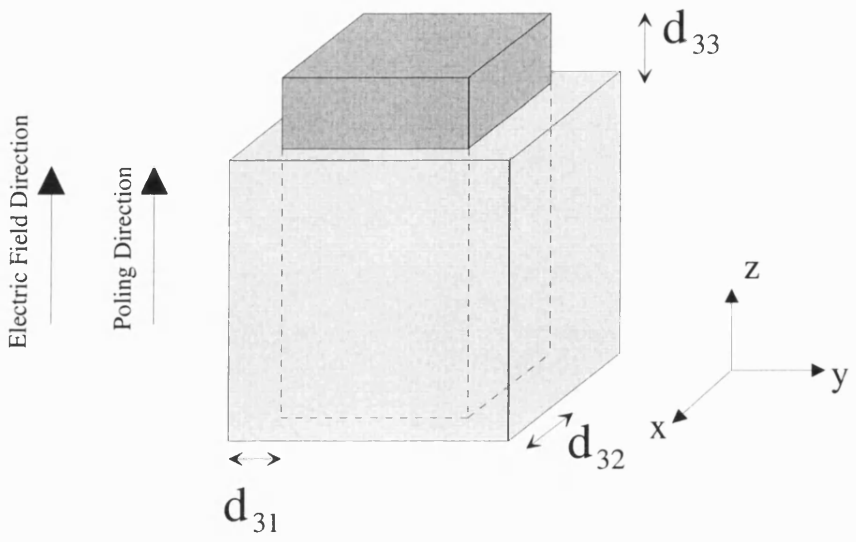

Figure 1-9: Definition of piezoelectric coefficients (d-coefficients).

Figure 1-9 represents a volume of piezoelectric material poled in the z direction as indicated. The light grey volume represents the original dimensions of the piezoelectric material before any electric field is applied. The dark grey volume shows the change in dimensions after an electric field has been applied to it. If both the electric field and the poling direction are as shown in the diagram, then the material will have a positive strain in the z (3) direction and a negative strain in the x (1) and y (2) direction.

The coefficient d_{ij} is the induced polarisation in direction 'j' per unit stress applied in direction 'i' or the mechanical strain induced in direction 'j' per unit field applied in direction 'i'.

Therefore the coefficient of d_{33} is the strain induced in the 3 direction by applying a field in the 3 direction or the charge developed per unit force in the 3 direction. The coefficient of d_{31} is the strain induced in the 1 direction by an electric field applied in the 3 direction or charge developed per unit force in the 1 direction.

As this thesis is examining hydrophone materials, the hydrostatic properties are of interest. The hydrostatic strain per unit electric field, or the charge generated per unit hydrostatic force, is given by d_h which is defined in Equation 1-3.

$$d_h = d_{33} + d_{32} + d_{31}$$

Equation 1-3: Definition of hydrostatic strain constant figure of merit d_h.

Figure 1-9 shows that d_{31} and d_{32} are negative with respect to d_{33}, i.e. as there is an expansion in the 3 direction there is a contraction in the 1 and 2 directions. If the material is assumed to be isotropic (i.e. $d_{31} = d_{32}$) then Equation 1-3 can be written as:

$$d_h = d_{33} + 2d_{31}$$

Equation 1-4: Commonly used definition of hydrostatic strain constant, d_h.

The units of d_h, if it is to be used as a sensor, are Coulombs per Newton (CN^{-1}). Hydrostatic sensitivity is typically measured in Volts per Pascal ($V\ Pa^{-1}$) and therefore the coefficient g_h is more appropriate for sensing applications and is defined as the electric field generated per unit hydrostatic stress, ($V\ m^{-1}\ Pa^{-1}$). The relationship between d_h and g_h are shown by the following equations.

Since d_h is the induced charge per applied hydrostatic force it can be written

$$d_h = \left(\frac{Q}{F_h} \right)$$

Equation 1-5: d_h in terms of force applied and charge induced.

where Q is charge and F_h is hydrostatic force.

Using basic equations of a parallel plate capacitor ($C=A\varepsilon_{33}/t$) and the relationship ($Q=CV$) between charge (Q), capacitance (C) and voltage (V) then,

$$Q = \frac{A\varepsilon_{33}V}{t}$$

Equation 1-6: Q in terms of AεV and t.

Where A is surface area (m^2), ε_{33} is the permittivity in the three direction ($F\ m^{-1}$) and t is thickness.

By combining Equation 1-5 and Equation 1-6, d_h can be written as follows.

$$d_h = \left(\frac{A\varepsilon_{33}V}{Ft}\right)$$

Equation 1-7: Combination of Equation 1-5 and Equation 1-6.

Re-organising gives

$$d_h\left(\frac{F}{A}\right) = \varepsilon_{33}\left(\frac{V}{t}\right)$$

Equation 1-8: d_h in terms of F/A (stress) and V/t (electric field).

This can be written in terms of hydrophone sensitivity, voltage developed per applied stress (V/σ).

$$\frac{V}{\sigma} = \frac{d_h t}{\varepsilon_{33}}$$

Equation 1-9: Hydrophone sensitivity (V/σ).

Hydrophone sensitivity (V/σ) for a given thickness of material is therefore dependant on d_h/ε. The electric field per unit hydrostatic stress is defined as the hydrostatic voltage constant, $g_h=V/t\sigma$, and from Equation 1-9 the relationship between g_h, d_h and ε_{33} is given by Equation 1-10.

$$g_h = \frac{d_h}{\varepsilon_{33}}$$

Equation 1-10: Relation between g_h and d_h.

Therefore for a *high sensitivity hydrophone* the material should exhibit a high charge per unit hydrostatic force (d_h) and a low permittivity (ε_{33}). This is the basis of piezocomposite structures which will be described later in the thesis.

The electromechanical coupling factor, k, is another useful figure of merit. This is the square root of efficiency of conversion of energy from mechanical to electrical or from electrical to mechanical and is defined as:

$$k^2 = \frac{\text{electrical energy converted to mechanical energy}}{\text{input electrical energy}}$$

or

$$k^2 = \frac{\text{mechanical energy converted into electrical energy}}{\text{input mechanical energy}}$$

Equation 1-11: Definition of coupling coefficient.

The properties of conventional dense PZT will now be discussed.

1.1.3 Properties of Different PZT Types

Many different compositions of lead zirconate titanate are used and each can be put into one of two groups, since piezoelectric materials can be designated as either hard or soft.

1.1.3.1 Hard and Soft PZT's

Many groups of materials can be classed into "hard" and "soft" subgroups. The terms "hard PZT" and "soft PZT" refers to how easily the piezoelectric domains align. Soft PZT exhibits little domain wall pinning, thus if the domain walls are free to move little energy is required to line up the domains. Because soft PZT materials are easily poled there are unfortunately easily de-poled. This can occur at modest temperatures or when exposed to high electric fields at room temperature, leading to a high loss material. Hence soft PZT materials are generally used for sensing applications due to their high charge generated per unit force (e.g. d_{33} and d_{31}), or for actuation purposes at low frequencies (<10kHz) or DC.

Hard PZT materials exhibit domain wall pinning and thus require higher electric fields to pole. This leads to hard PZT materials which remain poled under high temperatures, driving fields and mechanical stress. The d coefficients for hard PZT's tend to be

smaller than those of soft PZTs but they also have lower dielectric loss, which, along with their stability at high driving fields, lead them to use in applications as actuators at high AC fields.

1.1.3.2 Application of Hard and Soft PZTs

There are many applications of piezoelectric materials. The most common is the use of the direct piezoelectric effect to create a spark in order to light a gas flame. This direct effect can also be used in sensing applications where areas of high and low pressure deflect a ceramic producing an electric charge which can be measured.

The converse piezoelectric effect is used to produce small movements in actuators when exposed to an electric field, such as in accurate positioning systems.

Applications where the direct piezoelectric effect is used, as in sensing a strain and converting this to an electrical signal, tend to use soft piezoelectric ceramics. However, if high mechanical stresses are likely to be encountered hard PZT may be appropriate . Hard PZT's are used for applications where the ceramic is electrically driven at high frequencies and at high electric fields e.g. an ultrasonic bath. Figure 1-10 shows properties for a typical soft and hard PZT. The soft PZT-5H exhibits higher permittivity, d_{33} and dielectric loss and a lower Young's modulus and depole stress than the hard PZT.

	Relative Permittivity (const stress)	**Depole stress (MPa)**	**d_{33} pC N^{-1}**	**Dielectric loss**	**Young's Modulus (GPa) (unpoled)**
Soft PZT-5H	3400	44	593	0.04	48
Hard PZT-8M	800	>150	215	0.004	77

Figure 1-10: Properties of a selected soft and hard PZT[5]

The work in this report concentrates composites based on PZT for use in hydrophone devices; these are discussed in the following section.

1.1.3.3 The Hydrophone (Receiver) and Driver (Transmitter)

A hydrophone is essentially an underwater microphone. Acoustic waves in water (regions of localised high and low pressure) are directed into a piezoelectric material which converts the pressure variations into an electrical signal. This signal is passed to a preamp and analysed by a signal analyser.

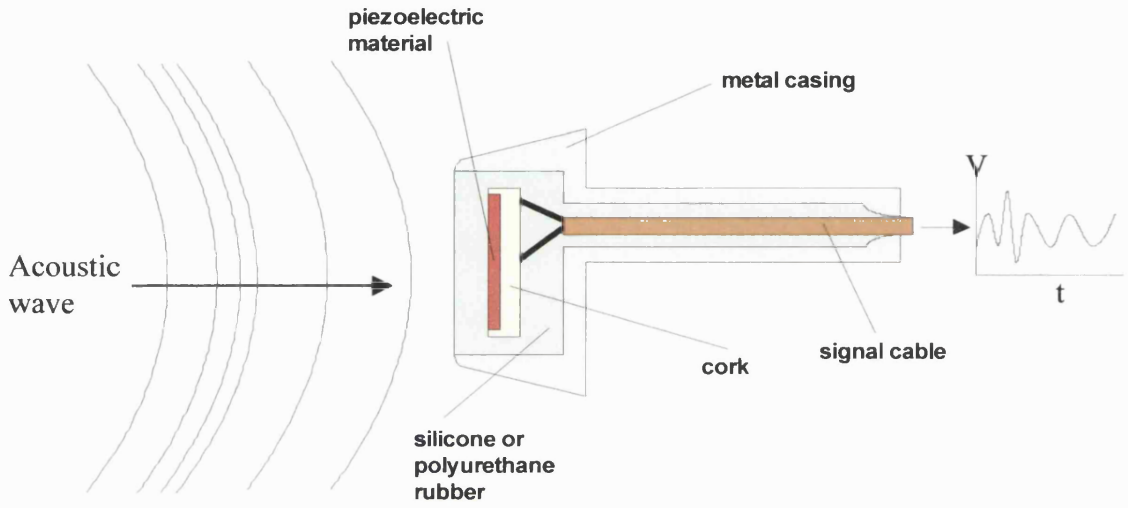

Figure 1-11: Schematic of a hydrophone (receiver). Acoustic waves are converted into electrical energy by the piezoelectric device.

Figure 1-11 shows a schematic of a traditional hydrophone (receiver). In operation acoustic waves are incident upon a silicone or rubber matching layer, which in turn transfers the pressure to the piezoelectric material. A hydrophone is passive and only receives signals from the water, however it is easy to envisage how the device could easily be modified to emit a signal i.e. the application of a voltage leads to strain in the piezoelectric material. A device used only for transmitting a signal is known as a driver. A single unit can be used to perform both tasks in a combined device. All three devices are used in SONAR (SOund Navigation And Ranging) applications.

The properties of the piezoelectric materials used in the three types of equipment vary significantly. For a hydrophone application (passive) device, a high sensitivity is required. Mechanical energy is transferred from the water to the device, therefore it is advantageous

for a high field per unit hydrostatic stress to be produced. This corresponds to the g_h figure of merit and soft piezoelectric materials can be used for this application. For active applications soft piezoelectric materials cannot be driven efficiently owing to their high loss, and therefore produce heat rapidly when driven. In addition, the high driving fields can partially de-pole and re-pole the piezoelectric ceramic.

A driver requires a different piezoelectric material, which must have a large remnant polarisation, such that de-poling does not occur during use. Hard piezoelectric materials are used for this application. They can be driven with large electric fields without excess heat build up and de-poling. In this application the piezoelectric ceramic produces strain which is transferred into the water, so it is advantageous for the selected material to have a large strain per applied electric field. This corresponds to piezoelectric coefficients d_{33} and d_h, depending on the mode of the driver and is shown in Figure 1-12.

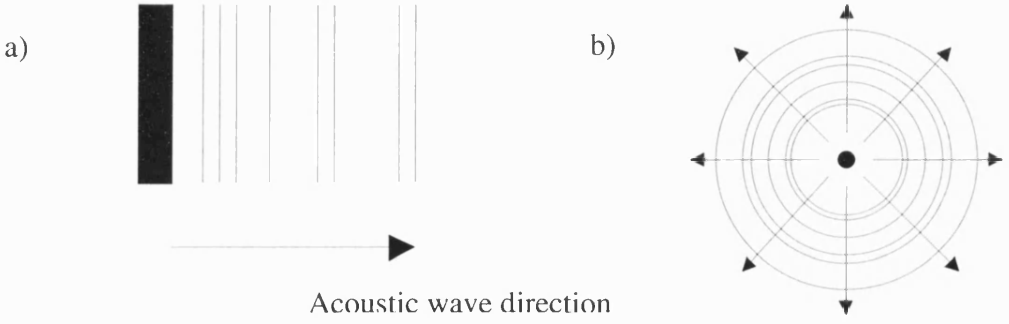

Figure 1-12: Example of two modes of sound wave propagation and corresponding d coefficient. a) single line source using d_{33} and b) point source using d_h.

If the device is to be used for sensing as for well as for driving then a compromise is necessary. The *hydrostatic figure of merit*, which is the product $d_h.g_h$ can be used to assess the performance of a device in both active and passive modes. A combined hydrophone and driver can be used where space or weight is restricted and when power requirements are low. A high hydrostatic figure of merit ($d_h.g_h$) is also reported to imply a high signal to noise ratio[6].

For a hydrophone device to work efficiently when submerged in water there must be efficient transfer of acoustic energy from the water into the piezoelectric material. Likewise, if an active device is to perform at its optimum then it has to be able to transfer energy from the piezoelectric driver into the water effectively. The difference in acoustic impedance of

the two different media, PZT and water for example, will determine the amount of energy transferred into and reflected by the hydrophone. The acoustic impedance (Z) of a material is defined as the product of the density and the sound velocity.

$$Z = \rho V$$

where Z = acoustic impedance
ρ = density
V = sound velocity

Equation 1-12: Definition of acoustic impedance.

The relationship between sound velocity, Young's modulus and density is given by Equation 1-13.

$$V = \left(\frac{E}{\rho}\right)^{\frac{1}{2}}$$

where E = Young's Modulus

Equation 1-13: Sound velocity and material properties relationship.

Substituting Equation 1-12 and Equation 1-13

$$Z = (\rho E)^{\frac{1}{2}}$$

Equation 1-14: Acoustic impedance as a factor of density and Young's modulus.

Once the acoustic impedance of each phase material is known, the fraction of energy reflected and transmitted at the interface of the two materials can be calculated from Equation 1-15.

$$R = \left(\frac{Z_2 - Z_1}{Z_2 + Z_1} \right)^2$$

where R = fraction of energy reflected

Z_1 and Z_2 are acoustic impedances of the two media.

Equation 1-15: Reflected fraction as a function of acoustic impedances.

Using these equations and substituting the properties of water and PZT-5H, 75% of the acoustic energy is reflected at the water / PZT interface. This efficiency is obviously unacceptable for hydrophone applications. The high reflected fraction (R) is due to the fact that acoustic impedances for PZT and water are significantly different. To efficiently transfer energy between two different media it is a requirement that the difference in acoustic impedances of both components ($Z_1 - Z_2$) should be reduced significantly.

To increase the efficiency of transfer between dense PZT and water, another material with an acoustic impedance of magnitude between those of the two specified materials is often inserted at the interface. Common materials are silicone rubber or low modulus polymers. For a polymer with a density of 3000kg m^{-3} and a modulus of 20 GPa, 50% of the incidental acoustic energy is transmitted at the water / polymer interface and 83% of energy is transmitted at the polymer / PZT interface. In total around 40% of energy is transmitted from water to the PZT. This is shown diagrammatically Figure 1-13 which shows that the "impedance matching layer" between the PZT and water reduces the amount reflected.

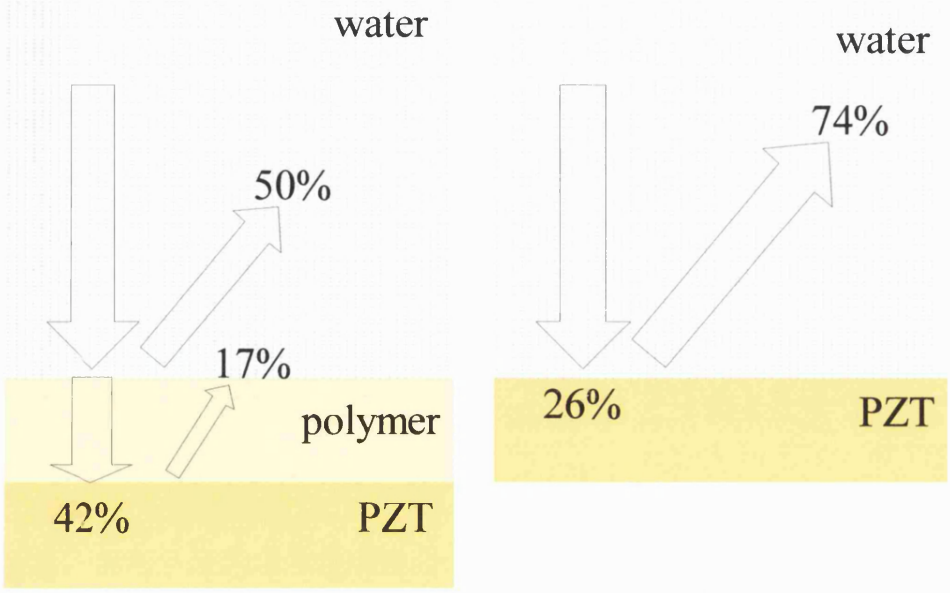

Figure 1-13: Schematic of acoustic energy reflection a) with and b) without matching layer.

It can be seen from this example that if the density and elastic modulus of the piezoelectric material itself was reduced and approached that of water, more acoustic energy would be transmitted into it and the need of a matching layer would be removed. This is one benefit of a piezocomposite material and will be discussed later in the thesis.

A large number of applications exist for piezoelectric transducers operating for acoustic applications. Primary uses are for sonar array systems, both active and passive. Civilian uses include ultrasound scanners for medical applications, proximity sensors in a range of new cars, high frequency speaker drivers for home hi-fi, even small speaker units in novelty birthday cards are made from piezoelectric transducers.

Of course there are many other uses for transducer devices other than those related to the propagation and sensing of acoustic waves. As actuators they can and are used in any application where accurate, fast, or small movements are required. For example, small accurate movements are required in the positioning of AFM probes, which uses the piezoelectric effect. Inkjet printers require very fast and accurate movement and piezoelectric elements are used to direct ink from the injector. Other applications include spark ignition systems and internal combustion engine injection systems.

1.1.4 Piezoelectric Devices and Piezocomposites

A piezoelectric device has many operating parameters. A number of these are determined by intrinsic factors such as the material selection, or device design and others by external factors such as attached electronics, space, cost or weight constraints. The important operating conditions related to the material selection of dense monolithic materials have been discussed for hydrophone applications. However, a piezoelectric material can behave radically different if it becomes part of a composite structure (a "piezocomposite"), which includes other phases, piezoelectric or passive. One of the most important factors in a composite material is its architecture and how the two or more material phases are interconnected to themselves and the other phases.

1.1.4.1 Connectivity in Piezocomposites

Traditionally research into piezoelectric devices has concentrated on producing monolithic samples with high densities. However, certain piezoelectric materials with low density, i.e. high porosity, have been shown to have much improved values for d_h and g_h. If the structure of the piezoelectric material contains pores, or a second phase such as a polymer it is termed a "piezocomposite". There are a number of different ways in which the two phases can be connected. These different arrangements are termed the 'connectivity' of the phases and the nomenclature used is now discussed[7].

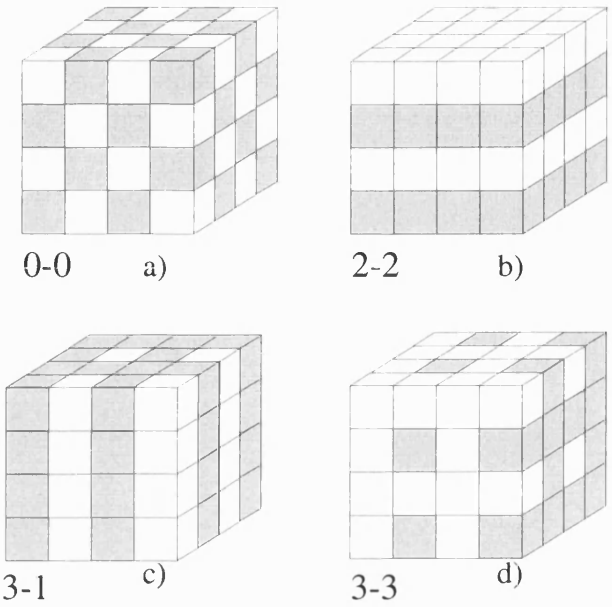

Figure 1-14: Examples of structures showing different connectivities. Adapted from (7)

Each phase has zero, one, two or three-dimensional connectivity to itself. This is denoted by two numbers in the form "X-Y". Schematic examples of selected connectivities for two phase composites are shown in Figure 1-14. The first number (X) refers to the piezoelectric or active phase, and the second number (Y) refers to the passive phase whether this be air or an introduced second phase such as a polymer. For example, a 1-3 composite corresponds to rods or pillars of piezoelectric in a continuous polymer phase and a 0-3 corresponds to individual piezoelectric particles in a continuous polymer phase, as shown with other common connectivities in Figure 1-15.

The work in this thesis is concerned with the 3-3 type of composite, which is shown in Figure 1-14d. In this type of composite each phase is connected to itself in three dimensions and produces two fully interpenetrating phases.

1.1.4.2 Common Connectivity Devices

There are many ways in which to produce a piezocomposite. Figure 1-15 shows some of the most common configurations of composites along with their respective connectivity. In each case the properties of piezocomposite depend on the architecture, volume fraction and properties of each phase.

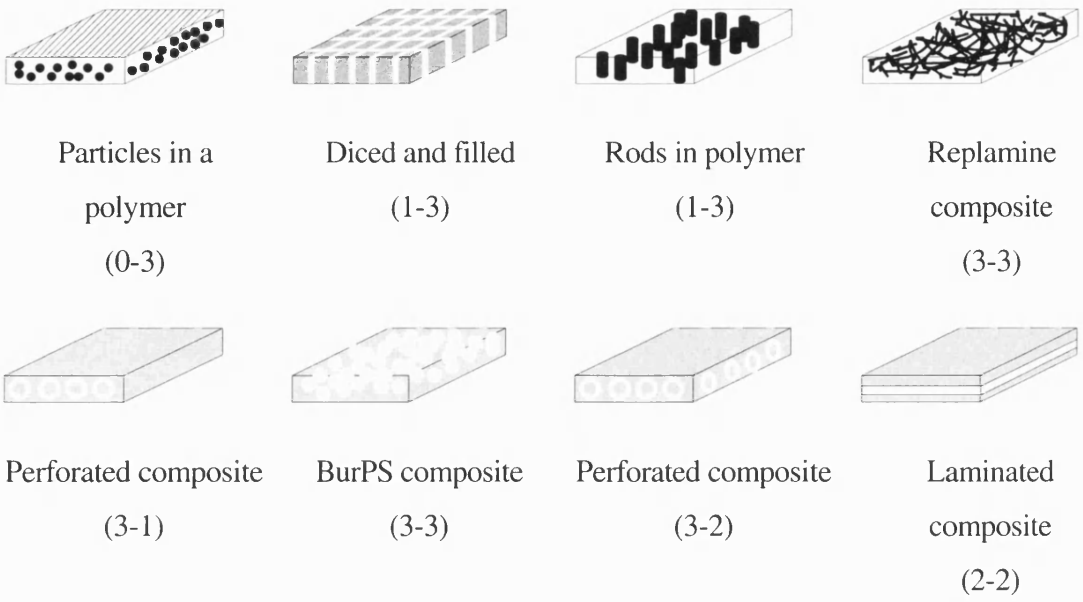

Figure 1-15: Different examples of piezocomposites with corresponding connectivities. From (7).

1.1.4.3 Mechanism Behind Connectivity Improvements

Hydrophones are often used at low frequencies (f<10kHz) in water. The speed of sound in water (v) is approximately 1500m s^{-1}. As $v = f\lambda$, the wavelength (λ) of the acoustic waves are typically 0.15m long or greater. A hydrophone would therefore sit completely within a single wavelength and the pressure on a hydrophone device at this frequency would be hydrostatic.

The charge per unit hydrostatic force $\left(\frac{Q}{F_h}\right)$ is represented by d_h and the sensitivity $\left(\frac{V}{m,Pa}\right)$ is represented by g_h. These two coefficients are related by the following equation.

$g_h = \frac{d_h}{\varepsilon_{33}}$ where ε_{33} is permittivity.

It has already been shown that to maximise the sensitivity of a low frequency hydrophone g_h should be maximised. This can be achieved by either having a low permittivity, ε_{33}, or a high

value of d_h. The advantage of some piezocomposites is that the polymer phase has a much lower permittivity than the piezoelectric phase. This lowers the composite permittivity and thus leads to an increase in g_h. In addition, the value of d_h can be increased by increasing the value of d_{33} relative to the value of d_{31} and effectively decoupling the d_{33} and d_{31} values.

3-3 piezocomposites can be regarded as highly porous piezoelectric materials where both the ceramic and the porosity are interconnected. Work to date has shown that these materials are promising as potential materials for low frequency hydrophones due to increased d_h and g_h values [7]. However, while there has been considerable work on systems such as 1-3 composites there is little work on understanding the role of the volume fraction of porosity and the mechanism of how high d_h values are achieved. This is the main aim of the thesis.

The production methods for these ceramic composites will now be discussed.

1.2 Fabrication Methods of Ceramic Composites

The production methods of piezocomposites will be discussed in subsequent sections with particular attention given to the production of 3-3 piezocomposites, i.e. piezocomposites with both phases interconnected in three dimensions, which is the subject of this thesis. The production of other connectivity composites will also be discussed where the methods used are relevant.

1.2.1 Established Production Methods

Porous piezoelectric structures can be manufactured in a number of ways. The most common methods of manufacture are discussed in the following sections, starting with simple and inexpensive methods used for mass production leading to complex and expensive methods used for high value applications. In addition, novel methods of production will be discussed despite these methods being used for research purposes only or being reserved for very specialist applications, where cost is secondary to performance.

In many cases the porous piezoelectric needs to be impregnated with a second, passive phase. This can be left as air, or a polymer or rubber can be infiltrated into the structure. The difficulty of this infiltration process is usually a function of the size and interconnection of the pores in the ceramic.

1.2.1.1 Incomplete Sintering

By far the most simple way to create a porous ceramic body is not to sinter the green body to full density. This technique of producing a porous ceramic sample creates small amounts of closed microporosity, which is very difficult to impregnate with a second phase of passive material. This procedure is not widely used as it often leads to poor mechanical and electrical properties of the device. It is for this reason that this method is not employed in the production of 3-3 piezocomposite structures.

1.2.1.2 BurPS (Burnt out Plastic Spheres)

The BurPS technique, which stands for "burnt out polymer spheres", was first used by Shrout, Schluze and Biggers[8]. This method involves the mixing of an inclusion material with the ceramic powder prior to the pressing stage. This inclusion material may be polymeric, organic or non-organic and whilst the most common shape of the inclusion is spherical, this is not a essential requirement. During subsequent heat treatment the inclusion material is burnt off using temperatures in the range of 300 – 600 °C and the fully sintered ceramic body is left with permanent pores within the microstructure.

Due to the fact that the inclusion material is used to produce the pores in the ceramic structure, the ceramic body can be fully sintered to produce optimum mechanical and electrical properties, unlike the incomplete sintering method described above. In addition, the size and geometry of the final pores in the ceramic body can be closely controlled by changing the size, shape and volume fraction of the inclusion material mixed into the ceramic powder at the start of the production process[8].

Anisotropy can be introduced into the structure by mixing in inclusion particles which are non-symmetrical. These can be aligned by the pressing process or by tape casting to produce anisotropy in the sintered ceramic sample.

The advantages of the BurPS method are numerous. The method requires no specialist equipment other than is normally used in a basic ceramic fabrication laboratory and it is thus cheap, quick and simple to perform. This method produces net shape fabrication of components, which is not always possible with some of the other techniques reviewed in this section.

The BurPS method does have some major drawbacks, for instance it can only be used to create porous samples with less than 50% porosity. If a higher degree of porosity is required, a large amount of volatile inclusion material is added to the ceramic powder which results in a poor green strength. The sample is also likely to collapse under subsequent heat treatment as the inclusions melt or are burnt out.

Careful selection of inclusion material is also important. Heat treatment of the green body means that the inclusion material should ideally sublime in order to minimise stress to the ceramic body whilst still in its green state[8].

The BurPS method is therefore appropriate for low to medium porosity ranges. To manufacture materials with porosities of over 50% volume fraction alternative techniques have been researched.

1.2.1.3 Polymer Foam Reticulation

Schwartzwalder and Somers[9] first patented the method of polymer foam reticulation in 1963. A polymeric sponge is impregnated with a ceramic slip, with a subsequent heat treatment of the sample to burn off the liquid in the ceramic slip and the original polymer sponge at a higher temperature. An extended heat treatment is then used to fully sinter the ceramic.

Careful selection of both the foam and the slip properties are required if this method is to be fully exploited. The foam selection is based upon the ability of the foam to burn off at a low temperature and, for convenience, not to emit any toxic products. As in the BurPS method, the inclusion foam should not introduce any significant stresses into the ceramic body during heat treatment. A number of different polymeric foams are suitable for this technique. The most commonly used foams are poly(urethane), poly(vinyl chloride), poly(styrene), cellulose and latex.[10]

In addition to selecting the foam, the ceramic slip needs careful preparation. The slip commonly has three components, ceramic powder, a suspension medium (usually water) and additives as binders. These ceramic slurries usually contain between 50 and 70% solids (by volume) and it is generally advantageous to use a fine particle size ceramic powder (<5μm). For improved adhesion of the ceramic slip to the foam, equi-axed particles of under 40μm with a narrow size distribution are desired[10]. By tailoring of the surface tension and viscosity of the slip, the polymer foam reticulation method can be used to produce structures with open, semi-open, and closed cell foams.

In addition to selecting pore type, the pore size and shape can be tailored to almost any requirement by selecting the appropriate starting foams. The grades for foams are quoted in pores per inch (ppi) and most typical foams used for this application are in the 15 to 60ppi range. Near net shape forming is possible, although as pore size increases this becomes more difficult due the large roughness at the edges of the foam body. Ceramic foam structures are difficult to machine as they have poor mechanical properties. As the porosity increases (>90% by volume), machining becomes impossible without damage to the sample.

As the impregnation process of the ceramic slip into the foam is the same for all types and pore sizes of foam, there is considerable scope for the production of complex structures with porosity gradients or even step changes in pore size and density, i.e. functionally graded structures, which will now be discussed.

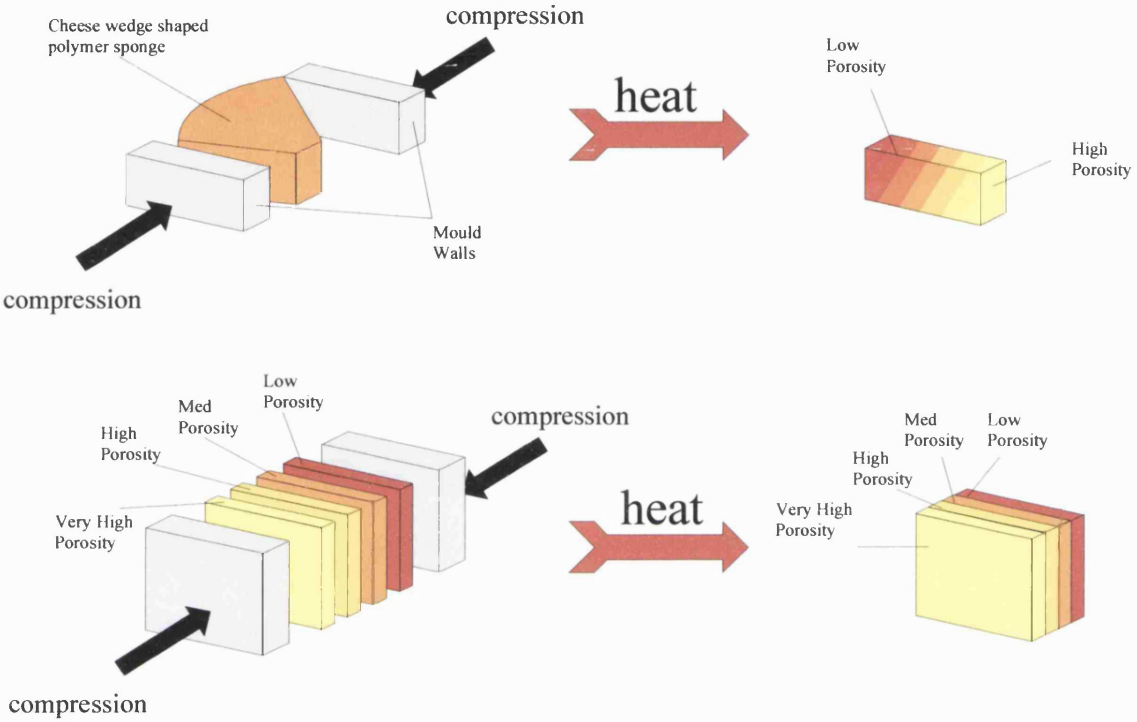

Figure 1-16: Method of producing variable porosity a) continuous gradient and b) incremental steps. After (10)

One method for achieving a porosity gradient across a sample was first reported by Cichocki & Trumble[10] and is shown schematically in Figure 1-16. Here polymeric sponges are cut into "cheese wedge" shapes, compressed into regular cuboids whilst being heat-treated. This produces a continuous porosity gradient throughout the sample. It is also possible to have step changes in porosity. This is achieved by using many different grades of foam, compressing them together and heat-treating the foam "sandwich". After impregnation and subsequent heat treatment of the foam, a porous ceramic with graded porosity is obtained. This structure can be useful where a less dense outer casing is required in order to aid the acoustic matching of the composite to the source medium.

The polymer foam reticulation is a simple process, which can be used to produce a wide variety of different porous ceramic structures[10]. For this reason it is widely used, and requires no specialist equipment other than that usually found in a ceramics laboratory.

1.2.1.4 Foaming Slurry

The foaming slurry process utilises the *in-situ* polymerisation of an organic monomer to stabilise the foams produced from a ceramic slip[11]. A standard ceramic slip is prepared in the same way as used in the polymer foam reticulation method previously discussed. A foaming agent is added to the mixture which is chemically or mechanically agitated using a high shear mixer. The polymerisation of the monomer traps the ceramic powder into the foamed structure and prevents the slip from collapse. In some cases the polymerised slip can be machined before heat treatment and sintering.

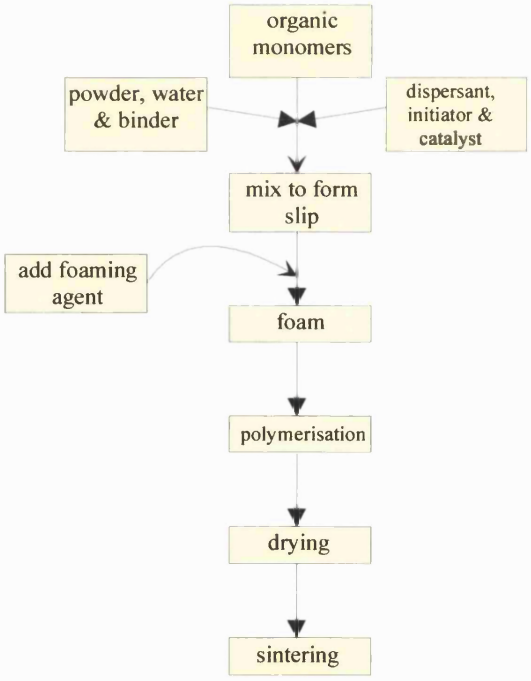

Figure 1-17: Process flow chart for the production of ceramic foams by a foaming slurry technique. After (11).

The amount of foaming agent in the slip and the viscosity of the slip determines the final density of the foam. This can be tailored to produce a wide range of final macrostructures from highly porous open cell foams to low porosity closed cell structures.

The polymerisation reaction needs careful control but once the reaction is complete the foams can be removed from the mould, machined if necessary, and heat-treated.

This method is used to produce porous ceramics with small pore sized (<0.5μm) closed cell foams. This is the only method reviewed capable of producing such a structure. Once a process is established, the technique can be scaled up or down with little user intervention.

1.2.1.5 Coral Replamine

The coral replamine method[12] is a double infiltration process which has mainly been superseded by the polymer foam reticulation method detailed previously.

The starting point for this method is a natural coral structure, which can be shaped into the desired final ceramic image. The coral structure is filled with molten wax, which solidifies. Hydrochloric acid, or an equivalent, is then used to leach out the coral phase which is usually $CaCO_3$, before the structure is re-impregnated with the desired ceramic slip. The slip contains a high volume fraction of solid ceramic powder, a dispersant and a binder.

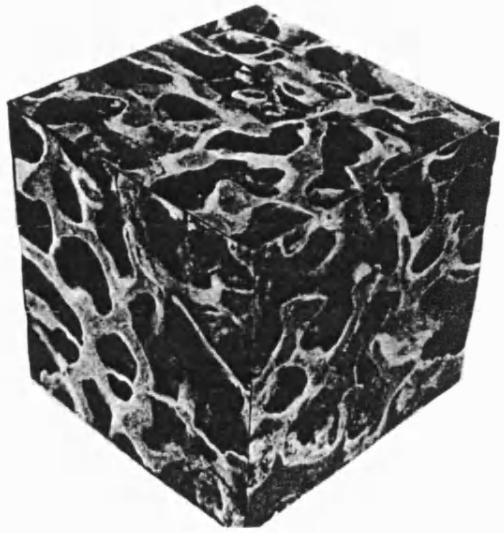

Figure 1-18: Simulated coral cube obtained from micrographs[12]. The pores are 60μm across.

A heat treatment at around 300 °C is carried out to burn out the wax phase before final sintering of the ceramic phase. The ceramic foam remains, which has the exact structure of the initial coral material, which can then be backfilled with a polymeric phase such as an epoxy or a silicone rubber if desired.

A simulated microstructural cube is shown in Figure 1-18. The pores in the figure are approximately 60μm and are open. This structure is typical of materials prepared by this production method. The advantage of this method is that the structure of the final ceramic is the same as the starting structure of the coral. The coral is mechanically strong and can be machined to the desired shape before the wax impregnation process begins. However machining ceramics is usually a costly process and this method is also time consuming, as up to three impregnation steps are required. It is for these reasons that this method is now rarely used.

1.2.1.6 Dice and Fill

This method of dice and fill, reported by Janas[13] in 1995 involves the direct machining of a pre-sintered, dense PZT ceramic body. A series of parallel cuts are made in a block of PZT, the block is rotated by 90° and the same cuts are made at right angles to the original set of cuts. This is illustrated schematically in Figure 1-19. A series of PZT rods attached to a base plate remain to allow ease of handling[13].

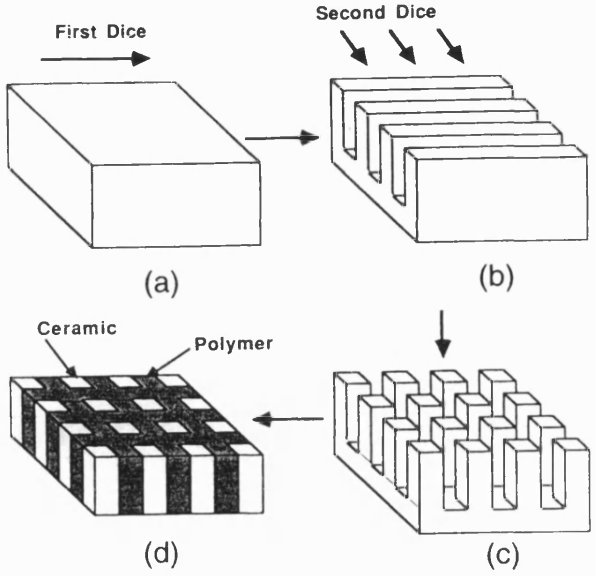

Figure 1-19: Schematic of the dice and fill technique. After (13).

This structure is backfilled with polymer and the composite is then removed from the base. This method is commonly used to produce 1-3 connectivity piezocomposites (piezoelectric rods in a polymer matrix), which have many uses, including hydrophones. It is very difficult to manufacture a 3-3 composite with this method. Multiple layers have to be produced and layered in a staggered format before sintering.

The structure of the final ceramic is limited by the width of the dicing saw used to cut the groves in the ceramic block. Piezoelectric rods measuring 100μm on each side have been produced, but require a blade around 25μm in width to perform such a task. Cutting at this scale is very time consuming. The key to such small-scale structures is a well sintered, fine grained, dense ceramic, strong enough to withstand fine scale machining[13].

1.2.1.7 Lost Mould Technique

The "lost mould" method is another procedure for producing fine scale, intricate detail piezocomposites. Again this method is a "double infiltration" method similar to the "dice and fill" method explained above and is suitable for producing 1-3 composites. A schematic of the process is shown in Figure 1-20 and starts with a negative of the desired piezoelectric phase in the form of a wax or polymer mould. The production of this mould can be costly as a metal mould insert is first needed (usually manufactured by lithography, galvanoforming and plastic moulding) in order to produce the high quality plastic mould.

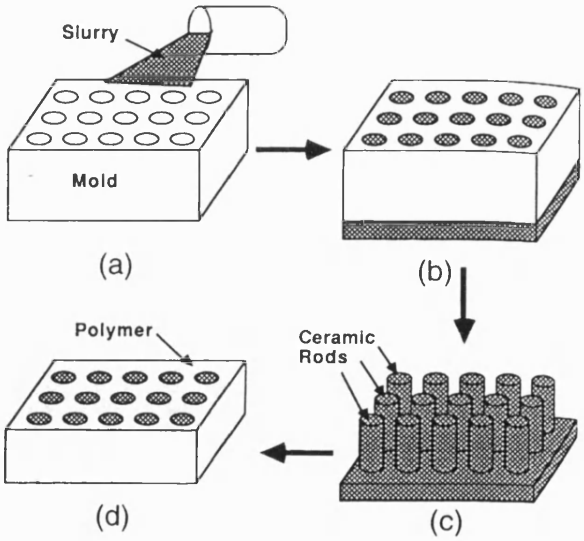

Figure 1-20: Schematic of the lost mould production method of piezocomposite manufacture. After (13).

This mould is filled with a ceramic slurry containing the desired piezoelectric compound and is allowed to dry. The mould is burnt off and the ceramic sintered, leaving a structure which can be back filled with a polymer. This technique can produce both 1-3 and 3-1 composites. An example of a 3-1 composite is a ceramic honeycomb structure with polymer rods as the second phase. The ability to produce these structures as well as the more common 1-3 composites is the major advantage of this method over other "double infiltration" methods.

The disadvantages of this method are similar to the "dice and fill". The process is time consuming and composites are expensive to manufacture, restricting samples produced by this method to areas where cost is a secondary issue.

1.2.1.8 Injection Moulding

Fine scale composites with 1-3 and 2-2 connectivities can be manufactured by injection moulding[13]. This method is versatile and can produce a wide variety of rod sizes, shapes and spacings. Figure 1-21 shows a schematic of the process. The process of injection moulding is simple and not time consuming. It is only possible to mass produce relatively small panels of piezoelectric rods but the panels can be arrayed together to form a large area prior to back filling with a polymeric second phase.

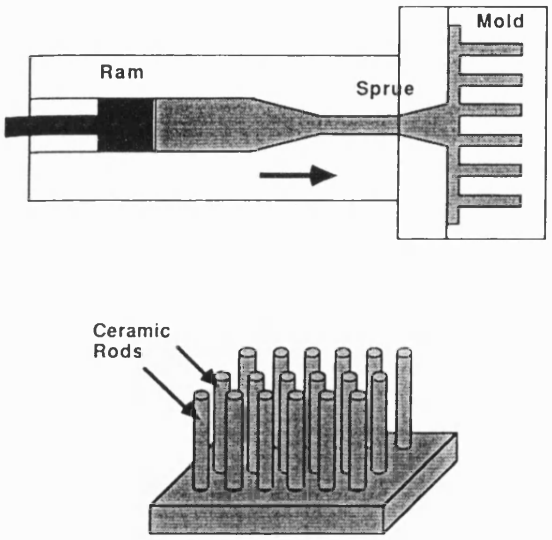

Figure 1-21: Schematic of ceramic injection moulding. After (13).

Injection moulding has the advantage of being able to produce multi-phase ceramic composites, should they be needed[13]. This method of manufacture is best suited to large volume production and not suited to prototyping for research purposes as the set-up of the equipment and machining of the moulds is a time consuming and costly exercise.

1.2.2 Novel Methods of Manufacture

A number of novel methods for manufacturing ceramic composites have been reported. These processes are generally time consuming and expensive, but the requirement to produce exact and fine structures means that novel process are sometimes used. Inkjet printing, ultrasonic cutting and piezoelectric fibre weaving are three manufacturing methods recently used to produce piezocomposites.

Ink jet printing can be used to freeform three-dimensional ceramic structures. These structures can contain small scale features. Whilst primarily used for 1-3 structures, it is possible to produce 3-3 structures by printing a sacrificial phase (such as carbon) to support overhanging volumes [14].

Ultrasonic cutting can be used to produce 1-3 composites much in the say way as in "dice and fill". The feature size can be reduced significantly if ultrasonic cutting is used in place of a conventional bladed cutter. However, this process is again costly and time consuming as well as not being suitable for 3-3 composites.

Finally, a method of producing a 3-3 interconnecting structure is by weaving piezoelectric fibres in a three dimensional pattern. These can then be sintered to produce a 3-3 composite. Fibres can be manufactured with relative ease, however care is needed during the weaving process to ensure the fibres are not damaged. This method produces a very intricate 3-3 composite but is costly due to the use of PZT fibres, and is time consuming[15].

The most common methods of processing piezocomposites and porous piezoelectric structures have been discussed. The advantage of 3-3 composites compared to other systems, such as 1-3 composites, is that relatively low cost materials and processes can be used to manufacture these materials (e.g. BurPS, polymer foams). The following sections will discuss the effect that porosity and a second phase has on mechanical and electrical properties of piezocomposites.

1.3 Properties of Ceramics as a Function of Porosity

The properties of piezoelectric composites can vary significantly from those of a monolithic material. The research presented in this thesis is primarily concerned with the electrical properties of piezocomposites, however mechanical properties are important in manufacturing and handling of piezoelectric composites.

The influence of porosity on both mechanical and electrical properties of porous materials is discussed in the following sections.

1.3.1 Mechanical Properties

The mechanical properties of piezoelectric composites are important in two ways. Firstly the manufactured composites have to be robust enough to cope with processing conditions. Many piezocomposites are manufactured in a number of stages, some of which expose the composite to mechanical and electrical stresses.

Secondly, any piezocomposite must be able to withstand any stresses, which are experienced under operating conditions. Fortunately during operation as a hydrophone device they are used in high precompression and are therefore not normally required to have high mechanical strengths. However, the increase in pressure on the hydrophone with water depth may be an important parameter.

A number of mechanical properties have been researched in the literature for structural ceramic foams. These are Young's Modulus (E), fracture toughness, (K_{IC}), flexural strength (σ_f), compressive strength (σ_c) and compressive strain to failure (ε_s). Unfortunately research into a full range of porosities for a given pore structure has not been completed. This is due to each individual method of production only producing porous structures with a restricted range of densities. To manufacture foams with all possible densities, different production methods must be used such as BurPS (for low porosity) and foam impregnation or another method (for high porosity). Each production method produces different microstructures which will therefore have an effect on mechanical properties.

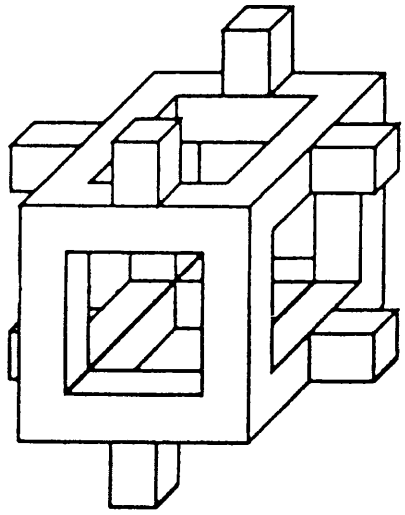

Figure 1-22: Open cell foam model. After (16).

The characteristic model of *a brittle* open cell foam is shown in Figure 1-22. As one would expect, Young's modulus changes significantly with the amount of porosity present. In many cases, the Young's modulus decreases with increasing square of porosity as shown in Figure 1-23, although this is not true for all materials [16]. In addition, as the number of pores per inch increases the probability of there being a significant number of closed pores as well as open pores increases, which will influence the mechanical properties.

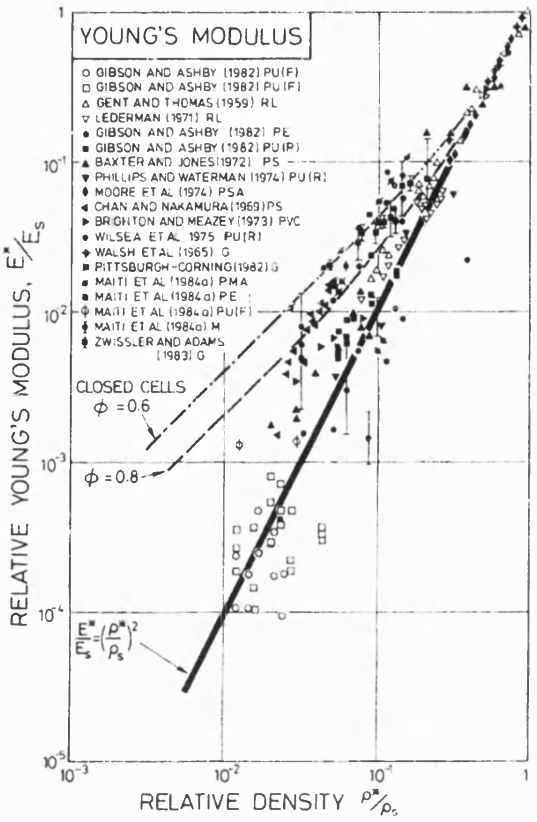

Figure 1-23: Young's modulus vs. density, after 16

Fracture toughness as a function of porosity is a well-documented property. Generally fracture toughness decreases with density, which is dependent on the cell edge strength[16]. To increase the edge strength and thus the fracture toughness, the ceramic foam needs to consist of thick walled large pores and microstructural defects such as cracks and microporosity have to be eliminated.

Under a tensile stress, Ashby's [16] model predicts that the struts parallel to the load direction will fail first, therefore the tensile strength of the foam will be related to that of the tensile strength of the cell edges. In reality the foam cells tend to be randomly oriented and not perfectly aligned as in Figure 1-22. This means that the failure mechanism is most likely to be bending. For a given density the tensile strength will increase with increasing strut strength. Again this property is enhanced by having a large celled, thick walled structure.

Tensile strength varies almost linearly with density. As previously discussed, at high numbers of pores per inch the dependency decreases which is due to an increase in the number of closed cells which affects results significantly[1].

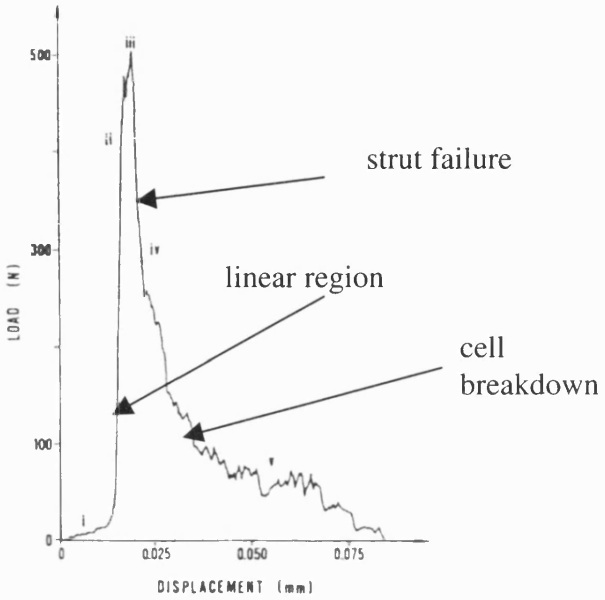

Figure 1-24: Typical load-displacement curve for a mullite foam[1].

Figure 1-24 shows a typical load curve for a compressive strength test on a porous ceramic. Initially, linear elastic behaviour is observed, with very few strut failures. This is represented by the approximately straight line to the left of the plot. At the peak load, large cracks propagate throughout the sample corresponding to strut failure and a large drop in load. It can be seen towards the right of the plot, in the noisy region, the load increases slightly before cell breakdown. This process continues until densification, where there can be a small but significant load increase.

Here the relationship between compressive strength and density is not as clear. There is a slight tendency for the compressive strength to increase with density, as one would expect, but the scatter from the data in the literature is very large[16]. Closed cells being present within the structure may be the cause of the discrepancy. These would have a larger effect on the compressive strength than on the tensile strength due to the mechanism of cell collapse. A collapsed cell can still bear load in compression, whereas it cannot in tension.

1.3.2 Piezoelectric Coefficients

A number of piezoelectric coefficients have been researched with respect to the effect of porosity on them. In this section d_{33}, d_{31}, ε_{33}, d_h, g_h, and $d_h \cdot g_h$ will be discussed with respect to varying porosity. There is little literature covering porous 3-3 piezoelectric composites and their properties as a function of porosity content, morphology and size. Only isolated cases are present in the literature, therefore a comparison across a wide range of densities is not possible. The research carried out in subsequent chapters of this thesis attempts to present a wider overview of piezoelectric properties of 3-3 composites over a wide range of porosities.

As defined in the first section, d_{33} is the strain per unit electric field parallel to the applied field and poling direction. This value decreases with reducing density as there is less bulk lying in this direction and is shown in Figure 1-25a. Initially, the reduced d_{33} would imply that porous structures would not be suitable for such applications as hydrophones. However, other properties change with porosity which make them considerably more attractive compared to the bulk material.

The d_{31} coefficient is the contraction normal to the applied field that accompanies the d_{33} expansion. This value is negative and also reduces in magnitude as porosity increases, effectively becoming closer to zero.

For 3-3 composites the value of d_{31} is more dependent on the density than d_{33} and for 3-3 composites it has been reported that there is a linear increase in d_h ($=d_{33}+2d_{31}$)with increasing porosity up to 50%[17]. The increase in d_h is up to 400%, when compared to a fully dense ceramic material. For 1-3 composites the d_h shows a high dependency at low ceramic volume fractions, reaches a maximum around 20% to 30% ceramic volume fraction, depending on structure and piezoelectric material used, and then decreases to around 60% of the peak value for a fully dense ceramic[17].

Permittivity, ε_{33}, is also highly dependent on porosity. For 1-3 structures there is an almost linear relationship between dielectric constant and porosity. For 3-3 structures the values are up to one third lower than 1-3's at around 20% porosity[17]. The permittivity, ε_{33}, decreases as the second phase volume fraction is increased due to the high permittivity ceramic being replaced by the low permittivity second phase, such as air or polymer. This is shown in Figure 1-25b.

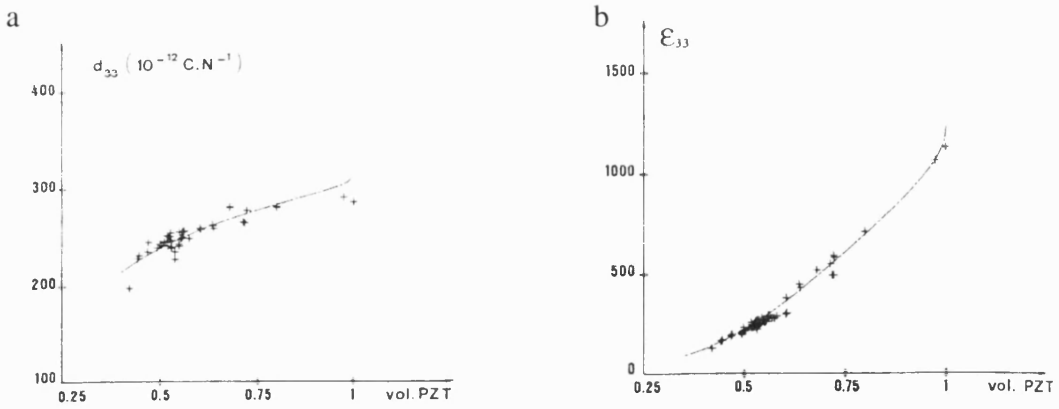

Figure 1-25:Graphs taken from (17) showing d_{33} and ε_{33} as a function of porosity. After (17).

Work to date has shown that 3-3 piezocomposites can lead to improved d_h and decreased permittivity (ε_{33}). It therefore follows that the electric field generated per unit hydrostatic pressure on the sample ($g_h = d_h/\varepsilon_{33}$) can be significantly increased. The high d_h and low ε_{33} also leads to very large increases in the hydrostatic figure of merit since $d_h.g_h = \frac{d_h^2}{\varepsilon_{33}}$. Figures reported by Guillaissier et al[17] show a significant increase in $d_h \bullet g_h$ for porous structures, although the range of porosities was limited as a single manufacturing method was used. A structure which contains 60% pores by volume had a $d_h.g_h$ which was 50 times that of the fully dense ceramic. As would be expected d_{33}, d_{31}, ε_{33}, d_h, g_h, and $d_h.g_h$ are all dependent on the level of porosity, but no work exists which determines these parameters across a large range of porosities.

The electromechanical coupling factor, k, is another useful figure of merit. This is the square root of efficiency of conversion of energy from mechanical to electrical or from electrical to mechanical and is defined as:

$$k^2 = \frac{\text{electrical energy converted to mechanical energy}}{\text{input electrical energy}} \text{ or}$$

$$k^2 = \frac{\text{mechanical energy converted into electrical energy}}{\text{input mechanical energy}}.$$

As with all the other properties discussed here it is also dependent on porosity[18]. For 1-3 piezocomposites the coupling coefficient rises sharply at low volume fractions, reaches a maximum between 60 – 80% and then reduces to around one tenth of its maximum value at 90% volume fraction of ceramic. No data for 3-3 composites has been reported.

This value of the coupling coefficient, k, is particularly sensitive to the mechanical properties of any second phase if present. For instance varying the Poisson's ratio for a polymer second phase from 0.3 to – 0.9 can increase the hydrostatic coupling factor from 15% to 55%[19] in 1-3 composite systems.

Whilst there is literature on 1-3 composite materials, there is limited knowledge related to 3-3 structures and the effect of porosity on the piezoelectric constants and figures of merit by either modelling or experimental work. Research to date has concentrated on a narrow range of porosities, which was limited by the production method used. The aim of this research is to evaluate a full range of porosities by using a variety of techniques to produce porous materials and to produce models to predict the piezoelectric properties of 3-3 composites.

This work will also help develop a understanding of how 3-3 structures lead to increased piezoelectric coefficients such as d_h and g_h. One possible method of modelling 3-3 structures is to use finite element modelling, which will now be discussed.

1.4 Finite Element Modelling

Finite element analysis is method of breaking down a structure into very small "elements" in which calculations can be undertaken which consider each element as a homogeneous set of properties. All these elements then contribute to the final overall property of the object in question.

The application of finite element analysis to piezoelectric modelling and property prediction has made possible calculations that, a few years ago, would have been impossible without very expensive dedicated workstations. Certain properties must be input into the finite element (FE) software package before solving a problem. These include all piezoelectric and mechanical constant matrices for both the piezoelectric and the passive phase, the degrees of freedom required in order to solve the problem to

completion, details of electrical and mechanical coupling, applied voltages and mechanical and electrical constraints[20].

1.4.1 Definition and Explanation of Terminology

The following section details the terminology used in finite element modelling. A more detailed description of finite element modelling of piezoelectric materials will be given in Chapter 2.

1.4.1.1 Finite Element, Nodes, Element Shapes

Finite element modelling, by its very nature, consists of dividing up a body into discrete but connected parts, namely finite elements. The model can be two dimensional or three dimensional where the elements are also two dimensional or three dimensional respectively. Two dimensional elements are commonly in the form of either triangles or quadrilaterals and three dimensional elements are normally tetrahedra, parallelepipeds or cuboids. Examples of typical elements are shown in Figure 1-26, which shows two and three dimensional elements.

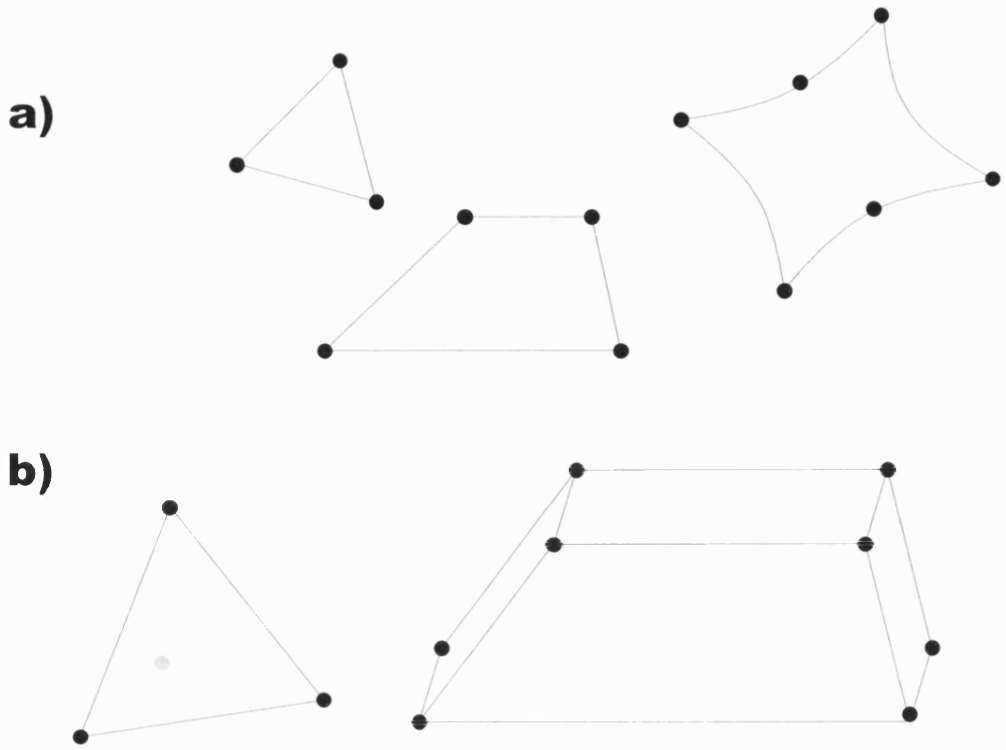

Figure 1-26: Examples of a) two dimensional and b) three dimensional elements.

Elements are connected to other elements by nodes which are points where, for example, degrees of freedom such as voltages and displacement may be applied. These are represented by the circular dots in Figure 1-26 located at the corners of the elements and on the sides, if the element sides are curved.

Once the body has been divided up, the element pattern is termed a mesh. A "coarse" mesh, Figure 1-27a is a mesh which contains a few large elements and a "fine" mesh, Figure 1-27b, is the opposite, a pattern containing many small elements.

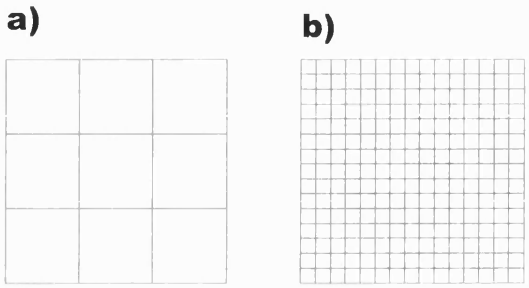

Figure 1-27: Different mesh sizes for a square, a) coarse mesh and b) fine mesh.

The selection of the mesh size is usually a compromise. Fine meshes tend to give more accurate results but the calculations require much more processing time compared to coarse meshes. Mesh size is a factor of computer power, available memory, desired result accuracy and body feature size and geometry.

1.4.1.2 Piezo-Modelling in the Literature.

Cases of thorough finite element analysis of piezocomposites are sparse in the literature. More common are mathematical analyses, which tends to produce adequate results but are many times more complicated to execute and are less versatile than finite element modelling. With mathematical analyses, it is not often possible to change the geometry of the model and introduce a second phase to the structure. In addition, complex shapes dramatically increase the complexity of an analytical model.

In terms of finite element modelling, Abatan et. al. modelled a solid piezoelectric rod subject to a temperature gradient. They demonstrated the ability of the ANSYS software package to perform this type of coupled field modelling successfully[20]. Bennet et. al. reported the modelling of 1-3 piezoelectric hydrophones[21]. They concluded that for the best hydrophone performance a low volume fraction of piezoelectric should be present and the second phase consisting of a soft, compressible polymer was advantageous. In addition, they report that the aspect ratio and the PZT rods should be minimised for effective stress transfer. Cover plates over the top and bottom of the device are also recommended and are generally seen as beneficial for 1-3 composites.

1-3 composites were modelled[22] by a mathematical method by Gibiansky and Torquato. They reported that hexagonal arrays of piezoelectric rod would result in optimum performance. In agreement with Bennet et. al. they stated that for optimal performance the volume fraction of piezoelectric should be kept low and the performance of the hydrophone is sensitive to the mechanical properties of the polymer matrix. They also state that using a polymer with a negative Poisson's ratio is beneficial to the performance of the composite.

There is no literature that concerns the modelling of 3-3 composites. Subsequent chapters address this and attempt to provide a general overview of 3-3 piezocomposite modelling and experimental analysis.

Experimental work to date on these composites involves a limited range of porosities and piezoelectric properties, but no complete understanding of 3-3 piezocomposites as a function of porosity or a mechanism for d_h enhancement has been put forward.

The aim of this work is to therefore develop finite element models of 3-3 structures and manufacture and test a range of 3-3 piezocomposite materials. Modelling of 3-3 piezocomposites will now be discussed (Chapter 2) and experimental results (Chapter 3) are to be compared.

2 Finite Element Modelling

2.1 Introduction to Modelling

Finite element analysis (FEA) is used to calculate the state of a solid, liquid or gas when a variety of loads are applied. These loads can be mechanical, electrical or thermal and are static, or dynamic. In FEA a body is divided into discrete but connected elements, which are used to calculate the state of the whole body under load.

All data about the physical condition of a body and all relevant material properties are input into an FEA computer program. A geometrical body is drawn to represent the physical likeness of the item to be modelled. Once loads and boundary conditions are applied to the geometrical body, the model can be solved. The solution process calculates the individual states of each element and sums them to create another model which represents the final state of the body. Post processing can then be carried out to ascertain the states of the different degrees of freedom of the model, i.e. displacement in a particular direction, strain, voltage, electric field etc.

All modelling undertaken in this thesis used the commercial finite element package ANSYS version 5.4 through 5.7.1.

2.1.1 Meshing Conditions

In order to solve an FE model each body has to be divided up into elements. The pattern that these elements form is called a mesh. There are a number of variables when choosing an appropriate mesh. The body can be meshed with a fine or coarse mesh. A fine mesh is one with a large number of small elements and a coarse mesh is one with fewer large elements. For example, consider the meshing shown in Figure 2-1b. A coarse mesh with properties similar to that in Figure 2-1b will be relatively quick to solve. However, it can be seen that due to the coarse mesh, the model shape differs slightly from that of the original geometry, Figure 2-1a. The fine mesh shown in Figure 2-1c can be seen to be a more accurate representation of the original geometry, however this model will take longer to solve than a coarse mesh and in certain cases will not be able to be solved due to memory processing time and disk space constraints. A compromise has to be reached between the required accuracy of the results and the available computer specifications. For the purposes of the modelling presented in this chapter however, accuracy was proven to be satisfactory with a relatively coarse mesh due to the regular geometry of the models used.

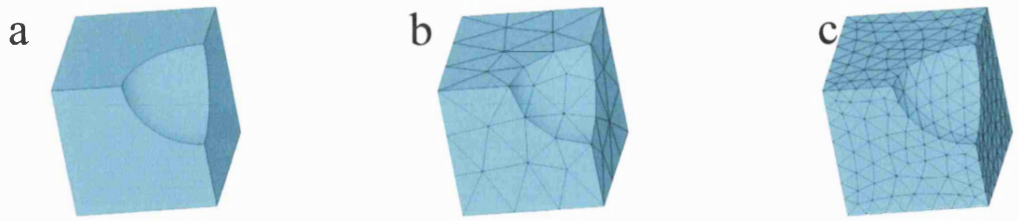

Figure 2-1: Example of a) original geometry with no mesh, b) coarse mesh and c) fine mesh.

In addition to the size of the mesh, it can be "free" or "mapped", and can contain elements of tetragonal, triangular, hexagonal or parallelepiped shaped elements. In addition, the mesh can be made up of irregular sized elements. If a certain area needs to be selected for special interest the elements can be refined in this section. This provides more accurate results in a localised section, without the need for a small element size throughout the whole body.

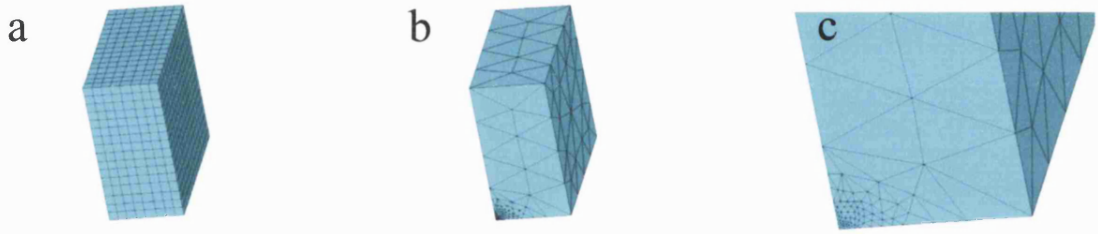

Figure 2-2: Meshes showing a) mapped mesh, mesh elements are of the same size, b) free mesh with elemental refinement in lower corner and c) close up of elemental refinement.

The examples in Figure 2-2 show a number of meshing options. A "mapped" mesh, shown in Figure 2-2a has a regular size and shape and can be used with regular shaped objects and elements. This enables a relatively coarse mesh to be used and the meshed shape still closely resembles the original body. However, only regular geometries can be meshed with this type of mesh and the shape shown in Figure 2-1 could not be meshed in this way.

With a "free" mesh, irregular shapes can be meshed. Figure 2-2b and c show a refined mesh around the lower corner of the body. This avoids long processing times by only having a fine mesh in areas of interest.

2.2 Solid Block Validation

To establish whether FEA using ANSYS can be used as a viable method for calculating and modelling the response of piezocomposites under mechanical loads and electrical fields, a series of validation tests were initially carried out. Specific geometries and loading conditions were modelled, where results from the modelling could be compared to both accepted values from manufacturers and values calculated from simple analytical expressions and material properties.

2.2.1 Calculation of Theoretical Values from Analytical Expressions

There are many compositions of PZT commercially available, as discussed in Chapter 1. For this study a soft PZT was chosen, namely PZT-5H, which is a commercially available soft PZT used for acoustic sensing applications. The materials properties required to undertake piezoelectric modelling using FEA are the compliance (poled) (s) or stiffness (poled) (c), piezoelectric coefficients (e) and permittivity matrices at constant strain (ε^S).

The relevant materials properties of PZT-5H are shown below[23].

s_{11} (10^{-12} Pa^{-1})	16.4	c_{11} (10^{10} Pa)	12.7
s_{12} (10^{-12} Pa^{-1})	-4.8	c_{12} (10^{10} Pa)	8
s_{13} (10^{-12} Pa^{-1})	-8.5	c_{13} (10^{10} Pa)	8.5
s_{33} (10^{-12} Pa^{-1})	20.8	c_{33} (10^{10} Pa)	11.7
s_{44} (10^{-12} Pa^{-1})	43.5	c_{44} (10^{10} Pa)	2.3
s_{66} (10^{-12} Pa^{-1})	42.6	c_{66} (10^{10} Pa)	2.4

e_{13} (Cm^{-2})	-6.5
e_{33} (Cm^{-2})	23.3
e_{15} (Cm^{-2})	17

$\varepsilon_{11}^S/\varepsilon_0$	1700
$\varepsilon_{33}^S/\varepsilon_0$	1470

If a simple block of PZT-5H is considered which is loaded under hydrostatic conditions the charge generated per unit hydrostatic force (CN^{-1}) or hydrostatic strain per unit electric field

(m V^{-1}) is given by d_h, where $d_h=d_{33} + 2d_{31}$. The d_{31} and d_{33} coefficients can be calculated from the above data and the following relationships, Equation 2-1 and Equation 2-2.

Equation 2-1 e_{33} in terms of d and c coefficients.

$$e_{33} = 2d_{31}C_{13}^{E} + d_{33}C_{33}^{E}$$

Equation 2-2: e_{31} in terms of d and c coefficients.

$$e_{31} = d_{31}\left(C_{11}^{E} + C_{12}^{E}\right) + d_{33}C_{13}^{E}$$

By substituting the values of $e_{33}, e_{31}, C_{13}^{E}, C_{12}^{E}$ *and* C_{33}^{E} into the equations above, d_{33} and d_{31} can be calculated.

Equation 2-3: Substituting values into previous equations.

$$23.3 = 2d_{31}(8.5) + d_{33}(11.7)$$

$$-6.5 = d_{31}(12.7 + 8) + d_{33}(8.5)$$

Equation 2-4: Solving for d_{31}.

$$-274.1\times10^{10} = 97.69d_{31}$$

$$d_{31} = -2.81\times10^{10} = -281pCN^{-1}$$

Equation 2-5: Substituting d_{31} into Equation 2-3

$$d_{33} = \frac{23.3-(-47.6)}{11.7\times10^{10}} = 6.06\times10^{-10} = 606pCN^{-1}$$

This gives values of d_{33} = $606pCN^{-1}$ and d_{31}=-$281pCN^{-1}$ and a d_h of $606 + 2(-280) = 46pCN^{-1}$

2.2.2 Finite Element Modelling

As a comparison with these calculated values a simple model consisting of a solid cube of PZT-5H was constructed. All materials properties (compliance, permittivity and piezoelectric coefficients) were input and a variety of types and sizes of meshing were performed prior to solving. Mapped and free meshes of sizes ranging from coarse to fine were used, and in each case the model was solved for both d_h and g_h. The effect of varying mesh sizes will be discussed later in Section 2.3.2.1. In both of these cases a solid cube of side length of 1m was constructed. Electrodes on the upper and lower surface were modelled by coupling the voltage degree of freedom of all the nodes on the top and bottom surface of the cube. This ensures that the voltage on all the nodes in each coupled set is equal, behaving in a similar fashion to a painted metallic electrode. Due to the symmetrical structure, symmetry was applied to three of the six surfaces.

In order to calculate d_h a potential difference was applied to the electrodes on the cube. The top electrode was set to a potential of 1V and the lower electrode was set to 0V, setting up an electric field of 1V m^{-1} in the poling direction.

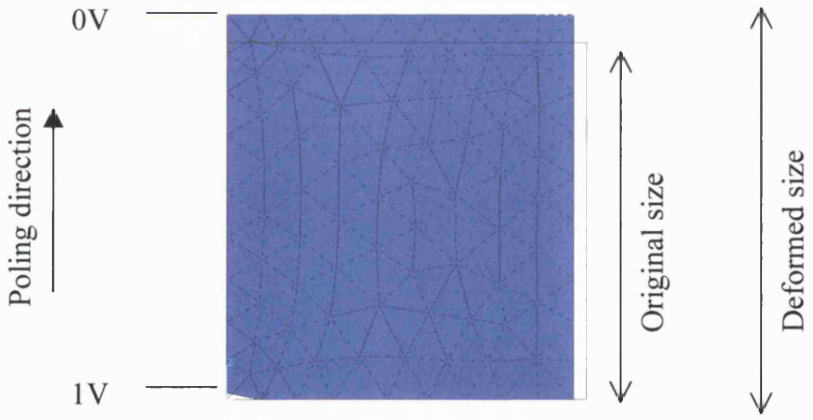

Figure 2-3: Post solution modelled cube showing deformation after application of electrical field.

After solving the model, Figure 2-3, there is a displacement of the cube compared to its position before any potential was applied to the electrodes.

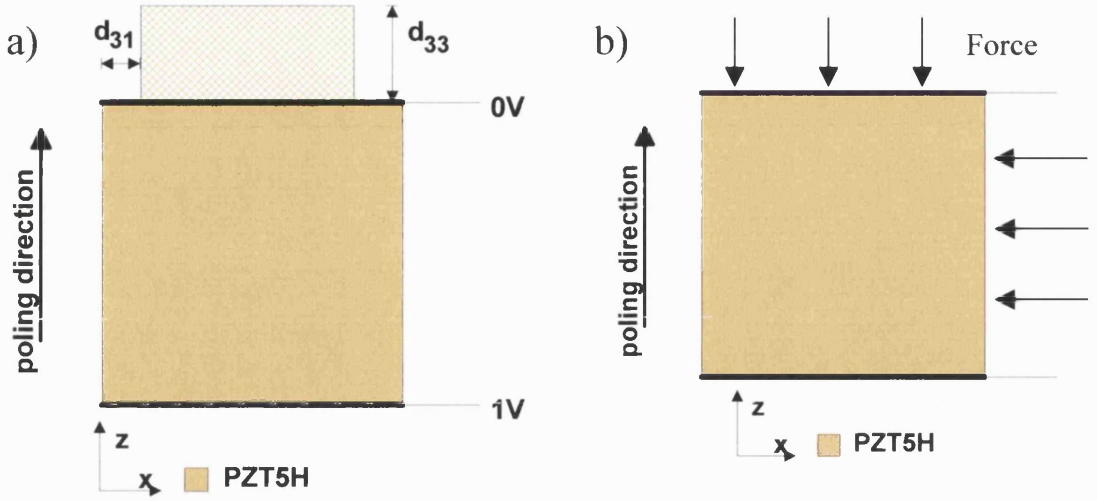

Figure 2-4: Schematic of calculation method of a) d_h , application of electric field and measurement of strain and b) g_h application of stress and measurement of electric field.

The displacement of the nodes of the top surface was calculated which provided a measurement of strain and d_{33}, as the electric field is $1Vm^{-1}$, Figure 2-4a. The average (negative) displacement of the nodes on the side of the cube allowed the d_{31} coefficient to be calculated in a similar fashion. These d_{33} and d_{31} coefficients were used to calculate the d_h coefficient for the cube.

The calculation of g_h is somewhat different and involves setting the lower electrode to a voltage of 0V while the upper electrode was free to float, i.e. open circuit conditions. A unit hydrostatic pressure was applied on three surfaces, acting to compress the structure. After solving, a potential difference and an associated electric field is developed between the two electrodes, which is used to calculate g_h. As all dimensions of the cube are 1m and the pressure is 1Pa, the electric field generated is effectively a direct measurement of g_h, (field per unit hydrostatic pressure).

Model results of d_{31}, d_{33}, d_h and g_h were compared to the calculated values using the appropriate analytical expression and the material properties as input data. It can be seen that the analytical and FEA values are with 1% of each other (Table 2-1).

	d_{31} pCN^{-1}	d_{33} pCN^{-1}	d_h pCN^{-1} ($d_{33}+2d_{31}$)	g_h $Vm^{-1}Pa^{-1}$ (d_h/ε_{33})
Data from manufacturer	-274	593	45	0.0015
Analytical	-280	606	46	0.0015
FEA	-282	607	43	0.0014

Table 2-1: Comparison of analytical and finite element results for dense PZT-5H. Figures used for input shown on p50.

2.2.3 Discussion of Discrepancies with Theory

There were small differences between the theoretically calculated data and the figures determined from the FE modelling. When using finite element modelling to model complex systems a number of points need to be considered. The first note to be made is that the data sheet containing the values for PZT-5H consists of directly measured values of large numbers of samples. Any measurement error or spread in the data is not reported with the data sheet.

Secondly FE modelling in a variety of circumstances often predicts higher values for mechanical and electrical properties than real life situations exhibit. There are many reasons for this, in the case of modelling PZT ceramics, the finite element method assumes a perfectly dense ceramic with uniform properties and poling, perfect mechanical electrical coupling, zero resistance electrodes and perfect geometry and surface finishes. In real situations and devices these factors can reduce the properties significantly from those predicted by FEA.

Finally, the modelling enlisted here assumes linear piezoelectric behaviour and that there is a linear relationship between field and strain and force and charge.

2.2.4 Reverse Poling Direction

The piezoelectric data tables and matrices are entered into the FE software in such a way that the poling direction is parallel to the z (3) axis and is in the positive direction. In order to further confirm the ability of finite element analysis to model, piezoelectric samples the piezoelectric data tables were entered to simulate poling in the opposite direction of the ceramic. In a real situation this would simulate a sample being tested in the opposite direction or the voltage being reversed during poling. In both of these cases the sample should, of course, behave the same as if it were poled or tested normally.

The modelling of the values of d_h and g_h was carried out in the same way as in Section 2.2.1. After solving and calculation of the figures of merit the values for the reversed poling direction corresponded directly with those for the conventional poling direction.

2.2.5 Meshing Solutions

As previously mentioned in Section 2.1.1, it is possible to mesh a structure with a fine or a coarse mesh. There is a large difference in the time it takes to solve a coarse mesh compared to a fine mesh. In order to establish the most time effective solutions, a model was meshed using different types and different sizes of mesh and the results were analysed.

Two models were chosen for this analysis. The simple cube model, as described in Section 2.2.1, and a more complex model containing pores, to be further discussed in Section 2.3. These two models were chosen as it was thought that a simple cube geometry, Figure 2-3, could yield high accuracy results with a relatively coarse mesh while a more complex shaped model would require a finer mesh. The more complex shape would therefore test the dependency of accuracy of results on meshing size and type.

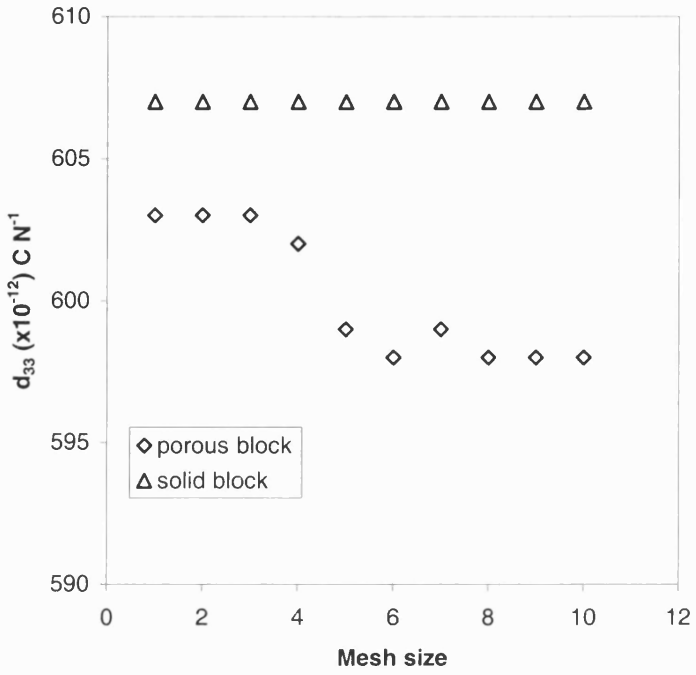

Figure 2-5: Dependence of mesh size on piezoelectric coefficients for a simple and complex geometry model.

It can be seen that for a solid block the mesh size is insignificant due to the simple geometry. However for a porous block, as shown in Figure 2-6a, it can be seen that a mesh size of lower than 4 is desirable. As the model shape becomes more complex a finer mesh is required to give accurate results.

2.3 Three Dimensional Interconnected Porosity Unit Cell

The aim of this research is to evaluate the effect of porosity on piezoelectric properties in 3-3 piezocomposites. In order to achieve this a model unit cell was considered which represents an interconnected 3-3 structure. This consisted of a cube of material with a pore in the centre that extended out to the faces in such a way that it produced an interconnected PZT-porosity structure. This unit cell can be seen in Figure 2-6a, which represents a simplified unit cell, and in Figure 2-6b which shows a real 3-3 piezocomposite structure.

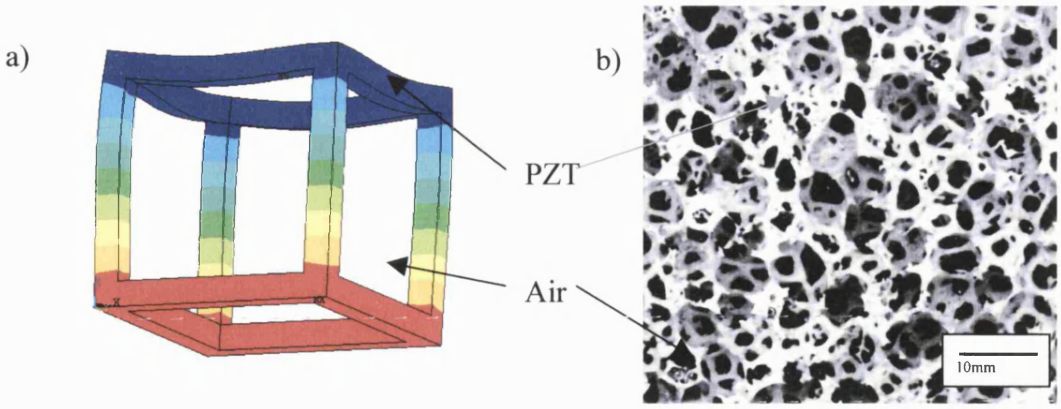

Figure 2-6: a) Simple 3-D porous block model and b) example of a ceramic foam structure.

This model was used in the modelling of piezocomposites to evaluate the variation of d_{33}, d_{31}, d_h, g_h, and permittivity as a function of porosity and PZT materials properties. Initially the model was constructed as shown in Figure 2-6, i.e. the pore space being a void (not impregnated with polymer). The model was created so that the strut thickness and hence the volume fraction of piezoelectric ceramic could be easily changed. The second section of the modelling introduced a polymer phase into the void region of the model to simulate a polymer back filled piezocomposite.

This model enables the volume fraction of either phase to be easily controlled by changing the PZT strut thickness. The properties of both the ceramic phase and the polymer phase can also be readily modified. Hence this simple model is a powerful tool to try to describe the change in properties of a 3-3 piezocomposite manufactured from various types of piezoelectric ceramic with a wide range of fillers and a variety of possible microstructures and phase volume fraction.

The model was solved for d_{33}, d_{31}, d_h, and g_h using the same method as described in Section 2.2. These figures of merit provide an indication of the potential in applications such as receivers (g_h), transmitters (d_h) or both ($d_h.g_h$).

2.3.1 Porous Model Without Polymer

As previously discussed the model was initially considered with no polymer second phase present, the porosity merely being a void. In addition to being a quick and efficient way of modelling it provided an insight into the behaviour of the porous piezoelectric ceramic phase under an applied electric field.

2.3.1.1 Results of Porosity Volume Fraction Versus Piezoelectric Properties

A macro input file was written which allowed the model to be adapted so that the ceramic volume fraction could be varied from just over 10% to just under 90%. The macro file loads the material properties, generates the geometrical structure (dependent on porosity volume fraction), meshes the model, applies the boundary conditions and loads and solves the model. The two extremes are shown in Figure 2-7, a total of seven different porosity volume fractions were modelled.

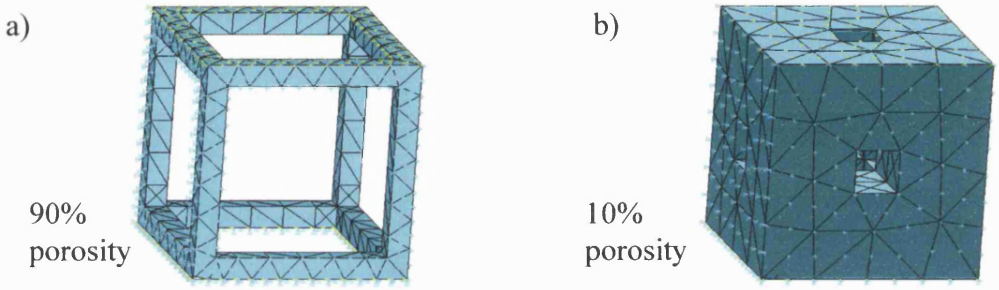

Figure 2-7: Example of a) high (90%) and b) low (10%) porosity volume fraction model.

In order to calculate the hydrostatic voltage constant, d_h, a potential difference was applied to the electrodes of the cube. The electrodes were modelled as if painted on the top and bottom surface of the ceramic by coupling the nodes in the voltage degree of freedom (i.e. all the nodes on each surface attain the same voltage value). An electric field was applied by setting the top electrode to a potential of 1V and the lower electrode was set to 0V. An example of a completed model with electrodes can be seen in Figure 2-8.

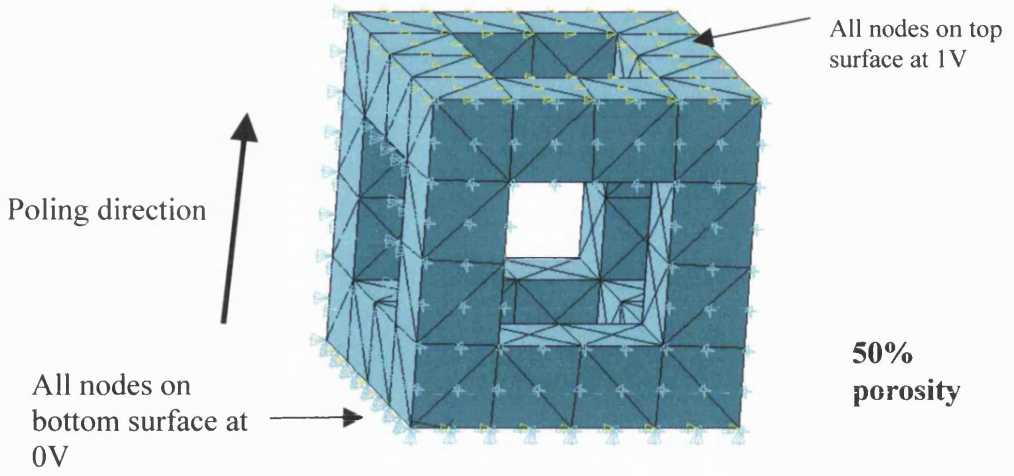

Figure 2-8: Completed 50% porous model showing electrodes (green) and symmetry (light blue) showing boundary conditions and loading for calculation of d_h.

After solving the model there is a displacement of the position of the cube compared to the position before the potential was applied to the electrodes. The average displacement of the nodes of the top surface was calculated, as was the average (negative) displacement of the nodes on the side of the cube. These figures were used, to calculate d_{33} and d_{31} respectively, which were used to calculate the d_h coefficient for the cube.

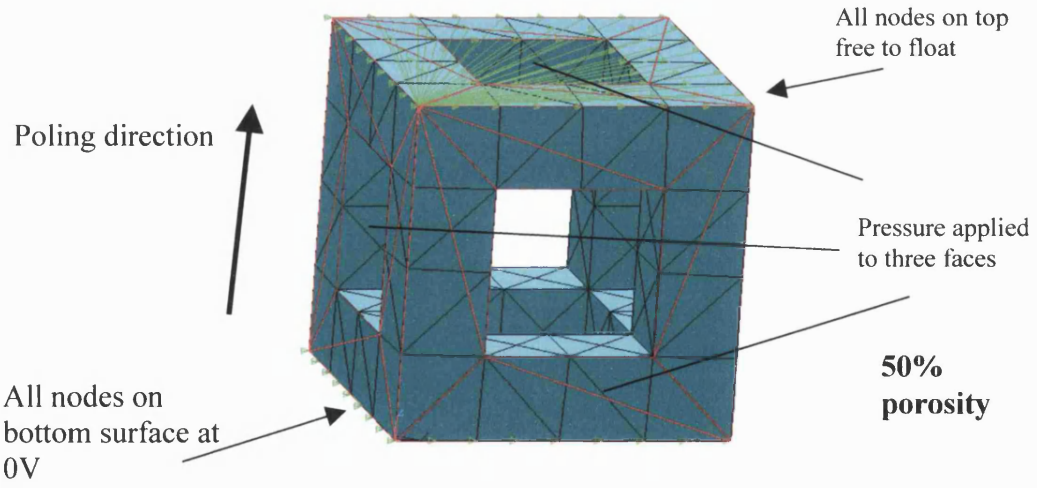

Figure 2-9: Completed 50% porous model showing electrodes (green) and symmetry (light blue) showing boundary conditions and loading for g_h.

A similar process was undertaken to calculate the hydrostatic voltage constant, g_h. The lower electrode was set to 0V and unit pressure was applied to the three free surfaces acting to compress the structure in a hydrostatic manner. As the surfaces to which the pressure was applied were not completely solid, due to the presence of porosity, pressure was applied to the PZT ceramic elements only. A typical model and boundary conditions are shown in Figure 2-9.

After solving this model, a potential difference is generated between the two electrodes. This voltage on the upper electrode can be directly related to g_h as the cube side is 1m and a hydrostatic pressure of 1Pa was applied.

All results of d_{33} and d_{31} for the various ceramic volume fractions were calculated and are shown in Figure 2-10.

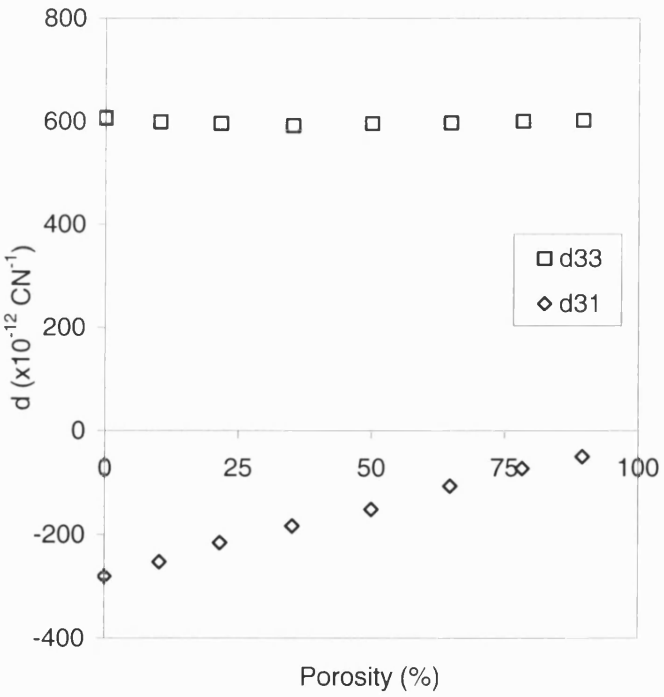

Figure 2-10: Chart showing d_{33} and d_{31} as a function of porosity for a simple porous model.

It can be seen from Figure 2-10 that the value of d_{33} appears to remain constant with respect to porosity whereas the value of d_{31} approaches zero as the porosity of the model increases. The values for d_{31} appear to be as one would expect. As the ceramic content is reduced the

overall d_{31} response decreases. However the result for d_{33} seem to be anomalous, the d_{33} coefficient appears not to change with volume fraction. This would point to a model with 100% porosity having a figure for d_{33} which would not be plausible as there would be zero ceramic present.

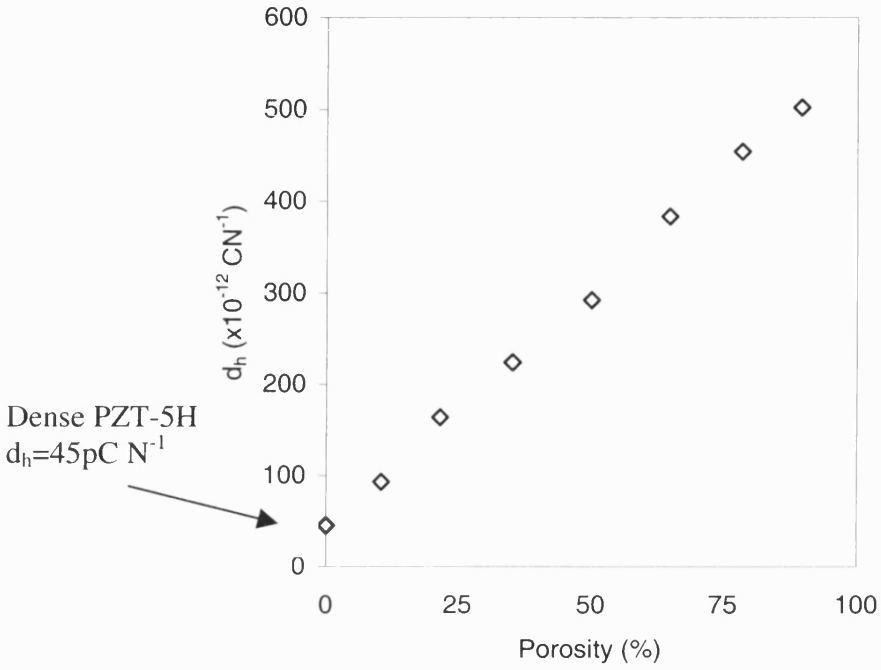

Figure 2-11: Effect of volume fraction of porosity on d_h.

The d_{31} and d_{33} results from Figure 2-10, are combined to calculate the hydrostatic strain constant, d_h. The results can be seen in Figure 2-11. This chart predicts that the figure of

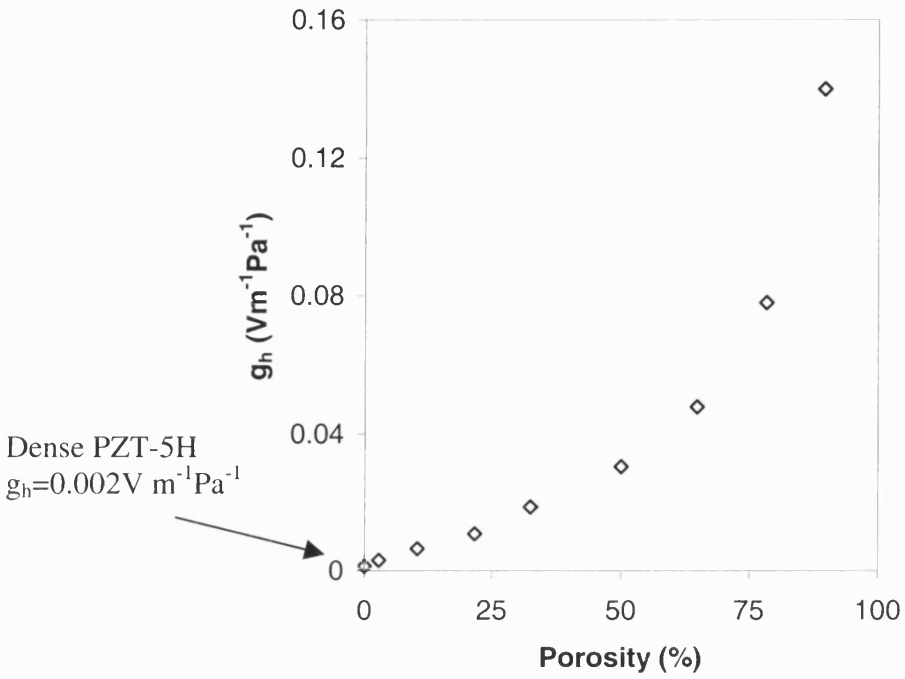

Figure 2-12: Effect of porosity on the g_h figure of merit.

merit, d_h, will increase with increasing porosity and the trend is also a linear one. As the value of d_{33} remains constant and the absolute value of d_{31} decreases, (i.e. becomes less negative) the value of d_h can be seen to approach the value of d_{33} as porosity increases. Clearly if this trend was extended to 100% porosity (i.e. no piezoelectric material present) there is a point where the predicted d_h must be incorrect.

The chart in Figure 2-12 shows the relationship of the hydrostatic voltage constant, g_h, (d_h/ε_{33}) with porosity. It can be seen that the modelled results show an increase in g_h with respect to increasing porosity. The improved g_h is observed as d_h is increasing and the permittivity is also decreasing with porosity. This data suggests a high porosity volume fraction material would be most suitable for high g_h applications (e.g. hydrophones). The effect of porosity on permittivity of the model can be seen in Figure 2-13.

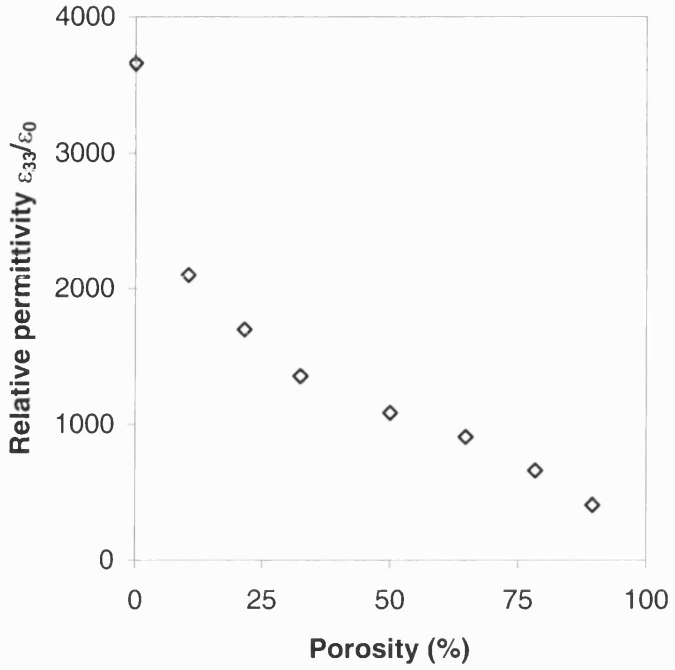

Figure 2-13: Effect of porosity on relative permittivity ($\varepsilon_{33}/\varepsilon_0$)

2.3.1.2 Proposed Model for Anomalous Results

Although the model predicts improved d_h and g_h figures of merit, the results presented in Figure 2-10 and Figure 2-11 appear to have some discrepancies as it would not be expected for the piezoelectric to have a constant d_{33} coefficient with porosity, particularly at the high levels of porosity examined. Investigation into these results required an analysis of the solved finite element model and the loading conditions and associated electric field.

The strain response from a piezoelectric material under electric loading is dependent on the electric field experienced by that sample, and for low electric fields it is generally linear. In the model developed, the strain response from applied loads, whether large or small is taken to be linear, i.e. application of twice the electric field produces twice the strain.

Examination of the electric field density of the solved model shows areas in the model with high electric field density and areas with low electric field density as shown in Figure 2-14.

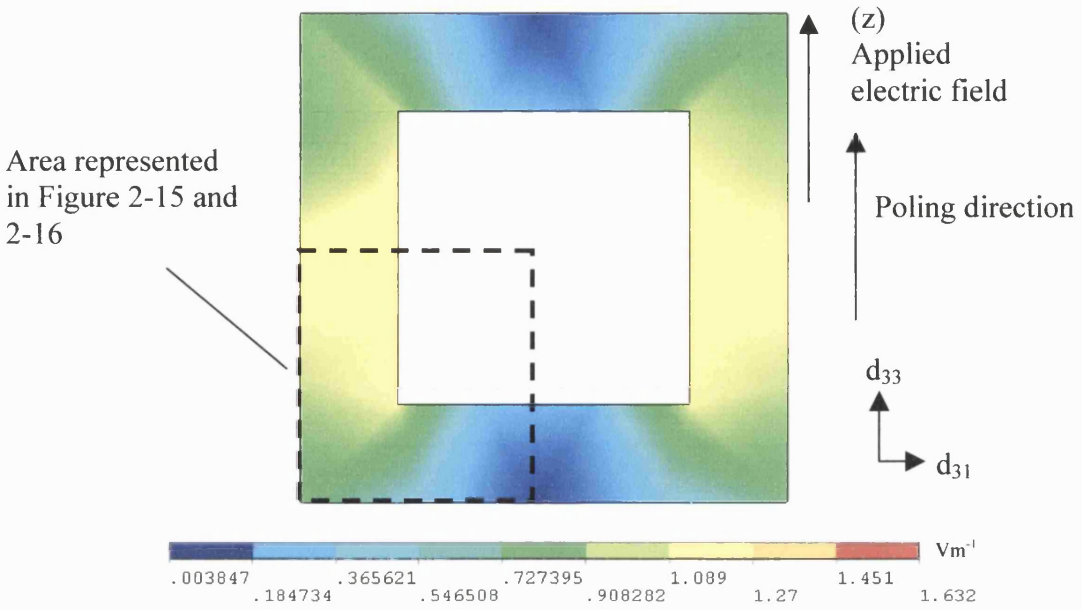

Figure 2-14: Porous model under electric field. The colours denote field intensity, deep blue indicates almost zero field, through to green indicating a high field.

The difference in electric field density, seen in Figure 2-14, is due to the geometry of the sample. Areas marked deep blue are those experiencing a near zero electric field and areas marked green are subjected to a relatively large electric field. Where there is a very low electric field present there will be little strain response from the ceramic. Conversely, high electric field areas will produce large strains.

It can be seen that in the case of the model type shown in Figure 2-14 most of the strain is being produced by the upright sections of the structure, which are aligned in the same direction as the applied electric field and the poling direction. The strain measured in this direction (z) is related to d_{33}. However, in the opposite (x) direction the majority of the strut is not subjected to any significant electric field and d_{31} is measured in this direction. The geometry of the sample, including the pore and electrode placement is such that the areas responsible for producing d_{33} are experiencing high field and the areas responsible for producing d_{31} are experiencing a low electric field. A schematic of this is shown in Figure 2-15 which represents a quarter of the model shown in Figure 2-14.

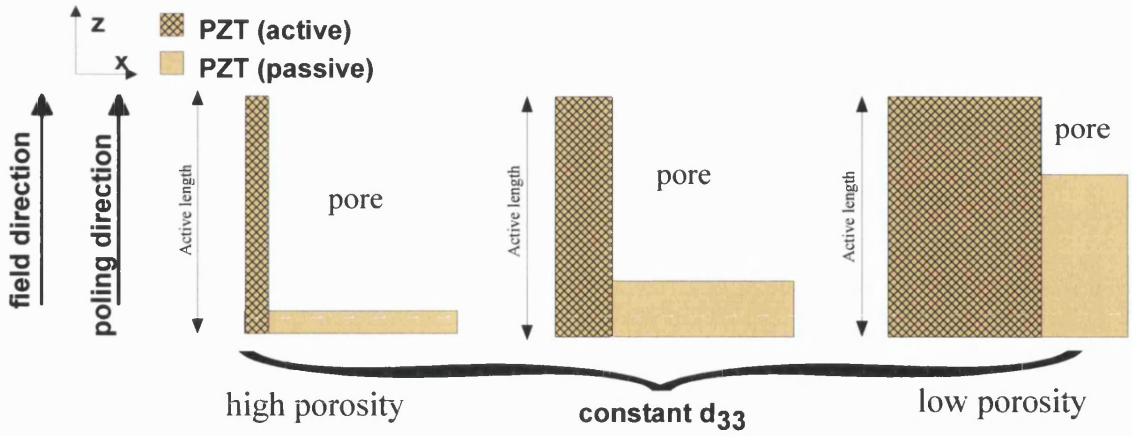

Figure 2-15: Schematic of how d_{33} varies with porosity. The active length corresponding to d_{33} does not change with porosity, leading to a constant d_{33}.

It can be seen in Figure 2-15 that as the porosity increases the length of the strut which is responsible for d_{33} does not change. This length is subjected to significant electric field, it follows that the whole of this length contributes to d_{33} and does not change with porosity. However, in Figure 2-16 although the length of the side that is responsible for d_{31} does not change the electric field is not significant over the whole length, as indicated by the field density in Figure 2-14.

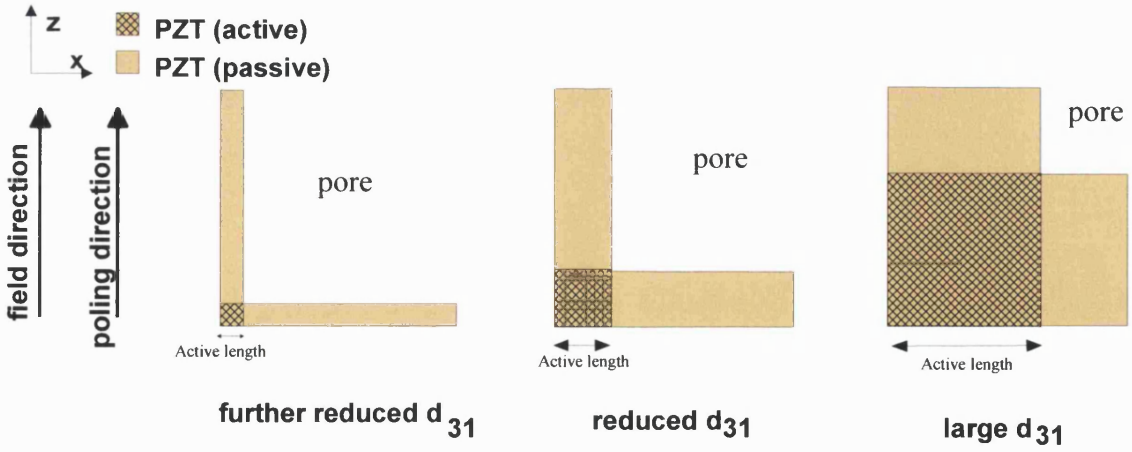

Figure 2-16: Schematic of how d_{31} varies with porosity. The region which contributes to d_{31} (active) decreases in length with increasing porosity and hence d_{31} reduces.

Areas of significant electric field are confined to the ends of the length, the same areas which are also responsible for d_{33}, which is denoted by the active length in Figure 2-16. Since the

active length decreases with porosity then the total strain in this direction and d_{31} will decrease with increasing porosity.

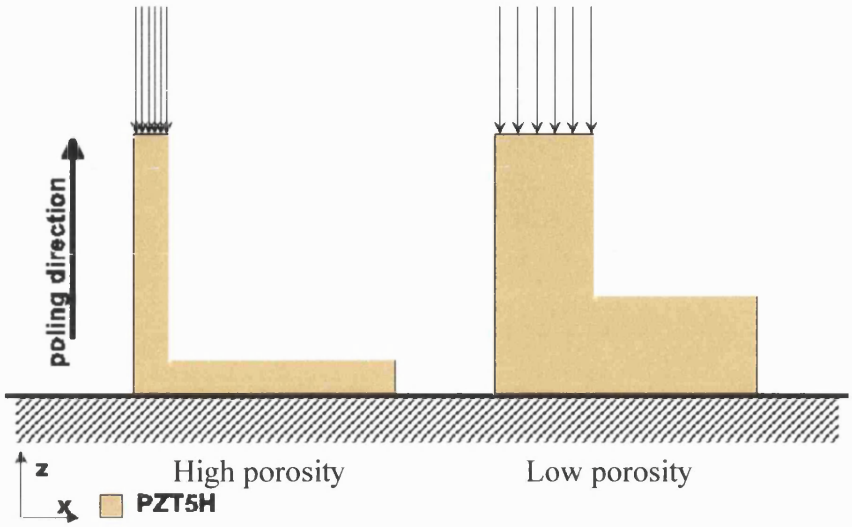

Figure 2-17: Schematic of g_h modelling. High porosity leads to high pressure and elevated g_h.

From these two cases it can be seen how the value for the d_{33} coefficient is constant and the d_{31} coefficient decreases as the porosity of the model increases. When these values are combined to calculate the d_h figure of merit it is seen to increase linearly with porosity and approach the value of d_{33} when d_{31} becomes zero.

The results for the g_h figure of merit can be explained as follows. A force is applied on each surface in order to produce a voltage. As the level of porosity increases the strut cross sectional area decreases which increases the stress in each individual strut, as the force applied is constant (Figure 2-17). This increase in stress produces an increased electric field and results in an increased electric field generated per unit hydrostatic stress, i.e. g_h. This effect can be shown by plotting the stress in an individual strut against the porosity. This is shown in Figure 2-18 and is similar to the g_h versus porosity data presented in Figure 2-12. This curve is only valid for the specific cubic model geometry discussed.

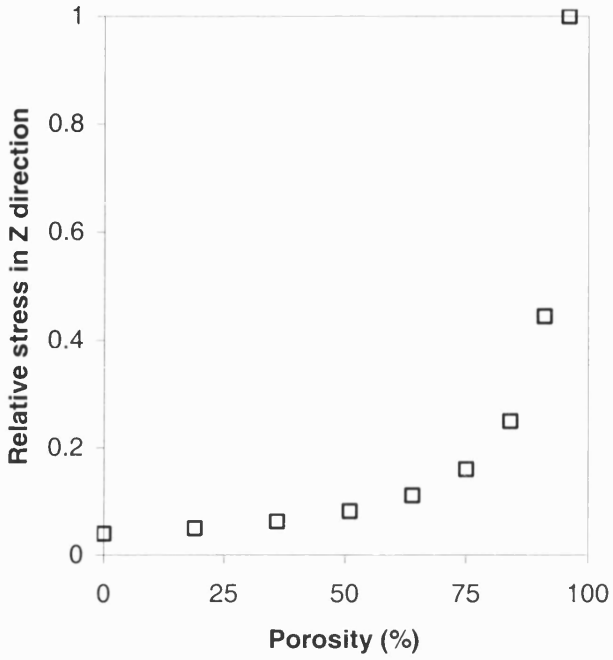

Figure 2-18: Chart showing the relative stress in a strut as a function of porosity. As porosity is increased each strut experiences a higher stress.

2.3.1.3 Limitations in PZT-Interconnected Porosity Model

This model is simplistic and there are a number of associated limitations. The model only contains a single phase of PZT ceramic. There is no interaction with another phase, such as air, or a secondary material, such as an impregnated polymer.

A major difference between the model and a manufactured sample is the geometry. The cube in the model has perfectly straight edges and struts that run parallel to the poling and applied field directions. This maximises the response of d_{33} and minimises that of d_{31}. The samples manufactured have more complex microstructures, which can be observed in Figure 2-6b and Chapter 3.

Despite the disadvantages of this model it can be used to modify and examine the influence of porosity, geometry, piezoelectric properties and second phase materials on figures of merit of 3-3 composites which will now be discussed.

2.3.2 PZT –Polymer Interpenetrating Model

Once the porous simple single phase model had been analysed a second phase was incorporated in order to simulate a polymer impregnated 3-3-piezocomposite structure. This was achieved by filling the void in the model with mechanical elements to represent a polymer phase. This second phase was then attributed material properties of a typical epoxy resin with an elastic modulus and Poisson's ratio.

Figure 2-19 shows both sections of the model that have been separated. The section in Figure 2-19a) is exactly as in the previous single component model and represents the piezoelectric phase. The section in Figure 2-19b) represents the polymeric phase and is the inverse of the piezoelectric phase so that when they are both combined a solid cube is formed with an interpenetrating PZT-polymer structure.

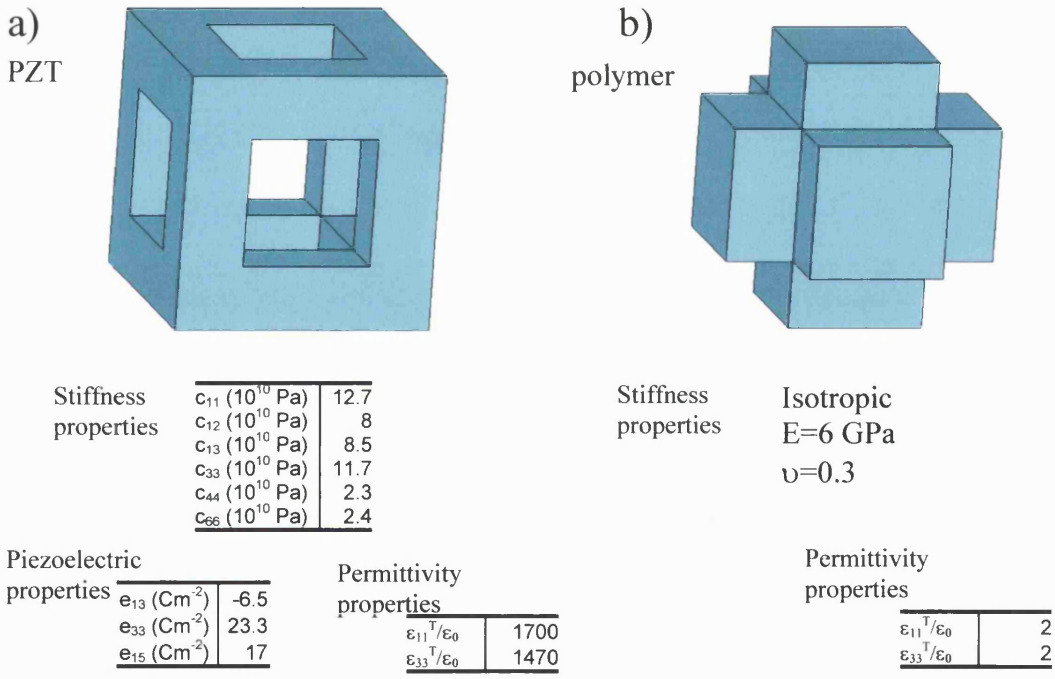

Figure 2-19: Example of two phase interpenetrating system a) outer section representing the piezoelectric phase and the b) inner section representing the polymer phase.

The two sections are attached using the "glue" command in the FE software. This command keeps the two volumes as separate entities but fixes the nodes on the adjacent surfaces so that they move as one node. This effectively produces a perfect bond between the piezoelectric and polymer phases. This allows the model to be solved as if the epoxy resin phase has been

set in the ceramic phase, which is common production procedure for composites with this type of connectivity.

The polymer phase is modelled as having only mechanical properties, a Young's Modulus and a Poisson's ratio. In further modelling the Young's modulus of the polymer was varied, as was the Poisson's ratio, which is discussed in section 2.4.2.

The electrodes on this two phase model were applied over the whole upper and lower surface of the model, including the polymeric sections. This was to mimic future production of the composites whereby painted electrodes would cover both polymeric and ceramic areas of the composite.

The figure of merit, d_h, was calculated in the same way as with the single phase model. With this multiphase model there is a contribution of displacement from the polymeric phase in addition to the ceramic phase. The nodal displacement from both the polymer and piezoelectric were averaged to calculate d_{33} and d_{31}. The figure of merit g_h was calculated using the same method as previously described (measurement of field generated per unit hydrostatic pressure).

2.3.2.1 Variation of Mesh Size for PZT-Polymer Model

As the two phase model contains a phase which had a geometry that had not been previously modelled, the effect of the results on mesh size for this system was investigated. The mesh size was varied and results calculated.

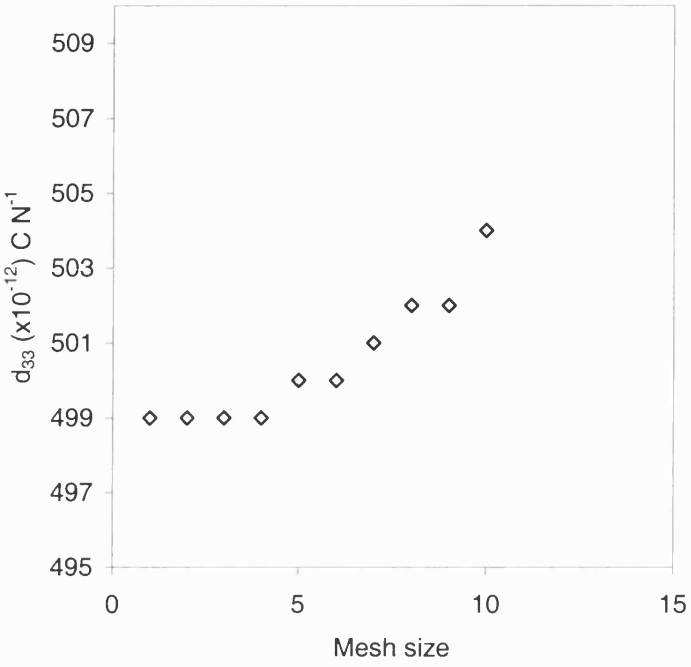

Figure 2-20: Graph showing d_{33} coefficient versus mesh size for PZT-polymer model.

It is to be noted that the solving times for the two phase models were significantly longer than the single phase models, which was an expected and unpleasant inconvenience. This is due to the glue command and the intersection of nodes at the "perfectly bonded" PZT-polymer interface. However reducing the solve time by decreasing the accuracy of the mesh was not pursued.

It can be seen from graph in Figure 2-20 that a mesh size of below 5 was desirable. A mesh size of 4 was used for all the polymer filled PZT composite models.

2.3.2.2 Piezoelectric Properties as a Function of Polymer Volume Fraction

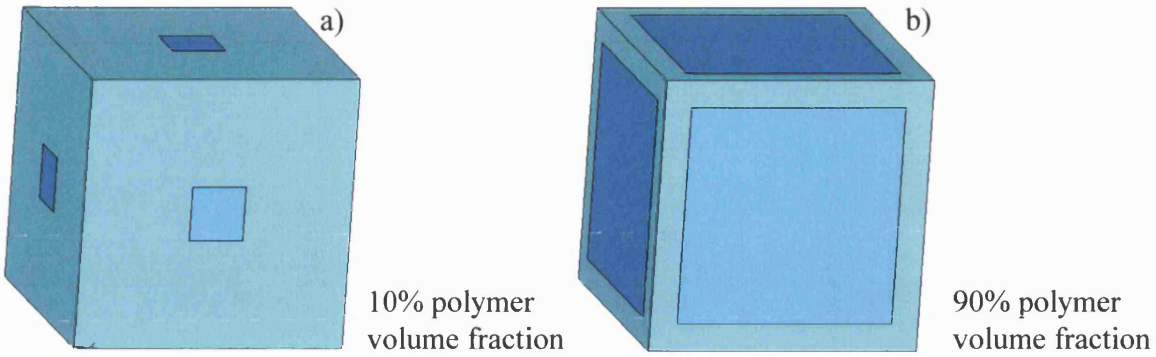

Figure 2-21: Example of a) high and b) low ceramic volume fraction material. The light blue volume is the ceramic phase and the dark blue volume is the polymeric phase.

A macro file was written which enabled the ceramic volume fraction to be varied from approximately 10% to just under 90%. The macro consists of a series of commands that are required to draw, mesh and apply all loads and constraints to the model which is entered into a text file. The text file is then loaded into the FEA program, which executes each command consecutively to build up the final FE model.

The two extremes are shown in Figure 2-21, a total of 8 different polymer volume fractions were modelled. These volume fractions correspond to various PZT strut thickness shown in Table 2-2.

strut thickness (m)	**0.1**	**0.15**	**0.2**	**0.25**	**0.3**	**0.35**	**0.4**	**0.45**
% volume polymer	89.6	78.4	64.8	50	35.2	21.6	10.4	2.8

Table 2-2: Table showing models solved, strut size (input variable) against polymer volume fraction. Cube side length was 1m.

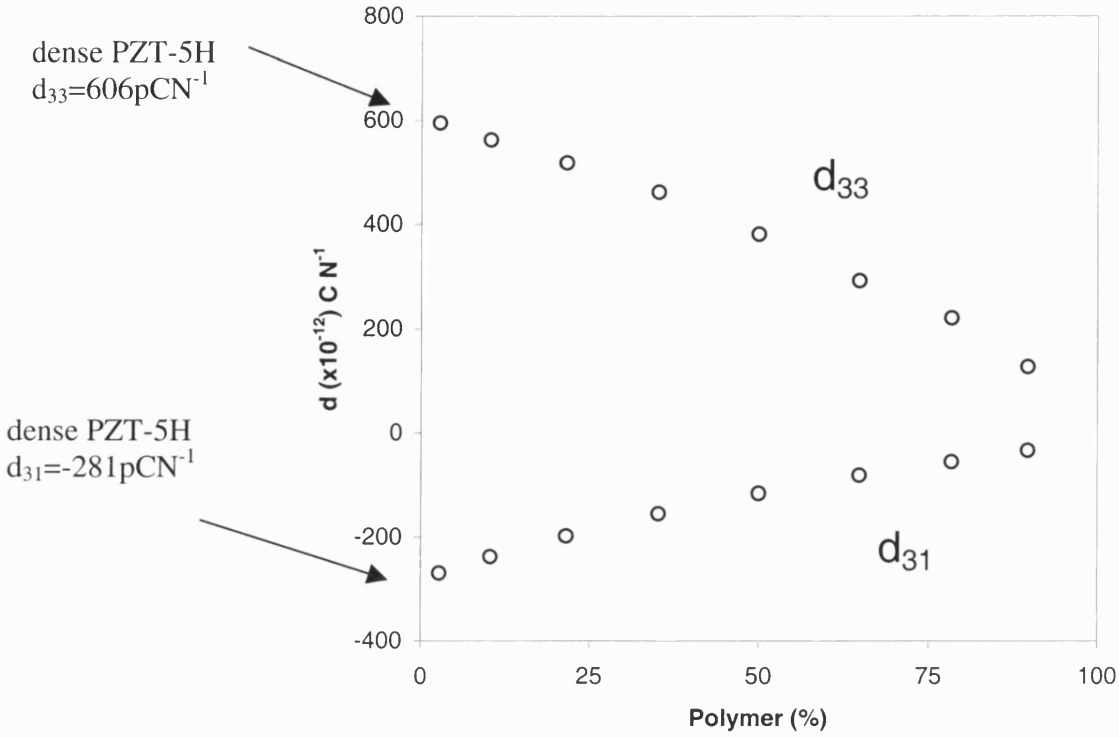

Figure 2-22: Chart showing d_{31} and d_{33} vs. ceramic volume fraction for a two-phase PZT-polymer model.

It can be seen in Figure 2-22 that the values for both d_{33} and d_{31} reduce in absolute terms as ceramic volume fraction decreases. This is different to the earlier one phase system model, where d_{33} remains constant with ceramic volume fraction.

The behaviour of d_{33} and d_{31} as a function of polymer volume fraction can be explained in a way similar to that described in Section 2.3.1.2.

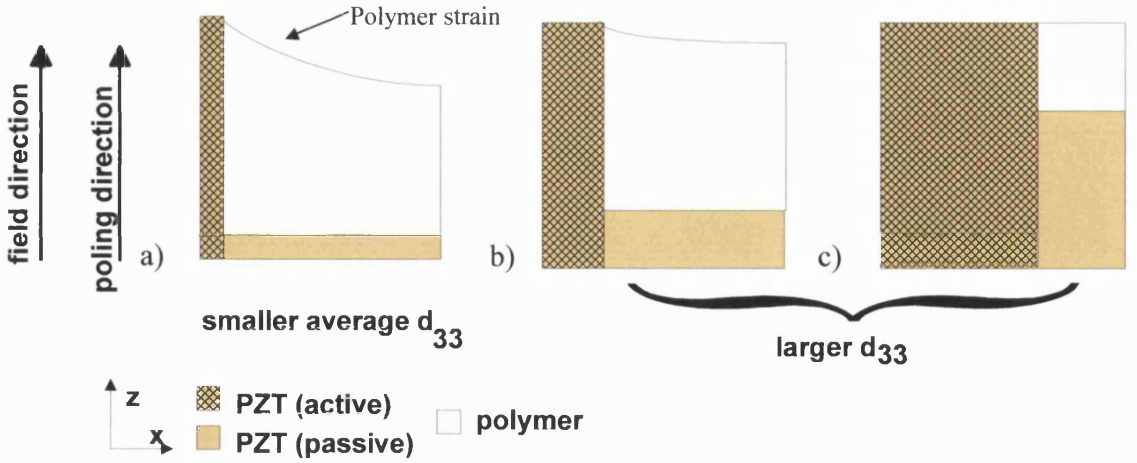

Figure 2-23: Schematic of how d_{33} varies with porosity in a two-phase model.

It can be seen in Figure 2-23 that the mechanism is similar to a single-phase, PZT-porosity, system but with different considerations due to the presence of the polymer phase. The displacement measured is the *average* displacement of both the polymer and ceramic components of the model. The polymeric phase reduces the average displacement of the system as it does not develop a strain under the application of an electric field. However, the polymeric phase, which is well bonded to the ceramic, strains with the piezoelectric due to its low stiffness. The polymeric phase strain decreases with increasing distance from the ceramic phase, as shown in Figure 2-23a. At low ceramic volume fractions (Figure 2-23a) the polymeric phase shows little strain and does not contribute to the displacement of the system significantly. At high ceramic volume fractions (Figure 2-23b and c) the polymeric phase strains are more pronounced.

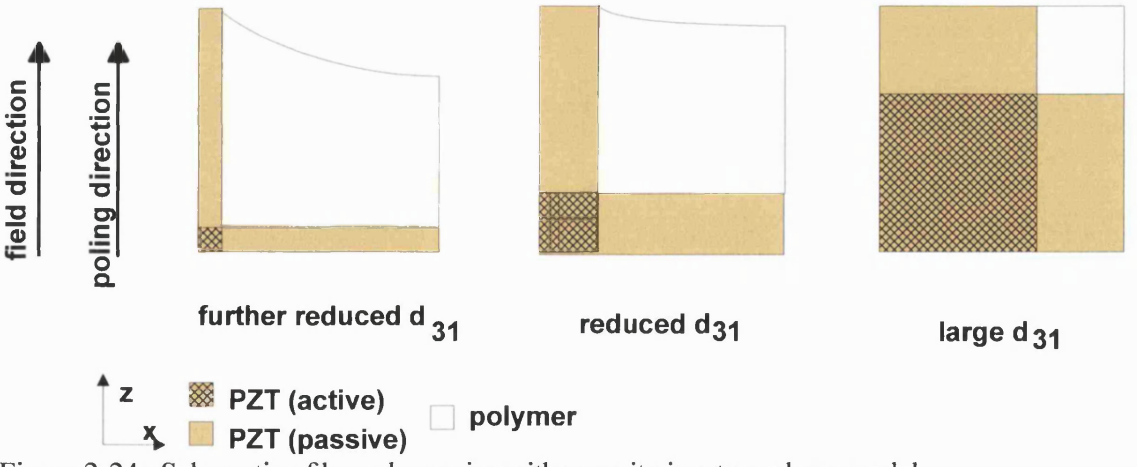

Figure 2-24: Schematic of how d_{31} varies with porosity in a two-phase model.

The polymeric phase, being passive, reduces the strain and hence the value of d_{33} with respect to the volume fraction of polymer present. Figure 2-24 shows that the reduction in d_{31}, with polymer volume fraction is dependent on the reduction in active PZT contribution to d_{31} as previously described.

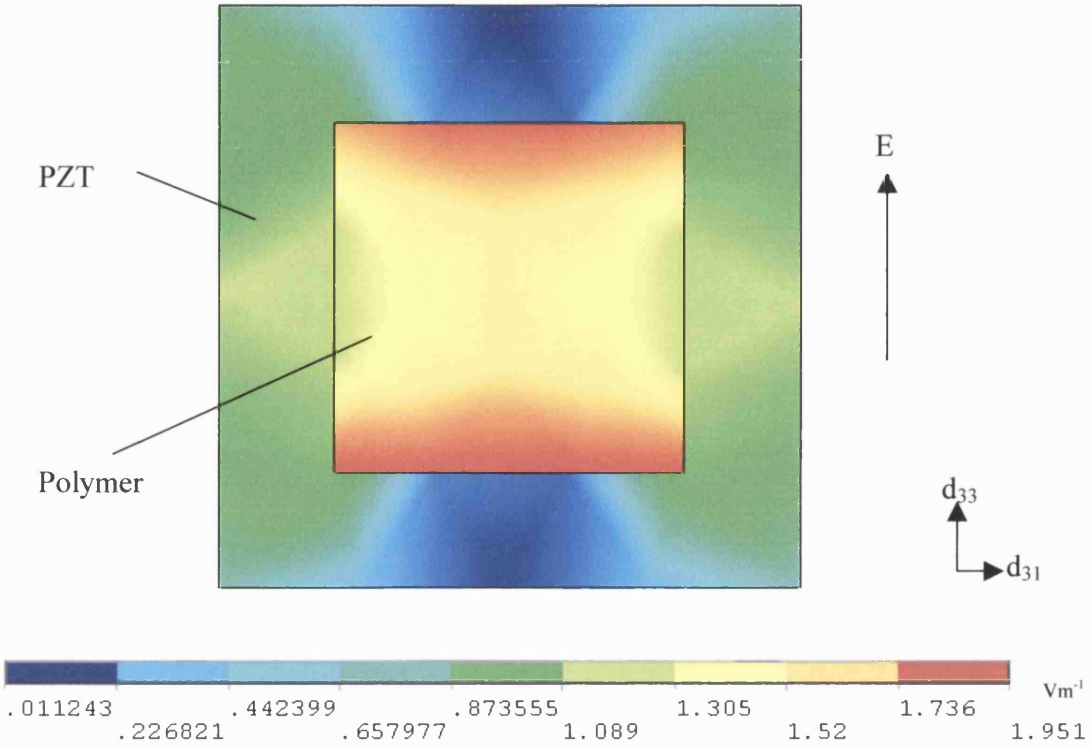

Figure 2-25: Solved model showing electric field strength in two phase model.

The reduction in the values of d_{31} can also be explained by examination of the electric field patterns in the same way as in Section 2.3.1.2. The electric field strengths in this two phase model can be seen in Figure 2-25. Again, areas that would potentially contribute to d_{31} (PZT struts in the 1 direction) are not exposed to a high electric field (blue area) due to the polymer phase, thus reducing d_{31}.

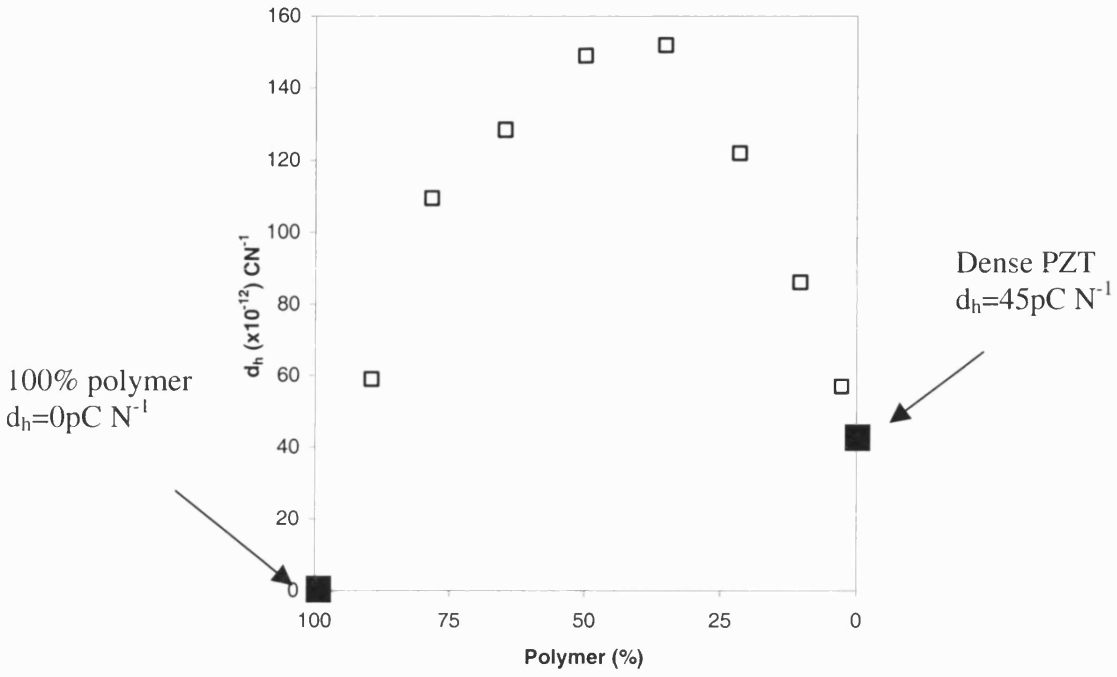

Figure 2-26: Chart showing the figure of merit d_h as a function of ceramic volume fraction for a PZT-polymer interpenetrating model. Polymer elastic modulus is 6GPa, Poisson's ratio ν=0.3

The results of combining d_{33} and d_{31} to obtain d_h as a function of volume fraction are shown in Figure 2-26. It can be seen that there is a peak in d_h around 40% polymer. The peak is due to the difference in relative decrease in both d_{33} and d_{31} as a function of polymer volume fraction.

At high ceramic volume fractions the volume fraction of the polymer phase is small in comparison to the whole composite and d_{33} and d_{31} are similar to the bulk values. The large negative contribution from d_{31} reduces the overall value of d_h, since $d_h=d_{33}+2d_{31}$. At low ceramic volume fractions the opposite is the case. Whilst there is little contribution to d_h from d_{31}, the large amount of polymeric phase reduces d_{33} and hence reduces d_h. The maximum value for d_h is at an intermediate ceramic volume fraction (60%). In this region d_{33} is still relatively large, but d_{31} has reduced to a much greater extent, leading to a high d_h. Thus from this data a composite of around 60% ceramic and 40% polymeric material would be favourable for use in a transmitter (high d_h) device which would increase d_h from 45pCN^{-1} for a dense material to above 150pCN^{-1}.

Therefore, although the model shows that increasing the polymer content decreases both d_{33} and d_{31}, the d_{31} coefficient decreases at a higher rate compared to d_{33} which leads to an increase in d_h. At higher ceramic volume fractions d_{33} decreases to small values and therefore d_h eventually falls.

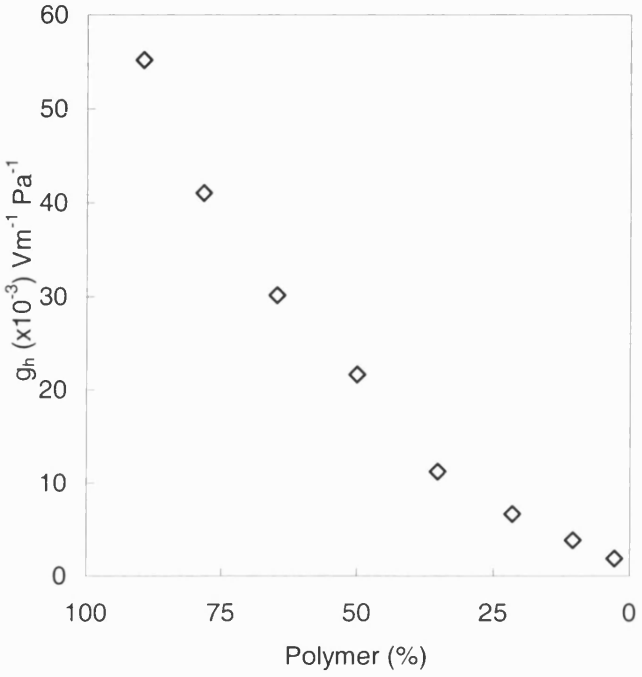

Figure 2-27: Chart showing g_h as a function of polymer percentage volume for a two phase PZT-polymer model.

Figure 2-27 shows the model results for g_h as a function of polymer volume fraction. The trend observed in Figure 2-27 is similar to the trend seen by the single component PZT-porosity model (Figure 2-12). The values of g_h appear to tend to infinity as the polymer volume fraction is increased. This is because the permittivity of the polymer phase is very small when compared to the PZT. Using the equation $g_h = d_h / \varepsilon_{33}$ it can be seen with a very small value of permittivity (e.g. $\varepsilon_r = 2$ for epoxy) g_h tends to a very large number as the composite tends to 100% polymer.

The model predicts significantly improved g_h values compared to the dense PZT-5H (located at the far right of Figure 2-27). The gradient of the curve in this, two phase, PZT-polymer

model is less severe than the single phase model (Figure 2-12). This is can be explained by reference to Figure 2-28.

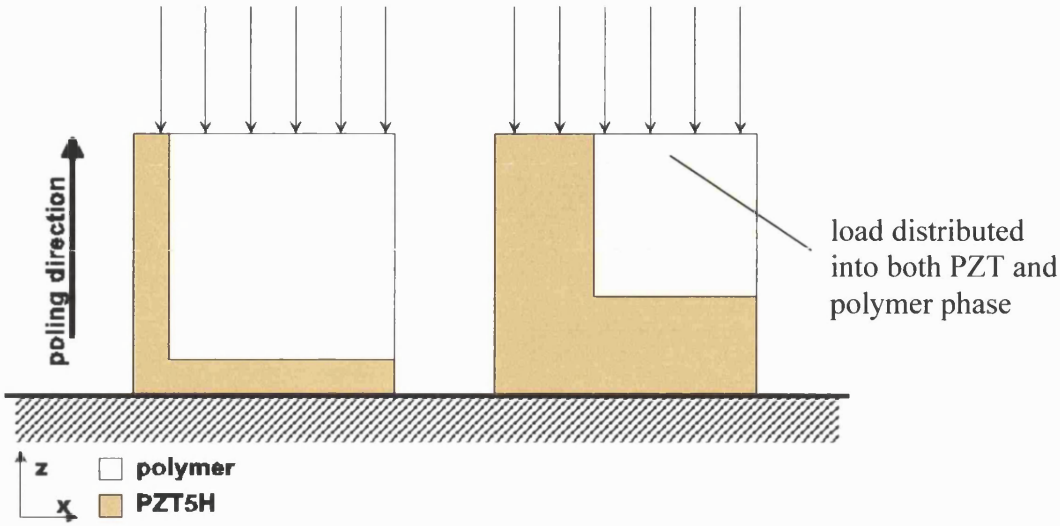

Figure 2-28: Schematic showing the increase in g_h with reduction of ceramic volume fraction.

When the second is phase present the pressure is applied over the entire surface of the composite. In this case all of the load is not carried by the ceramic phase (as in the single phase model) and some of the load is carried by the polymer phase. This distribution is dependent on the relative values of the ceramic and polymer Young's moduli and the relative sizes of the surface areas on which the forces are applied. As the passive polymer phase is experiencing some of the load the total stress in the ceramic phase is reduced and hence g_h is reduced. The ceramic phase, being of higher Young's modulus compared to the polymer, is still subjected to the majority of the stress and hence the increase in g_h is observed with increasing polymer volume fraction due to the ceramic struts experiencing a higher mechanical stress.

2.3.2.3 Limitations of PZT-Polymer Model

For the two-phase PZT-polymer model there are limitations which are not present in the single phase model. As mentioned previously, the polymer and PZT phases are perfectly joined together. This means that there is perfect stress transfer between the polymeric phase

and the ceramic phase. This may not be the case in an actual manufactured samples where inconsistencies in bonding could affect properties of the composite.

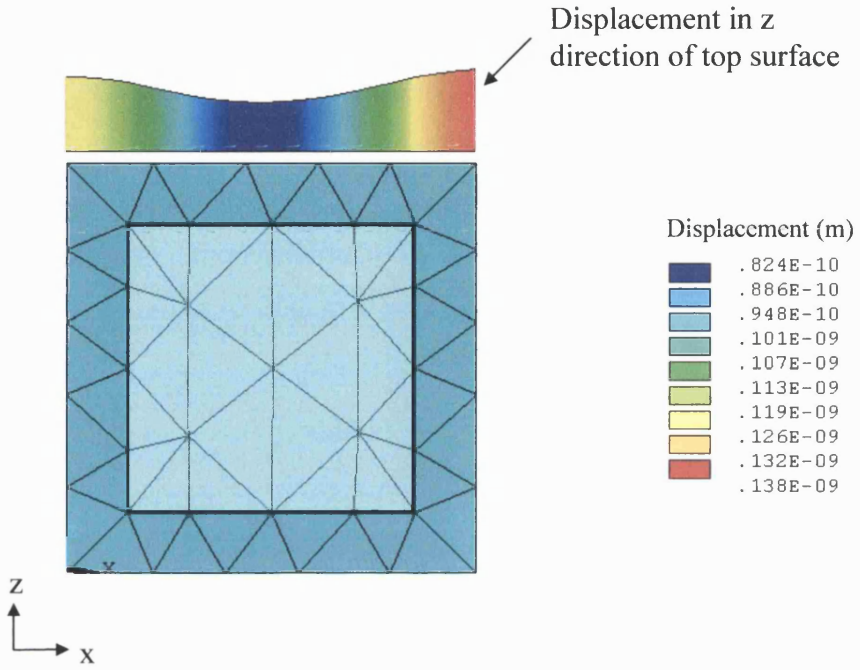

Figure 2-29: Solved model showing displacement of two phase system after application of an electric field. The colour bar along top shows displacement of top surface.

Secondly, the model is a single unit cell considered to be representative of a larger foam / porous structure. It can be seen from Figure 2-29 that there is a "dimple" in the top surface where the polymer has strained less than the ceramic phases. If this were a single cell in a larger structure there would not be an area void of material as both phases are continuous. There would however be a constraint that might affect the overall loading conditions of the model and further modify d_{33} and d_{31} values.

The largest limitation is that the model is assumed to be representative of a single foam unit cell. In most real foam structures, Figure 2-6, there is no direct continuous path between the top and bottom electrodes and the path between the electrodes can be extremely tortuous.

2.3.3 Choice of PZT for 3-3 Piezocomposite

The material chosen for the ceramic phase has been PZT-5H. This is a soft PZT with high values for d_{33} and d_{31} (606 and -281pC N^{-1} respectively).

The model has shown that in order to obtain a high value for d_h, the d_{33} and d_{31} values can be de-coupled in such a way as it is possible to reduce the absolute value of the d_{31} coefficient without significantly reducing d_{33}. As $d_h = d_{33} + 2d_{31}$, when d_{31} is reduced to zero then d_h will tend to d_{33}, which was observed in the initial stage of modelling.

It follows that if the d_{33} and d_{31} coefficients can be independently changed then piezoelectric materials suitable for property enhancement via a 3-3 piezocomposite route should have high values of d_{33} and d_{31}. Some materials exhibit relatively high d_h coefficients in their dense form, such as $PbNb_2O_6$ which has a d_{33} of $85pCN^{-1}$ and a d_{31} of $-9pCN^{-1}$. This equates to a d_h of $66pCN^{-1}$ which is higher than dense PZT-5H ($45pCN^{-1}$). However incorporating $PbNb_2O_6$ material into a 3-3 composite would not be beneficial as the d_{31} is already low and the d_{33} is only $85pCN^{-1}$.

A high ε_{33} can lead to a low g_h for the bulk material. However this does not restrict the material choice for inclusion into a composite as the introduction of air or polymer into the structure reduces the effective permittivity considerably.

In order to investigate this theory, different models with varying piezoelectric properties were examined. Example materials such as a hard piezo-ceramic, PZT5A and PZT7A were chosen for their low values of both d_{33} and d_{31}.

2.3.3.1 Modelling Different PZT Types

The modelling was carried out using the square pore model as shown previously. The porosity was varied from 3% to 90%. The pore in the unit cell was filled with polymer (6GPa) and values of d_{33}, d_{31} were computed and the d_h figure of merit was calculated.

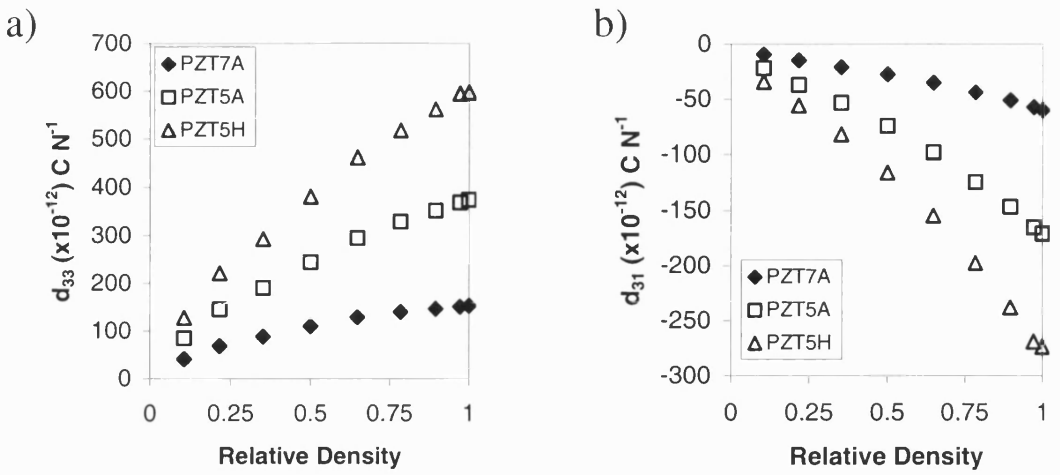

Figure 2-30: Graphs showing a) d_{33} and b) d_{31} as a function of relative density for three PZT types, 7A, 5A and 5H.

The graphs shown in Figure 2-30 show both a) d_{33} and b) d_{31} plotted against relative density for different the PZT types. It can be seen that a similar behaviour is exhibited by all three types of PZT. The d_{33} and d_{31} values for PZT5H are larger in both cases. Although the values for d_{31} are high for PZT5H, when these are combined with the higher values of d_{33} into the d_h figure of merit, the d_h values are significantly higher than PZT7A and PZT5A, as seen in Figure 2-30. PZT-7A and PZT-5A both have low values of d_{33} and d_{31}. For PZT7A, $d_{33} = 153 pCN^{-1}$ and $d_{31} = -60 pCN^{-1}$ and for PZT5A $d_{33} = 374 pCN^{-1}$ and $d_{31} = -171$.

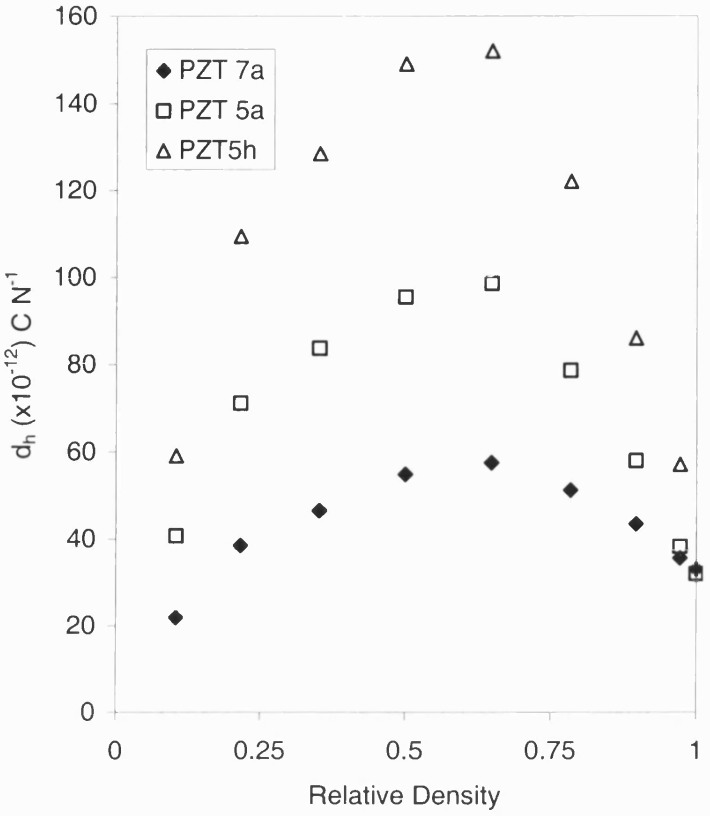

Figure 2-31: Graph showing d_h with respect to relative density for three PZT types, 7A, 5A and 5H.

The figure shown in Figure 2-31 shows the values of d_h plotted against relative density for three different types of PZT. It can be clearly seen that all three types of PZT have a similar trend with respect to d_h versus relative density. Although in dense form the materials have similar d_h values the values for PZT-5H composites are highest due to higher d_{33} values of the material compared to PZT-7A and PZT-5A. From modelling these different types of PZT it can be concluded that if 3-3 connectivity piezocomposites are to be manufactured, then a material should be chosen that has high values of both d_{33} and d_{31}, such as PZT-5H.

2.4 Polymer Properties and their Influence on Figures of Merit

In addition to the electrical properties, the mechanical properties of the passive second phase may have a strong influence on the final properties of the piezocomposite. This was achieved by changing either the Young's modulus or the Poisson's ratio of the polymer in the FE model and calculating the figures of merit as previously discussed.

The Young's modulus was varied from 2GPa up to 10GPa in increments of 2GPa. This range was chosen to include most commonly available second phase materials such as silicone rubber (E≈2GPa) up to a hard epoxy resin (E≈8GPa). At each value for Young's modulus a full range of ceramic volume fractions was modelled, as in the case of the previous models, from 10% up to 90%.

The second material property to be investigated was Poisson's ratio. This was investigated because as the polymer strains and displaces with the piezoelectric phase in the 3 direction, the contraction of the polymer in the 1 and 2 directions is directly related to its Poisson's ratio. It was thought that this action would affect the strains in the model unit cell and therefore the calculated values for d_h and g_h. The Poisson's ratio was varied from –0.35 up to 0.45 which considers all second phase material candidates ranging from rubbers with a high Poisson's ratio to novel materials that have a negative Poisson's ratio. Negative Poisson's ratio materials have been shown to improve figures of merit in 1-3 composites[22].

2.4.1 Results From Changing Young's Modulus of Polymer Phase

The results obtained by changing the Young's modulus are shown in Figure 2-32. The general trend of d_h versus polymer volume fraction observed in Figure 2-26, was also observed with a maximum value of d_h at around 50% polymer volume fraction. It can be seen that as the Young's modulus of the polymer changes the location of the maximum value for d_h also changes. With high stiffness polymers the maximum is situated at around 35% polymer volume fraction. This rises to around 55% polymer volume fraction with low stiffness polymers.

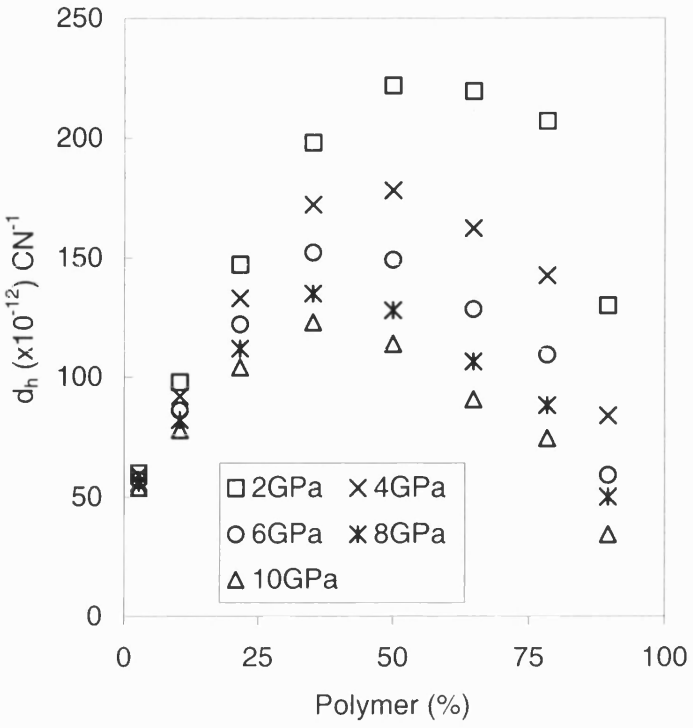

Figure 2-32: Graph showing the variation in d_h with change in polymer volume fraction and polymer Young's modulus.

It can also be seen from Figure 2-32 that composites modelled with a low stiffness polymer exhibit higher values of d_h than higher stiffness polymers. This factor is significant, for a 50% polymer volume fraction composite the d_h value using a 2GPa stiffness polymer is approximately double that of a 10GPa polymer stiffness composite. The effect of polymer volume fraction is most important around the central region of the graph, where d_h is at a maximum. This will be explained later in the thesis.

2.4.1.1 Piezoelectric Coefficients as a Function of Young's Modulus

The results in the previous section showed the d_h coefficient with respect to polymer volume fraction and Young's modulus. The d_h values were calculated from the individual d_{33} and d_{31} values, which can be seen in Figure 2-33.

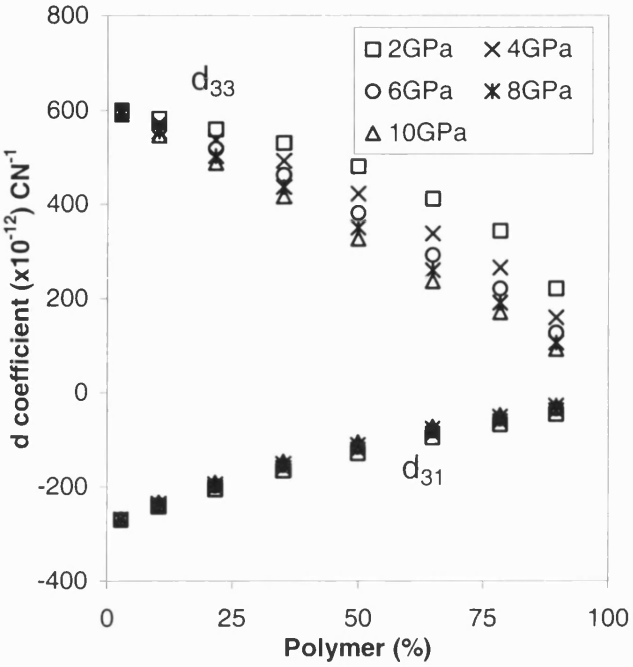

Figure 2-33: Graph showing values for d_{33} and d_{31} as a function of polymer volume fraction for various polymer Young's moduli.

The same trend of d coefficient versus polymer volume fraction, present in Figure 2-22, is also present here. It can now be observed how the d_h versus polymer volume fraction curves in Figure 2-32 are formed. At low polymer volume fractions the (absolute) values for d_{31} reduce at a faster rate with respect to polymer volume fraction than d_{33}, leading to improved d_h. At high polymer volume fractions the decrease in d_{33} leads to an eventual fall of d_h.

It can also be seen from Figure 2-33 that the effect of the polymer Young's modulus on the value of d_{33} is larger than the value of d_{31}. Increasing polymer stiffness leads to a reduced d_{33}, but has little effect on d_{31}. It is this effect that leads to an increased d_h over the whole porosity range for low Young's modulus polymer composites.

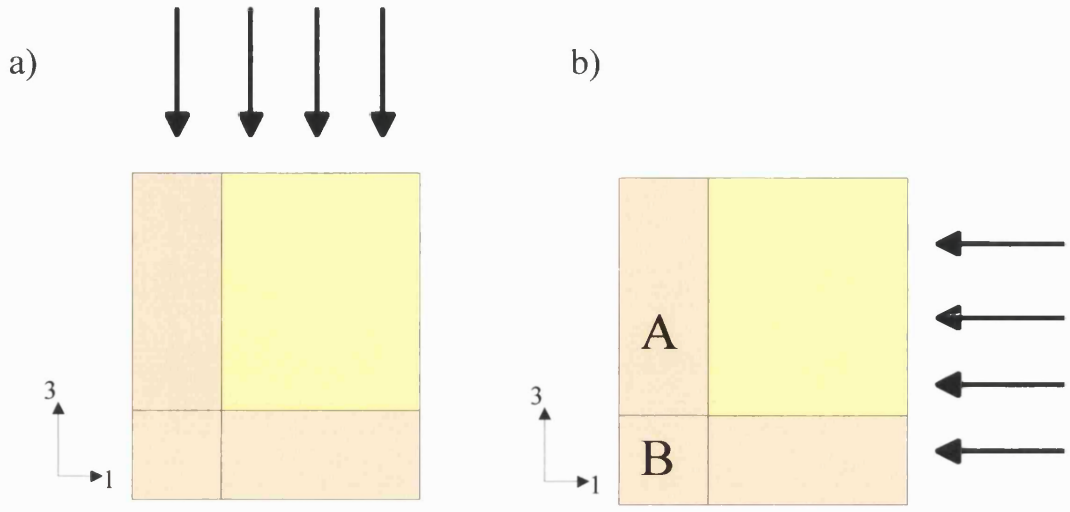

Figure 2-34: Effect of variation of the Young's modulus of the polymer on d_{33} and d_{31}.

Figure 2-34 shows a diagram of a quarter of a unit cell. Considering Figure 2-34a, as the Young's modulus of the polymer increases, an increasing amount of load is transferred into the polymer phase. This reduces the load in the piezoelectric ceramic struts and therefore as the Young's modulus of the polymer phase increases d_{33} will decrease. In the case of d_{31}, Figure 2-34b), a low polymer Young's modulus will cause the majority of load to be transferred by the ceramic strut into area B which contributes to d_{31}. As the Young's modulus of the polymer phase increases an increased load will be transferred into the polymer phase and thus into region A. As loads in both A and B regions contribute to d_{31} the increase of load into area A is balanced by the decrease in load in region B and there is little change in the value of d_{31} with Young's modulus, as shown in Figure 2-33.

2.4.1.2 Hydrostatic Voltage Coefficient (g_h) Values

Values for g_h were also calculated for a range of Young's moduli for the polymer phase. The results can be seen in Figure 2-35. A general trend of increasing g_h with gradual increase in polymer volume fraction is observed.

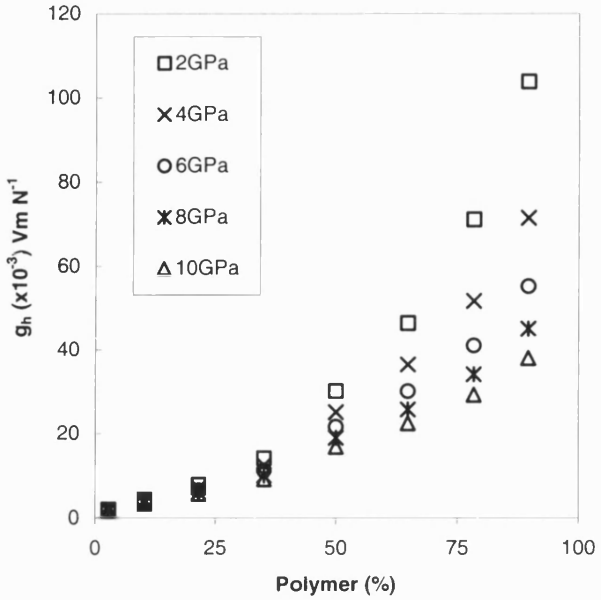

Figure 2-35: Graph showing g_h as a function of polymer volume fraction for various Young's modulus polymer values.

Again, higher g_h values are associated with the composites modelled with a low stiffness polymer second phase. As observed with the d_h coefficients, the g_h values for low stiffness polymer phases are significantly higher than those with stiffer inclusions. For example, at approximately 75% polymer volume fraction the value for g_h with a 2GPa polymer inclusion is over double that (70 x10^{-3}Vm N^{-1}) for the same volume fraction with a 10GPa polymer inclusion (30 x10^{-3}Vm N^{-1}).

In the case of the g_h values, the influence of the Young's modulus of the polymer on g_h seems to increase with increasing polymer volume fraction. This seems logical, as with larger amounts of polymer in the composite, changing the properties of the polymer would have a larger effect, also seen on d_{33} results. This is not the case with the d_h values, due to the fact that the d_h is dependent on the d_{33} and d_{31} coefficients which are independently changing as a function of polymer volume fraction.

2.4.1.3 Permittivity of 3-3 Piezocomposites

In the first chapter it was shown that the relationship between d_h and g_h is $d_h = \frac{g_h}{\varepsilon_{33}}$. As the d_h and g_h figures have been calculated as a function of polymer volume fraction and elastic modulus this equation was used to calculate the effective permittivity of the composite. The results are shown in Figure 2-36.

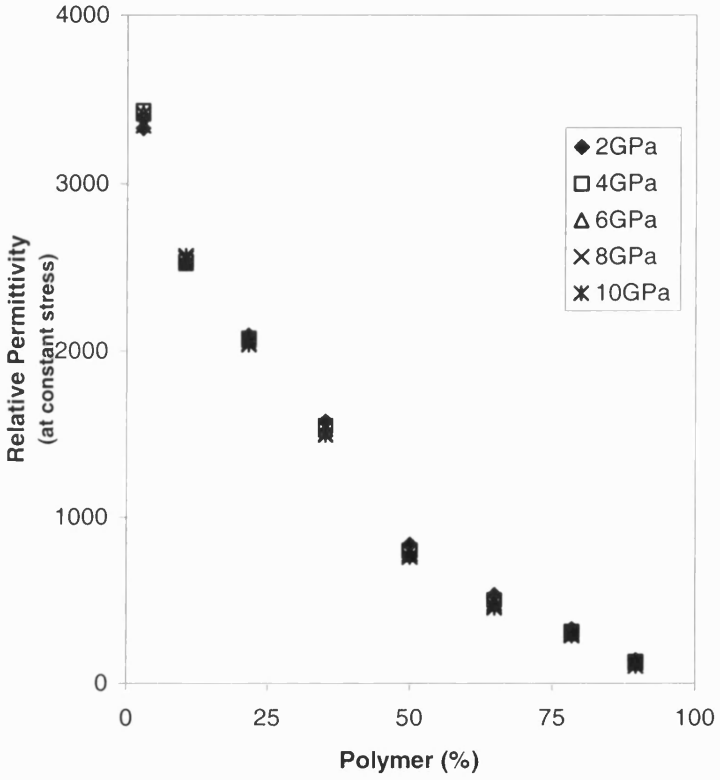

Figure 2-36: Chart showing permittivity versus polymer volume fraction for various Young's modulus polymer values.

This shows the composite permittivity values as a function of polymer volume fractions at various different values of Young's modulus. It can be seen from the figure that the permittivity decreases with increasing polymer volume fraction, but does not vary with the changing Young's modulus of the polymer phase, as expected.

2.4.2 Results from Changing Poisson's Ratio of the Polymer

As stated earlier, the Poisson's ratio was also modified within the finite element model as it was thought that changing the Poisson's ratio of the polymer would alter the stress and strain distribution in the composite as a load was applied. The Poisson's ratio was varied from -0.4 up to 0.45 in an attempt to model a wide variety of possible second phase materials. The polymer volume fraction modelled was constant in this case (50%).

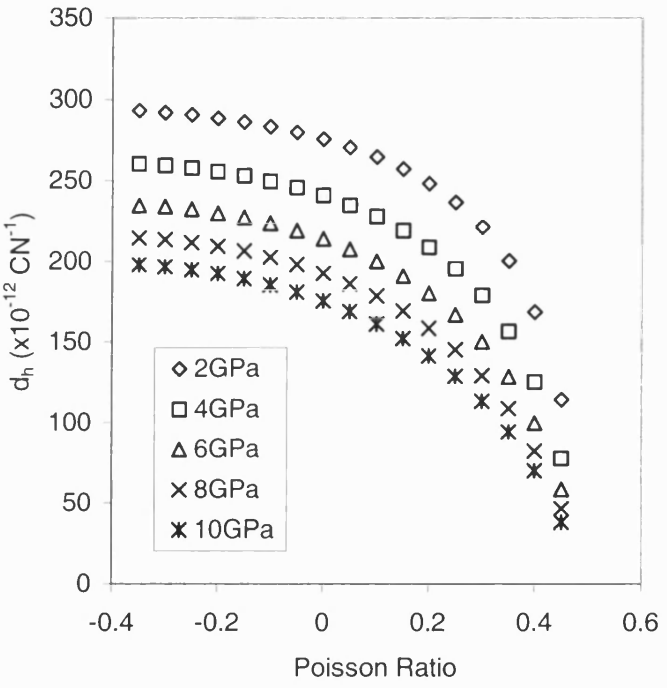

Figure 2-37: Chart showing d_h vs. Poisson's ratio for various Young's modulus polymer values. Polymer volume fraction is 50%.

The d_h results calculated for varying Poisson's ratio are shown in Figure 2-37 for a composite with 50% volume fraction of polymer. There are a number of trends present in the chart. It can be seen that, as before, a low Young's modulus polymer phase produces the highest values of d_h for a given Poisson's ratio. In addition, reducing the Poisson's ratio of the second phase has the effect of increasing the value of d_h for a given Young's modulus of polymer. Reducing the polymer's Poisson's ratio reduces its contraction in the 1 and 2 directions as it expands in the 3 direction with the ceramic material. This reduced contraction has the effect of reducing d_{31} and hence increasing d_h. However, as the Poisson's

ratio is reduced to below values of -0.1 no significant increase is observed. Therefore, unlike 1-3 composites there is no benefit in using negative Poisson's ratio filler materials and using typical epoxy materials with a Poisson's ratio of approximately 0.3 is sufficient.

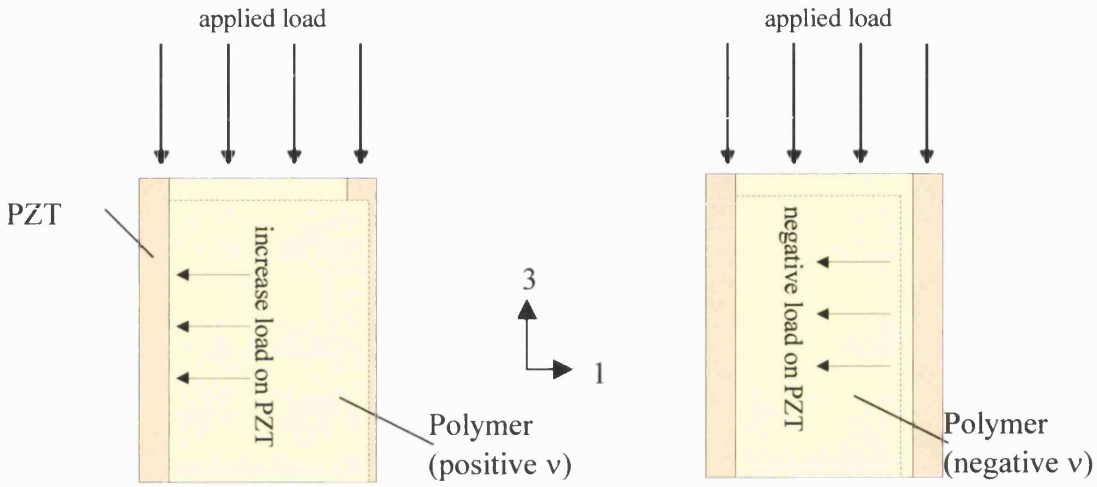

Figure 2-38: For 1-3 composites negative Poisson's ratio fillers produce high d_h values due to enhancing the "piston" motion of the composite.

Figure 2-38 shows that with 1-3 composites a filler material with a negative Poisson's ratio is advantageous due to the absence of any ceramic material in the 1 direction. Reducing the Poisson's ratio leads to a reduction in the load on the ceramic in the 1 direction and reduces the value of d_{31}. The lower value of d_{31} leads to an increased d_h.

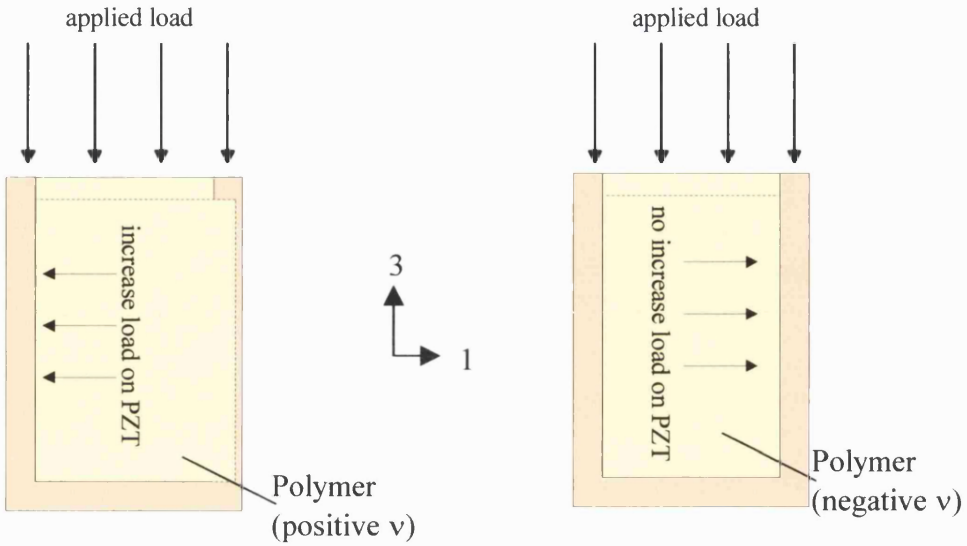

Figure 2-39: Ceramic in the 1 direction inhibits the polymer phase so that negative Poisson's ratio materials have little effect in 3-3 composites.

This effect is much less prominent in 3-3 composites, Figure 2-39, as ceramic present in the 1 direction inhibits the movement of the polymeric phase and greatly reduces the effect of any load produced by a negative Poisson's ratio filler material. Thus d_{31} does not decrease with decreasing Poisson's ratio and the value of d_h is relatively constant at low values of ν.

2.4.2.1 Influence of Poisson's Ratio on d_{33} / d_{31} Coefficients

The individual d_{33} and d_{31} coefficients used to calculate the chart shown previously are shown in Figure 2-40 and Figure 2-41.

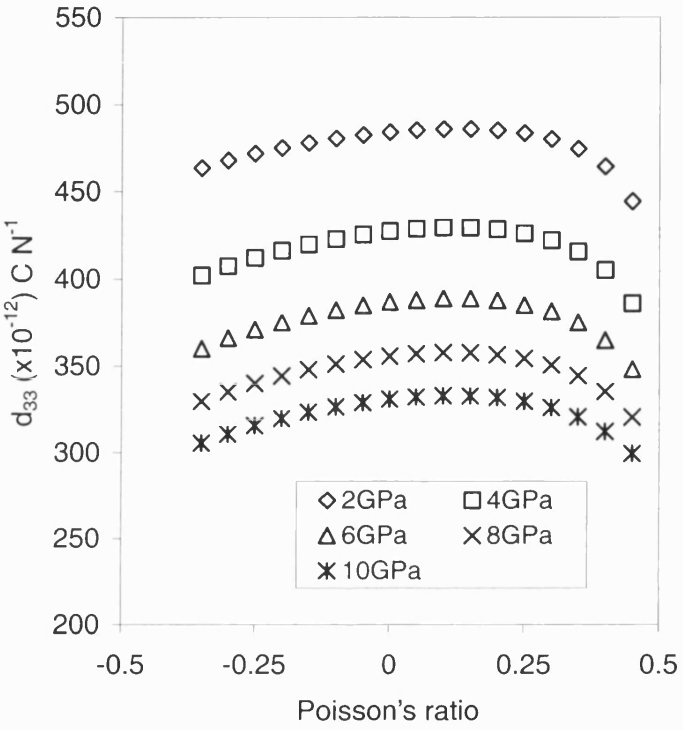

Figure 2-40: Chart showing d_{33} vs. Poisson's ratio for various Young's modulus polymer values. Polymer volume fraction is 50%.

Figure 2-40 shows the values of d_{33} against Poisson's ratio. As usual the composites with the lower stiffness polymer exhibit higher values of d_{33} for a given Poisson's ratio. For a given polymer stiffness, the d_{33} varies with Poisson's ratio and there is a d_{33} maximum at a Poisson's ratio of approximately 0.1. The location of the maxima is the same for the whole polymer stiffness range.

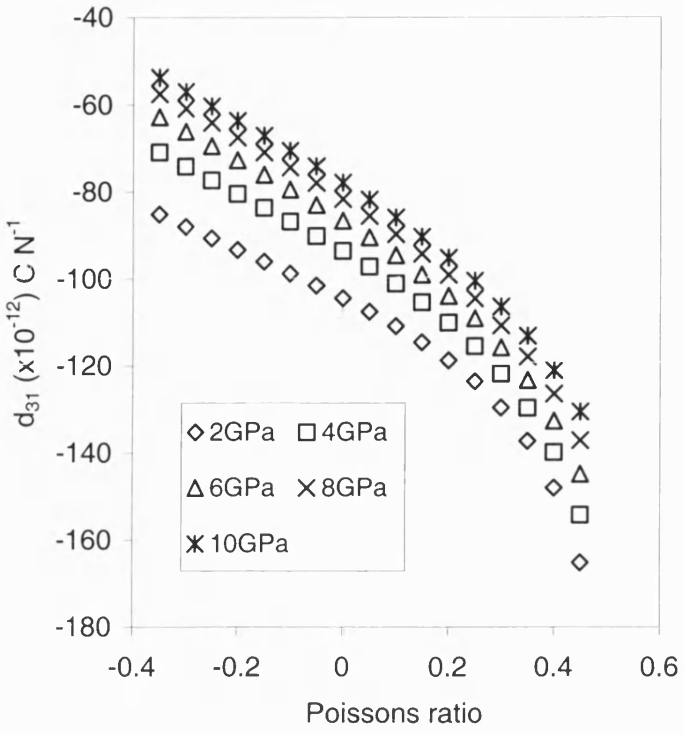

Figure 2-41: Chart showing d_{31} vs Poisson's ratio for various Young's modulus polymer values.

As would be expected, the d_{31} coefficient is highly dependent on Poisson's ratio. Reducing the Poisson's ratio for a given stiffness of polymer leads to a gradual decrease in d_{31} due to the reduced contraction in the 1 and 2 directions as the polymer expands in the 3 direction.

2.4.2.2 Influence of Poisson's Ratio on Hydrostatic Voltage Constant (g_h)

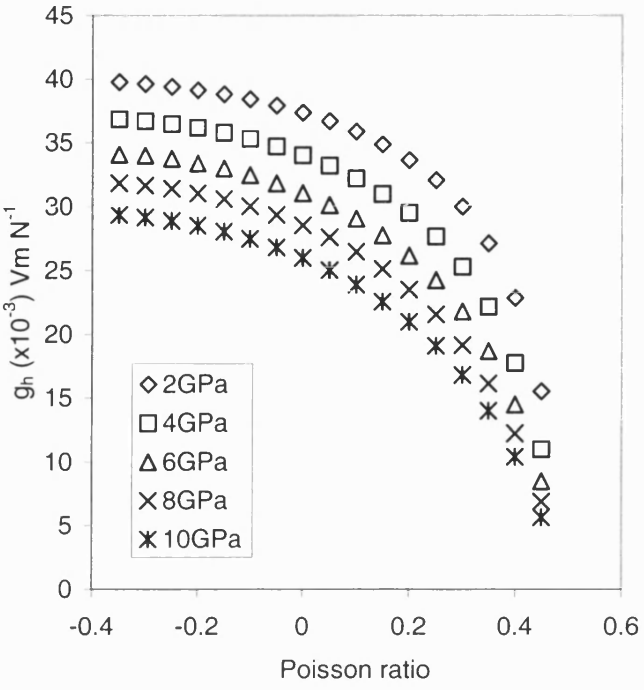

Figure 2-42: Graph showing g_h as a function of Poisson's ratio for various Young's modulus polymer values.

Figure 2-42 shows g_h as a function of Poisson's ratio for a composite with 50% polymer volume fraction. As $g_h = d_h/\varepsilon_{33}$ and permittivity does not depend on Poisson's ratio the trend is similar to that seen for d_h versus Poisson's ratio, Figure 2-40.

The value of g_h reduces dramatically as Poisson's ratio increases above 0.3, however reducing Poisson's ratio below 0.1 does not produce a significant increase in g_h.

2.5 Analytical Comparison

The only previous significant modelling work on 3-3 piezocomposites was an analytical model developed by Rittenmyer et al [25] to predict the properties of 3-3 piezocomposites. The physical shape of the model was the same as the finite element models investigated in this chapter. The results from the analytical modelling are compared to FE to examine if similar observations are made between the two different types of model. In addition, advantages of both the analytical modelling and FE modelling will be outlined.

2.5.1 Outline of Analytical Method (Rittenmyer Model)

The Rittenmyer model consists of a series of piezoelectric columns within which certain sections are assumed to be active for the contribution to the d_{33} and d_{31} coefficients, much in the same way as described in section 2.3.1.2.

Figure 2-43 shows the basis of the model. The shaded region in a) shows the region assumed to contribute to the d_{33} coefficient and permittivity, and the shaded region in b) is the volume assumed to contribute to d_{31}. From these figures values of d_h and g_h can be calculated assuming a stress independently applied in the z (3) direction and x (1) direction.

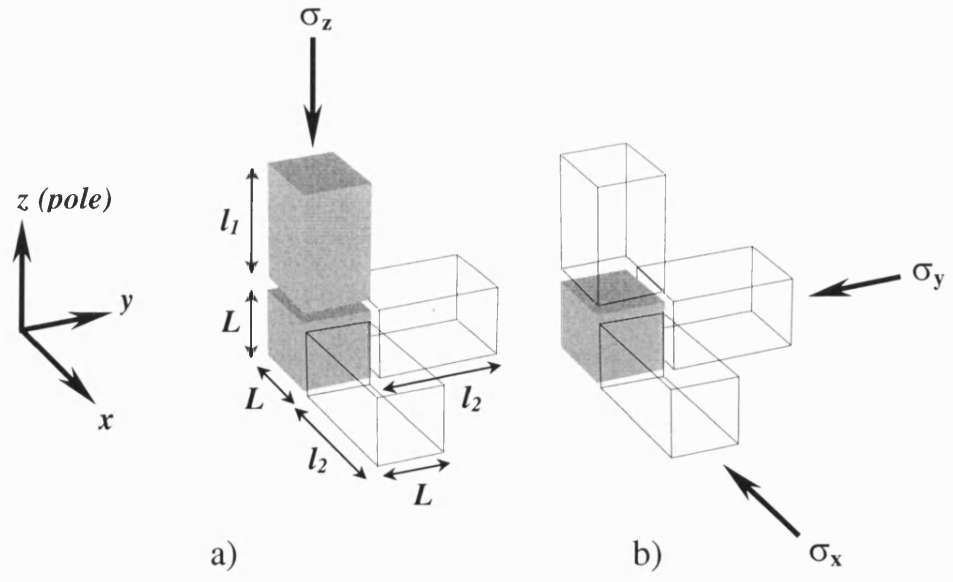

Figure 2-43: Diagram after (42) showing active regions in producing a) d_{33} and b) d_{31}.

Using the model shown, equations were formed using composite theory to predict the d_{33}, d_{31} and permittivity of the composite structure for a given volume fraction of ceramic.

2.5.1.1 Equations and Assumptions

The model assumes that due to the high stiffness of the ceramic it bears all of the load applied to the composite and that the polymer phase bears no stress. For this assumption an equation was derived for d_{33} (Equation 2-6).

$$d_{33}^{Composite} = \frac{v^{d33PZT}.d_{33}^{PZT}}{v^{d33PZT} + (1 - v^{d33PZT}).\frac{s_{33}^{PZT}}{s_{33}^{Polymer}}}$$

Equation 2-6: d_{33} for the composite in terms of material properties and geometries.

where,

v^{d33PZT} = volume fraction of PZT contributing to $d_{33}^{Composite}$

$v^{Polymer}$ = volume fraction of polymer and inactive PZT = $1 - v^{d33PZT}$

s_{33}^{PZT} and $s_{33}^{Polymer}$ = longitudinal compliance's of active PZT and polymer respectively (a value of 0.1 has been assumed for the ratio $s_{33}^{PZT}/s_{33}^{Polymer}$ [7])

d_{33}^{PZT} = 590 x 10^{-12} m V^{-1} for PZT-5H and $d_{33}^{Polymer}$ = 0 for the polymer phase

In a similar fashion d_{31} can be expressed by Equation 2-7.

$$d_{31}^{Composite} = d_{31}^{PZT}.v^{d31PZT} = \frac{d_{31}^{PZT}.L^3}{(L + l_1).(L + l_2)^2}$$

Equation 2-7: d_{31} for the composite in terms of material properties and geometries.

These two equations give d_{33} and d_{31} as a function of ceramic volume fraction. The values of d_h calculated from these can be seen in Figure 2-44. Although the absolute values differ

from the FE modelling presented in this chapter, similar trends in d_h and g_h as a function of polymer volume fraction are observed as in Figure 2-44.

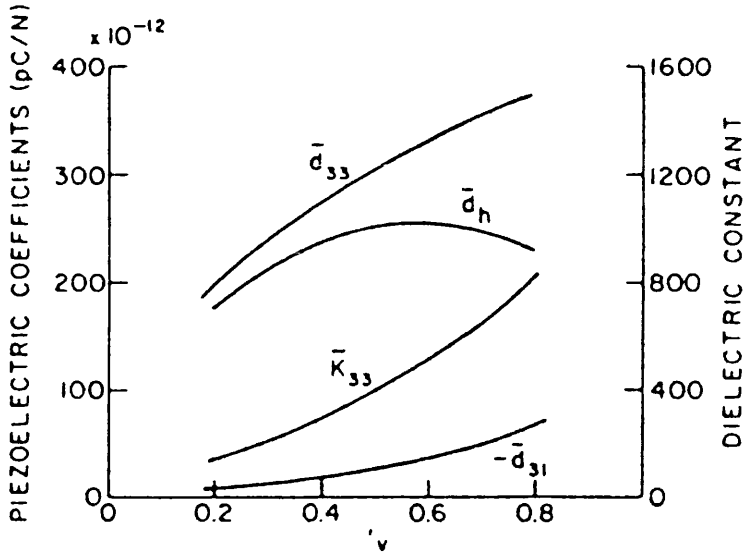

Figure 2-44: Rittenmyer model, after (25) analytical modelling of d_{33}, $-d_{31}$ d_h and ε_{33} (k_{33}) with respect to polymer stiffness.

The Rittenmyer model states the assumption, that the ceramic being much stiffer than the polymer, it bears all the stress. However it is of interest to note that Equation 2-6 assumes a constant ratio of S_{PZT} / S_{POLY} = 0.1 for the compliances of the two materials. The disadvantage of this model is that it is unable to consider varying elastic moduli as a small change in the S_{PZT}/S_{POLY} ratio produces a large change in the output of the model. As the equations for d_{33} and d_{31} are derived by considering loads applied independently, the loading is not truly hydrostatic. In addition, the influence of Poisson's ratio on the figures cannot be considered.

Finally, the values of d_h and g_h predicted by the analytical model are greater than those predicted by finite element modelling due to the oversimplification that the ceramic experiences all of the applied load.

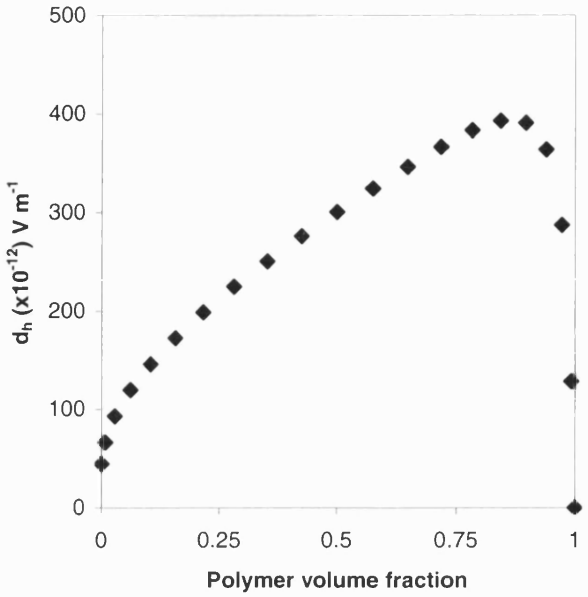

Figure 2-45: Modified analytical modelling showing trend as Young's modulus of the polymer phase approaches zero.

If the S_{PZT}/S_{POLY} ratio is changed in the analytical model to lower values (i.e. lower polymer Young's modulus) the curve tends towards the initial FE modelling of the PZT porosity model shown in Figure 2-11. As the Young's modulus of the polymer phase approaches zero and the S_{PZT}/S_{POLY} approaches zero then Equation 2-6 reduces to $d_{33}^{compoosite} = d_{33}^{PZT}$ as observed in the initial FE modelling. This demonstrates one of the weaknesses in both the initial FE modelling and the analytical modelling.

Bowen extended this analytical model to consider both the load which is experienced by the ceramic and the polymer to allow the influence of polymer elastic modulus on d_h and g_h for 3-3 piezocomposites to be investigated[26].

2.5.2 Discussion of Limitations and Merits of Both Methods

Both the FE modelling and the analytical modelling have produced similar results to each other. Although the absolute values are different there are striking similarities in the trends evident on both sets of charts. FE and analytical modelling have advantages and disadvantages, which allow them both to be used in different circumstances.

One of the main disadvantages with FE modelling is the amount of computer power required to process models. Solving the model on a faster computer can solve this time constraint but this reduces the usefulness of the process.

A disadvantage of the analytical model is that in considering the unit cell as a parallel series of solid cuboids the model considers the application of force in each direction separately. Therefore, any effect on d_h and g_h due to the Poisson's ratio of the polymer is not modelled.

The analytical model solves instantly as it is merely a matter of changing values in a spreadsheet, and all the figures of merit can be calculated, for a whole range of both porosities and polymer Young's moduli. The finite element model uses different boundary conditions to calculate the effective figures of merit of the composite and is therefore more time consuming.

The main disadvantage of the analytical model is that the equation is only valid for a particular geometry. For every new shape of unit cell a new analysis and equation has to be developed and it is often not possible to formulate equations for complex shapes which are more representative of a real ceramic microstructure.

Finite element modelling is ideal for this area. Any size or shape of model can be constructed within the FE package, solved and analysed. Any number of elements can be added and any geometry can be modelled. The only constraints are the physical memory and processing time available. Given time, complex models can be solved with ease.

The preliminary models of 3-3 piezocomposites have been discussed. In order to determine experimental results to compare with model predictions, 3-3 composites were manufactured and tested. These results are presented in the following two chapters.

3 Experimental Production

As the aim of this research is to optimise 3-3 piezocomposites, in terms of porosity volume fraction and structure, a variety of processes were involved with the manufacture and testing of piezocomposites with various architectures.

The following chapter will discuss procedures used in the processing, manufacture, testing and optimisation of 3-3 piezocomposites. These will include sintering of PZT, poling of PZT and the different manufacturing methods of producing 3-3 piezocomposite structures.

3.1 Sintering Profiles

The sintering of the active ceramic body is one of the most important stages in its production; a change in the sintering conditions can change the grain size, introduce porosity and even change the stoichiometry of the material.

In the following section the sintering characteristics of PZT-5H will be discussed as this was the piezoelectric material used to manufacture the piezocomposite components.

3.1.1 Sintering Dense PZT

The main factor when considering optimising the sintering conditions of a ceramic is the final density of the sintered body. A high density, >95% theoretical, is required to obtain good mechanical and electrical properties. An investigation into the possible sintering profiles (temperature and time) and conditions was undertaken.

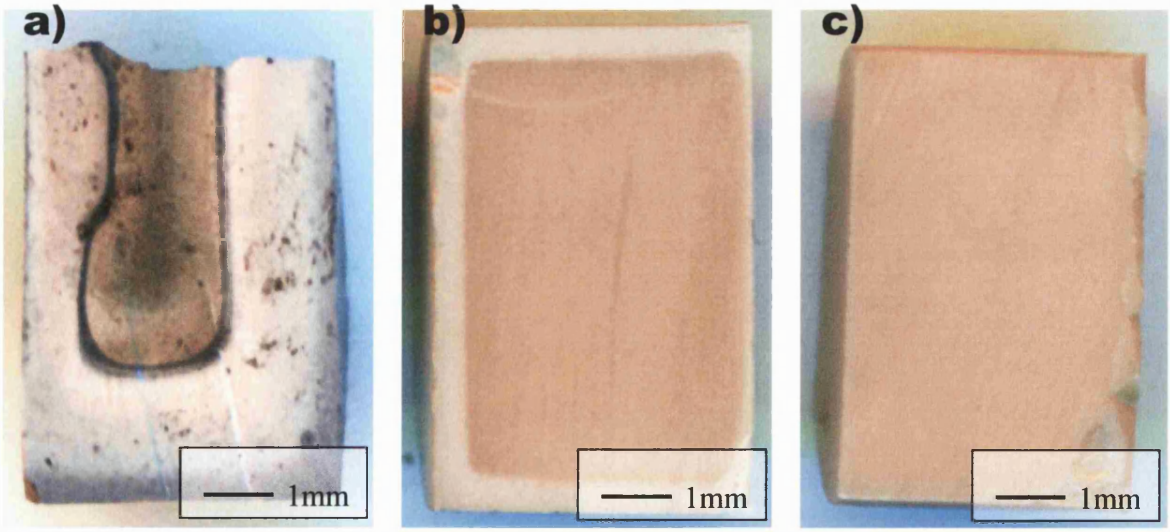

Figure 3-1: Examples of three different sintering schedules. a) 1250°C / air, b) 1225°C / air and c) 1225°C / lead atmosphere.

The initial temperature chosen to sinter the PZT was 1250°C, a time of 2 hours was chosen and Figure 3-1a shows a cross-section of a body sintered at 1250°C. The colour variations through the section of the material are due to lead loss in the ceramic. Further sintering conditions were examined, Figure 3-1b shows the effect of reducing the sintering temperature and time to 1225°C for 2hrs. In this case a more homogeneous structure is observed and the lead loss is confined to the very outer few millimetres of the body. This minor lead loss was found to be eliminated by sintering the body in an enclosure with excess PZT powder present, which is shown in Figure 3-2. Figure 3-1c shows a section of the sintered body obtained using this method of heat treatment, indicating a homogeneous structure with no observable lead loss.

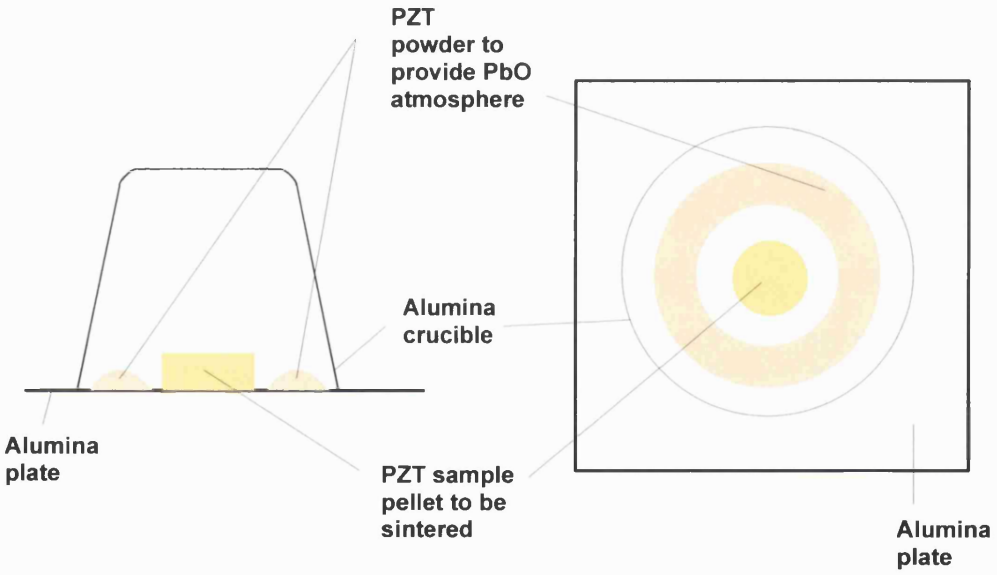

Figure 3-2: Schematic of enclosure for sintering PZT based ceramics.

Further studies on the sintering conditions of PZT bulk samples were carried out. Sintering temperatures were chosen between 1000°C and 1250°C in an attempt to optimise the sintering temperature. Samples were sintered for two hours and their densities were measured and compared to the powder manufacturer's density figure of 7500kg m^{-3}. Figure 3-3 shows the results of the different sintering temperatures on the final measured density.

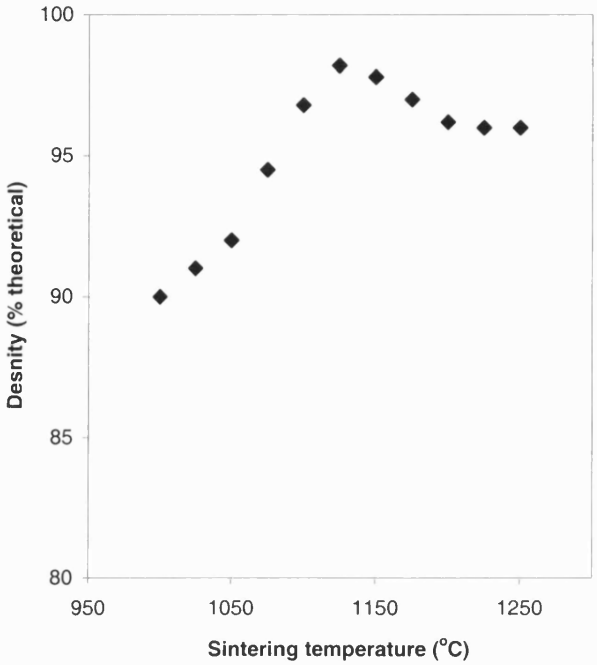

Figure 3-3: Chart showing final density of sintered sample against sintering temperature.

Figure 3-3 clearly shows a percentage theoretical density maximum of 97% for samples sintered at 1125°C and all further heat treatment was carried out at this temperature for 2 hours.

3.1.2 Sintering High Porosity PZT Bodies

Sintering solid bodies differs slightly from sintering high porosity or foam structures as shown in Figure 3-4. The foam structures have a large surface area to volume ratio compared to the dense pellet samples. This large surface area can lead to an increased lead loss in the sample, as shown in Figure 3-4a. It is for this reason that it is important to place the foam sample inside the crucible with a large excess of PZT power to eliminate lead loss, Figure 3-4b.

Figure 3-4: Examples of a) lead loss during sintering and b) no lead loss during sintering.

3.2 Poling

Once the piezocomposite is manufactured, poling is necessary in order to obtain a piezoelectric response, as previously discussed in section 1.1.1.5. There are two accepted ways to pole piezoelectric materials, the first and most common method is to apply an electric field and heat in an oil bath, the second method is known as "corona poling".

As it was necessary to manufacture poling equipment for this research it was decided to pole samples by the corona poling method as this equipment could be constructed in-house and has been shown to be useful for poling piezocomposites [3]. This method is particularly useful in poling porous structures, which would become infiltrated with oil if traditional oil bath poling was used.

A diagram of the equipment is shown in Figure 3-5. The sample is placed in the position indicated in the figure at a fixed distance below the needle from which the corona point originates.

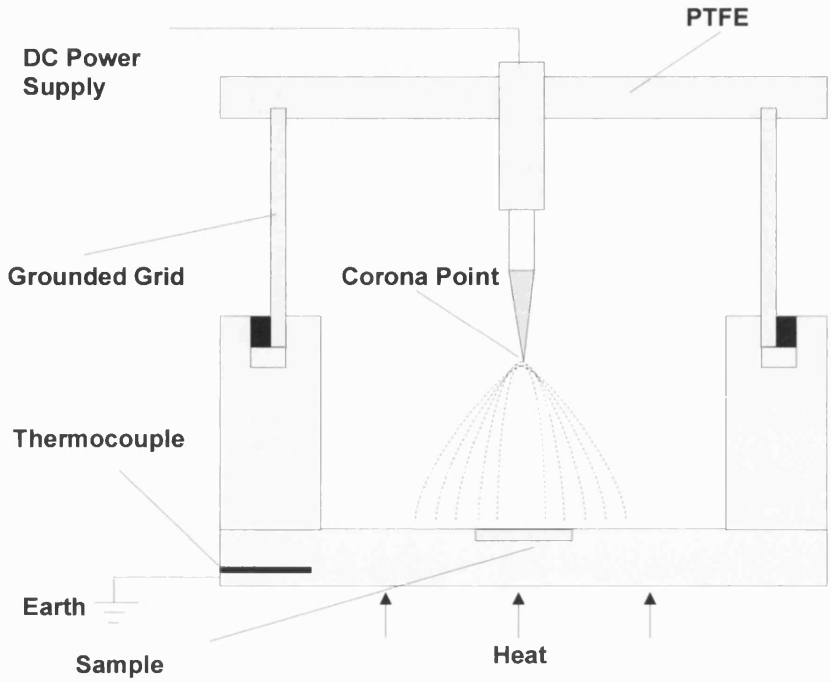

Figure 3-5: Schematic of the constructed corona poling rig, approx 130mm diameter.

Whilst at an elevated temperature (80°C), which is continuously monitored by a thermocouple, a potential difference is applied for a fixed period of time between the corona point and the earthed base. The sample is then cooled whilst remaining in the poling rig with the electric field constantly applied. Once the sample has cooled sufficiently the electric field is removed and the sample is removed from the rig. The piezoelectric disc is now poled and a piezoelectric response can be observed, for example a charge per unit force is generated.

3.2.1 Poling Optimisation (Dense Samples)

In order to assess the ideal conditions under which corona poling occurs a number of different poling conditions was examined. This involved such variables as the voltage applied to the corona point, the temperature at which the sample was elevated to, and the position of the sample in the poling rig. The results will be discussed in this section.

3.2.1.1 Influence of Applied Voltage

The DC power supply attached to the poling rig enabled the voltage to be varied between 0 and 30kV, which was held for 10 minutes at the poling temperature. The temperature was set to 110°C maximum and the samples were cooled to 50°C before the voltage was removed.

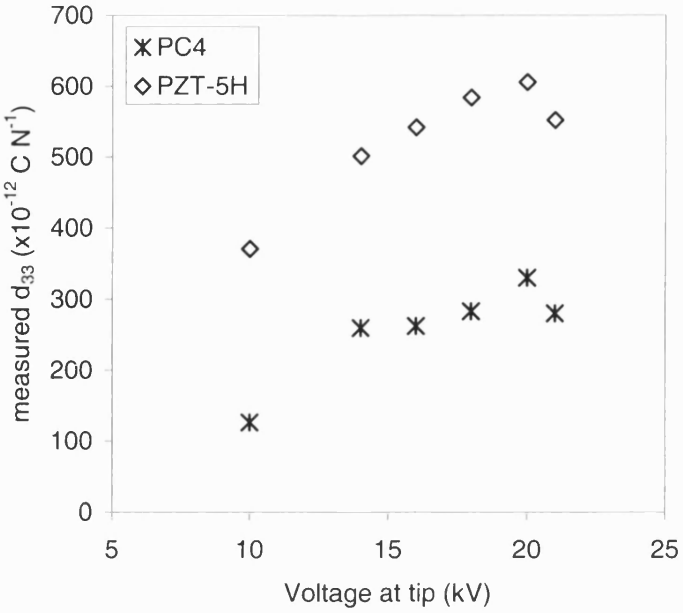

Figure 3-6: Chart showing d_{33} versus poling voltage indicating optimum d_{33} at 20kV.

The degree of poling was evaluated by measuring the d_{33} coefficient 24hours after poling. The equipment used to measure d_{33} will be described in the following chapter.

The graph in Figure 3-6 shows the values of d_{33} measured by poling at various tip voltages for two different types of PZT (PC4 and PZT-5H). The chart clearly shows that the optimum poling voltage is reached at 20kV for both types of PZT. If this voltage is exceeded, the sample incurs damage whilst being poled due to dielectric breakdown and also electrical discharge occurs between the corona point and the base of the poling rig. All subsequent poling was carried out at 20kV with the corona point at a distance of 30mm from the base.

3.2.1.2 Influence of Temperature

As previously discussed, the samples were initially heated to a fixed temperature and an electric field was applied before the samples are cooled under the influence of an applied electric field. The temperature at which the samples were maintained and poled, was varied in order to assess the optimum poling temperature of the samples.

The temperature of the poling rig was monitored by a thermocouple, the position of which can be seen in Figure 3-5. The pink area in the diagram was constructed of solid aluminium, which had two repercussions. Firstly, the poling rig would take a long time to heat up and cool down and secondly the temperature of the thermocouple, which was closer to the heat source than the sample, would be slightly higher than the temperature of the sample.

It had been reported by Waller[3] et al. that during corona poling of PZT-5H the sample must be above 80°C. In practice, this translated to a thermocouple temperature of around 100°C. It was found that if the samples were to be heated to a thermocouple temperature of 110°C in and electric field and then cooled to 50°C, poling was satisfactory and d_{33} values of approaching 600pCN^{-1} were observed for PZT-5H.

3.2.1.3 Poling Profile from Centre of Corona Point

It can be seen from the schematic of the corona poling rig in Figure 3-5 that the strength of the field used to pole the samples will vary with the position of the sample inside the poling rig. For example, it would be expected that samples placed directly under the corona point would experience a higher field compared to those placed at the edge of the base plate. This factor is important as it defines the area into which samples have to be placed in order to fully pole the material, and hence the number of samples that can be poled at any one time.

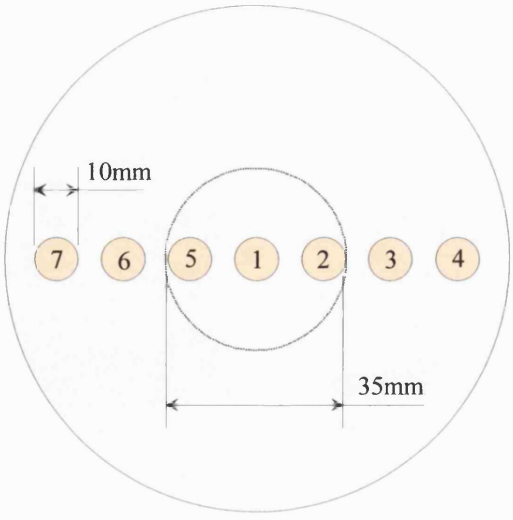

Figure 3-7: Position of samples for poling field comparison and area of optimum poling is indicated.

A number of 10mm diameter samples were placed inside the poling rig at the positions indicated in Figure 3-7. Poling was carried out in the optimum manner as described by Section 3.2.1.1 and the d_{33} of the samples was measured both immediately after removal from the poling rig and after 24hrs. Measurement of d_{33} after a period of 24hrs after poling was undertaken, as there can be considerable ageing and reduction in d_{33} during this period.

The results of this experiment are indicated in Figure 3-7. This shows an optimum region for poling in the area of samples 5, 1 and 2, which is the area marked on the diagram and is directly below the corona point. Outside this area there is a significant reduction in the d_{33} of the samples and hence poling is not suitable in this region. Therefore the number of 10mm diameter samples poled at any one time was restricted to three.

3.2.1.4 Optimised Corona Poling Conditions

To summarise, corona poling was chosen as a quick, easy and small scale method to pole piezoelectric samples. The optimum conditions for poling were investigated and found to be as follows:

i) voltage at needle to be at 20kV, 30mm from base of rig,

ii) heating up to 110°C (as read from thermocouple at base),

iii) restricting the number of discs to be poled to three samples in the centre of poling rig,

iv) cool to 50°C before removal of voltage.

If these guidelines were followed, fully poled PZT5H samples could be prepared with d_{33} values comparable to the manufacturers figure of $d_{33} = 593$ pC N^{-1}.

3.2.2 Poling of Porous Samples

The poling of porous ceramics and polymer impregnated ceramics can differ from the poling of dense materials. These factors are outlined below with experimental steps undertaken to ensure the sample is poled adequately.

There are a number of differences in poling porous samples. These stem from two microstructural factors, the first is that the thermal conductivity of the porous samples is much lower than that of a dense samples and secondly the nature of any second phase (i.e. air and polymer) present in the composite.

Due to the low thermal conductivity of the porous samples, the temperature indicated by the thermocouple needs to be higher than that when poling dense samples. This is to ensure the whole of the sample is above the temperature for efficient poling (80°C). With porous samples the value of d_{33} from the manufacturer of the PZT powder was no longer relevant, but it was found that there was no benefit in d_{33} by increasing the temperature above 110°C for the low porosity (BurPS samples) and 130°C for high porosity (foam based) samples.

When polymer impregnated piezocomposites were being manufactured it was found that poling of the ceramic must be carried out before the polymer phase was impregnated into the porosity. This is due to the low permittivity of the second phase preventing the ceramic phase from being subject to the large electric field needed to pole the bulk material. This problem was not apparent with PZT-air composites due to the mechanism of corona poling, section 1.1.1.5. After the porous ceramic was poled it could then be impregnated with a second phase.

3.3 Production Methods

Two methods were chosen to produce porous piezoelectric ceramic samples. These methods were the burnt off plastic spheres (BurPS) method and the polymer foam reticulation method. These methods were chosen, as each process enables the manufacture of different ranges of porosity volume fraction. Both of these methods are outlined in the first chapter of this thesis. They were chosen for the ease of use, lack of need for any specialised equipment and flexibility of the processes.

3.3.1 BurPS Process

The BurPS method is an established method of manufacture of porous materials. The schematic in Figure 3-8 shows the method utilised in the production of porous samples.

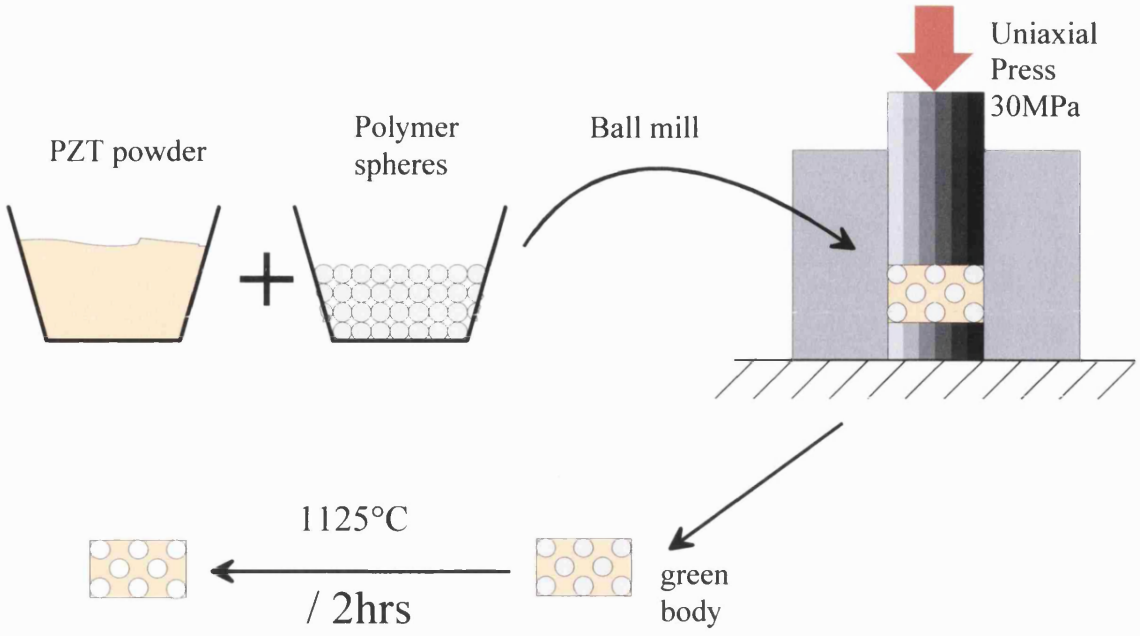

Figure 3-8: Schematic of the BurPS method of manufacture.

Ceramic powder is mixed by a ball milling process with polymer spheres of the required size. After milling the mixture is uniaxially pressed at 30MPa in the same way as conventional ceramic processing.

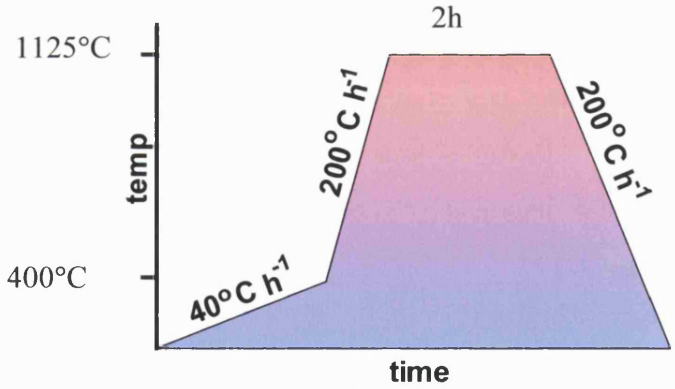

Figure 3-9: Temperature profile for sintering of BurPS porous PZT composites.

An initial heat treatment, a relatively slow heating to 400°C was used to burn off the polymeric component, and further heating to 1125°C to sinter the ceramic was carried out as shown in Figure 3-9.

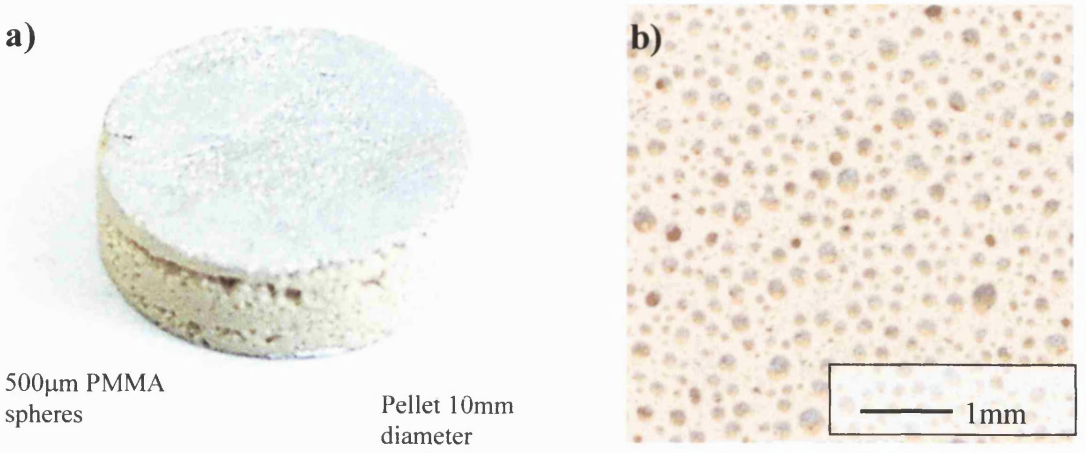

Figure 3-10: Example of a structure produced by the BurPS (PMMA inclusion) method, a) complete pellet, and b) microstructure.

An example of a typical sintered BurPS produced sample is seen in Figure 3-10a) which shows a high porosity (approx 40% porous) pellet with visible pores. The close up of the microstructure is shown in Figure 3-10b) which shows uniformly distributed large pores which are formed due to the burn out of the plastic spheres.

The size and amount of porosity can be easily modified by changing the size and shape of the inclusion material and the ratio of inclusion material to ceramic powder (Table 3-1). The BurPS production methods using different inclusion materials will now be discussed, namely PMMA (poly methyl methacrylate) , PEO (polyethylene oxide), CS (cornstarch) and SR (self raising flour).

Designation	Inclusion material	Source
PMMA	poly methyl methacrylate	Struers Mounting resin-3
PEO	polyethylene oxide	Union Carbide polyox resin
CS	Cornstarch	Sainsburys
SR	Self raising flour	Sainsburys

Table 3-1: Properties of inclusion materials.

3.3.1.1 PMMA Spheres / Production & Microstructure

The BurPS method was carried out with large poly(methyl methacrylate), PMMA, spheres of two different sizes, approximately 500μm, and 100μm in diameter.

Difficulties arose during production due to the relatively large size of the 500μm PMMA spheres. The samples in the green state after pressing were fragile and difficult to handle. It was only possible to manufacture the samples using the large PMMA spheres to a minimum of 40% ceramic content (60% final porosity). Above this limit the heat treatment often destroyed the samples, as shown in Figure 3-11.

Figure 3-11: Cracked and distorted sample after heat treatment.

This cracking and delamination is caused by poor mixing of the PMMA spheres with the ceramic powder prior to pressing. Commonly, ceramic powers are mixed using a liquid phase (either water or alcohol) to ensure thorough mixing. This procedure was not applicable to mixing PMMA spheres and PZT ceramic powder as the density of the spheres (1.2Mg m^{-3}) is similar to that of water and the density of PZT is relatively high (7.5Mg m^{-3}). Any attempt to mix the powders within a fluid resulted in the PZT sinking to the bottom and separating from the PMMA.

Dry mixing was subsequently used, and the variation in mixing means that some samples could be sintered successfully and others did not survive the heat treatment. Samples that did survive were poled and tested.

Samples produced with the small, 100μm, PMMA spheres appeared to be more robust in the green state that those produced with the large spheres, but the limit of 40% ceramic content (60% final porosity) was still apparent.

Inspection of the microstructure of the samples produced using PMMA spheres showed cracking.

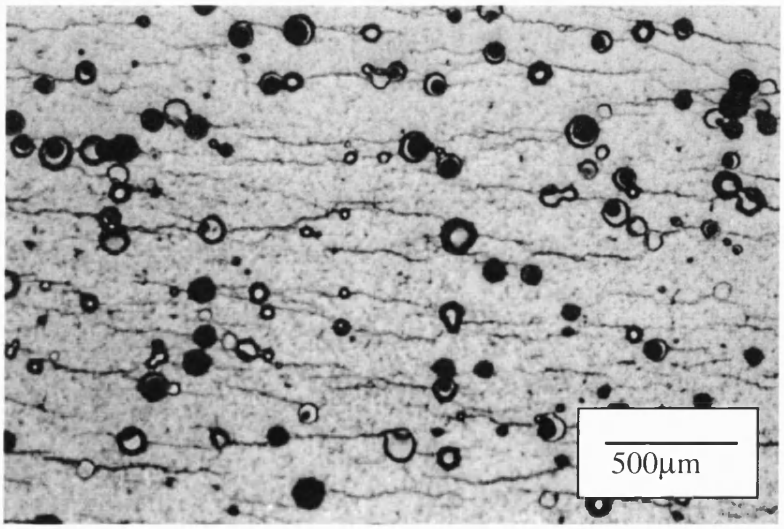

Figure 3-12: Optical micrograph showing cracking of samples produced using PMMA spheres. The sample was examined prior to poling.

The cracks run perpendicular to the pressing direction and are caused by the pressing forces compressing the soft ceramic powder more than the hard PMMA spheres. As the pressure is removed from the sample, the powder expands a small amount and cracks / lamination defects are created in the sample. Similar cracks have been reported by Rittemyer [25] which were thought to be cracks generated during poling. In this work the cracks are present in unpoled samples and are therefore likely to be caused by pressing.

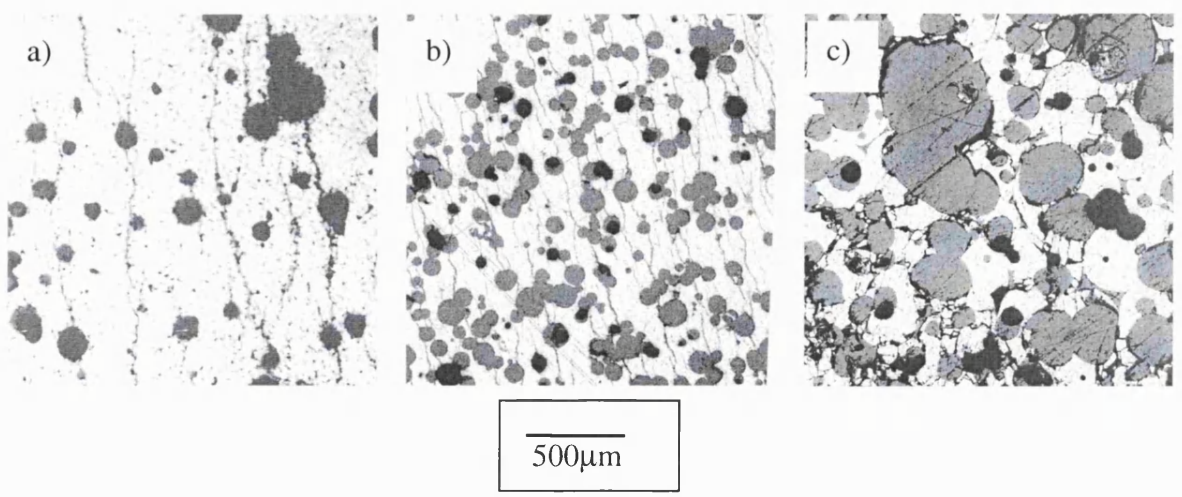

Figure 3-13: Examples of microstructures using PMMA and the BurPS method. a) low, b) medium and c) high porosity.

Samples were produced using the BurPS method with poly(methyl methacrylate) as a inclusion material and ranged from 40% dense to 97% dense. The samples were then poled and electrically tested using the methods outlined in the next chapter.

3.3.1.2 PEO Spheres / Production & Microstructure

In addition to PMMA spheres, and in an attempt to reduce the cracking seen in the microstructure in the PMMA based material, a lower stiffness polymer was chosen as an inclusion material. Poly(ethylene oxide) (PEO) was mixed with PZT powder in various ratios to produce porous ceramic samples.

The samples produced by pressing PEO appeared to be of higher green strength than both sizes of PMMA samples. However, it was still not possible to successfully produce and sinter samples with less than 40% density (60% porosity). An example of the limit of porosity can be seen in Figure 3-14, which shows damage to the body during heat treatment, caused by extensive cracking and deformation.

Figure 3-14: Photograph showing 40% dense sample produced by BurPS using PEO as inclusion material.

The polymer softens during initial stages of the heat treatment and when present in high volume fractions causes distortion of the green body. In addition, at high temperatures whilst burning off the polymer, the large amounts of gas produced by the high polymer volume fractions causes cracks. With lower amounts of inclusion material this process occurs more slowly and the volatile gasses have time to exit the sample through the interconnected porosity.

Figure 3-14 shows an optical micrograph showing the structure of a sample produced by the BurPS method using PEO as an inclusion material. It can be seen that the obvious round pores observed when using PMMA are not present in the PEO sample, which is probably related to the deformation of the PEO during pressing. On closer inspection the microstructure reveals that there are no cracks in the bulk as a result of the inclusion material during pressing. A range of porosities can be seen in micrographs in Figure 3-16 which show that as the porosity volume fraction increases the pores become interconnected.

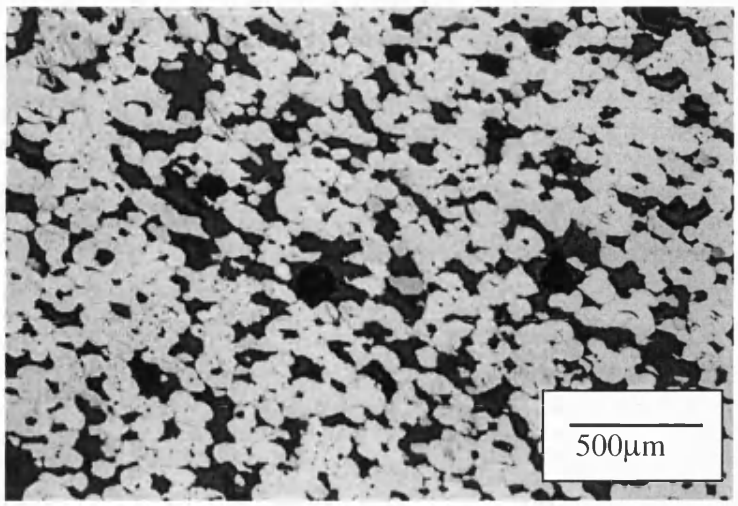

Figure 3-15: Optical micrograph showing the structure of PEO produced BurPS samples. Note the absence of cracks as seen in the sample produced using PMMA as the inclusion material.

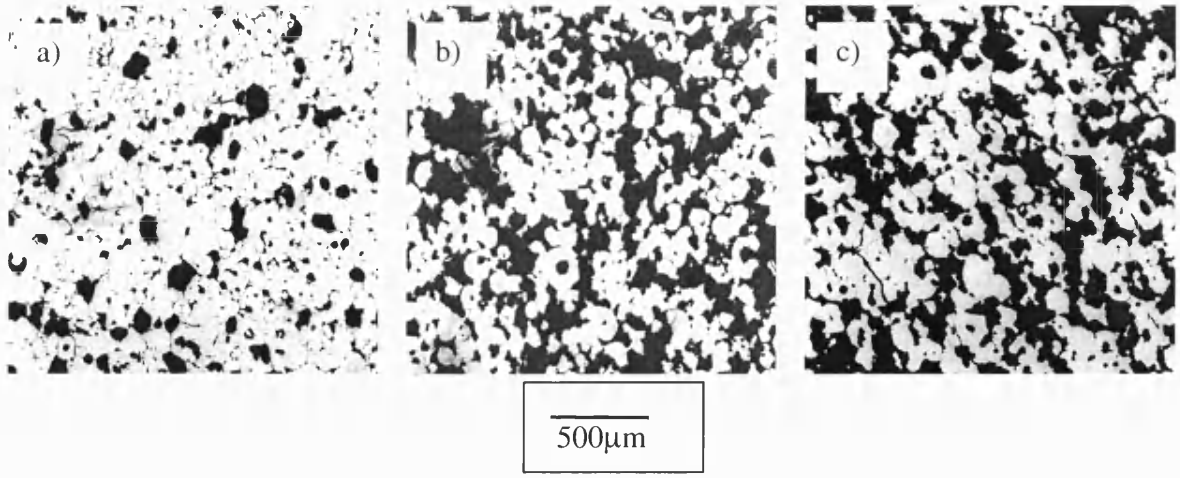

Figure 3-16: Examples of microstructures manufactured by BurPS using PEO as the inclusion material, a) low porosity b) medium porosity and c) high porosity.

Samples were produced using the BurPS method with poly(ethylene oxide) as a inclusion material from 40 to 97% dense, poled and electrically tested.

3.3.1.3 Production of Small Scale Porosity

The PMMA and PEO materials used to produce the BurPS samples provide relatively large pores. In order to manufacture smaller porosity two small scale powders were used to mix with the ceramic powder in an attempt to produce a finer microstructure. The powders used

were cornstarch (CS) and self-raising flour (SR). These were chosen for their ability to be cleanly burnt away during heat treatment due to their organic nature. Both powders are readily available and have small particle sizes, 10μm for both cornstarch and self raising flour.

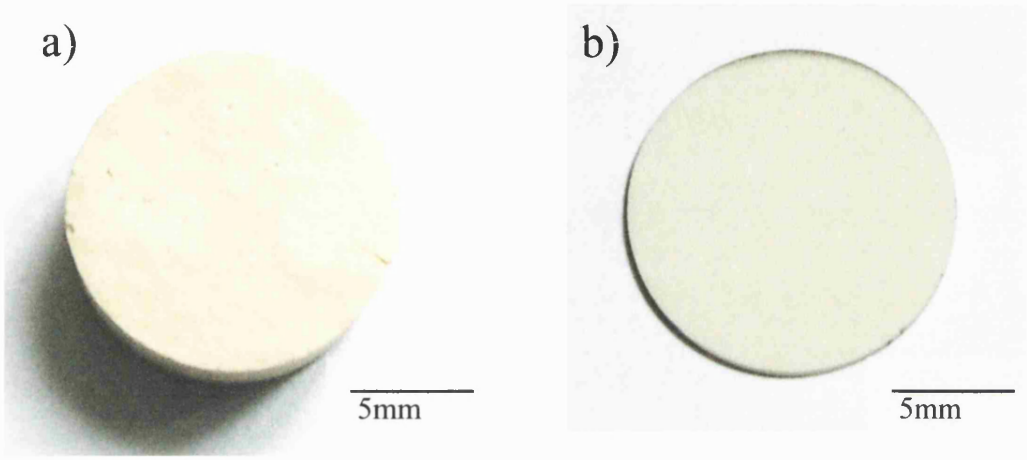

Figure 3-17: Photograph showing a) cornstarch (CS) and self raising (SR) sample.

Samples produced had no macroscopic inhomogeneities visible with the naked eye such as cracking or delamination, as shown in Figure 3-17.

Microstructures of CF and SR samples can be seen in Figure 3-18 and Figure 3-19 respectively.

Although the samples produced by BurPS using these two inclusion materials (CS and SR) appeared to have superior mechanical properties, it was not possible to successfully produce samples with densities of under 40%, for the same reasons outlined with the PMMA and PEO samples. Both the CS and the SR aided pressing, and although samples with high volume fractions of CS and SR were produced in the green stage, subsequent heat treatment rendered the samples useless caused by extensive cracking due outgassing of the CS and SR.

In total, four different inclusion materials were successfully used to produce porous PZT based ceramics via the BurPS method (PMMA, PEO, CS and SR). The size of the inclusion had a marked effect on the strength of the sample at the green stage, as would be expected. Large inclusions produced poor mechanical properties in the green stage, and small inclusions producing good mechanical properties at the green stage.

However, there was a limit to the amount of porosity that could be introduced into a sample with all the inclusion materials. This was approximately 40% density (60% porosity). This limit was observed regardless of inclusion size and mechanical properties at the green stage.

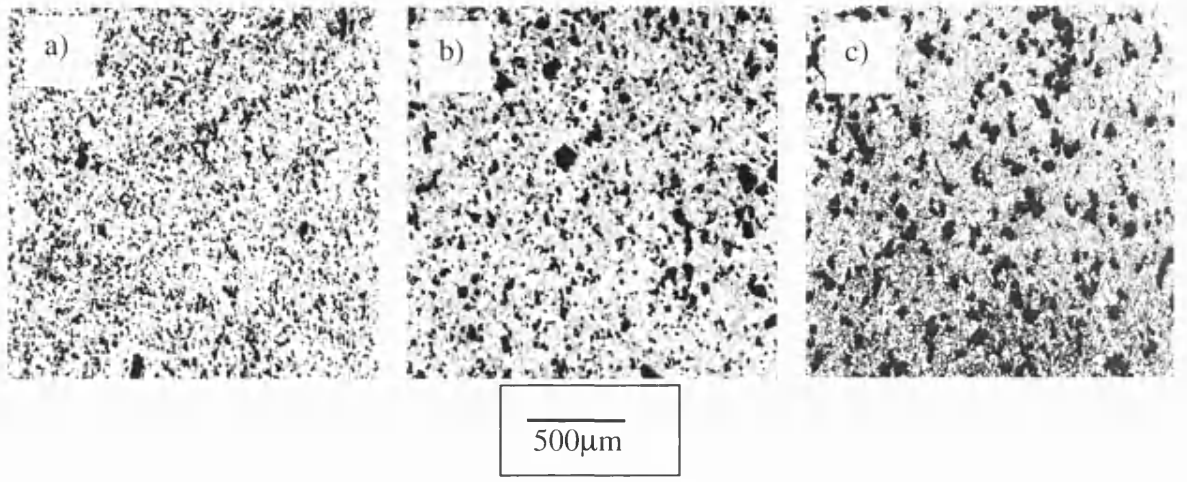

Figure 3-18: Examples of microstructures manufactured by the BurPS method using SR as the inclusion material. a) low porosity, b) medium porosity and c) high porosity.

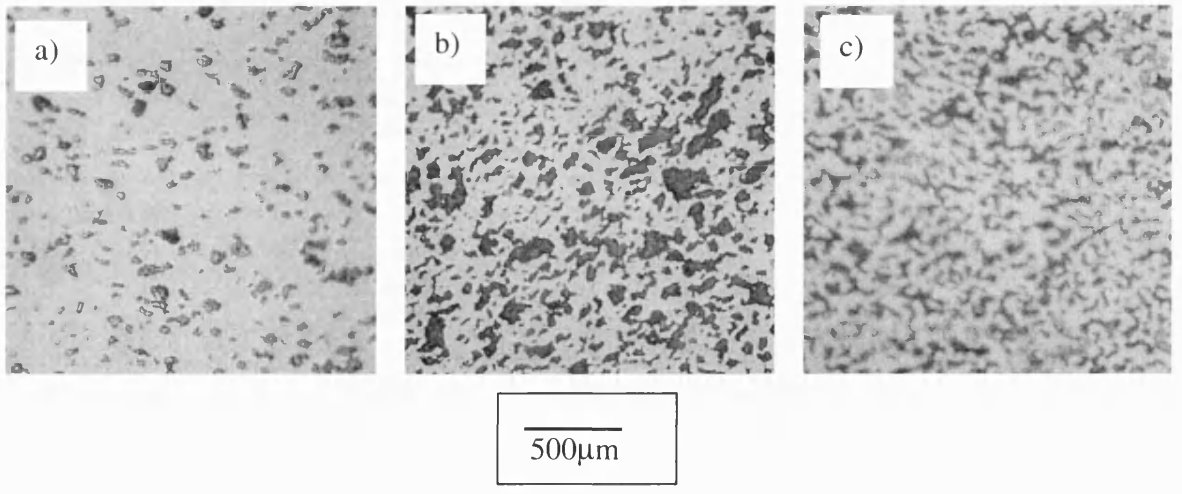

Figure 3-19: Examples of the microstructure of samples manufactured by the BurPS method using CF as the filler material. a) low porosity, b) medium porosity and c) high porosity

This limit is due to the removal of the second phase during heat treatment. At the high inclusion content, after the inclusion material burnt out, there is insufficient structure in the sample to support itself during heat treatment. Because of this porosity limit it was necessary to employ another method of producing porous ceramics, which would lead to samples of porosity of 60% and above.

3.3.2 Reticulated Foam

The reticulated foam method was used to produce ceramic composites with very high volume fraction of porosity (above 80%). Provided the variables are carefully controlled, it is a versatile method and can be used to produce ceramic foams of different pore pitches, pore densities and even aspect ratios.

A selection of foams was chosen from a manufacturer (Sydney Heath and Son Ltd. Stoke-on-Trent), which were polyurethane foams of different pore pitches. The frequency of the pores is measured in ppi (pores per inch). The range chosen for ceramic fabrication was from 8ppi up to 45ppi. The intention was to coat the polymer foams with a PZT based slip, heat treat the coated slip, burn out the polymer and sinter the remaining PZT foam.

3.3.2.1 TGA on Foams

Thermo-gravimetric analysis was carried out on a selection of the foams supplied to determine the heat treatment necessary to burn out the foam once they are coated with the dried ceramic powder slip.

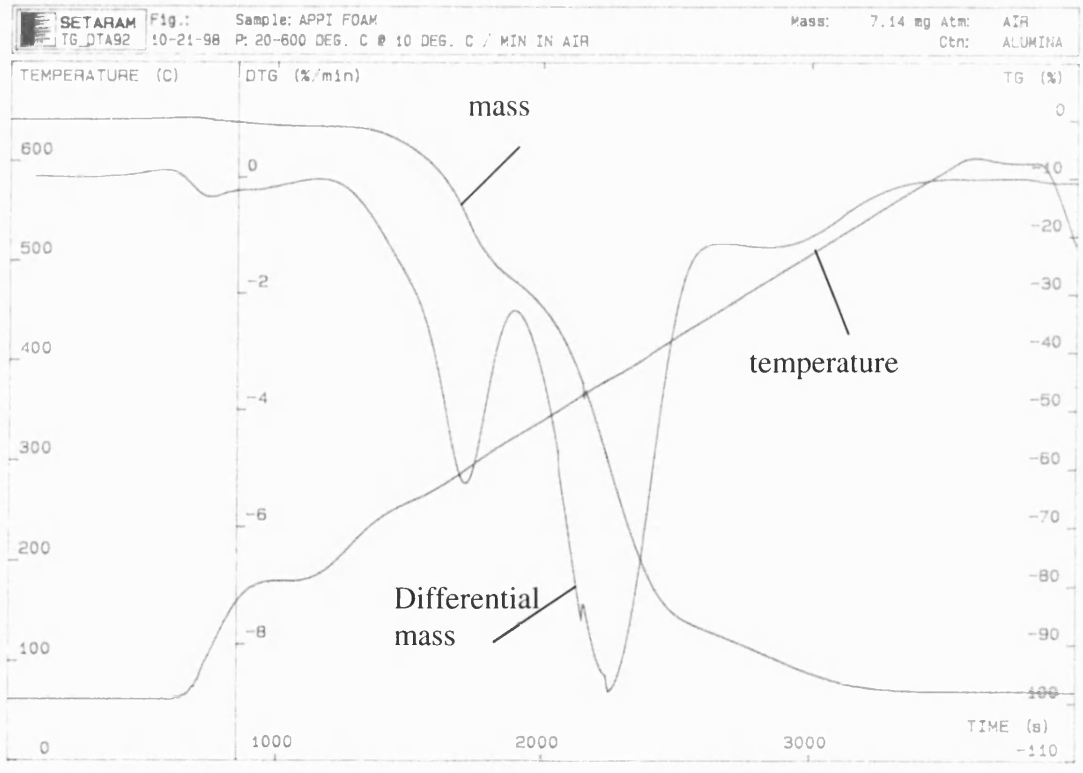

Figure 3-20: TGA curve for polyurethane foam.

The samples were placed in a Setaram TG_DTA92 for analysis.

It can be seen on the chart that the maximum weight loss rate is at 400°C and therefore it can be assumed that all the foam can be burned off with conventional heat treatment by a slow heating rate and a dwell time at 400°C. This temperature profile was incorporated into all heat treatment programmes where the reticulated foam method was used to produce porous ceramics.

3.3.2.2 Selection of Foam Pore Density

Four foams were chosen with a wide variation in pore sizes. Examples of these foams can be seen in Figure 3-21.

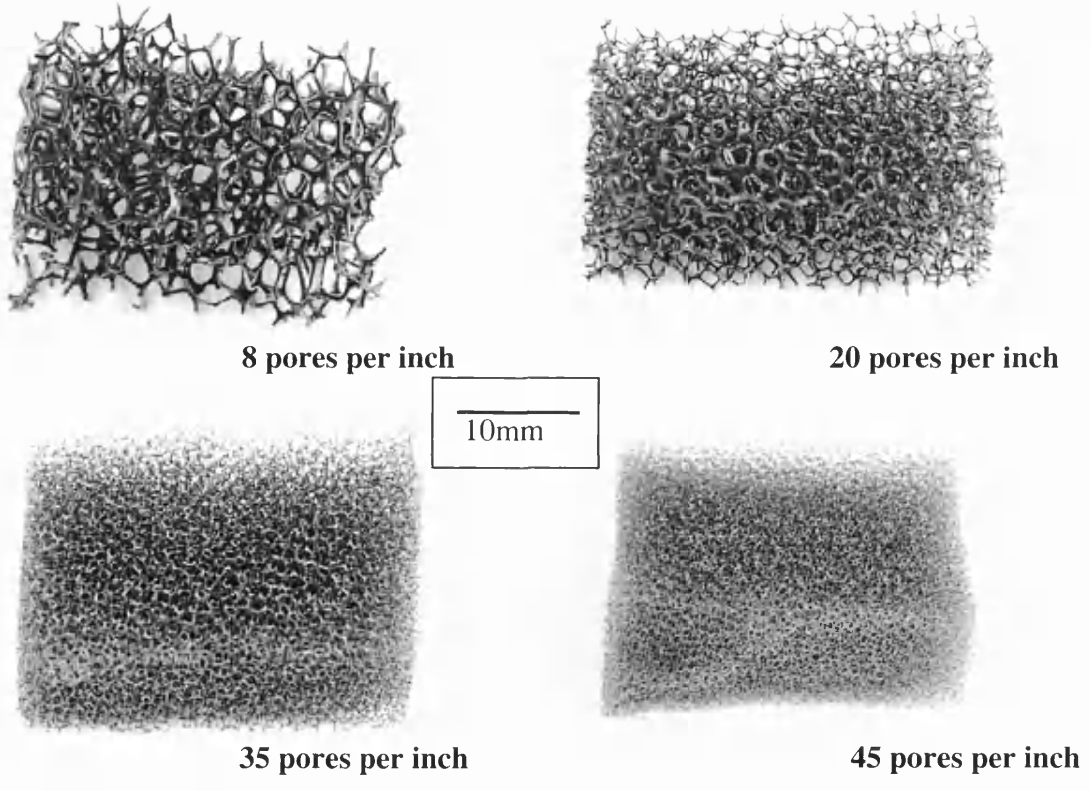

Figure 3-21: Examples of the four types of foams used in ceramic production.

The foams were chosen to be open foams with a narrow pore size distribution to enable the slips to enter the foam and provide a narrow pore size distribution in the final ceramic. In addition, the chosen foams burn out cleanly and have adequate mechanical properties to

support a heavily loaded ceramic slip. The different pore pitches were selected with a view to producing final ceramic samples of different porosity and a variety of microstructures.

3.3.2.3 Tuning of Slip Viscosity and Content

A ceramic slip, a mixture of PZT, water and binder, is used to impregnate and coat the foam before heat treatment in order to produce the porous ceramic. The properties, impregnation depth and coating thickness of the final coated foam are very sensitive to the properties of the ceramic slip. There are two main factors that influence the coating of the foam, the first is the amount of ceramic present in the slip and the second is the adhesive properties of the slip. Both of these factors affect the viscosity of the slip, which determines the quantity of slip entering a foam of specific pore size, and also the quantity of slip remaining on a foam of specific pore size after the impregnation process is complete.

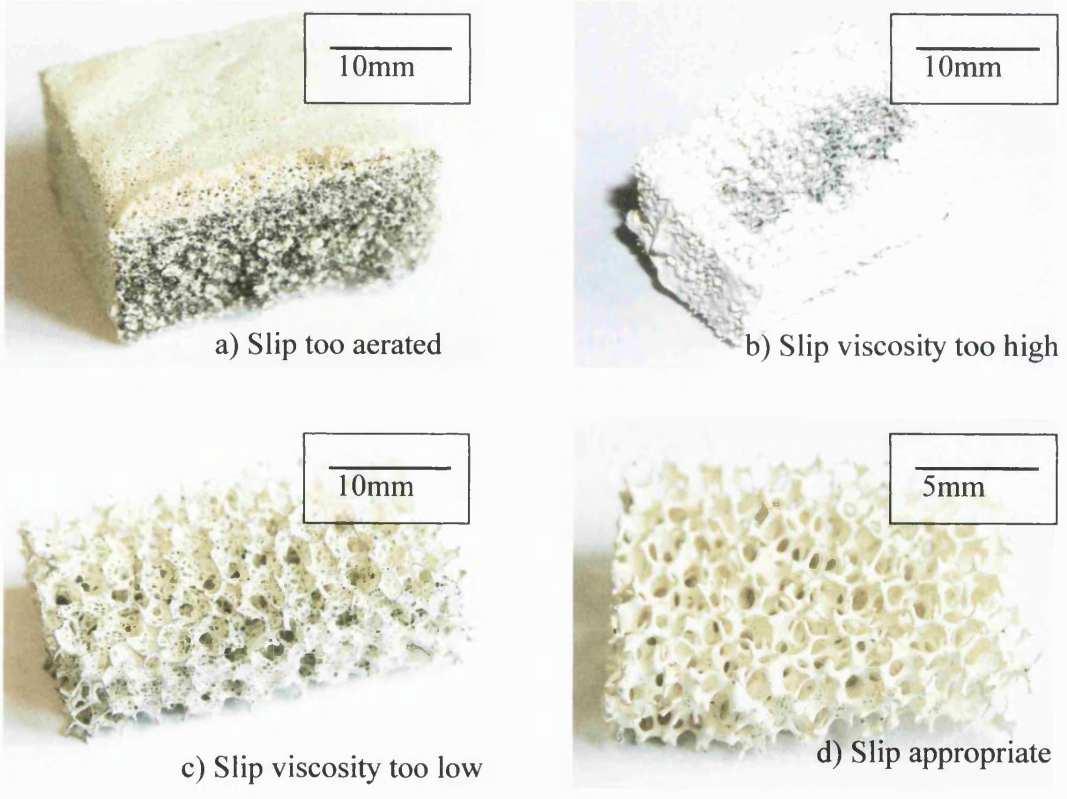

Figure 3-22: Examples of a, b and c) inappropriate slips and d) good slip – foam combination.

The images in Figure 3-22 show examples of incorrect slip and foam combinations. Figure 3-22a shows the impregnation of a fine foam (45ppi) which has been impregnated with a

low viscosity aerated slip. There has been incomplete impregnation into the foam sample due to over aeration of the slip. Figure 3-22b) shows the impregnation of a high viscosity slip into a fine foam (45ppi). Here there is good impregnation in the outer layers but not in the centre of the foam sample due to the high viscosity of the slip.

Figure 3-22c shows a slip with a viscosity which is insufficient to be impregnated into a coarse foam (20ppi), with very thin joining sections observed with little ceramic present. Figure 3-22d) shows a good slip – foam combination. It can been seen that the slip has achieved good even coverage over the foam (no black foam is visible) with a good thickness of coating.

SLIP PROPERTIES	Increasing Ceramic Loading →		
Increasing PVA loading ↓	Insufficient slip retention – too fluid		Low adherence to foam
		Good Impregnation Good retention Sufficient ceramic content	
	Insufficient ceramic content		Low impregnation – too viscous

Figure 3-23: Slip properties as a function of ceramic loading and PVA loading.

By varying the ceramic and the Poly Vinyl Alcohol (PVA) content, which modifies viscosity, the slip can be modified to find the optimum condition to produce a homogenous impregnation with sufficient slip coating to the polymer. Insufficient coating thickness leads

to cracks when the polymeric foam is burnt out and insufficient impregnation leads to large voids in the centre of the ceramic structures.

Figure 3-23 shows an overview of the slip production. At low ceramic and low PVA loading the slip is fluid and is not retained in the foam when removed from the bulk slip. Increasing the PVA loading improves the adhesion to the foam, however insufficient ceramic is present in the slip to provide a good coating and a stable structure during heat treatment.

A high ceramic content and low PVA content will result in a viscous slip with low adherence to the foam. A high ceramic and high PVA loading will result in a highly viscous slip which cannot impregnate the foam.

A moderate level of PVA loading in the slip provides a viscosity which is sufficiently low to impregnate the foam and will be retained in the foam. A moderate amount of ceramic loading will provide a stable structure during heat treatment and keep the viscosity sufficiently low to enable impregnation. Two grades of slip were identified and used for different foam samples. These are outlined in Table 3-2.

	Thick slip (8ppi-20ppi) foams	Thin slip (<20ppi foams)
Water	200ml	200ml
Ceramic	300g	200g
PVA	5g	3g

Table 3-2: Composition of thick and thin ceramic slips for foam impregnation.

In addition to the properties of the slip, the impregnation method also influences the final properties of the product. This will be discussed below.

3.3.2.4 Dipping Methods

Three different dipping methods were used in order to accompany the different slip viscosities outlined previously.

Ceramic slips with low viscosities require only a simple dipping method. This can be achieved by simply submerging a piece of foam of the required geometry into a volume of ceramic slip, as shown in Figure 3-24a.

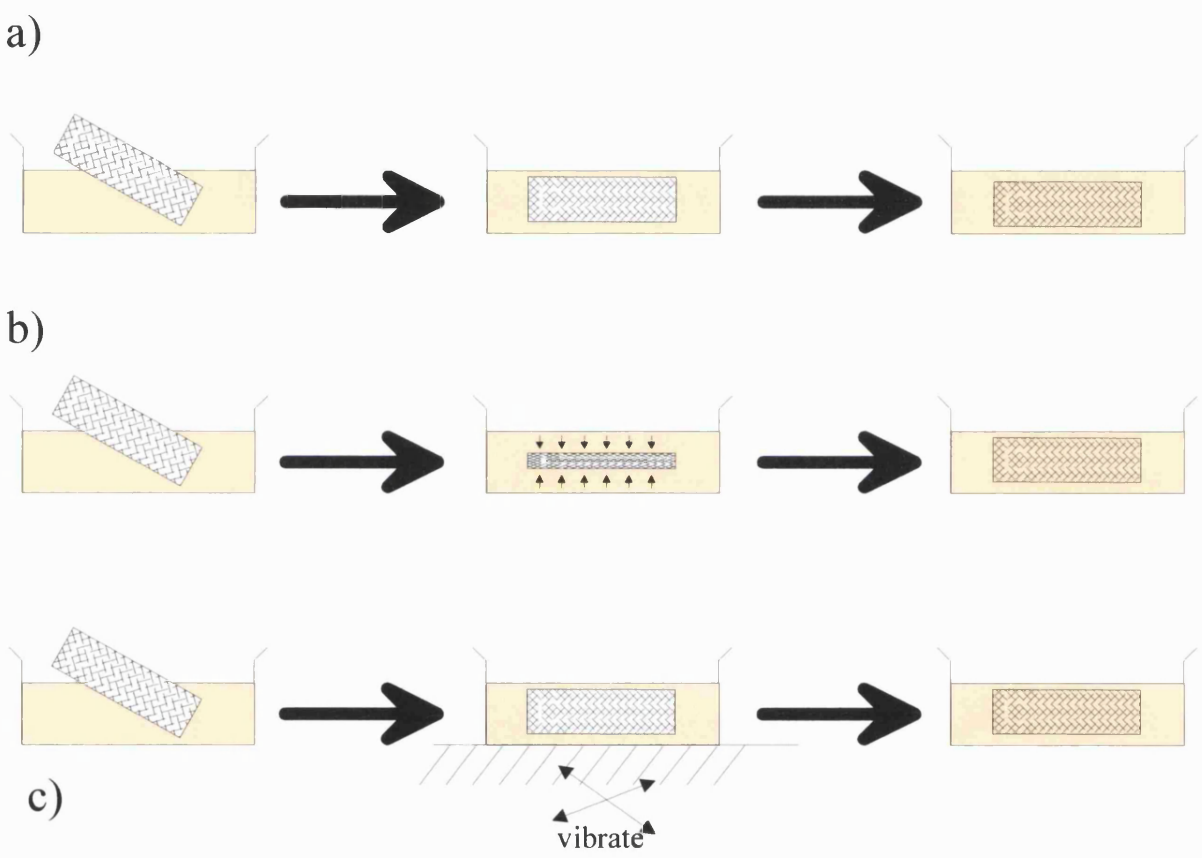

Figure 3-24: Dipping procedures for low viscosity slips. a) standard dipping, b) compression dipping and c) vibration dipping.

The ceramic slip will impregnate the foam and the foam can be removed for drying and heat treatment. For this technique to be successful it is not possible to use a viscous slip. Therefore the amount of ceramic introduced into the foam is small and the technique is only suitable for foams with many fine pores where a thin coating of slip may be adequate.

If the viscosity of the slip is increased the slip will not impregnate the foam without external forces and another impregnation method has to be used.

After the foam is inserted into the volume of ceramic slip it is compressed to expel any trapped air. The foam is then allowed to recover to its original size under its own elasticity. During this recovery process the ceramic slip is forced into the foam. This procedure, shown in Figure 3-24b, allows more viscous slips to be used than in the "simple dipping" procedure. However, if the ceramic slip is too viscous the elasticity of the foam sample is insufficient to return it to its original shape and the foam piece remains compressed. In this last case a final dipping method is used. The foam piece is submerged in a volume of viscous ceramic slip and the slip is placed on a vibration table, commonly used for sieving ceramic powders, shown in Figure 3-24c. The vibrations from the table slowly dislodge the air from inside the foam and lead to ceramic slip impregnation. If this method does not fully impregnate the foam piece then the slip is considered to be too viscous for this method of porous ceramic fabrication.

By tailoring the viscosity and ceramic content of the slip and using the impregnation methods discussed, a wide range of polymer foams can be manufactured.

3.3.2.5 Importance of Drying of Foams

Once the sample has been impregnated by the method described in the previous section the slip-coated foam is dried before it is heat treated to burn off the polymer foam and sinter the ceramic. This drying stage is crucial to the production of crack free final samples.

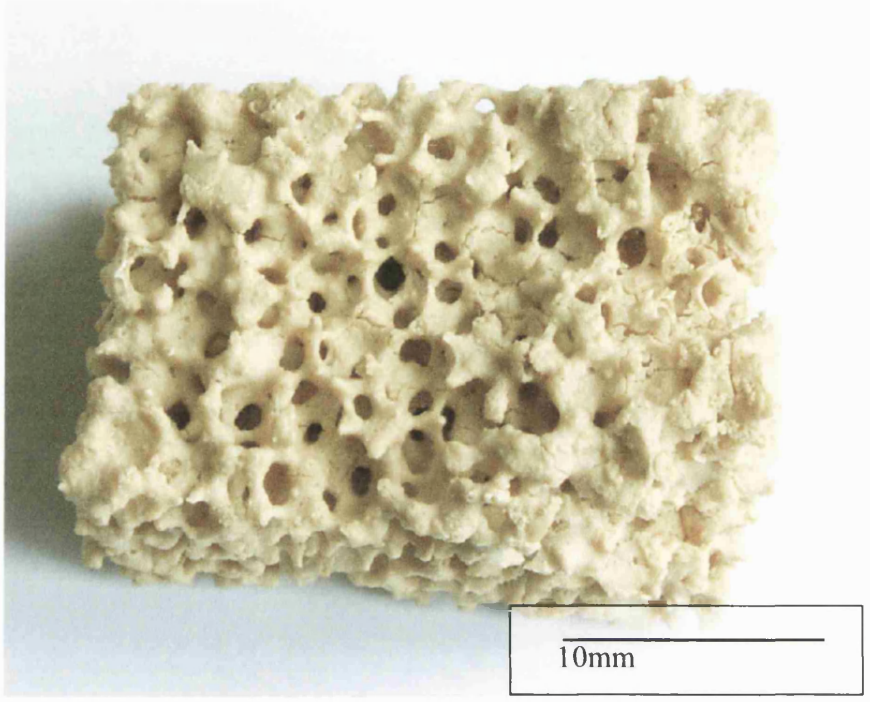

Figure 3-25: Photograph showing cracking of sample subjected to inadequate drying conditions.

Samples placed in the furnace for heat treatment directly after impregnation experienced cracking due to the rapid shrinkage associated with rapid loss of water. It was found that after impregnation the best results were obtained by letting samples to "rest" for 3 days, then placing in a warm (40°C) drying cupboard for 2 days prior to heat treatment. This ensured a slow release of water, a reduced shrinkage rate and no cracking.

3.3.2.6 Production & Microstructure

Heat treatment was performed at 1125 °C for 2 hours in a PZT powder rich atmosphere. Excess PZT powder was required during sintering due to the large surface area of the foams relative to the other types of porous ceramic, such as the BurPS materials.

Micrographs of the foam samples in Figure 3-26 show a reasonably dense microstructure and a highly porous macrostructure.

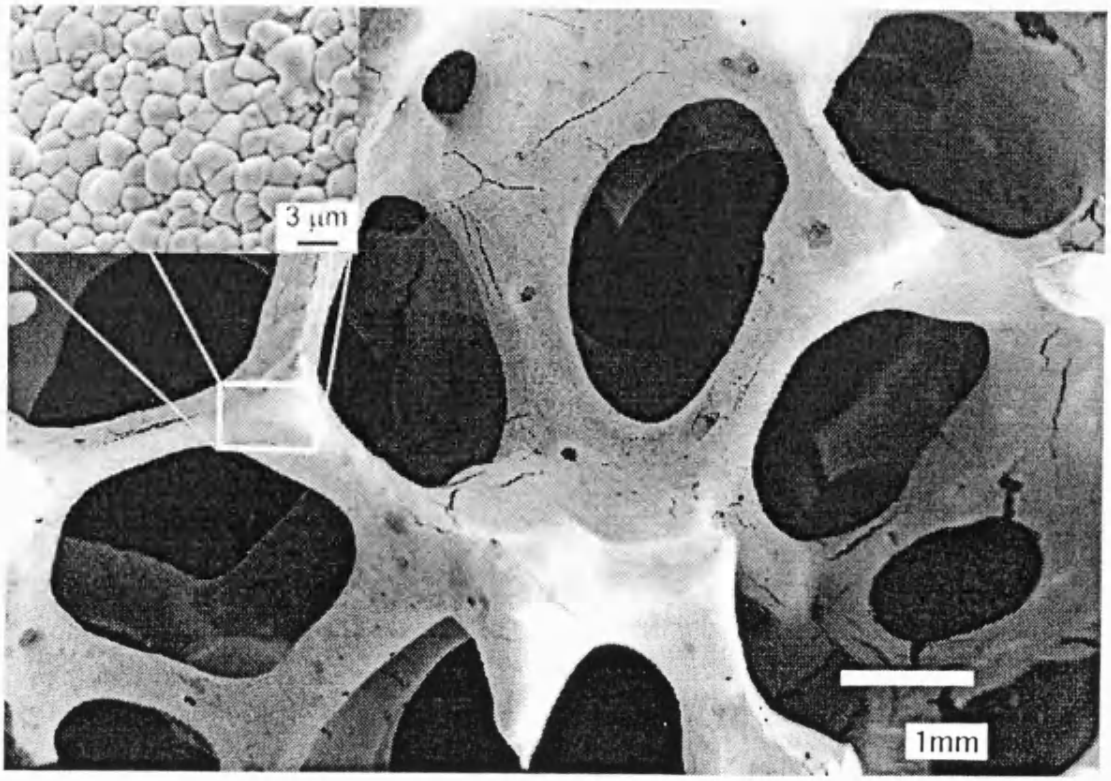

Figure 3-26: Micrographs showing macrostructural porosity and dense microstructure.

Figure 3-26 is a low magnification image of the foam and shows the struts of the reticulate foam structure of a 90% porous PZT sample produced by the reticulated foam method. The inset image shows a high magnification image of the microstructure, i.e. the microstructure of a strut. Density has been estimated by threshold image analysis to be 95%.

A number of alternative methods of manufacture of piezo-composites were carried out, with less success, such as the epoxy mix method described below.

3.3.3 Epoxy Mix Method

The methods discussed until now involve creating a porous ceramic body and then impregnating it with a polymer. An alternative is to create the composite *in situ* by mixing the non heat treated PZT powder (or calcined PZT power) directly with an epoxy polymer in its liquid form.

A number of samples were produced by mixing different ratios of PZT powder with epoxy resin in its liquid state. The mixture was left to polymerise and was then machined to the desired shape, resulting in a ceramic composite.

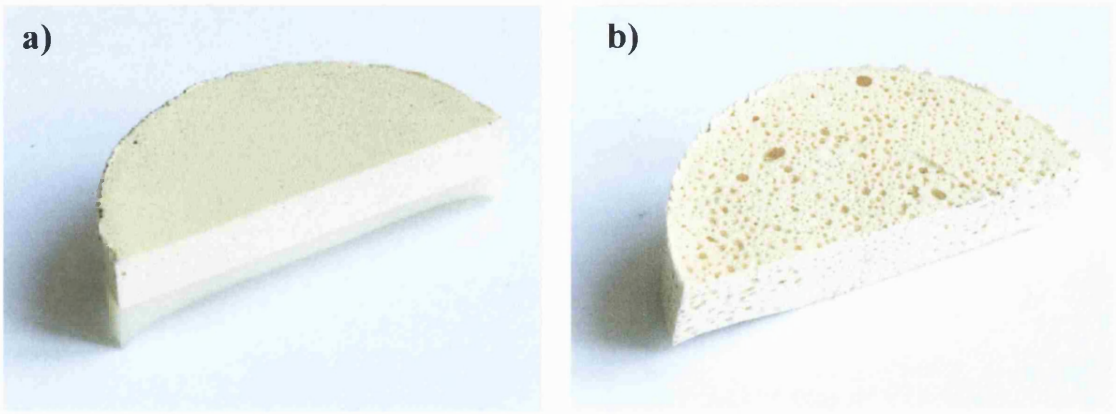

Figure 3-27: Photographs of the structures of the composites made by epoxy-mix method. a) low PZT volume fractions (30g polymer – 30g PZT) and b) high PZT volume fraction (30g polymer – 150g PZT).

An example of the final structure of the composite can be seen in Figure 3-27. At low ceramic volume fractions the PZT powder settles to the bottom of the mixture before the epoxy polymerises, Figure 3-27a. At high PZT volume fractions the increased viscosity due to the increased ratio of ceramic is sufficient to avoid settling of the PZT powder and even induce trapping of air in the structure. This method was carried out for untreated PZT powder, heat treated PZT powder (1125°C for 2 hours) and crushed PZT powder.

This processing is relatively easy but it is likely that the ceramic phase is not continuous and the structure represents a 0-3 composite.

4 Experimental Testing

After manufacturing and microstructural analysis, a number of experimental testing methods were carried out to assess the suitability of the produced porous or composite ceramics for use as hydrophone devices. This testing involved measuring the density of samples, the piezoelectric response and the electrical properties of the ceramic samples. The aim is to investigate the piezoelectric properties (d_{33}, d_{31}, d_h, g_h, $d_h.g_h$) and permittivity (ε_{33}) as a function of porosity and microstructure and relate it to the modelling results.

4.1 Experimental Procedures

There were three main areas of testing performed on the piezocomposite samples. Density measurements were carried out, a piezometer was used to measure and calculate d_{33}, d_{31}, and an LCR meter was used to measure and calculate capacitance and permittivity. The experimental procedures will now be discussed and results will be discussed in subsequent sections.

4.1.1 Density Measurement

Density measurements were carried out using a geometric method and using the Archimedes method.

Calculating the density geometrically involves measuring the mass and volume of the sample and simply comparing the measured density to the theoretical density of 7500kg m^{-3}.

The Archimedes density is calculated by initially weighing the samples in the dry state. The samples are then boiled in distilled water for 30 minutes so that the water impregnates the open porosity. After the water has cooled, the samples are weighed when suspended in water. The samples are removed from the water, any excess surface water is removed and they are weighed wet in air. The following equations are used to calculate the bulk density and apparent porosity.

$$\frac{W_a}{W_c - W_b} \times D_1 = \text{Bulk Density}$$

$$\frac{W_a}{W_a - W_b} = \text{Apparent solid density}$$

$$\frac{W_c - W_a}{W_c - W_b} \times 100 = \text{Apparent porosity}$$

W_a = Weight dry in air

W_b = Weight suspended in water

W_c = Weight wet in air

D_1 = Density of immersion liquid

Equation set 4-1: Equations for calculating density by the Archimedes method.

The bulk density refers to the density of the ceramic phase and includes any material porosity; apparent porosity is the measure of any open porosity in the body.

The figures from the density measurements were used to examine the electrical and piezoelectric properties of porous 3-3 composites with respect to porosity.

4.1.2 Piezometer - d_{33} and d_{31}

A Take Control PM25 piezometer was used to measure the piezoelectric properties (d_{33} and d_{31}) of the ceramic samples. This piezometer determines the relevant piezoelectric coefficient by applying a force, at a predetermined low frequency (97 Hz), to the piezoelectric sample which is inserted into a spring-loaded clip. The frequency of the tests is well below the resonant frequency of the sample.

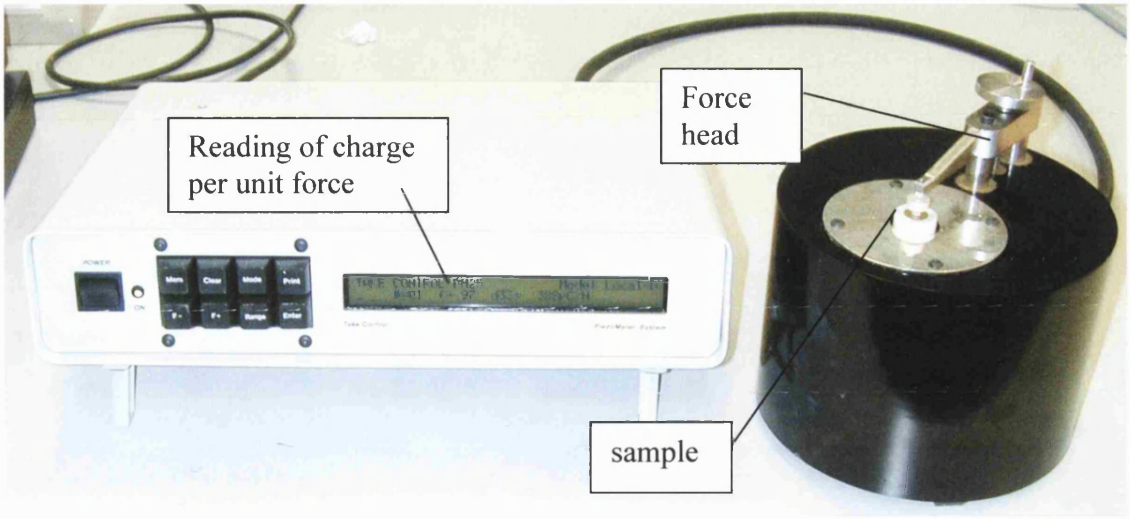

Figure 4-1: Photograph of Take Control PM25 piezometer system.

An oscillating force of 0.1N is applied to the sample and the charge generated at the surfaces is recorded which allows the charge per unit area to be calculated. The measurement for d_{33} (charge per unit force) is taken directly from the piezometer output but the measurement for d_{31} has to be calculated from a raw reading of the sample data.

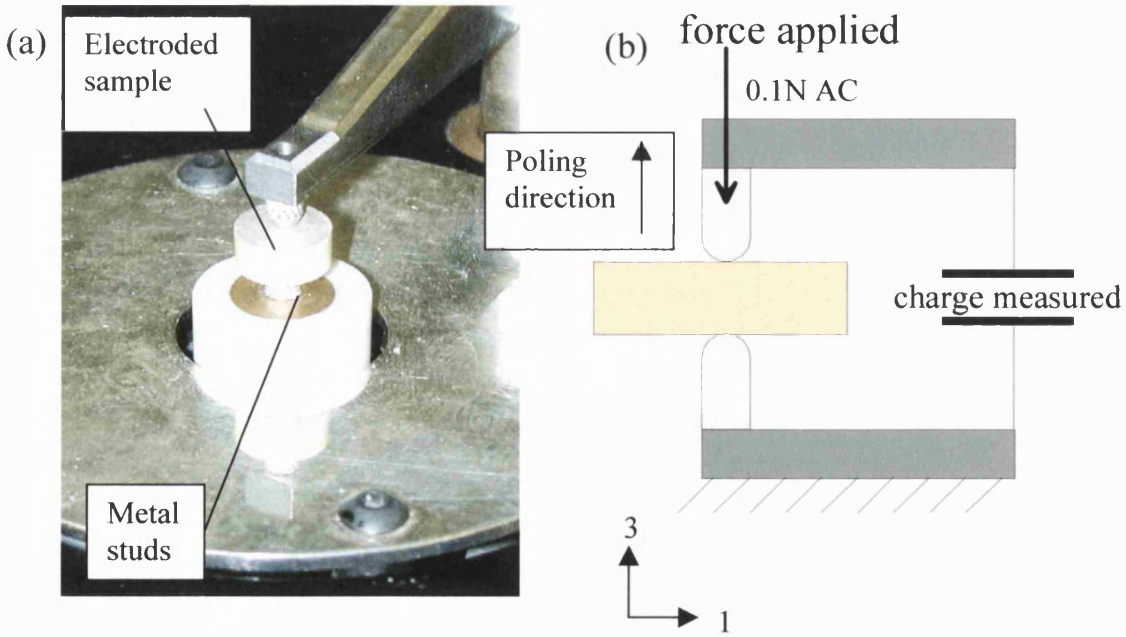

Figure 4-2: a) Image of piezometer load head and b) schematic showing d_{33} measurement.

4.1.2.1 Measurement of the d_{33} Coefficient

An image and schematic of the experimental set up used to measure d_{33} can be seen in Figure 4-2. A force is applied via the metallic studs at 97Hz and the charge per unit force developed by the piezoelectric sample is measured and displayed on the control box as a direct reading of d_{33}. For the d_{33} measurement, the charge is measured on the same area over which the force is applied. This is shown in Figure 4-3.

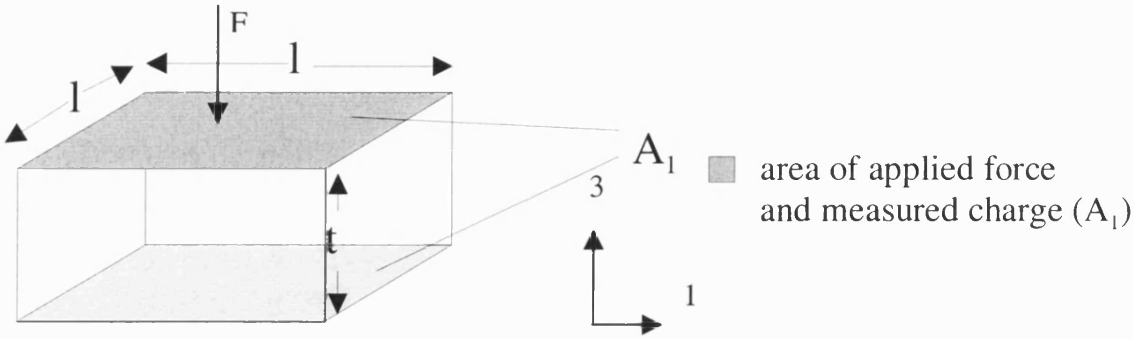

Figure 4-3: Schematic of d_{33} calculations. Charge measured over same area as force applied.

Therefore, d_{33} is the charge measured in the 3 direction per unit force applied in the 3 direction on the sample. Hence:

$$d_{33} = \frac{Q/A_1}{F/A_1} = \frac{Q}{F}$$

where

Q = charge (C)

F = applied force (N)

A_1 = Area (m^2)

Thus the d_{33} measurement can be read directly off the instrument as the charge per unit force.

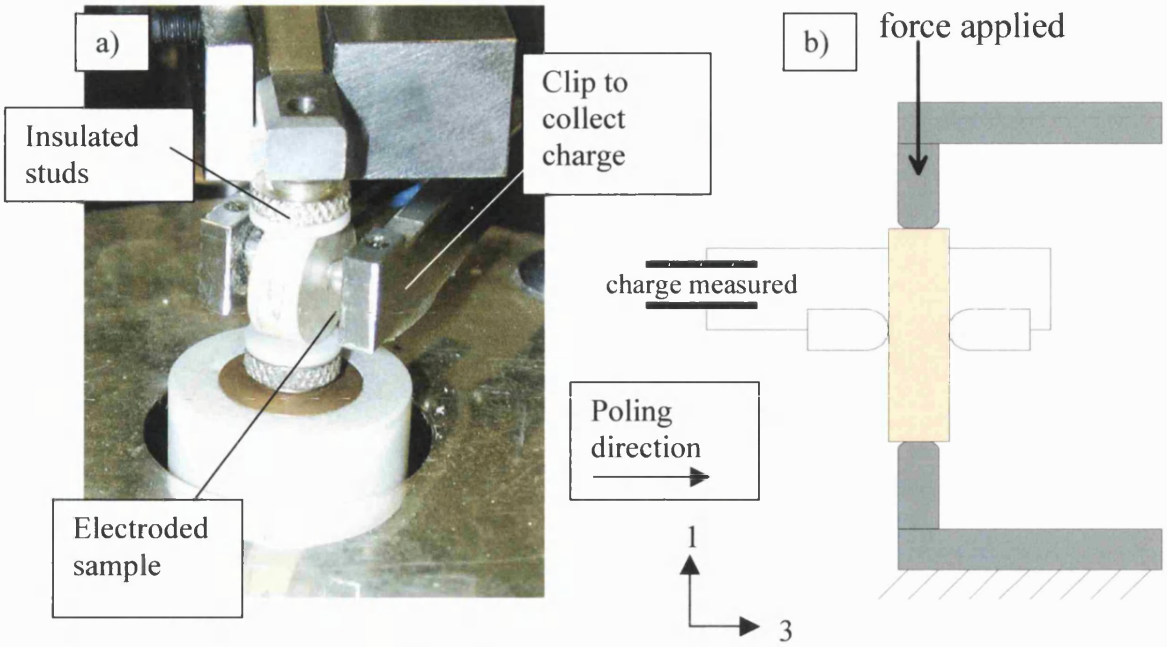

Figure 4-4: a) Photograph and b) schematic showing force head during d_{31} measurement.

The measurement of d_{31} is more complex. The sample is rotated by 90° and the force is now applied in the 1 direction. The metallic studs are replaced by insulating studs as shown in Figure 4-4, and the charge is collected from the electrodes by a spring-loaded clip. As the charge is now measured from a different surface to that of the applied force a "shape factor" must be taken into account.

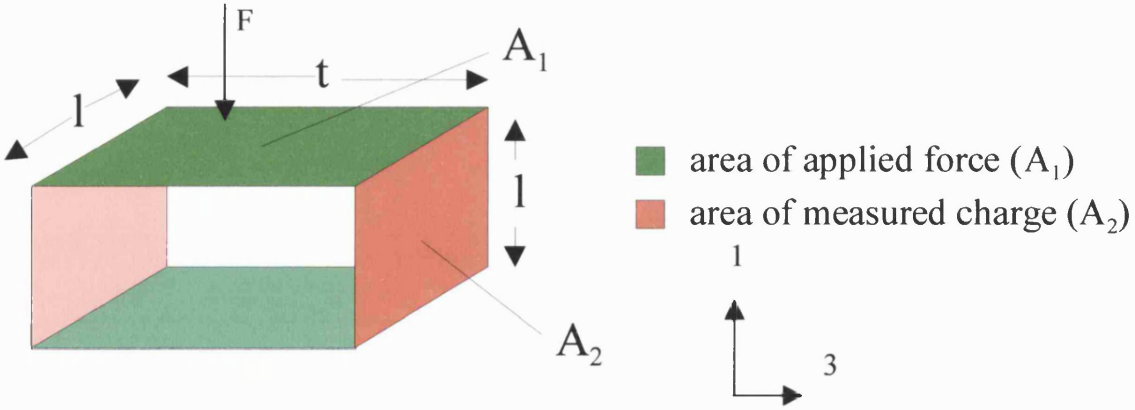

Figure 4-5: Schematic of d_{31} calculations. Charge is measured over a different area compared to applied force.

In this case d_{31} is the charge developed in the 3 direction per unit applied force in the 1 direction. The charge and force are incident on the faces shown in Figure 4-5 and the d_{31} coefficient is now defined as:

$$d_{31} = \frac{Q/A_2}{F/A_1} \quad \text{but } A_1 \neq A_2 \qquad A_1 = l.t \text{ and } A_2 = l.l$$

$$d_{31} = \frac{Q}{F} \bullet \frac{A_1}{A_2} = \frac{Q}{F} \bullet \frac{t}{l} \text{ C N}^{-1}$$

The output taken from the piezometer is a direct reading of charge per unit force (Q/F). Therefore the output has to be multiplied by the shape constant (t/l) of the sample to calculate d_{31}.

4.1.3 LCR Measurements

A Hewlett Packard HP4263B LCR meter was used to measure the sample capacitance. Samples were placed between the two large electrodes and a small fixed pressure contact was made by a torque-limited micrometer shown in Figure 4-6.

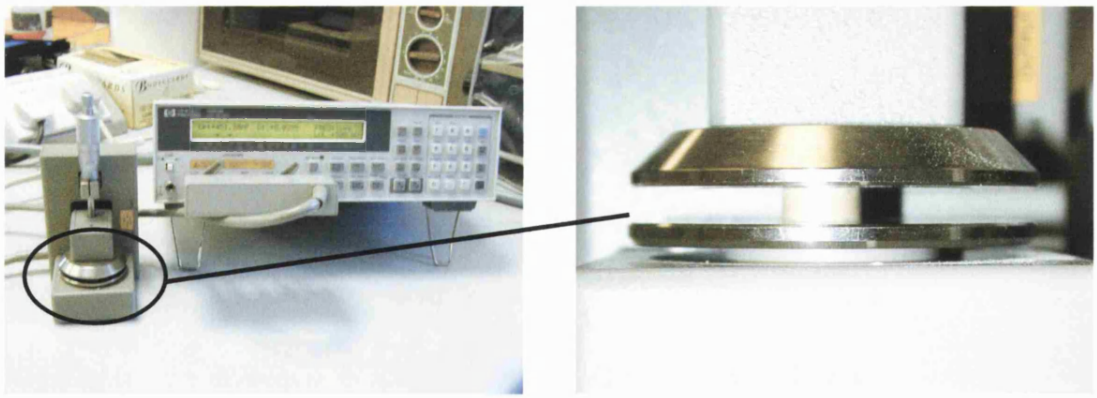

Figure 4-6: LCR meter showing measurement of capacitance. Sample diameter 10mm.

All capacitance measurements were taken at a voltage of 1V and at a frequency of 1kHz.

By measuring the physical dimensions of the sample tested, the permittivity could be calculated from capacitance using the following equation:

$$C = \frac{\varepsilon_0 \varepsilon_r A}{t}$$

Equation 4-2: Relationship for a parallel plate capacitor.

C = capacitance (F)

ε_r & ε_0 = relative permittivity and permittivity of free space respectively (Fm^{-1})

A = area of plate (m^2)

t = thickness of sample (m)

4.1.4 Coupling Coefficient Measurements

An Agilent 4294A Precision Impedance Analyzer was used to measure the frequency of the resonance and anti-resonance of a selected number of samples. The sample was placed between the two wire electrode contacts shown in Figure 4-7.

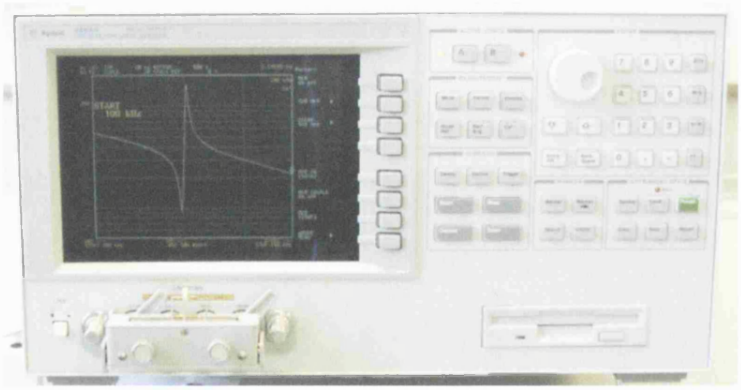

Figure 4-7: Impedance analyser showing a frequency sweep of a sample.

The impedance analyser performed a frequency sweep between 100kHz and 1MHz and recorded the impedance of the sample. An example of the graphical output can be seen on the screen of the analyser and also in Figure 4-8.

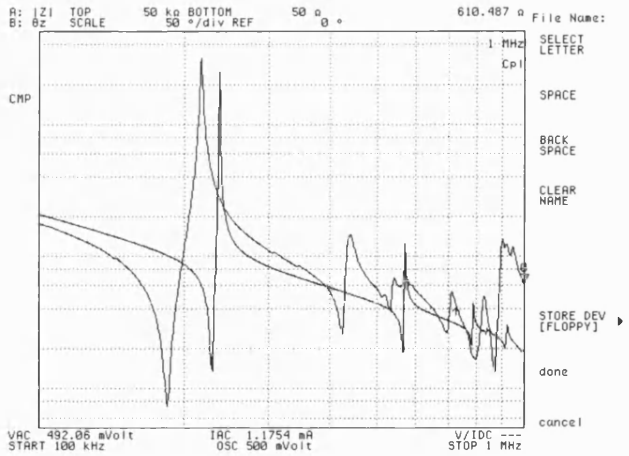

Figure 4-8: Graphical output showing frequency versus impendence.

The values of frequency at the resonance and anti-resonance were used to calculate the coupling coefficient, K_{eff}, using the following equation.

$$K_{eff} = \sqrt{1 - \left(\frac{f_r}{f_a}\right)^2}$$

Where

f_a = frequency of anti-resonance

f_r = frequency of resonance

The results obtained by using these techniques will now be listed and discussed as a function of porosity for the 3-3 piezocomposites.

4.2 Results

All of the results obtained from electrical testing of the porous piezocomposites are detailed in the following sections.

4.2.1 Preliminary Results

As the results from the manufactured samples will be presented, it is useful to review the trends predicted by the finite element modelling. These will be outlined below.

4.2.1.1 d_{33} / d_{31} Coefficients

Before discussing the experimental data it is necessary to briefly examine the general trends observed from the FE modelling. The "d" coefficients, d_{33} and d_{31} are the piezoelectric strain coefficients and measure charge per unit applied force or strain per unit applied electric field.

For modelling of porous PZT with no second phase present the results for d_{33} are approximately constant with respect to relative density, and the results for d_{31} gradually decrease with increasing porosity. However, for the two phase PZT-polymer model both d_{33} and d_{31} gradually decrease with increasing polymer volume fraction.

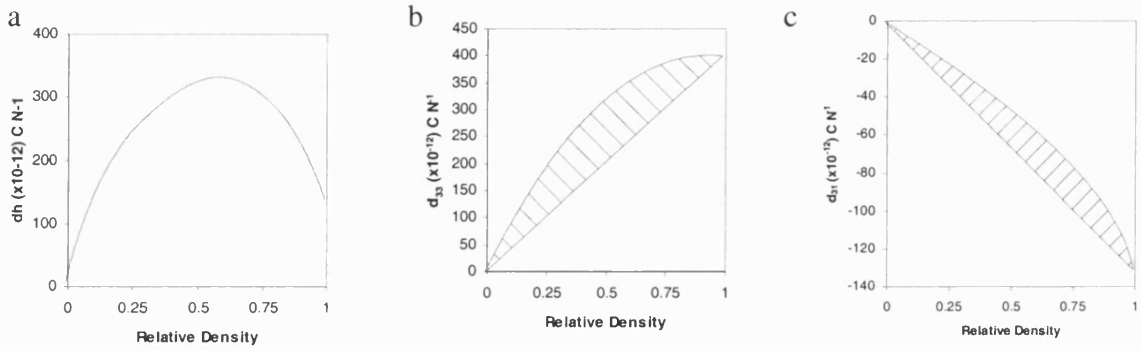

Figure 4-9: Examples of the trends found when modelling a) d_h, b) d_{33} and c) d_{31}

The modelling reported in Chapter 2 predicted trends regarding the influence of porosity on the d coefficients. The trends reported can be seen in Figure 4-9. The coefficient d_h has a maximum at approximately 50% porosity and both d_{33} and d_{31} vary with porosity from between a linear relationship and an upper limit shown by the charts in Figure 4-9. These trends are represented well in the experimental results and will be discussed after the general g_h and permittivity trends have been discussed.

4.2.1.2 Hydrostatic Voltage Coefficient (g_h)

The experimental values of g_h were calculated using the results from the d_{33} and d_{31} coefficients and the permittivity measurements using the relationship,

$$\varepsilon_{33} = \frac{d_h}{g_h}$$ where: ε_{33}= permittivity (F m^{-1})

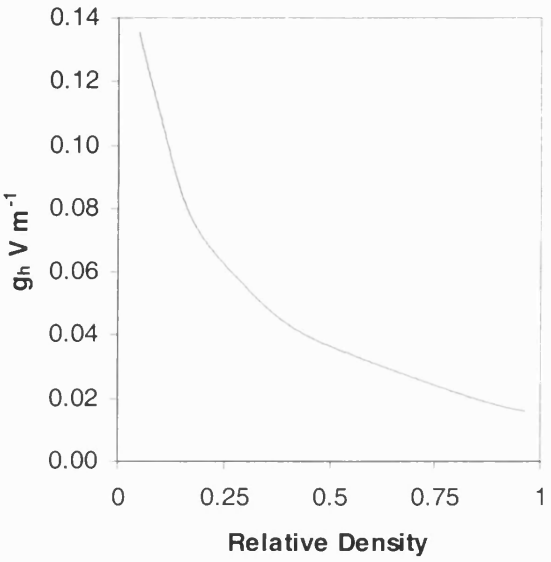

Figure 4-10: Example of the trend found when modelling g_h with finite element analysis.

The general trend calculated by finite element modelling is shown in Figure 4-10. It can be seen to decrease with increasing relative density.

4.2.1.3 Permittivity

The permittivity was calculated using values of d_h and g_h from finite element analysis. The FEA predicted trend for the variation of permittivity with porosity can be seen in Figure 4-11.

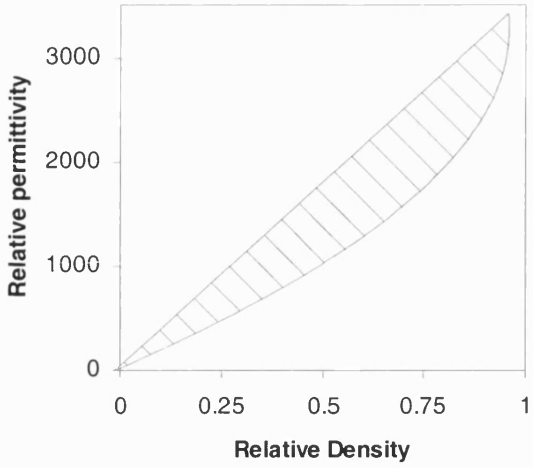

Figure 4-11: Model prediction of permittivity variation with relative density.

The experimental results will now be discussed with particular emphasis on how the results compare to the general trends observed in the finite element modelling.

4.2.2 Discussion of Results

4.2.2.1 Porous PZT Materials

The results for the porous samples are shown in the following section. The values of d_{33}, d_{31}, d_h, ε_{33}, and g_h are plotted against porosity which enables a comparison to be made against different porosities for the same production method and properties that relate to dense PZT5H, whose properties are shown in Table 4-1. General comparisons between production methods will also be discussed.

4.2.2.2 Poly Ethylene Oxide (PEO) Based Materials

The results for the PEO BurPS samples are shown below. The inclusion material of PEO produces a medium pore (approximately 100μm) size with no apparent cracking in the structure, as discussed in Chapter 3.

d_{33} pCN^{-1}	d_{31} pCN^{-1}	d_h pCN^{-1}	g_h Vm^{-1}	$d_h.g_h$ Pa^{-1}	ε_r
606	-281	44	1.63×10^{-3}	72×10^{-15}	3400

Table 4-1: Figures of merit for dense PZT-5H

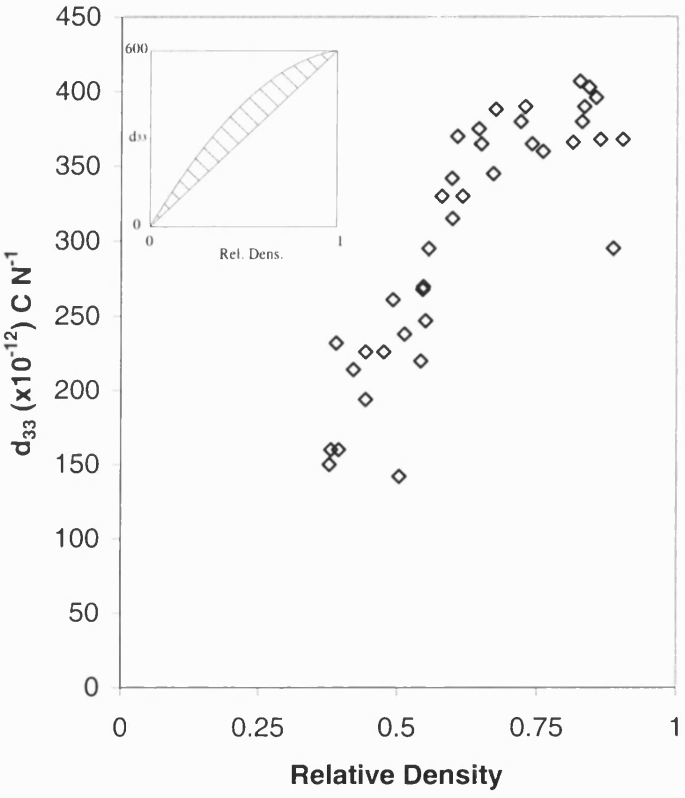

Figure 4-12: Results of d_{33} with respect to porosity for the PEO series of samples.

Figure 4-12 shows the results of d_{33} with respect to porosity for PEO based porous materials and the inset shows the trend predicted by FEA. It can be seen in Figure 4-12 that as density increases so does the value for d_{33}. In the region of approximately 0.6 to 0.9 relative density there is relatively slow decrease in d_{33}, but below 0.6 the rate of decrease of d_{33} is increased. The results follow the trend predicted by FEA. Some scatter of experimental results is observed which can be due to either errors in measuring and calculating the density or errors

in the measurement of d_{33}. In addition, inhomogeneities in the structure of the samples such as local regions of high porosity or low porosity can affect the measured value of d_{33}. However, there is good agreement of experimental results with the predicted trend of d_{33}.

It should be remembered that the porosity range is limited by the manufacturing method. In this case samples below 0.35 relative density could not be manufactured.

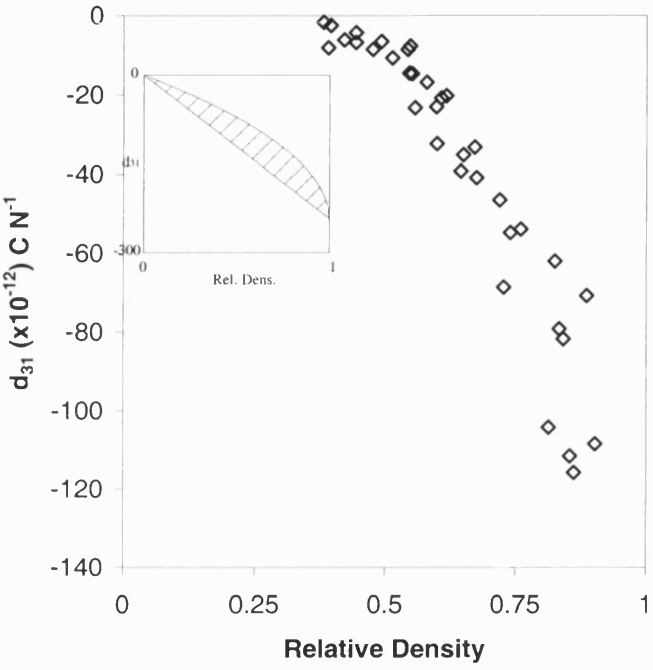

Figure 4-13: Results of d_{31} with respect to porosity for the PEO series of samples.

The chart shown in Figure 4-13 shows the experimental results indicating the variation in measured d_{31} with relative density. The trend predicted by FEA is shown in the insert. The results show that as the relative density increases the absolute value for $-d_{31}$ decreases (the negative value to d_{31} reduces). The results in themselves follow an approximate straight line and $-d_{31}$ decreases more rapidly than d_{33}, as predicted by the modelling. It is this rapid reduction in d_{31}, compared to d_{33} which leads to an improved d_h coefficient.

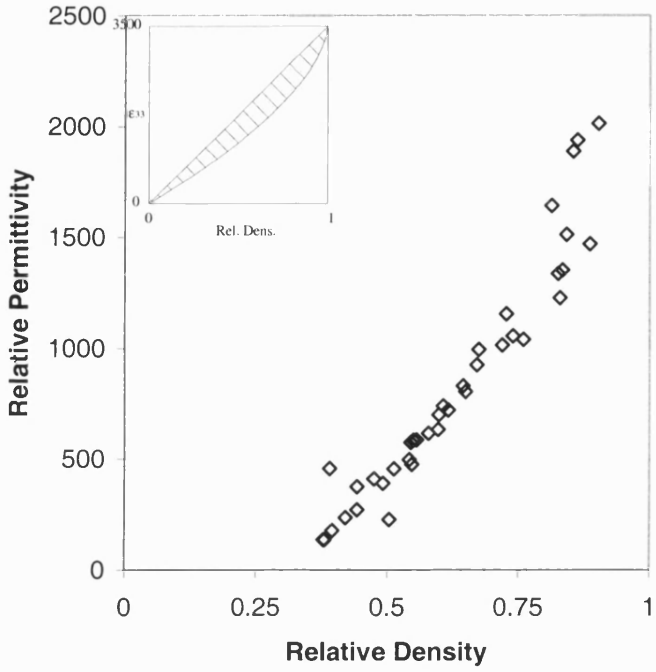

Figure 4-14: Results of relative permittivity with respect to porosity for the PEO series of samples.

The chart in Figure 4-14 shows the experimental values of permittivity with respect to porosity. The inset shows the trend predicted by FE. There is a gradual decrease in permittivity with increasing porosity as observed by the FE model. However, the experimental results are shifted to a higher relative density, i.e. the permittivity decreases more quickly than the FE model predicts. Again this is thought to be for the reasons outlined above, with localised areas of high or low porosity affecting the results.

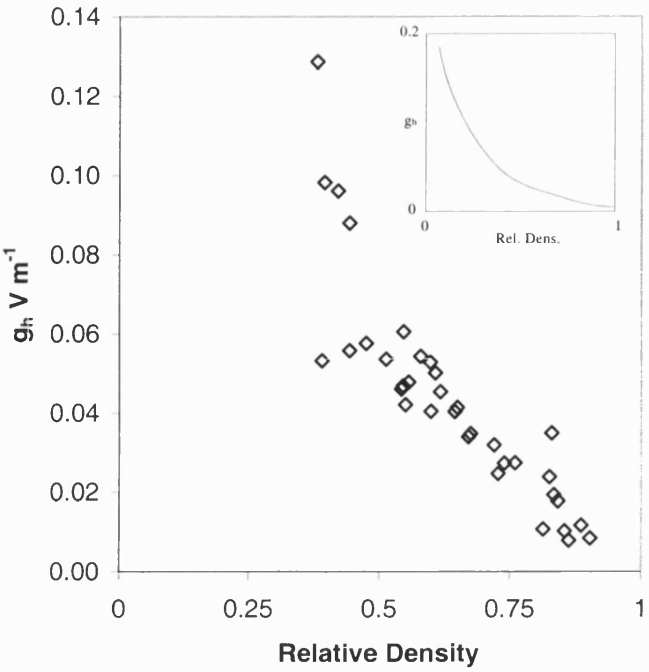

Figure 4-15: Results of g_h with respect to porosity for the PEO series of samples.

Figure 4-15 shows the experimental results for the measurement of g_h with respect to relative density. The inset, again, shows the predicted results from FEA. The result show that as relative density reduces the value of g_h increases and the trend predicted by FEA is similar to the experimental results. Again the experimental trend appears to be shifted to the high relative density area of the graph and g_h increases more rapidly than the predicted FE model data. This is due to the more rapid reduction in the experimental permittivity data.

There is lower scatter in the experimental results compared to the d_{33} and d_{31} data which is due to the low scatter in the permittivity data (Figure 4-14).

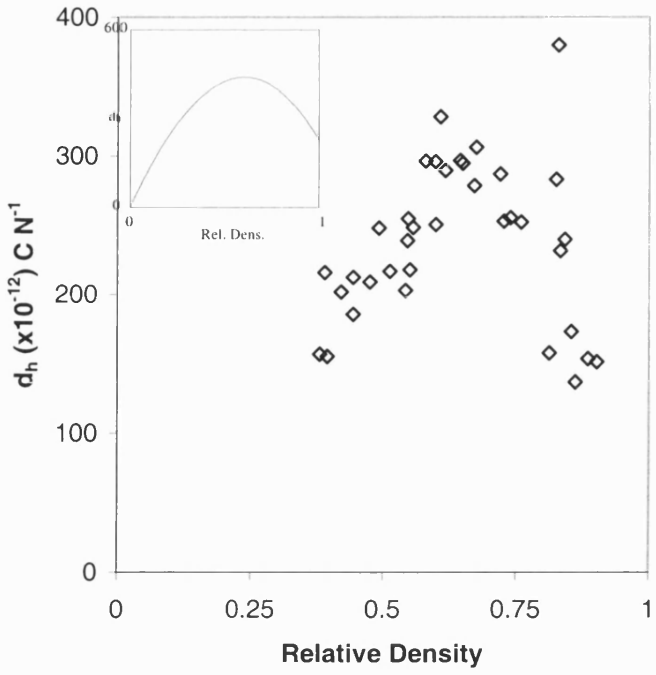

Figure 4-16: Results of d_h with respect to porosity for the PEO series of samples.

Figure 4-16 shows the experimental results of d_h which were calculated from the results of d_{33} and d_{31}. The results vary with relative density and show a peak at around 60-65%. The inset shows the FEA modelling trend and the experimental results appear to fit reasonably well as the finite element modelling peak in d_h is typically in the 50 – 60% porosity region.

4.2.2.3 PMMA Based Materials

The following figures show the experimental results from the PMMA sphere additions. These samples had 100μm pores and cracks running normal to the poling direction, as discussed in Chapter 3.

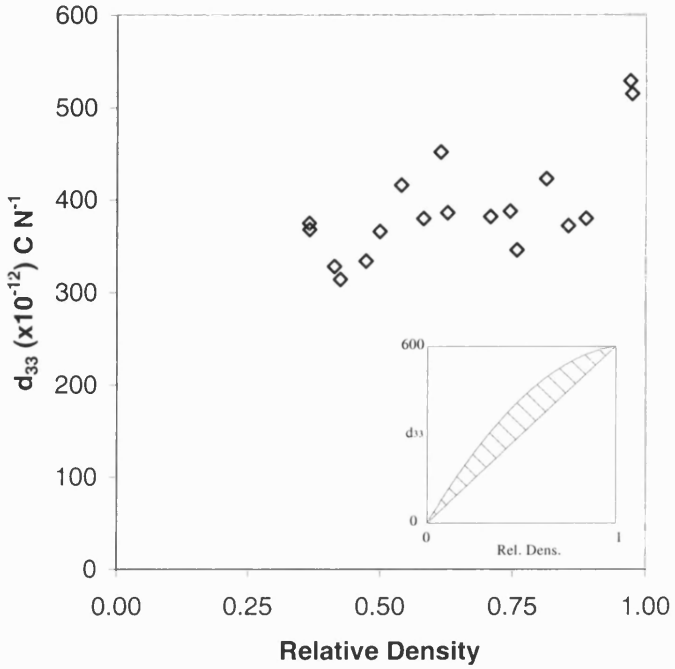

Figure 4-17: Results of d_{33} with respect to porosity for the PMMA (100μm) series of samples.

The results shown in Figure 4-17 are the experimental results for BurPS samples made with 100μm PMMA inclusion spheres and present the results of d_{33} with respect to relative density. The inset shows the FEA modelled trend. It can be seen that as relative density increases, d_{33} also increases. This decrease in d_{33} is not as pronounced as in the FEA trend, and the experimental results demonstrate that relatively high d_{33} values are obtained even at high levels of porosity. For example, at 50% density d_{33} values are still in excess of $300pCN^{-1}$.

The limit of the BurPS methods with the PMMA samples is 0.35 relative density and samples of lower density could not be manufactured for the reasons outlined in Chapter 3.

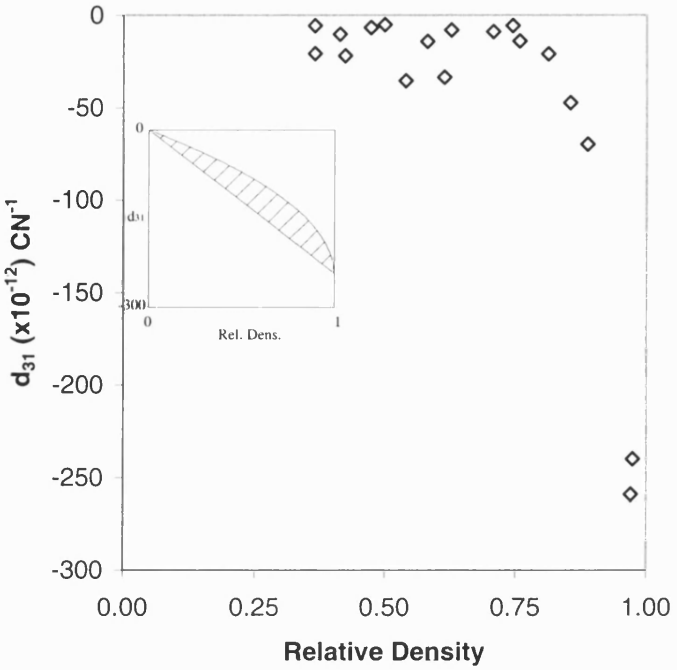

Figure 4-18: Results of d_{31} with respect to porosity for the PMMA series of samples.

Figure 4-18 above shows the results of d_{31} against relative density for the 100μm inclusion PMMA BurPS samples. The inset, again, shows the predicted trend from FEA. In this case there is a rapid decrease in $-d_{31}$ as the level of porosity increases. The decrease in $-d_{31}$ is more rapid than that observed in the FE modelling and for the PEO based materials.

The relatively high values of d_{33} shown in Figure 4-17 and the rapid reduction in these $-d_{31}$ values should lead to large d_h values.

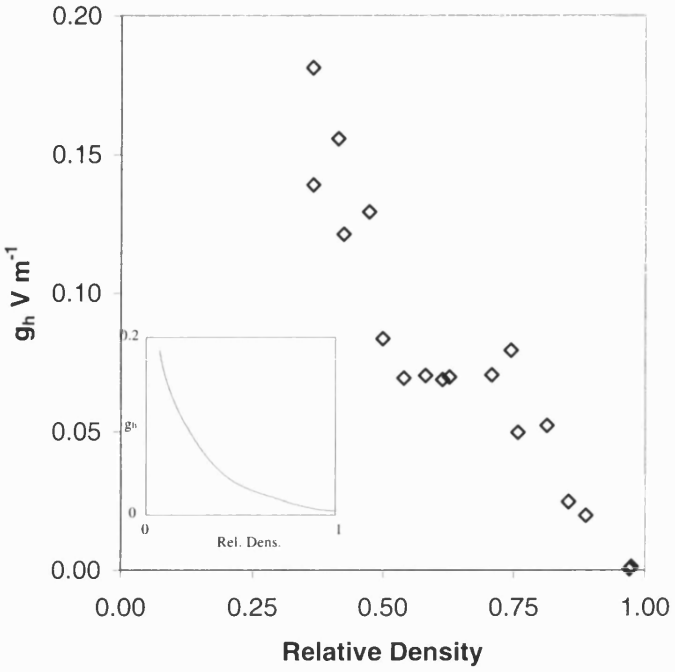

Figure 4-19: Results of g_h with respect to porosity for the PMMA series of samples.

Figure 4-19 shows the experimental results for the values of g_h with respect to relative density for the PMMA BurPS inclusions. The value of g_h can be seen to increase with decreasing relative density (increasing porosity).

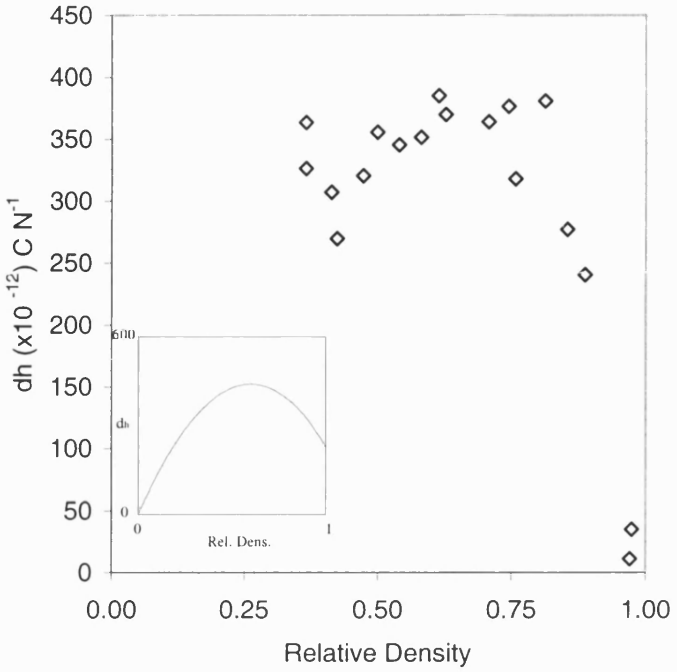

Figure 4-20: Results of d_h with respect to porosity for the PMMA series of samples.

The chart in Figure 4-20 show the experimental results of d_h with respect to relative density for the PMMA (100μm) inclusion samples produced by the BurPS method. The results show a maximum value of d_h (approximately 400 pC N^{-1}) over the 0.6 to 0.7 relative density range. These points fit the predicted FEA model shown in the insert.

The high values of d_h are associated with the relatively constant d_{33} values and low d_{31} values shown in Figure 4-18 and Figure 4-19 respectively.

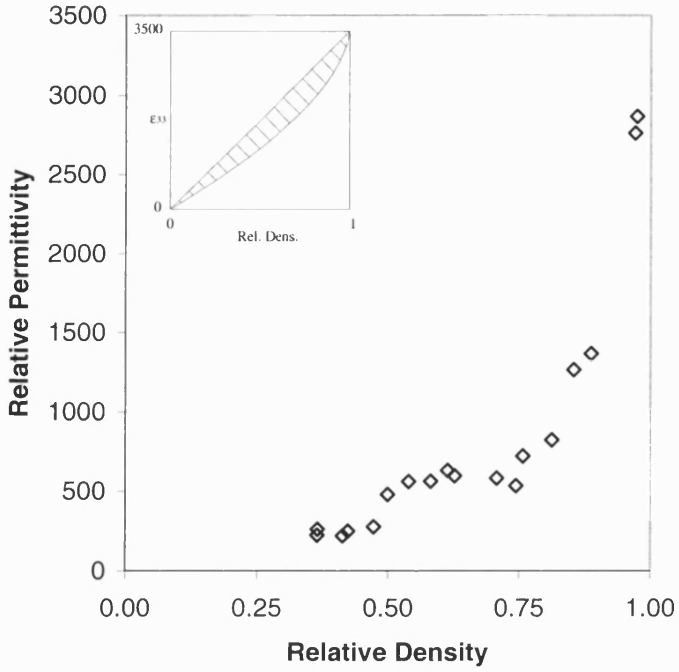

Figure 4-21: Results of relative permittivity with respect to porosity for the PMMA series of samples.

The experimental results shown in Figure 4-21 show the relative permittivity with respect to relative density for the PMMA large inclusion samples made by the BurPS method. This chart shows an increase in relative permittivity with increase in relative density. The experimental results shown in the figure follow the trend predicted by the FEA modelling with a slight shift towards the high relative density end of the chart. i.e. the experimental data results in more rapid decrease in permittivity with porosity. This is probably associated with the high degree of cracking perpendicular to the measurement direction which is present in the PMMA based materials.

4.2.2.4 Self Raising Flour (SR) Based Materials

The results of electrical testing (d_{33}, d_{31} and permittivity) performed on the self-raising flour materials follow.

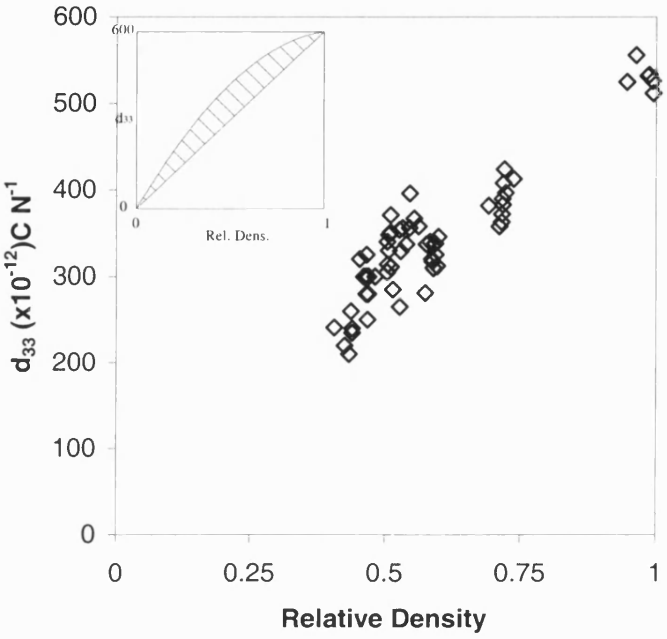

Figure 4-22: Results of d_{33} with respect to porosity for the SR series of samples.

The chart shown in Figure 4-22 shows the experimental data for d_{33} with respect to relative density for the SR series of samples made by the BurPS method. The inset shows the trend predicted by FEA. The results show an increase in the value of d_{33} with increasing relative density. The results follow the trend predicted by FEA closely. The good agreement of the results is thought to be because of the increased homogeneity of the samples, which is in turn due to the small size of the pores. Less scatter is also observed in these materials due to the more homogeneous microstructure.

Samples below 0.4 relative density could not be manufactured, again, due to the limitations of the BurPS method.

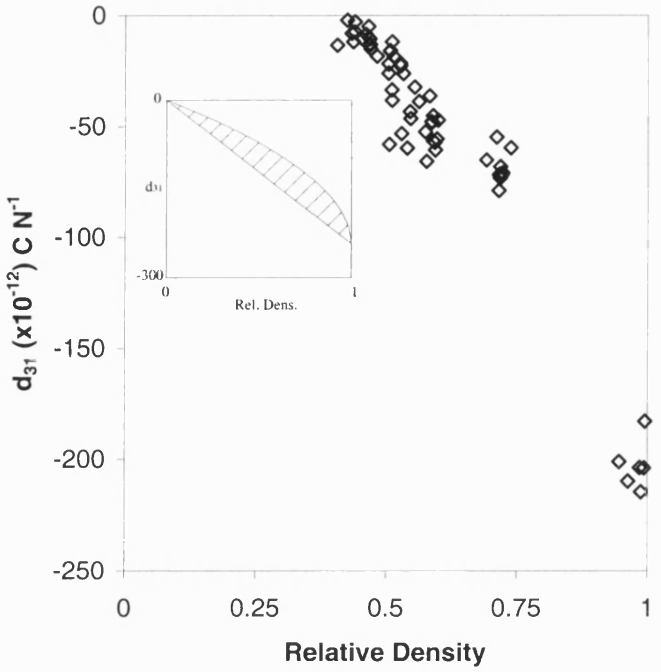

Figure 4-23: Results of d_{31} with respect to porosity for the SR series of samples.

Figure 4-23 shows the results obtained of d_{31} with respect to relative density for the BurPS SR series of samples. The absolute value of d_{31} can be seen to increase with increasing relative density. The relatively low scatter is related to the increased homogeneity of the samples made by using the SR material. The results closely follow the trend predicted by the FEA inset.

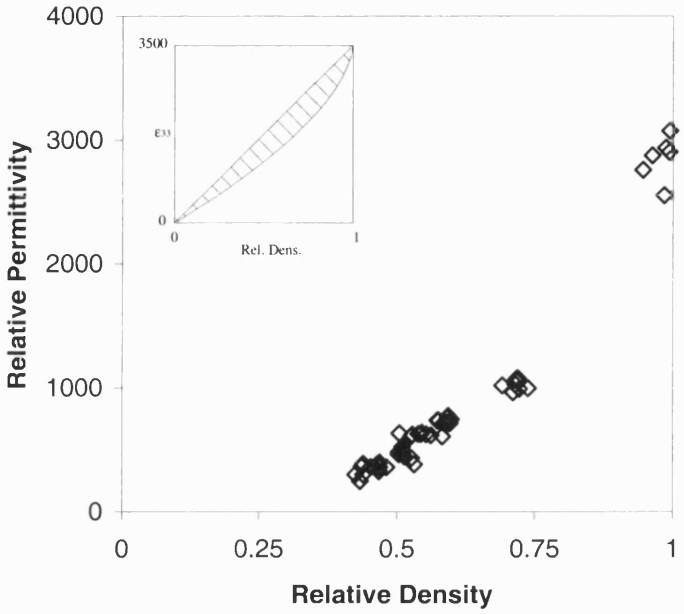

Figure 4-24: Results of relative permittivity with respect to porosity for the SR series of samples.

The relative permittivity is shown in Figure 4-24 with respect to the relative density for the SR BurPS samples. It is shown that the permittivity increases with respect to the relative density of the samples. This is also shown in the FEA trend included in the insert. There is good agreement with both the experimental results and the FE modelling.

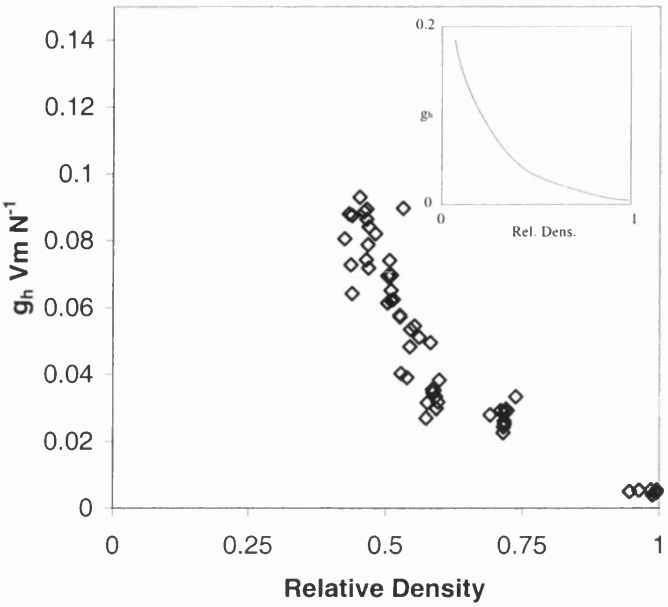

Figure 4-25: Results of g_h with respect to porosity for the SR series of samples.

The chart shown in Figure 4-25 shows the experimental data for g_h with respect to relative density for the SR series of BurPS samples. It can be seen that the value of g_h increases with reducing relative density. The FEA trend is shown in the insert. The correlation between the experimental results and the FEA modelling is very good, although the experimental results are shifted to the high relative density area of the chart. i.e. the experimental g_h increases more rapidly than the FE model predicts.

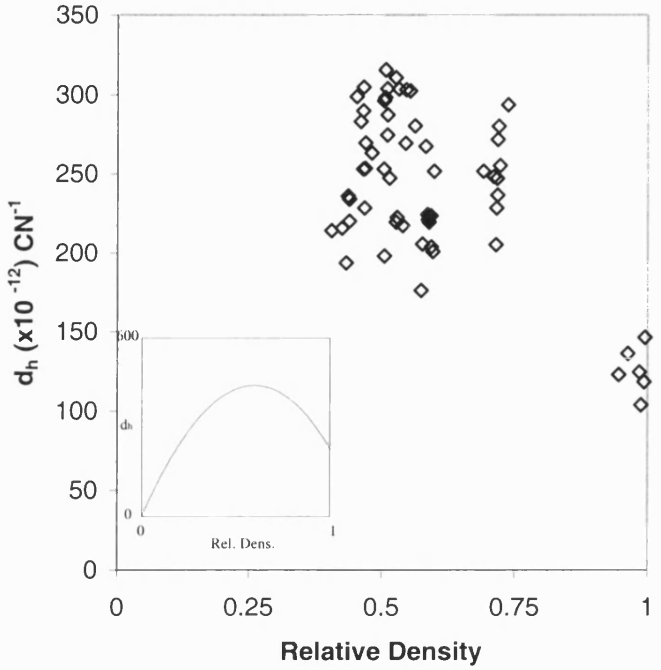

Figure 4-26: Results of d_h with respect to porosity for the SR series of samples.

The results shown in Figure 4-26 show the values obtained for d_h for the SR series of samples made by the BurPS method. A broad peak can be seen in the centre of the chart with maximum d_h values being at around 60% relative density. There is a significant amount of scatter in the values for d_h present on this chart but a trend can be seen to be similar to that calculated by FEA.

The SR samples appear the most homogeneous of all the materials produced by the BurPS process. For this reason the coupling coefficient, as defined in section 1.3.2, was measured for a range of densities.

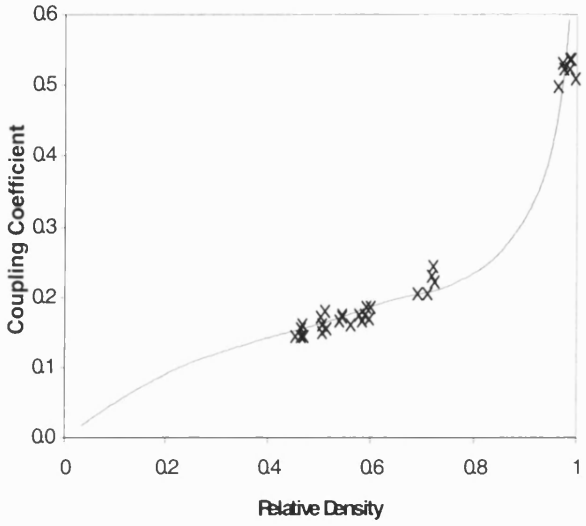

Figure 4-27: Graph showing coupling coefficients K_{eff} versus density of SR BurPS manufactured material samples.

The graph shown in Figure 4-27 shows a graph showing coupling coefficient versus relative density. The results show that there is a reduction in the coupling coefficient as porosity is introduced into the material. It can be seen that there is little scatter in the values and the experimental results follow the trend predicted by Bowen et al[27] shown by the solid line.

4.2.2.5 Corn Starch (CS) Based Materials

The results for the experimental data for the CS (cornstarch) series of samples are shown below. In this case there was only a limited range of porosity that could be manufactured as the cornstarch acted as a sintering aid. Samples manufactured with a large amount of cornstarch present, which would be expected to produce samples with over 50% porosity, still had a high sintering shrinkage and produced materials with relative densities of 0.65.

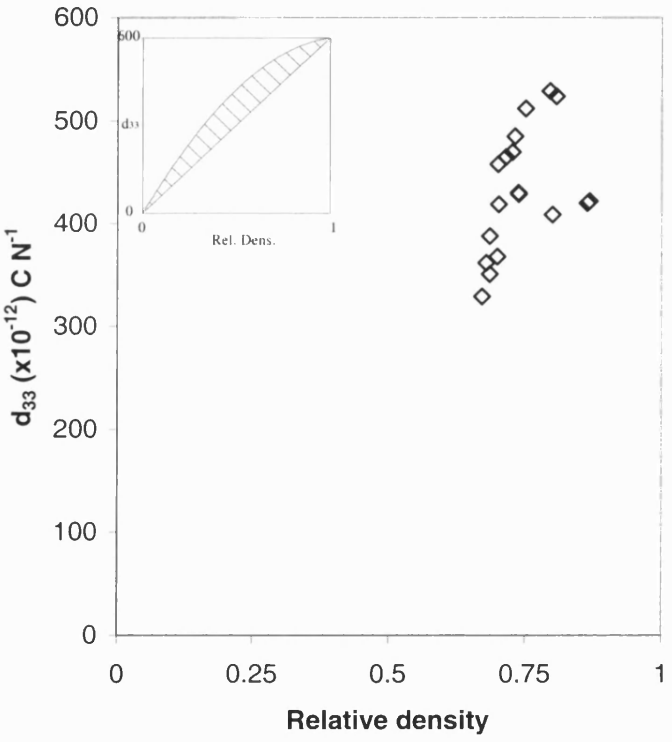

Figure 4-28: Results of d_{33} with respect to porosity for the CS series of samples.

The results shown in Figure 4-28 show the values of d_{33} for the CS range of samples made by the BurPS method. It can be seen that the value of d_{33} increases with increasing relative density. The trend predicted by FEA is shown in the inset but due to the limited range of densities produced, no correlation can be made.

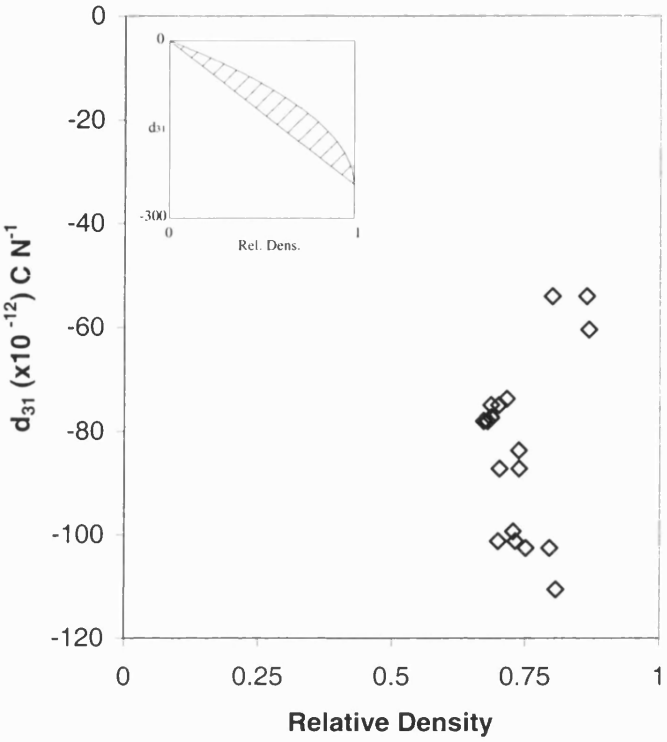

Figure 4-29: Results of d_{31} with respect to porosity for the CS series of samples.

Figure 4-29 shows the results of the d_{31} measurements of the CS series of samples made by the BurPS method. Due to the limited density range of samples produced by this method no correlation can be made to the FE trends.

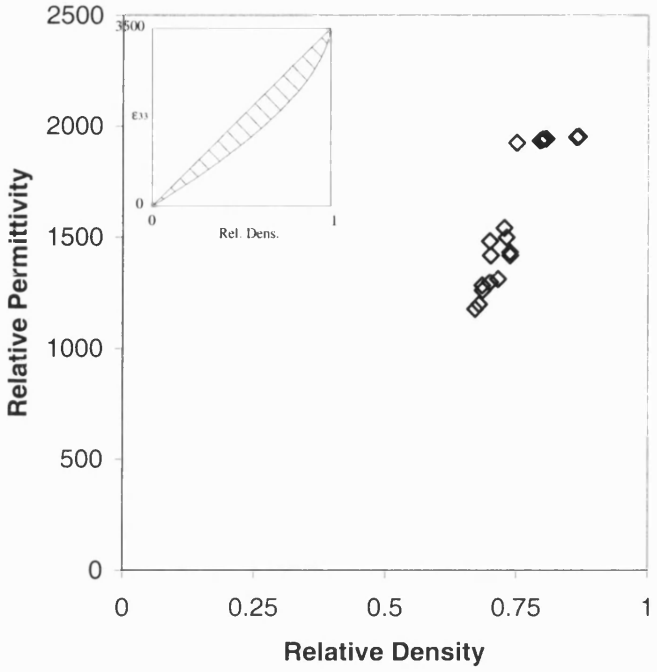

Figure 4-30: Results of relative permittivity with respect to porosity for the CS series of samples.

The chart shown in Figure 4-30 is the experimental results of the relative permittivity of the samples made by the BurPS method with CS inclusions. The chart shows the increase of relative permittivity with increasing relative density. The FEA trend is shown in the insert.

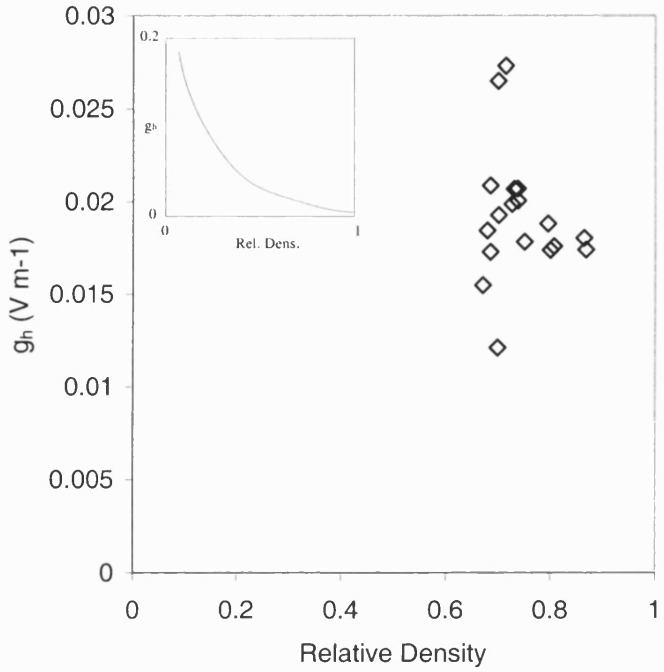

Figure 4-31: Results of g_h with respect to porosity for the CS series of samples.

Figure 4-31 shows the results for the g_h figure of merit with respect to relative density for the CS series of samples. For the cornstarch samples there is a large amount of scatter and no correlation between g_h and porosity is observed.

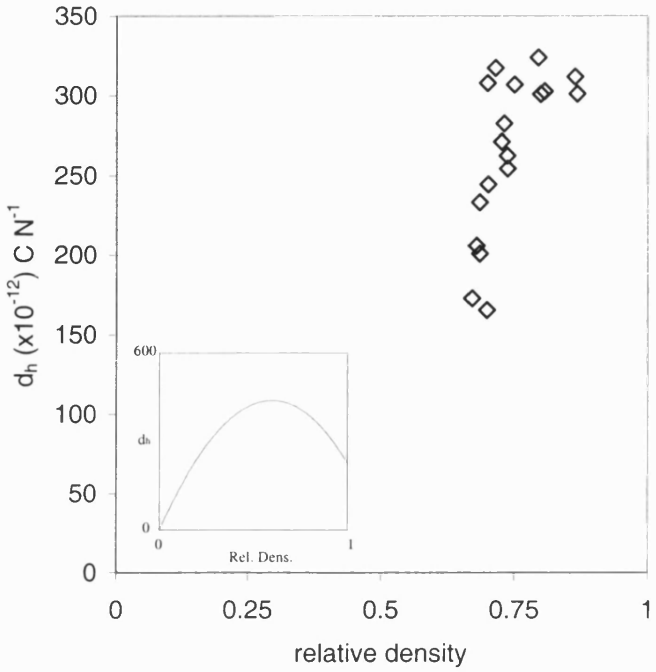

Figure 4-32: Results of d_h with respect to porosity for the CS series of samples.

The chart in Figure 4-32 shows the calculated values of d_h for the CS series of BurPS samples and again the limited density range means that no correlation can be made. The large scatter in the CS data is probably due to the fact that although many of the CS samples are of similar density, the microstructure varies significantly as they contain different amounts of porosity at different sizes.

4.2.2.6 Reticulated Foam Based Materials

The results for the experimental data for the foam based materials, which were used to manufacture materials with porosities of over 60%, are shown below. Again there was only a limited range of porosities that could be manufactured, however, the range for the foam materials was between 0.1 and 0.3 relative density. For each density the sample properties were measured before (PZT-porosity) and after polymer impregnation (PZT-polymer composite).

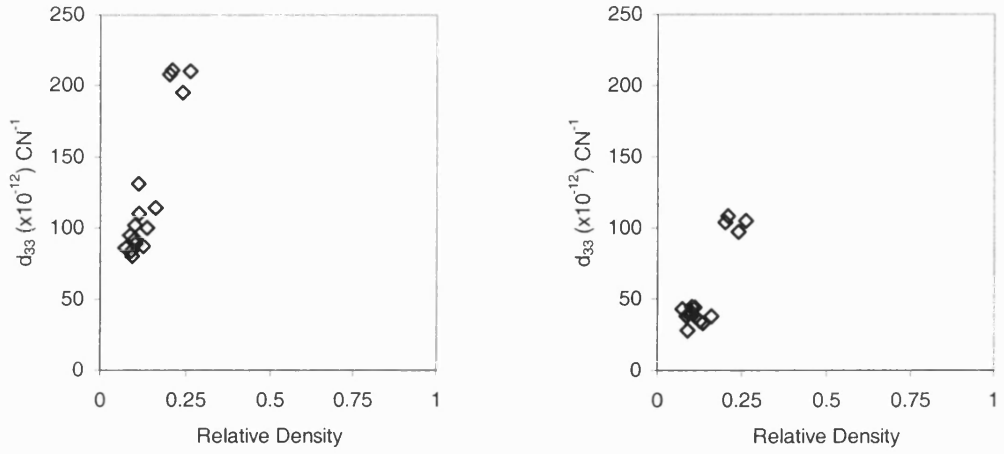

Figure 4-33: Graph showing d_{33} versus relative density for the foam based materials, a) PZT-porosity and b) PZT-polymer composites

The graphs in Figure 4-33 show the values of d_{33} with respect to relative density for both the a) PZT-porosity foams and the b) PZT-polymer foams. It can be seen that the value of d_{33} increases with ceramic volume fraction in both the graphs. The values in Figure 4-33b corresponding to the PZT-polymer composite are significantly lower than those in Figure 4-33a. This is due to the inactive polymer suppressing the piezoelectric effect, as described in Chapter 2.

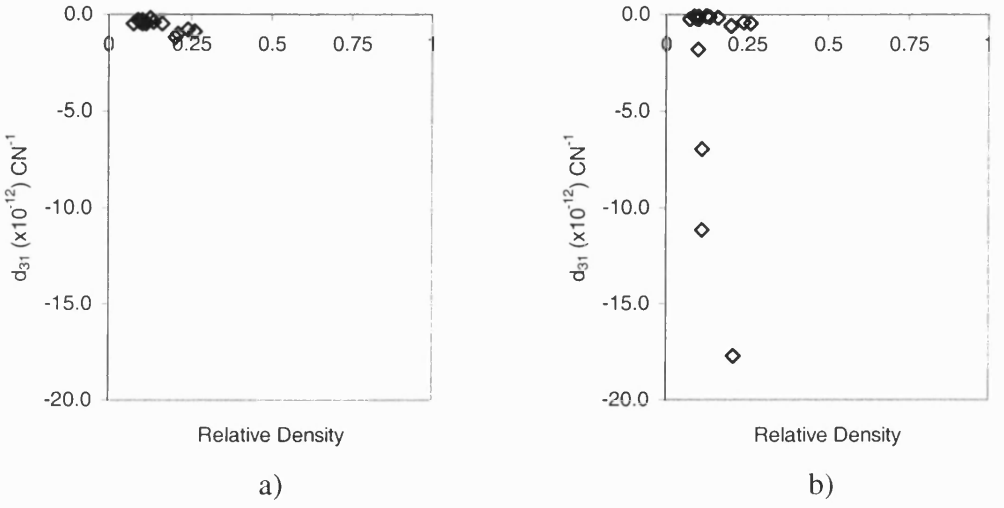

Figure 4-34: Graph showing d_{31} versus relative density for the foam based materials, a) PZT-porosity and b) PZT-polymer composites

The graphs above in Figure 4-34 show the values of d_{31} with respect to relative density for the a) PZT-porosity and the b) PZT-polymer foam based materials. It can be seen that for most of the materials tested the values of d_{31} are extremely small (<5pCN^{-1}). These low values of d_{31} coupled with relatively high values of d_{33} mean that the values for the d_h of the foam based materials will be high. These values of d_h are shown below.

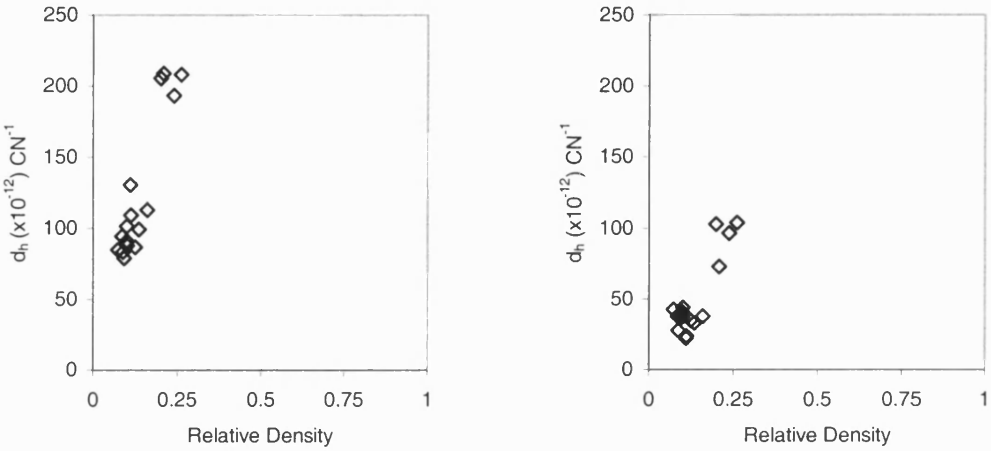

Figure 4-35: Graph showing d_h versus relative density for the foam based materials, a) PZT-porosity and b) PZT-polymer composites

The graphs in Figure 4-35 show the values of d_h with respect to relative density for the a) PZT-porosity and b) PZT-polymer reticulated foam based samples. It can be seen that the values of d_h increase with increasing ceramic volume fraction as predicted by the FE modelling in the low ceramic volume fraction condition, Figure 2-31. However, even at the low values of relative density the values of d_h observed are higher than those of dense PZT-5H (approximately 44pCN^{-1}). The values of d_h for the PZT-porosity samples Figure 4-35a are approximately double the value of the PZT-polymer samples shown in Figure 4-35b.

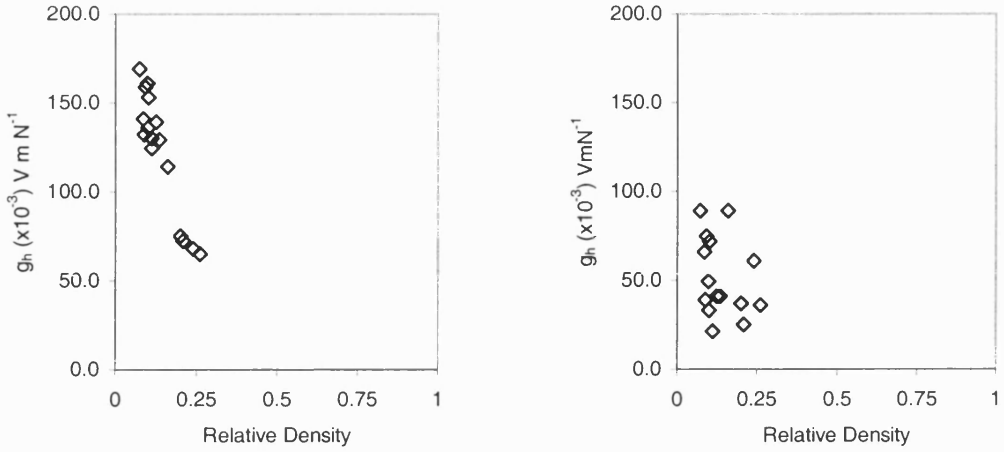

Figure 4-36: Graph showing g_h versus relative density for the foam based materials, a) PZT-porosity and b) PZT-polymer composites

The graphs shown in Figure 4-36a and Figure 4-36b are the values of g_h with respect to relative density for the PZT-porosity and the PZT-polymer foam based materials respectively. For the PZT-porosity samples a clear trend can be seen of increasing g_h with reducing ceramic volume fraction. This trend is not observed in the results for the PZT-polymer materials. This is due to suppressed values of d_h leading from anomalous readings of d_{31} for a small number of samples, as shown in Figure 4-34b.

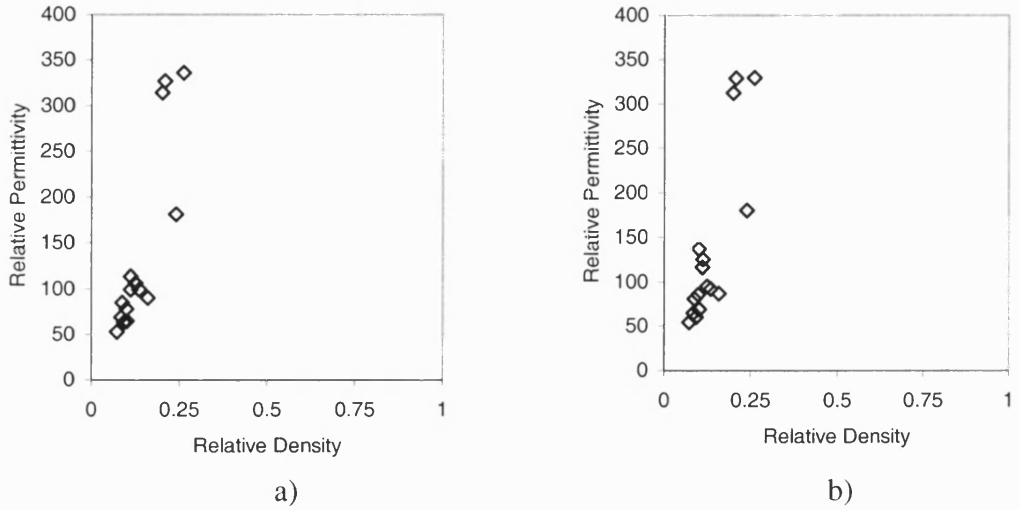

Figure 4-37: Graph showing relative permittivity versus relative density for the foam based materials, a) PZT-porosity and b) PZT-polymer composites

The graphs in Figure 4-37a and Figure 4-37b show the values of relative permittivity for the PZT-porosity and the PZT-polymer foam based materials respectively. It can be seen from the graphs that the values of permittivity are similar regardless of the second phase material (air or polymer) This is expected as the relative permittivity of the polymer is approximately $\varepsilon_r=2$. A trend is observed of increasing permittivity with increasing ceramic volume fraction, which is also expected.

It is observed that for the foam based materials the PZT-porosity foams consistently achieve higher figures of merit than the PZT-polymer based foam materials. This would make the PZT-porosity materials more desirable for use in piezoelectric applications. However, the PZT-porosity materials are extremely brittle and difficult to handle. In addition, the application of electrodes to the surfaces in order to test the samples is not trivial. Once these ceramic foams have been impregnated with polymer, they become robust enough to withstand machining, their surfaces can be readily electroded and they can be tested with ease. It is for this reason that much future work on highly porous 3-3 composites has been carried out on these PZT-polymer foam materials as shall be outlined in Chapter 7.

5 Refinement of Finite Element Modelling

The finite element modelling carried out and reported in Chapter 2 used a single shape of unit cell, as shown in Figure 2-7. From the experimental work carried out in manufacturing the piezocomposites and the macrostructural analysis, it is evident that the model used in the FE analysis is relatively simple and does not accurately represent the real composite structures.

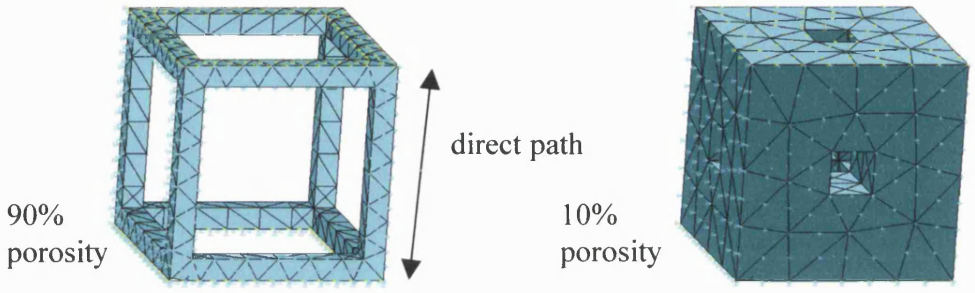

Figure 5-1: Example of a high (90%) and low (10%) ceramic volume fraction model.

This unit cell was originally chosen to be a simple model that would solve relatively quickly with the ability to be readily changed to incorporate different porosities and second phase materials. The model also allowed an understanding of the mechanisms by which high d_h, and g_h coefficients are generated. It was decided to create a number of models with unit cells, which more accurately resemble the structures seen in the production of the BurPS and reticulated foam materials. This was done with a view to a more accurate analysis of the microstructures in finite element modelling.

One of the principle reasons the FE modelling refinement was carried out was to avoid a direct path from the top of the model through to the bottom, as seen in Figure 2-7. The cube unit cell modelled in Chapter 2 had an obvious direct path between both electrode surfaces. This was thought to not fully represent the real microstructure, especially for the reticulated foam composites.

5.1 1D BurPS Model

The BurPS method of manufacture produces two distinct types of microstructure, which can be identified at low porosity and at high porosity. At low porosities the structure can be approximated to a single spherical pore in a solid cube of material and can be regarded as 3-0 connectivity (see Figure 3-16a). An example of the model unit cell can be seen in Figure 5-2a, the unit cell is a cube and has been cut in half to show the spherical pore in the centre. The term 1D BurPS model is used as the unit cell is symmetrical in all directions, unlike the 3D BurPS mode discussed later.

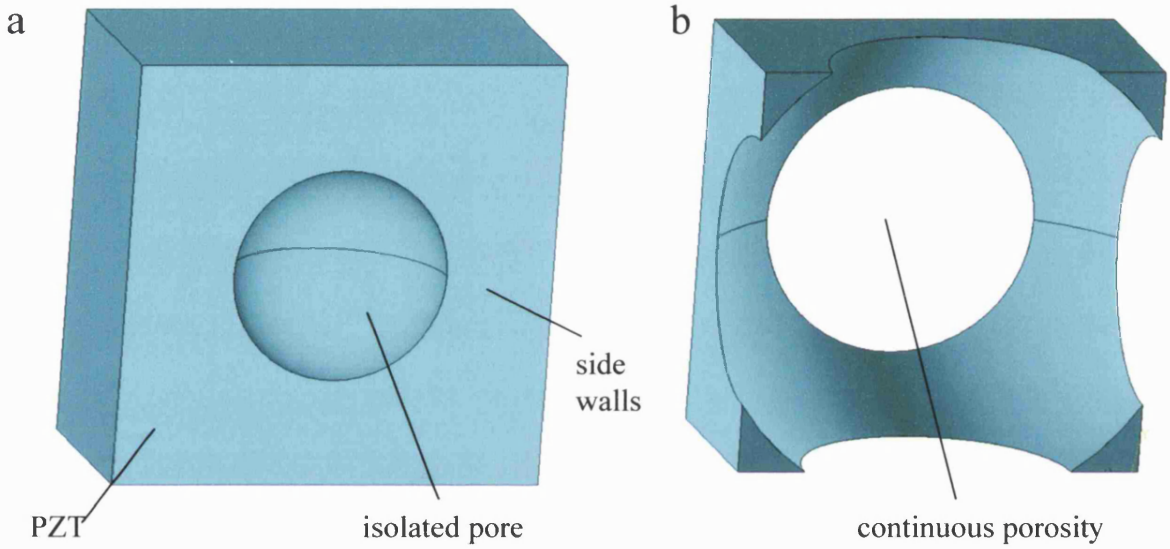

Figure 5-2: Example of unit dissected cell used for 1-D BurPS modelling. a) low porosity (3-0) and b) high porosity (3-3).

The whole cubic cell has symmetry applied to this model so that it appears to be part of a larger model. This type of unit cell is representative of modelling discrete, non-connected pores in a ceramic matrix (3-0 connectivity).

It can be seen that once the radius of the spherical pore in the centre of the cube reaches a value greater than half of the cube side length the model changes from discrete pores to represent a continuous pore system in a ceramic matrix (3-3 connectivity). This is representative of the BurPS process whereby isolated pores become interconnected at high porosities. This interconnectivity can be seen in the microstructures in Chapter 3, Figure 3-16c.

Models were developed where the radius of the pore was varied from a small value (5% of the cube side length) to close to approximately 75% of the cube side length, in an attempt to model the transition from discrete to continuous pores.

5.1.1 1D Burps Model PZT Only Results

The results for the modelling of 1D BurPS structures can be seen in the following figures. The d_{33}, d_{31} and d_h piezoelectric coefficients as a function of density are presented. In all figures it can be seen that values around 50% relative density are not represented. This is an artefact of the modelling procedure. At 50% relative density the edges of the pore were very close to the edges of the cube, and the meshing of the model was difficult, shown in Figure 5-3, with a very fine mesh required in order to represent these areas.

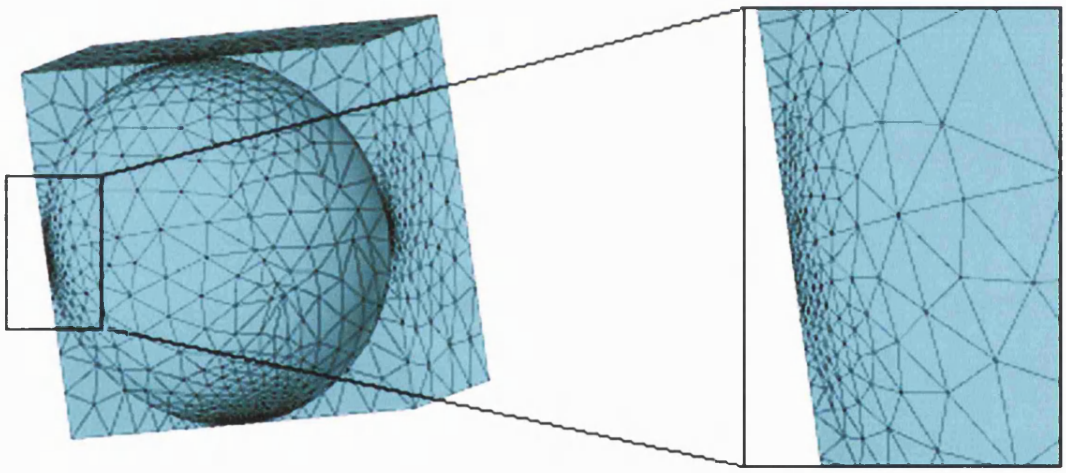

Figure 5-3: Tight mesh needed around thin walled sections of the 50% relative density 1-D BurPS model.

The chart shown in Figure 5-4 shows the values of d_{33} plotted against relative density for the model described above.

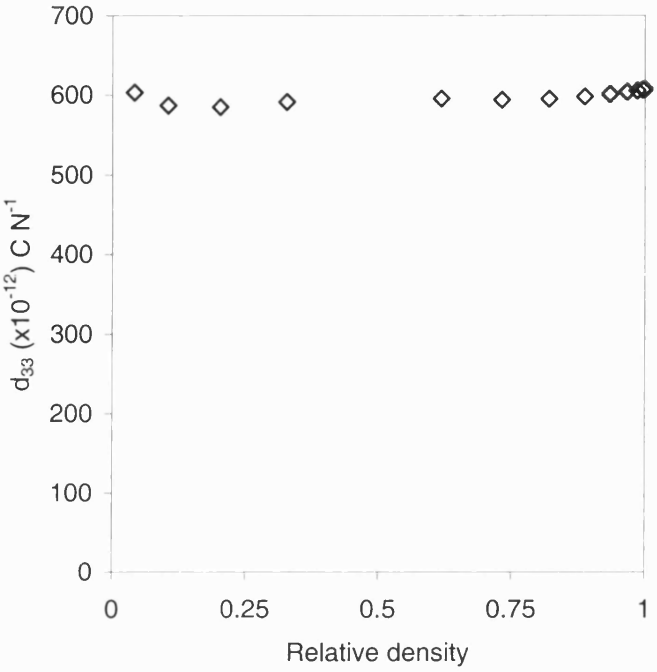

Figure 5-4: Chart showing d_{33} against relative density for the 1D BurPS model PZT-porosity.

This chart is similar to other charts for d_{33} with a PZT-porosity cubic model system. The values of d_{33} are high at around 600 x10^{-12} C N^{-1} regardless of the relative density of the model. This is the value of d_{33} for the dense material.

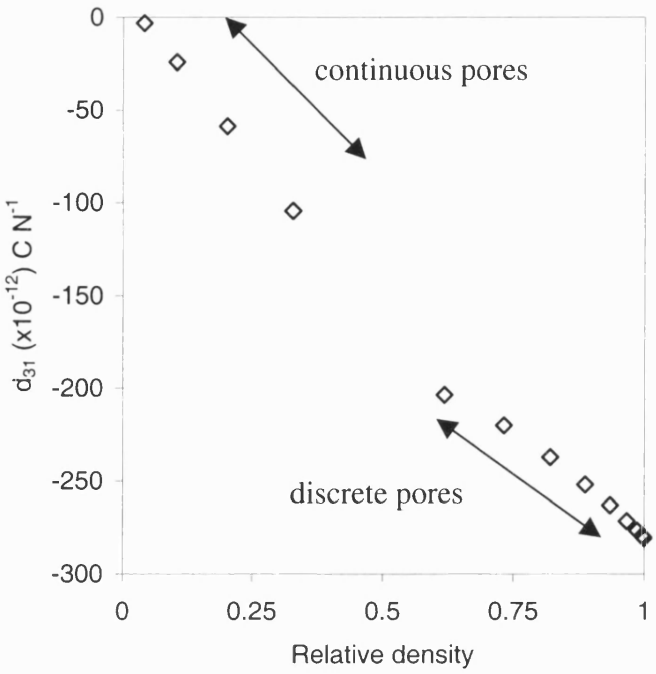

Figure 5-5: Chart showing d_{31} against relative density for the 1D BurPS model PZT-porosity.

The chart shown in Figure 5-5 shows the values for d_{31} for the 1D BurPS, PZT porosity, model. It can be seen that the absolute value of d_{31} increases with density. The trends appear to behave differently at high porosities (continuous pores) than at low porosities (discrete pores). At low values of relative density the change in d_{31} with respect to relative density is higher than that at higher relative densities, due to the steeper gradient.

This effect is due to the presence or absence of the sidewalls of the cube in the model. At high values of relative density there is a large amount of bulk ceramic in the sidewalls of the model which does not contribute to the d_{31} coefficient. At low relative densities these sidewalls are not present (see Figure 5-2b) and reducing the density removes d_{31} active material only and thus has a larger influence on the gradient of the curve in this area of the chart.

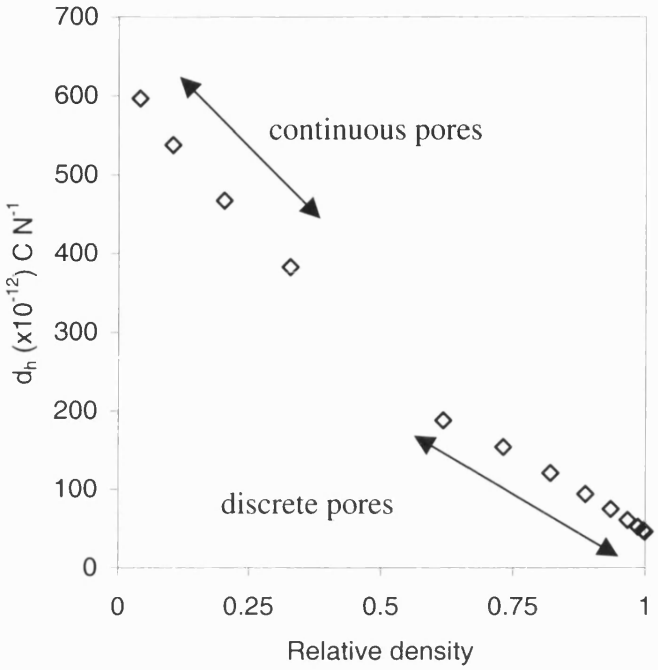

Figure 5-6: Chart showing d_h against relative density for the 1D BurPS model PZT-air.

This chart shows the values for d_h as a function of relative density for the 1D BurPS model for a PZT only unit cell. Since the values of d_{33} are approximately constant, the chart shown in Figure 5-6 is the same shape as the chart for d_{31} shown previously. This shows that the value of d_h increases with decreasing relative density. This chart is similar to the chart shown in Chapter 2 for the square pore system, which has continuous porosity regardless of relative density. The difference being that the gradient changes around 50% relative density, which has been previously explained.

5.1.2 1D BurPS model – PZT Polymer Composite Results

The model shown above was also taken into consideration with a polymer phase filling the pore up to the cube boundary. The modelling was repeated with a polymer of 6GPa Young's modulus and a Poisson's ratio of 0.3.

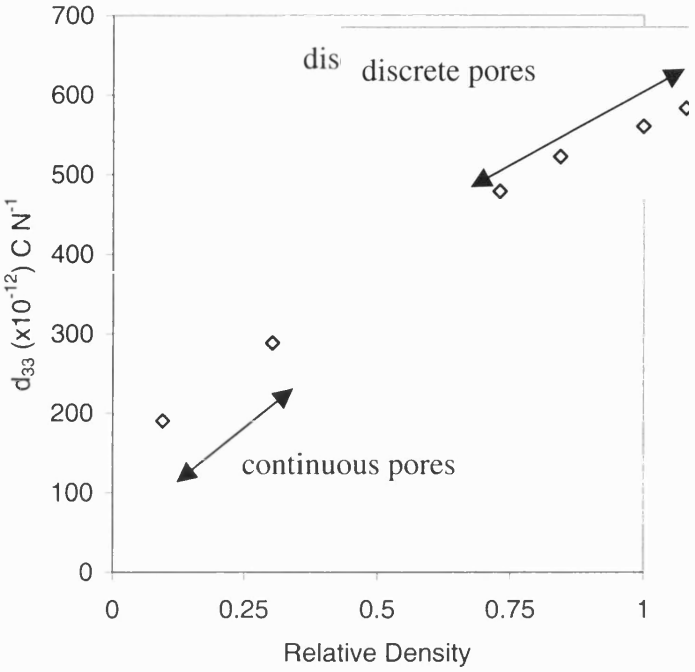

Figure 5-7: Chart showing d_{33} against relative density for the 1D BurPS model PZT-polymer composite.

The chart shown in Figure 5-7 plots the values of d_{33} with respect to relative density for the 1D BurPS model with polymer as the second phase. It can be seen that the value of d_{33} increases with increasing relative density. These results are similar to those shown in Chapter 2, when modelling a square pore in which d_{33} decreases with increasing polymer content as some of the load is taken up by the inactive polymer phase. This chart also exhibits a change in gradient between low and high relative densities, as did the PZT - porosity model for d_{31}. This is for the same reasons as the previous chart, and is caused by the increased removal of d_{33} active material per unit relative density change in the highly porous structures that do not have inactive sidewalls.

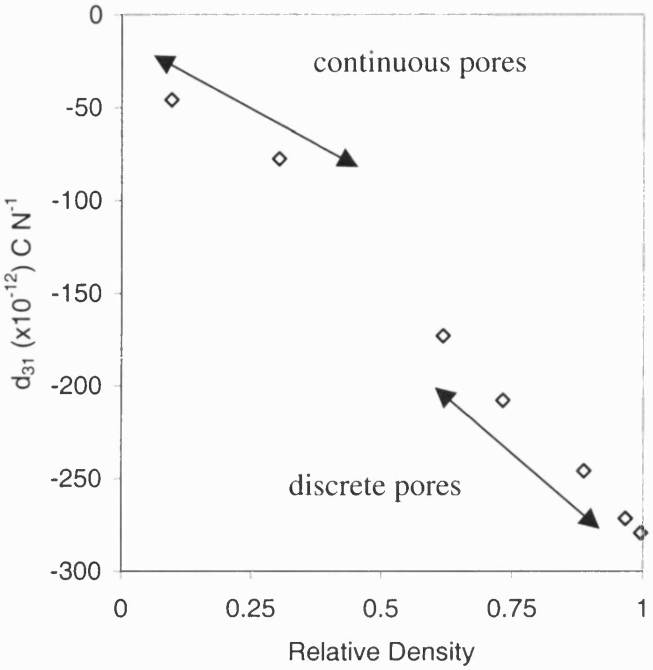

Figure 5-8: Chart showing d_{31} against relative density for the 1D BurPS model PZT-polymer composite.

The chart shown in Figure 5-8 is the modelled values for d_{31} with respect to relative density for the 1D BurPS model with polymer as a second phase. It can be seen that the absolute values of d_{31} increase with density. At low relative densities (continuous pores) the change in d_{31} with respect to relative density is smaller than at high densities.

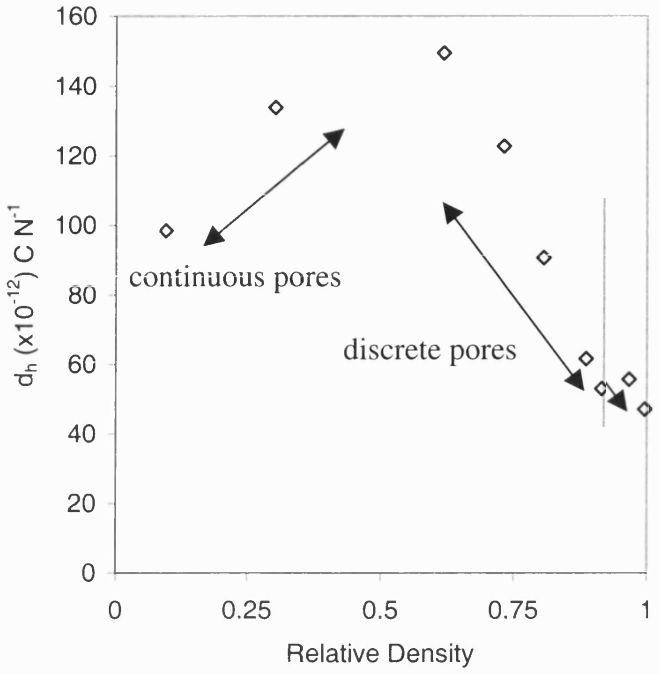

Figure 5-9: Chart showing d_h against relative density for the 1D BurPS model PZT-polymer composite.

The chart shown in Figure 5-9 is the calculated values of d_h with respect to relative density for the 1D BurPS model with polymer as the second phase.

It can be seen clearly that there is a peak in the value of d_h. Although no direct values are available from around 50% relative density, it can be seen that the peak value for d_h will be in the 30 – 60% region. The peak value is 150 $x10^{-12}$ C N^{-1} which is three times higher than the figure for dense PZT5H (44pCN^{-1}).

These results show that it is important to take into account the microstructure of the material as it is unlikely all of the porosity is continuous in the real materials, especially at relatively high densities.

5.2 3D Burps Model

The model mentioned above represents the BurPS materials manufactured with high porosities. In order to further develop this model in a 3D unit cell, two spheres have been removed from a solid cube from opposite corners. This allows a higher level of porosity to be examined before the two spheres overlap, as compared to a central spherical pore. An example of this model can be seen in Figure 5-10.

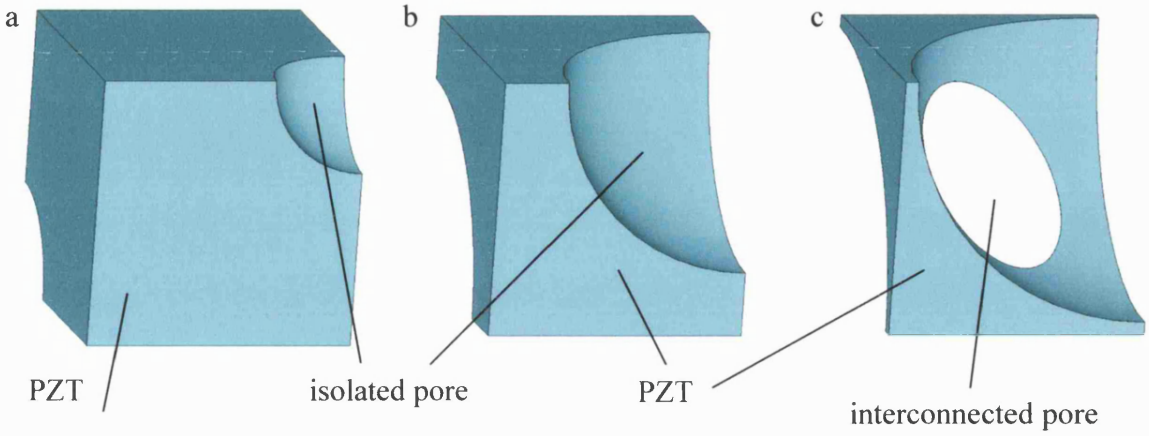

Figure 5-10: Example of the 3D BurPS modelling, a) low porosity, b) medium porosity and c) high porosity.

The pore radius in this model was varied between 10% of the cube side and 110% of the cube side length. This model is representative of the condition where the BurPS method has been used to create microstructures, which range from discrete pores to interconnected pores.

5.2.1 3D BurPS Model, PZT Porosity Results

The following three graphs are the piezoelectric d coefficients for the 3D BurPS model with PZT as the only phase present (i.e. no polymer). The values of density were varied between 0 and 100% porosity. As with the 1D, single pore model there is a range in which no results could be obtained due to meshing restrictions. This is at approximately the 25% relative density level and is due to the presence of thin walls.

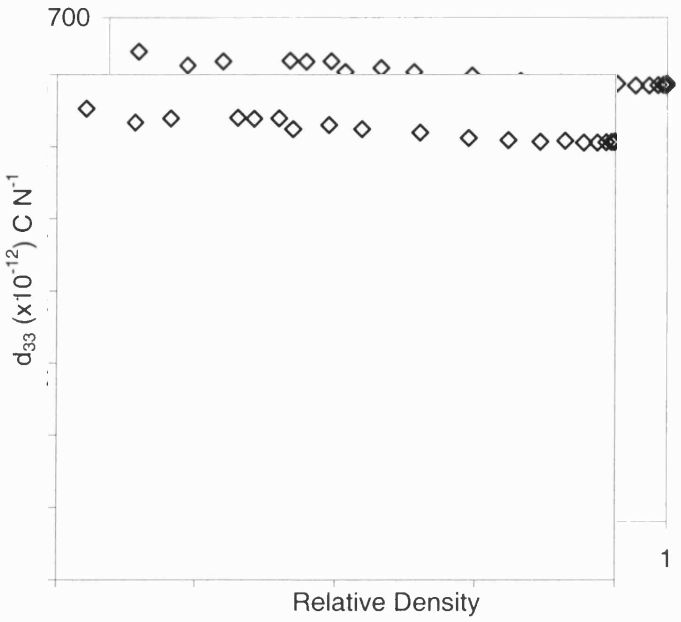

Figure 5-11: Chart showing d_{33} against relative density for the 3D BurPS model PZT-porosity composite.

The chart in Figure 5-11 shows the values of d_{33} with respect to relative density for the 3D BurPS model using a single PZT phase.

As with other charts showing d_{33} in a single-phase model, the value of d_{33} is approximately constant with respect to relative density. Again the values are around 600 x10^{-12} C N^{-1}, the value for dense PZT-5H. This is due to a uninterrupted path between the two electrodes at the top and the bottom of the model. Even in highly porous model structures there is a direct route between the two electrodes (Figure 5-10c).

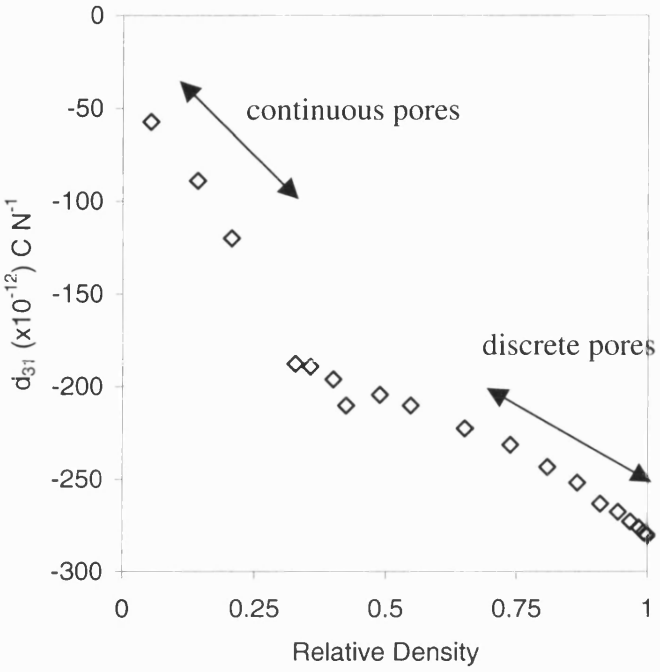

Figure 5-12: Chart showing d_{31} against relative density for the 3D BurPS model PZT-porosity composite.

The chart in Figure 5-12 shows the values of d_{31} with respect to relative density for the 3D BurPS model with a single PZT phase and no polymer present.

It can be seen that the absolute value of d_{31} increases with increasing relative density. In addition, a gradient change is observed at approximately 25% relative density. This is the value at which the two pores on opposite faces of the cube meet and create a single, complex interconnected pore in the model, as shown in Figure 5-10c.

The reasons for this gradient change are similar to those explained in the 1D BurPS model. The removal of non-active d_{31} materials occurs at high relative densities, which leads to a relatively slow reduction d_{31} with relative density. At low values of relative density, the removal of material leads to removal of d_{31} active regions, thus reducing the d_{31} value more rapidly.

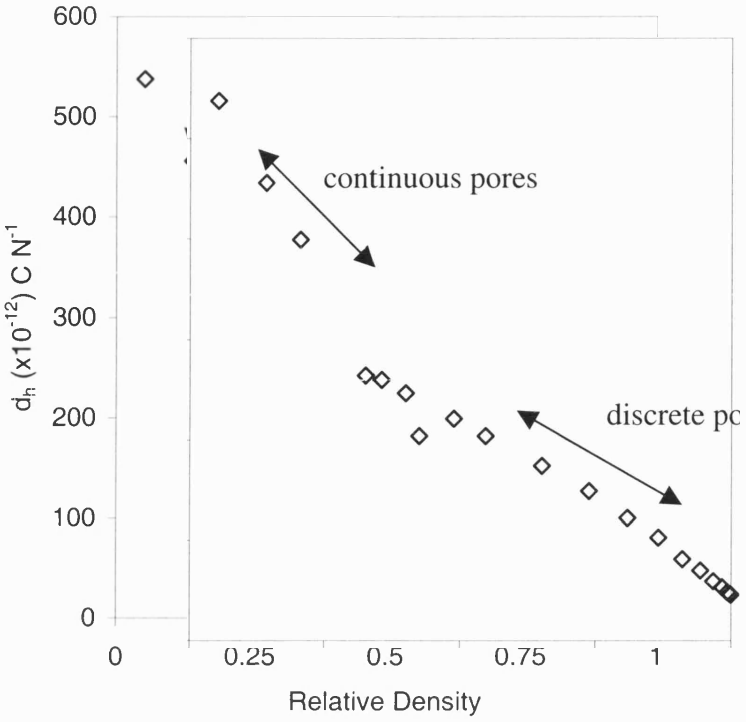

Figure 5-13: Chart showing d_h against relative density for the 3D BurPS model PZT-porosity composite.

The chart shown in Figure 5-13 is the calculated values of d_h for the 3D BurPS model of a single PZT phase with porosity. As this graph is a combination of the previous charts and the d_{33} values are approximately constant, this chart resembles that of the d_{31} chart.

The overall trend is for the value of d_h to increase with decreasing relative density.

5.2.2 3D BurPS Model – PZT -Polymer Composite Results

The 3D BurPS model above was also taken into consideration with a polymer phase filling the pores up to the cube boundary. The modelling was repeated with a polymer of 6GPa Young's modulus and Poisson's ratio of 0.3.

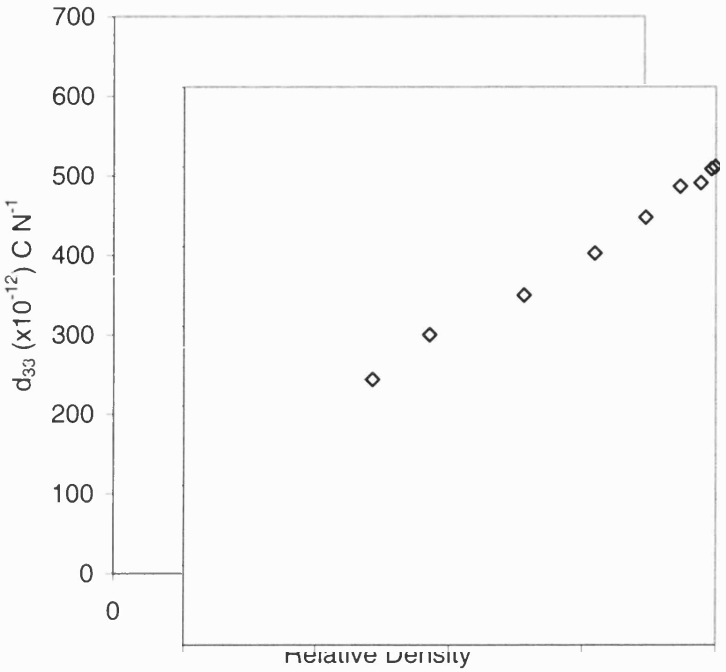

Figure 5-14: Chart showing d_{33} against relative density for the 3D BurPS model PZT-polymer composite.

The chart in Figure 5-14 shows the values of d_{33} for the 3D BurPS model with a polymer phase filling the existing pore space. It can be seen that the value of d_{33} decreases with decreasing density.

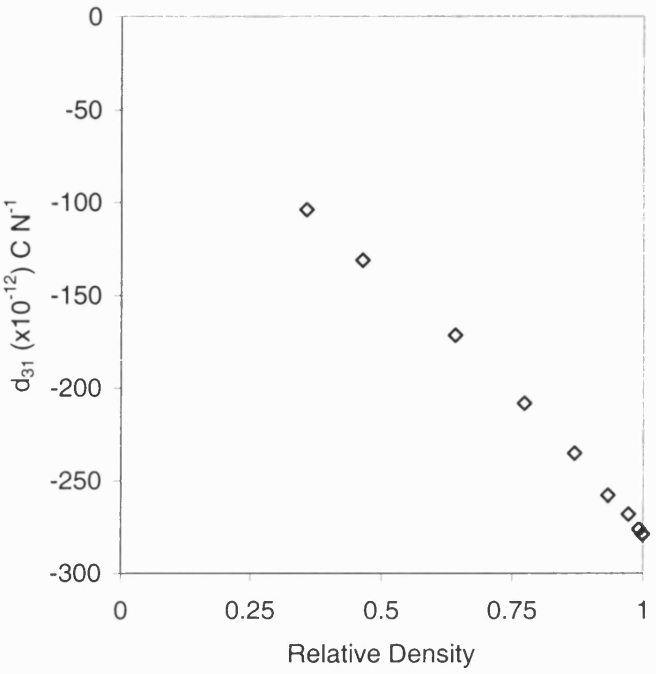

Figure 5-15: Chart showing d_{31} against relative density for the 3D BurPS model PZT-polymer composite.

The chart shown in Figure 5-15 shows the values of d_{31} with respect to relative density for the 3D BurPS model using a two phase PZT - polymer model.

It can be seen that the absolute values of d_{31} increase with increasing density. This relationship is approximately linear.

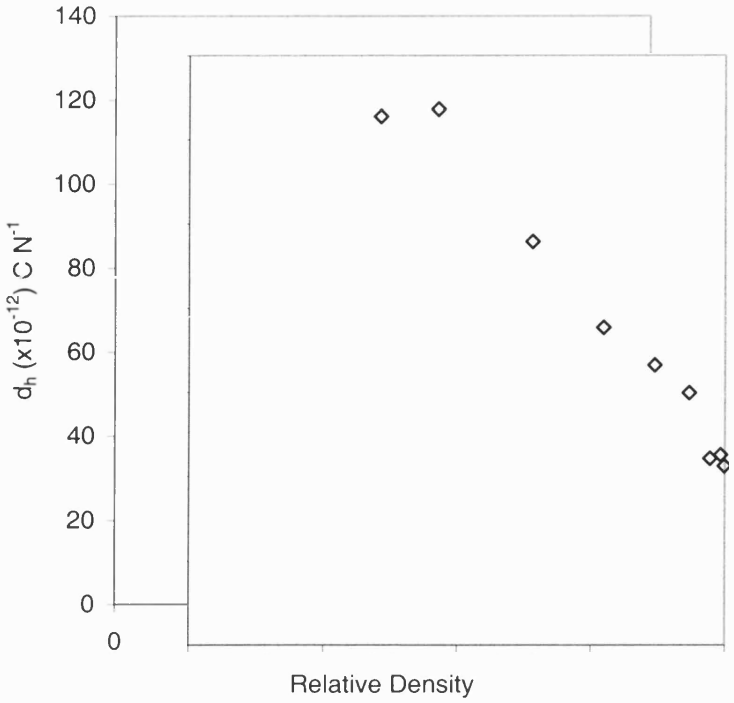

Figure 5-16: Chart showing d_h against relative density for the 3D BurPS model PZT-polymer composite.

The chart in Figure 5-16 shows the calculated values of d_h for the 3D BurPS model of a two phase, PZT polymer system.

It can be seen from the graph that there is an increase in d_h. The maximum value shown is around 130 x10^{-12} C N^{-1} at 50% density, which is approximately 2.5 times the fully dense value.

The modelling presented previously completes the modelling for the BurPS structures. The foam structures, however, have not been represented. This is a much more complex task. If a unit cell is to represent a foam structure accurately it has to be an open structure with obvious struts, no direct path from the top of the structure to the bottom of the structure, and it must be able to have symmetry applied to it successfully. Unfortunately it is not possible to model large areas of the foam material due to the enormous number of calculations

needed, therefore two unit cells were chosen, namely the "hex" model and an "Ashby" model discussed below.

5.3 Hexagonal Model

The idea of the "hex" model was to represent the reticulated foam structure as a three-dimensional porous hexagonal faced structure. An example of this can be seen in the real foam structures in Figure 3-21. In this way the wall thickness is varied which changes the total porosity of the model.

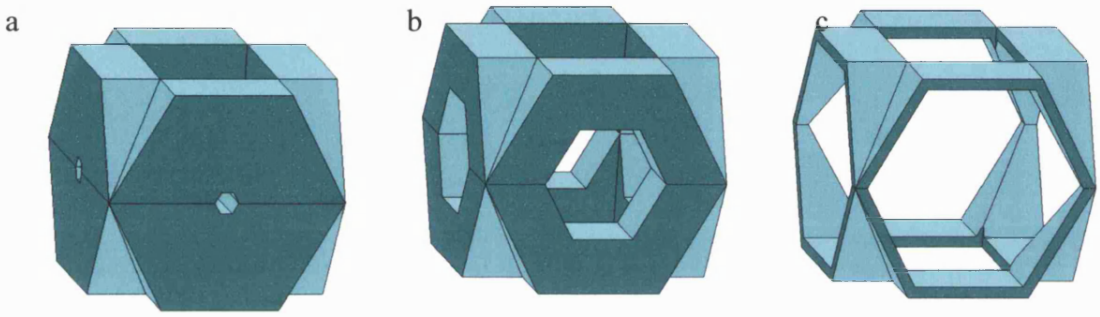

Figure 5-17: Example of the "hexagonal" modelling, a) low porosity, 30%, b) medium porosity, 55% and c) high porosity, 90%.

Examples of low (30%), medium (55%) and high porosity (90%) can be seen in Figure 5-17. Due to the way that the model is constructed it is impossible to achieve a full range of relative densities. As the strut thickness was varied between thin and thick, the actual relative density of the model varied between 10% and 70%.

This model was solved for both PZT-porosity unit cell and a PZT - polymer composite, where the void in Figure 5-17 is filled with a polymer having a Young's modulus of 6Gpa and Poisson's ratio of 0.3.

5.3.1 Hexagonal Model - PZT Only Results

The chart in Figure 5-18 shows the values of d_{33} with respect to relative density for the hexagonal model using a single phase PZT porosity model.

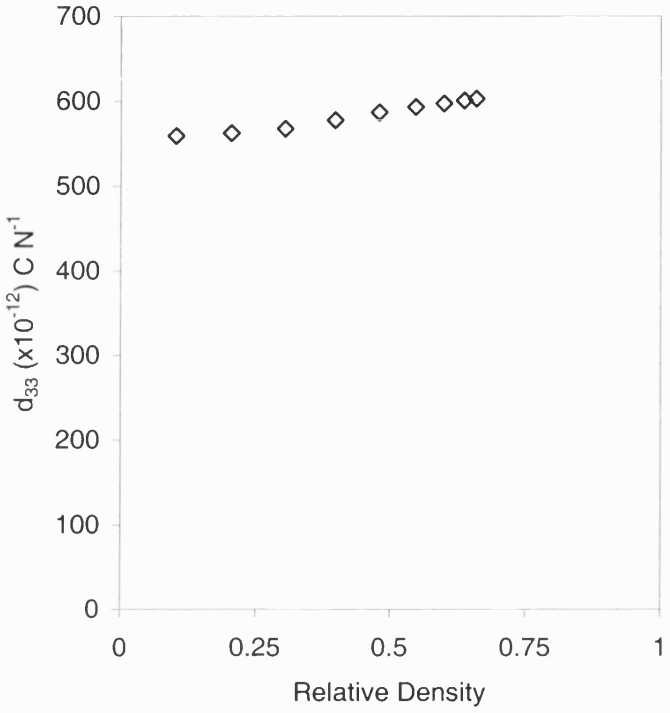

Figure 5-18: Chart showing d_{33} against relative density for the hexagonal model PZT-porosity.

It can be seen that all the values are approximately 600 x10^{-12} C N^{-1}, but there is a reduction in d_{33} as porosity is increased.

The values increase with increasing relative density. This is different to all the previously modelled unit cells due to the absence of a direct path from the top of the model to the bottom of the model. Therefore, as the model is made more porous there is material being removed which contributes to the d_{33} and the path between the electrodes is increasing in tortuosity.

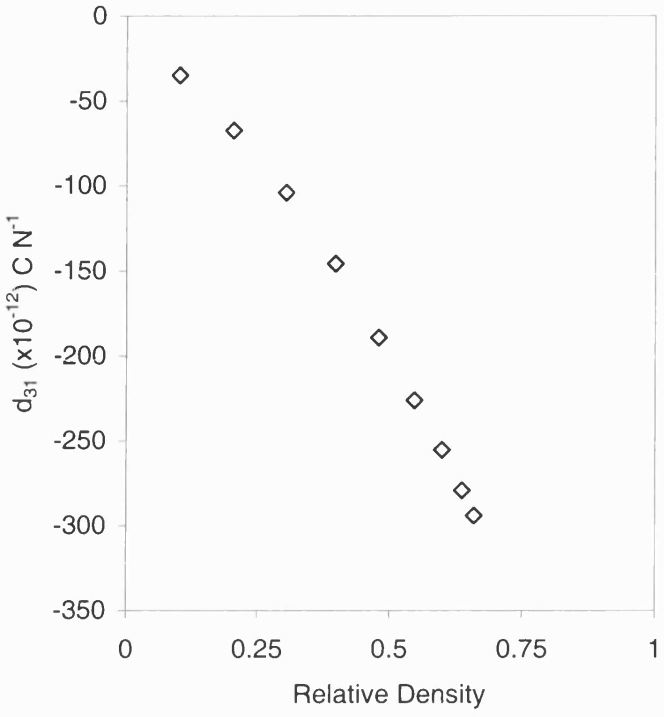

Figure 5-19: Chart showing d_{31} against relative density for the hexagonal model PZT-porosity.

Shown in Figure 5-19 is the chart for the values of d_{31} with respect to relative density for the hexagonal model using a single phase, PZT - porosity, model.

It can be seen that the absolute value of d_{31} increases sharply with increasing relative density. The trend shows a curve with a higher gradient at high relative density than at lower relative density. This is due to the way that the porosity changes in the model. The most direct connection between the top and bottom of the model (and thus the highest electric field) is close to the inner pore (Figure 5-20).

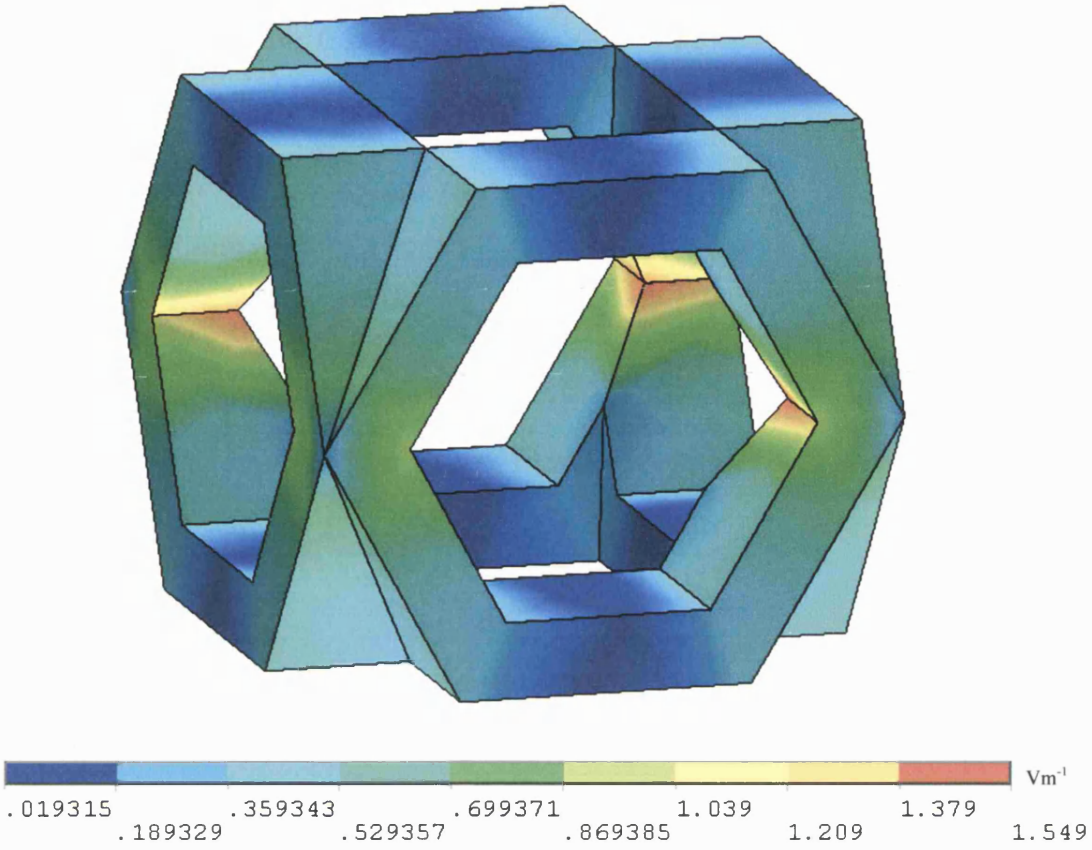

Figure 5-20: FE model showing areas of high electric field (red). The inside of pore walls are areas of highest electric field.

As the inner pore region is exposed to high electric field, it is active in contributing to the d_{33} and d_{31} response. However, as the porosity increases, it is this area that is removed from the model. As the porosity volume fraction increases there is a less direct route between the two electrodes at the top and bottom of the model. This reduces the electric field intensity and thus d_{31}. As the model becomes more porous more material is removed, but this material is less active (experiences a lower electric field) and so produces a smaller change in d_{31} as relative density decreases.

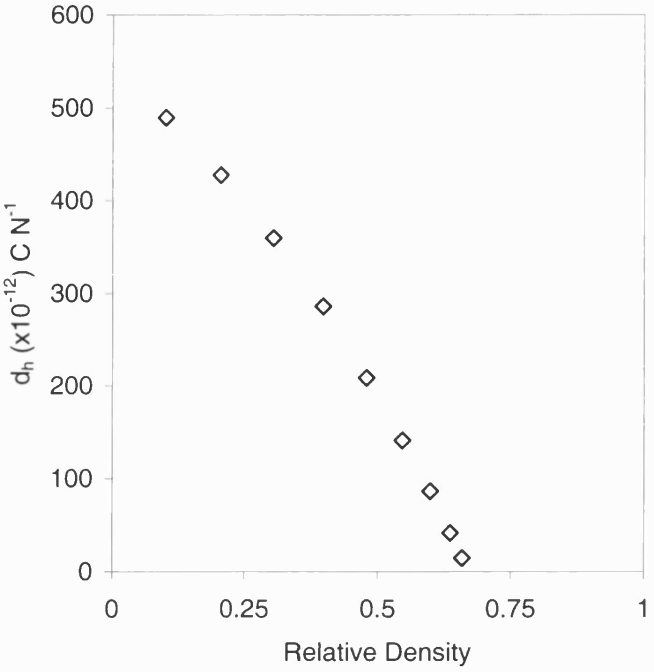

Figure 5-21: Chart showing d_h against relative density for the hexagonal model PZT-air.

The chart shown in Figure 5-21 is the calculation of the values of d_h for the hexagonal model using a single, PZT – porosity phase. As there are only small changes in the values of d_{33} and there are large changes in the values of d_{31} the chart showing d_h is similar to that of d_{31}.

The value of d_h increases with a reduction in relative density. The value of d_h decreases sharply as porosity is introduced into the model. The gradient of the curve is higher at high relative densities than at low values. This is due to the effect of porosity on d_{31}, as explained previously.

5.3.2 Hexagonal Model – PZT Polymer Composite

The model shown above was also taken into consideration with a polymer phase filling the pore up to the cube boundary, rather than just a void. The modelling was repeated with a polymer of 6GPa Young's modulus and Poisson's Ratio of 0.3.

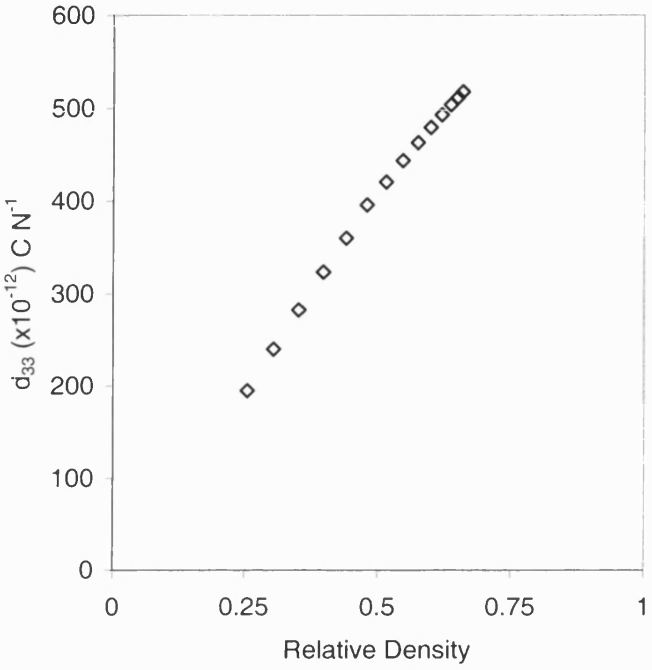

Figure 5-22: Chart showing d_{33} against relative density for the hexagonal model PZT-polymer.

The chart in Figure 5-22 shows the values of d_{33} for the hexagonal model with a two-phase PZT - polymer system.

It can be seen that the values of d_{33} increase with increasing density. The chart shows a slight curve, which is due to the removal of high field regions of d_{33} active material making a more tortuous path between the top and bottom of the model.

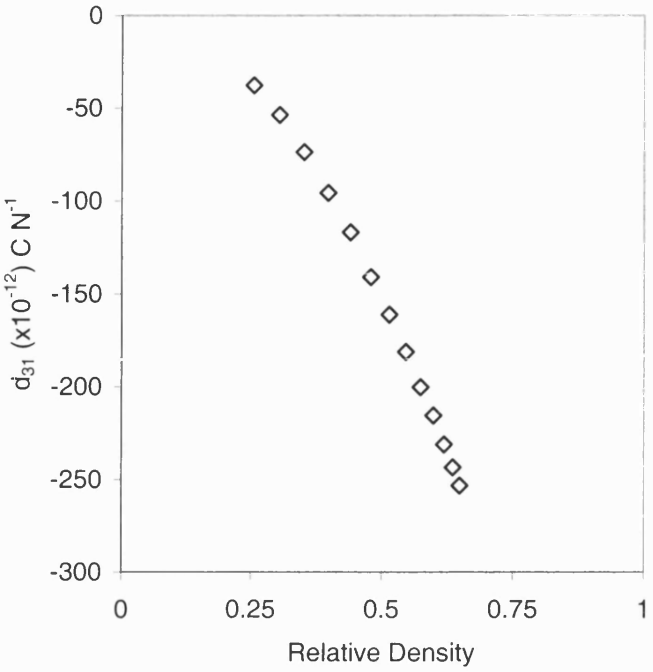

Figure 5-23: Chart showing d_{31} against relative density for the hexagonal model PZT-polymer

Figure 5-23 shows a chart with the variation of d_{31} with respect to relative density for the two-phase hexagonal model.

It can be seen that the absolute value of d_{31} increases sharply with increasing density. This is similar to the single phase model but the presence of the polymer is leading to a slightly higher rapid decrease in $-d_{31}$, due to a physical restraint on the ceramic which reduces contraction in the x and y directions. This reduction is due to the lack of strain from the inactive polymeric phase.

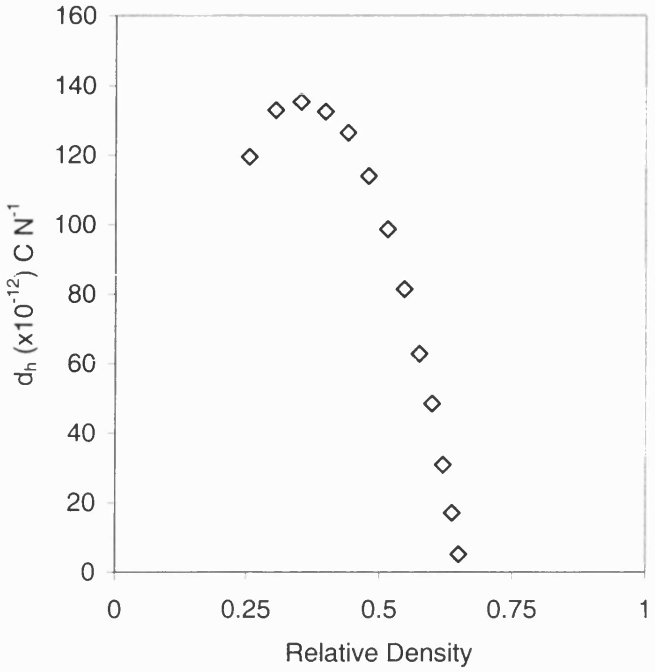

Figure 5-24: Chart showing d_h against relative density for the hexagonal model PZT-polymer

The chart in Figure 5-24 shows the calculated values of d_h with respect to relative density for the hexagonal model using a two phase, PZT - polymer model.

A very well defined peak can be seen in the chart. This gives a maximum value of d_h at around 30% relative density. The maximum value is $140x10^{-12}$ CN^{-1}, which is approximately three times greater than the value for dense PZT. The value of d_h drops off sharply as the relative density of the sample is changed in either direction from this maximum which is situated at a lower relative density than the original square pore model.

5.4 Ashby Model

The Ashby model, as the name suggests, is based on a unit cell of a "typical open cell foam structure"[16] and has been used to develop mathematical expressions for the mechanical properties of foams as a function of porosity. The aim here is to use a similar structure to examine the effect of porosity on d_{33}, d_{31} and d_h. Modifications have been made to enable symmetry to be applied and reduce the processing time. Examples of low (60%), medium (75%) and high porosity (95%) Ashby structures can be seen in Figure 5-25.

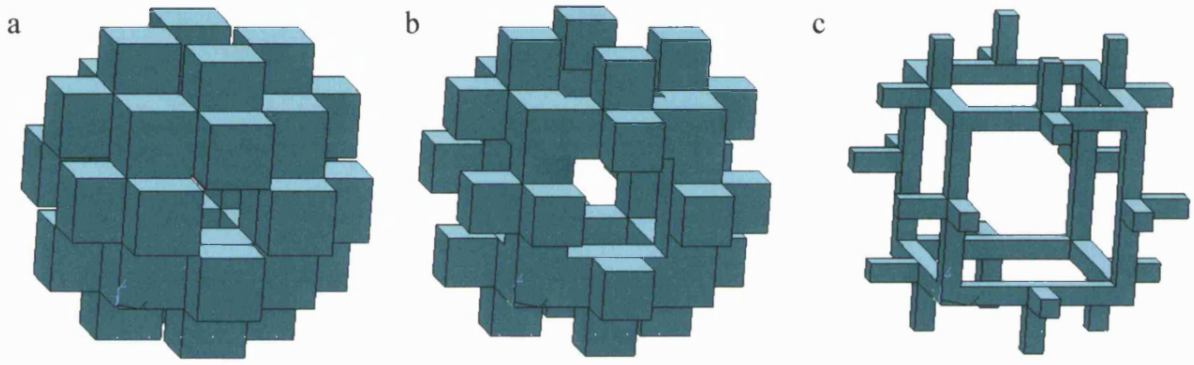

Figure 5-25: Example of the Ashby modelling, a) low porosity, 60%, b) high porosity, 75%, and c) very high porosity, 90%.

This model was also designed to avoid a direct path from the top to the bottom of the model as with the previous models (1D, 3D BurPS and hexagonal).

Due to the geometry and meshing restrictions of the model, only a limited range of porosities was modelled. These range from 5% relative density up to approximately 40% relative density.

5.4.1 Ashby Model – PZT Only Results

The chart shown in Figure 5-26 shows the values for d_{33} for the Ashby model using a single phase PZT – porosity structure.

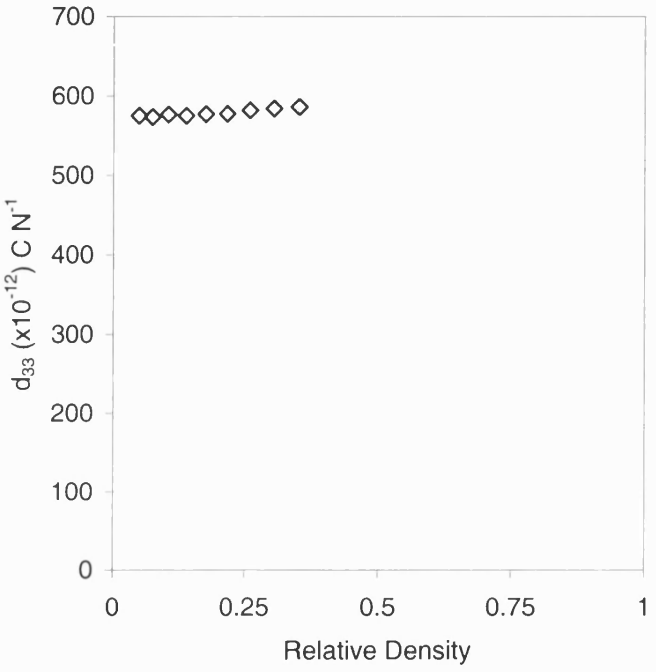

Figure 5-26: Chart showing d_{33} against relative density for the Ashby model PZT-porosity.

It can be seen that the values increase slightly with increasing relative density. This behaviour is similar to the hexagonal model for a single PZT phase and is explained in the same way. Removal of volumes increases the path length from the top to the bottom of the electrodes and removes d_{33} active volumes subjected to high electric fields, thus reducing d_{33} slightly.

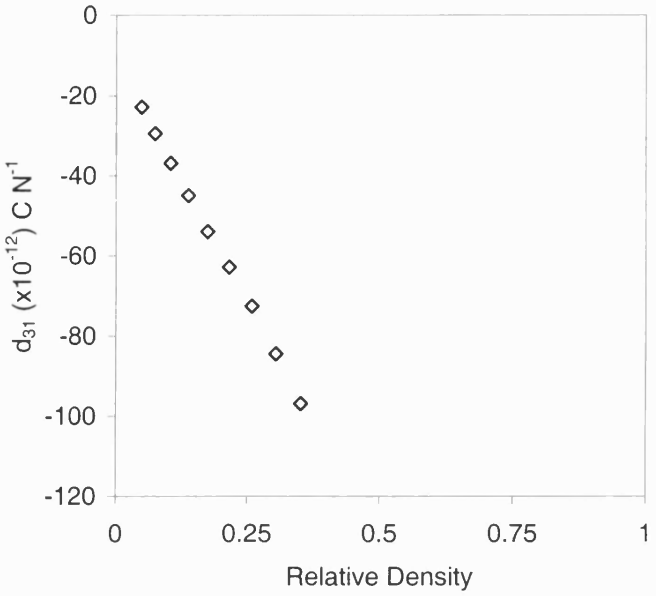

Figure 5-27: Chart showing d_{31} against relative density for the Ashby model PZT-air.

The chart shown in Figure 5-27 shows the values of d_{31} with respect to relative density for the Ashby model with a single PZT phase.

It can be seen that the absolute value for d_{31} increases rapidly with relative density. This is due to the same mechanism as the d_{33} results for the single-phase hexagonal model. The change in this model is more dramatic due to the block like nature of the model. The field path from top to bottom is indirect and so field concentrations build up on the inner side of the model. These volumes are the first to be removed as the volume fraction of porosity increases.

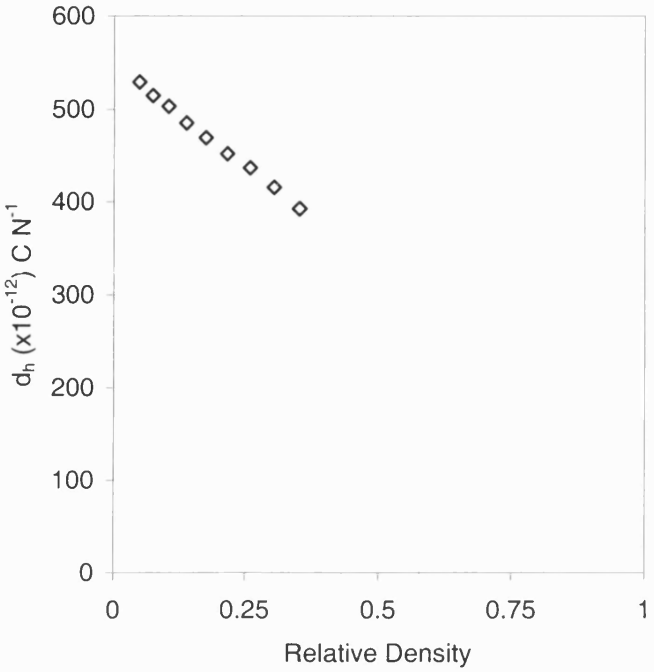

Figure 5-28: Chart showing d_h against relative density for the Ashby model PZT-air.

The chart in Figure 5-28 shows the calculated values for d_h with respect to relative density for the Ashby model with a single PZT phase.

It can be seen that d_h increases with decreasing relative density in a linear fashion. As the change in the values of d_{33} is small compared to that of the d_{31} results, the chart is similar to that shown for the d_{31} values.

5.4.2 Ashby Model – PZT Polymer Composite Results

The Ashby model above was also taken into consideration with a polymer phase filling the pores up to the cube boundary. The modelling was repeated with a polymer of 6GPa Young's modulus and Poisson's ratio of 0.3.

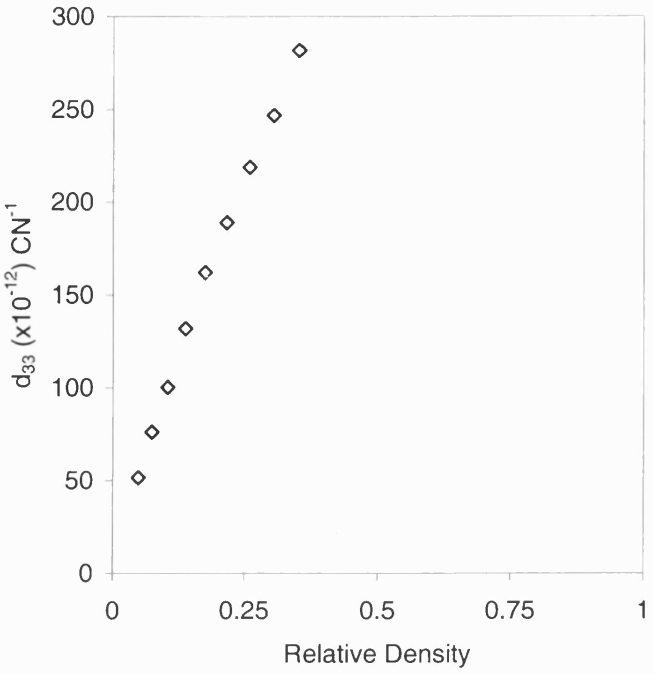

Figure 5-29: Chart showing d_{33} against relative density for the Ashby model PZT-polymer composite.

The chart shown in Figure 5-29 shows the variation of d_{33} with respect to relative density for the Ashby model using a two phase PZT – polymer composite.

The chart shows the very high variation of d_{33} with relative density. This steep gradient is due to the polymer phase not straining with the ceramic structure, thus the average displacement of the top surface is greatly reduced. This is because a high proportion of the top surface area of the model is polymeric and only the struts are PZT, see Figure 5-25c.

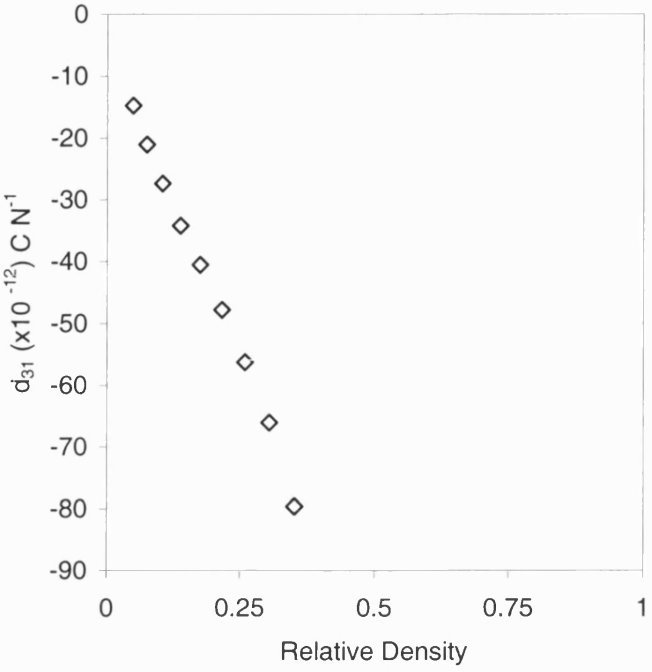

Figure 5-30: Chart showing d_{31} against relative density for the Ashby model PZT-polymer composite.

Figure 5-30 shows the variation in d_{31} with respect to relative density for the Ashby model using a two phase PZT – polymer composite.

It can be seen that the absolute value of d_{31} increases with increasing density. The magnitude of d_{31} with a polymer phase present in the model is lower than that with no polymer phase present. This is due to the polymer restraining the contraction of the ceramic in the x (1) and y (2) directions.

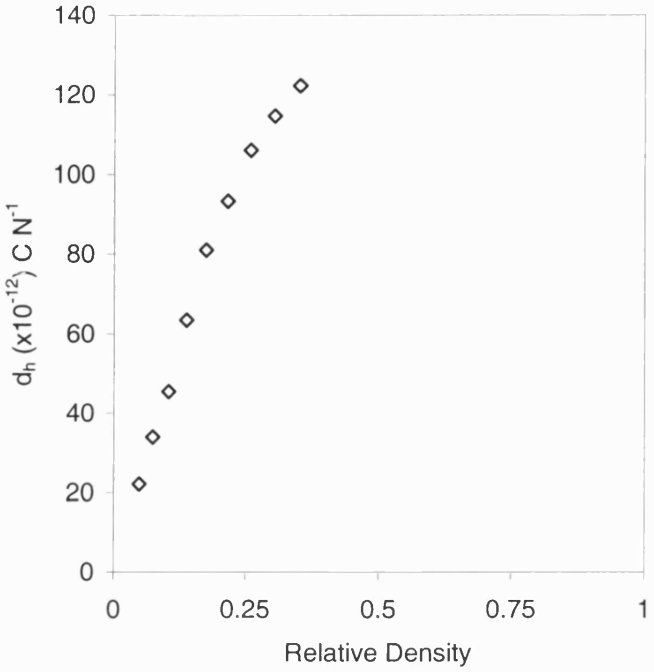

Figure 5-31: Chart showing d_h against relative density for the Ashby model PZT-polymer composite.

The chart shown in Figure 5-31 presents the calculated values of d_h for the Ashby model using a two phase PZT – polymer composite.

Unfortunately due to the restriction of densities available from this unit cell, a wide enough range of densities could not be modelled in order to be able to see a maximum in the value of d_h. However a value of 125 $x10^{-12}$ C N^{-1} was obtained for a 40% ceramic model, which is comparable to the maxima of the previous models.

A range of model unit cells have been examined in an attempt to model more closely the types of microstructure observed in manufactured 3-3 piezocomposites. The work has shown that the rate at which d_{33}, d_{31} and d_h change with porosity is highly dependent on pore type and shape and whether discrete or continuous pores are present.

It was hoped that the refinement of finite element modelling would more closely resemble the experimental results of the PZT porosity materials. Unfortunately these results differ little from the original square pore model. For a more accurate model, multiple pores must be modelled. However the work does show that the figures of merit are sensitive to pore geometry and the presence of discrete or interconnected pores, as observed in the range of

materials manufactured. The modelling of large multiple pore structures requires great processing power and computer resources that were not available during the term of this research.

The modelling and experimental work will now be discussed and final conclusions reported.

6 Discussions and Conclusions

6.1 Manufacturing Constraints

There is no manufacturing method that has the ability to easily produce a complete range of composites in the full range of relative densities. Five methods of manufacture were used, four BurPS based methods (SR, CS, PMMA, PEO) and a reticulated foam method.

It can be seen in Figure 6-1 that there is a large overlap in the range of densities that can be produced by the various BurPS methods.

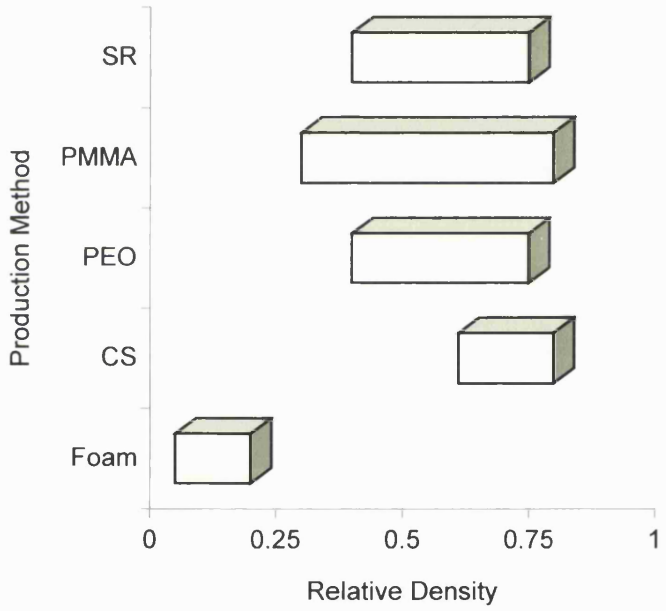

Figure 6-1: Chart showing the range of densities each manufacturing technique can produce.

If high density ceramics (>75%) are required the most effective method of producing them is the BurPS method using CS (corn starch). The cornflour also acts as a pressing and sintering aid. Increasing the amount of cornflour in each sample leads to a high shrinkage and consistently to high density samples. However, cornflour has a small particle size and produces small and uniformly distributed pores in the ceramic phase. To create a porous

ceramic using PMMA, for example, leads to regions of high local porosity and regions with high local density.

Using the BurPS method with PMMA produces the widest range of densities, from 30% dense to approximately 80% dense. Unfortunately pressing ceramics with PMMA spheres creates cracks in the ceramic body. During pressing the PMMA compresses and on release of pressure expands to cause cracking. The PMMA BurPS technique produces round, well defined pores of around 100μm in size.

The PEO, whilst producing a similar pore size to the PMMA did not produce cracks in the composite. This inclusion material also leads to non-spherical, poorly defined pores. An advantage of the pores not being spherical was the fact that there was more interconnectivity at a given porosity than PMMA.

The BurPS method using SR (self-raising flour) produces small well distributed pores in a respectable range of densities (40 – 75% dense). Due to the small pore size, the mechanical properties were good and the surfaces were smooth which aided electrode attachment.

6.2 Properties of 3-3 Composites

In all of the results presented there appears to be an increase in the d_h, g_h and $d_h.g_h$ figures of merit for porous samples or PZT polymer composites over the dense material equivalent. A discussion and explanation of the increase of these values will be provided in the following sections.

6.2.1 Explanation of Increase in Hydrostatic Strain Coefficient (d_h)

The d coefficients have been shown to vary significantly with relative density. In the basic and further enhanced modelling of a single phase system (PZT-porosity) it was observed that the value of d_{33} was often independent of relative density. In the practical results and the modelling of a two phase PZT polymer composite (both basic and advanced modelling) a large variation of d_{33} was seen with respect to relative density. This is reflected in the experimental values reported for d_h. Figure 6-2 shows the values for d_h with respect to relative density for the single phase PZT-porosity model and the two phase PZT-polymer model.

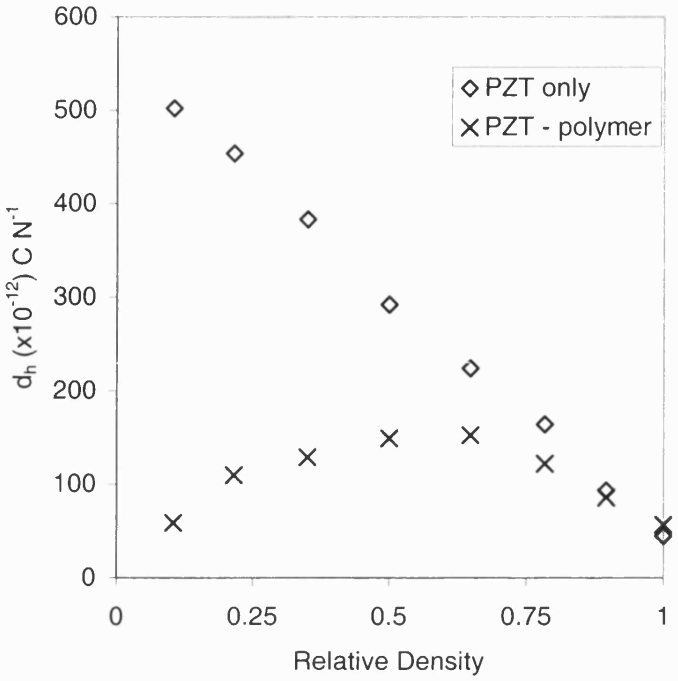

Figure 6-2: Comparison of d_h against relative density for a) PZT porosity model and b) PZT polymer composite model.

This discrepancy can be explained with reference to the models used to calculate the values of d_{33}. Considering the first case of the single-phase PZT-porosity model.

6.2.1.1 Explanation of Basic Modelling

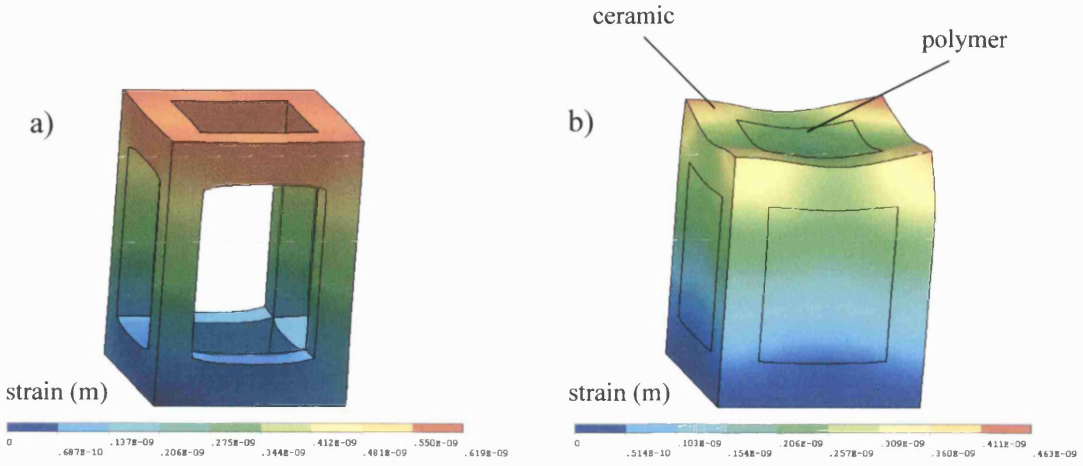

Figure 6-3: Comparison of the two types of models, a) PZT porosity and b) PZT - polymer composite.

The models shown in Figure 6-3 show the PZT only model and the PZT-polymer composite. It can be seen that the upper surface displacement of the polymer phase in Figure 6-3b is not as high as the ceramic displacement as the polymer is an inactive phase.

For the PZT – polymer model (Figure 6-3b) the displacement (strain) of the solved model was calculated by averaging the displacements of the nodes at the top of the model. For the PZT only model (Figure 6-3a) there is only a single-phase present, all the nodes are on the PZT structure and thus only these nodes were averaged.

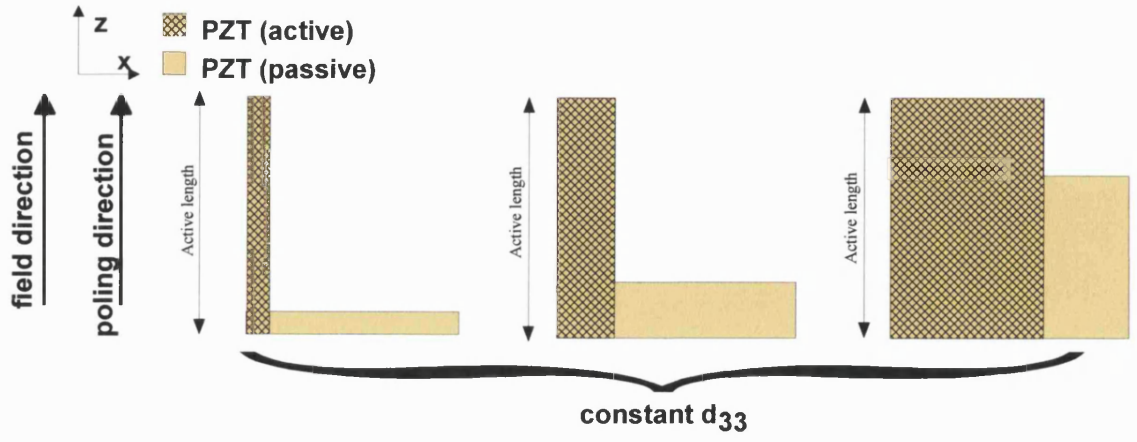

Figure 6-4: Schematic of how d_{33} varies with porosity.

In this basic cubic model shown in Figure 6-4 there is a direct path from the top electrode to the bottom electrode. This assures a high electric field in the areas responsible for producing a high translation in the z direction. The areas shown in the figure do not change in length with changing porosity, which assures a constantly high value of d_{33} for the PZT porosity model regardless of relative density.

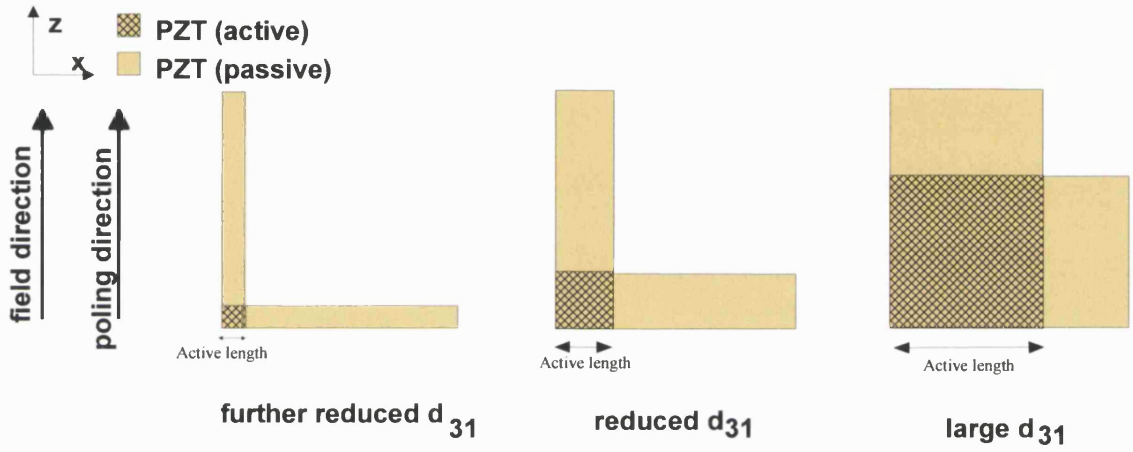

Figure 6-5: Schematic of how d_{31} varies with porosity.

If the same schematic is shown for the areas responsible for the production of d_{31}, Figure 6-5, it can be seen that the active length responsible for producing the d_{31} contraction decreases with relative density. This change in length is caused by the pore causing the electric field in the areas adjacent (above and below) the pore to be reduced (Figure 6-6a). If the active length for d_{31} is reduced then the overall value of the contraction in the x direction will be reduced.

This effect has been confirmed by analysis of the modelling results. The reduction in the electric field is clearly visible in the regions adjacent (above and below) to the pore and the active regions can be seen in both the high and low porosity models, Figure 6-6.

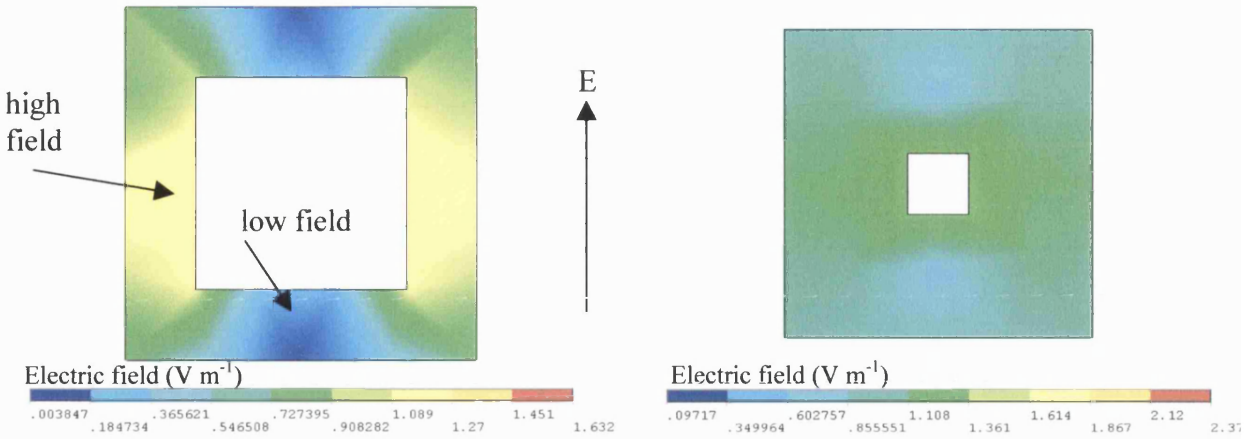

Figure 6-6: FE modelling showing high electric field in areas indicated by hashed areas in Figure 6-5.

This effect leads the value of d_{33} to be effectively independent of relative density. The absolute value of d_{31}, however, reduces as porosity increases for the reasons detailed above. This leads the value of d_h to increase almost linearly with porosity with d_h tending towards the value of d_{33} as d_{31} approaches zero.

The modelling was repeated with a polymeric phase present, which had purely mechanical properties. Assumptions were made that there was a perfect bond between the polymer and the ceramic phases. It was shown that the values of d_{33} varied significantly with porosity and polymer stiffness. In this case the polymer will slightly restrict the movement of the ceramic but, more importantly, it will only extend in the z direction in the region where it is directly attached to the ceramic phase.

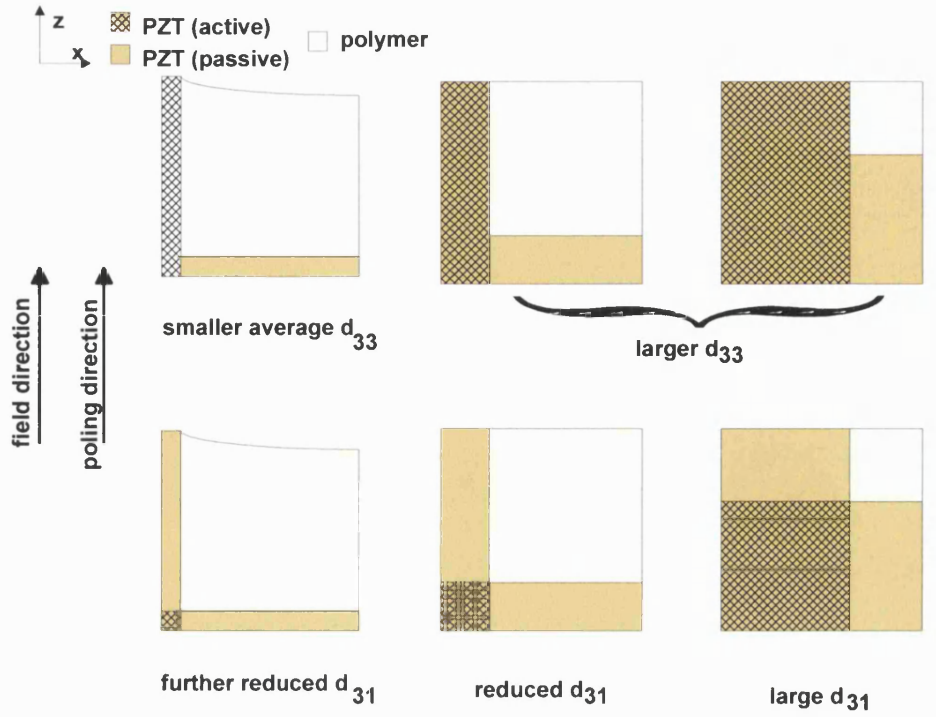

Figure 6-7: Schematic of how d_{33} and d_{31} vary with porosity in a two-phase model.

At high polymer volume fractions the displacement of the surface will be uneven. Areas of displacement under an electric field are the piezoelectric ceramic phase and the surrounding polymer. Non-displaced areas are areas of polymer far from the ceramic. Since the d values are calculated from the average displacement of the surfaces the polymeric phase decreases the value of d_{33}. This decrease is more prominent with a stiffer polymer as the strain developed in the polymer decreases with increasing polymer stiffness. The d_{31} coefficient is less sensitive to polymer stiffness as increasing the stiffness merely results in more load being experienced the previously non-active region at the expense of the load carried by the active region.

6.2.1.2 Experimental Results

It can be seen from the results in Chapter 3 that the values of the d coefficient vary with ceramic volume fraction. The following set of figures combine and present experimental data for all the manufactured materials in order to make a direct comparison.

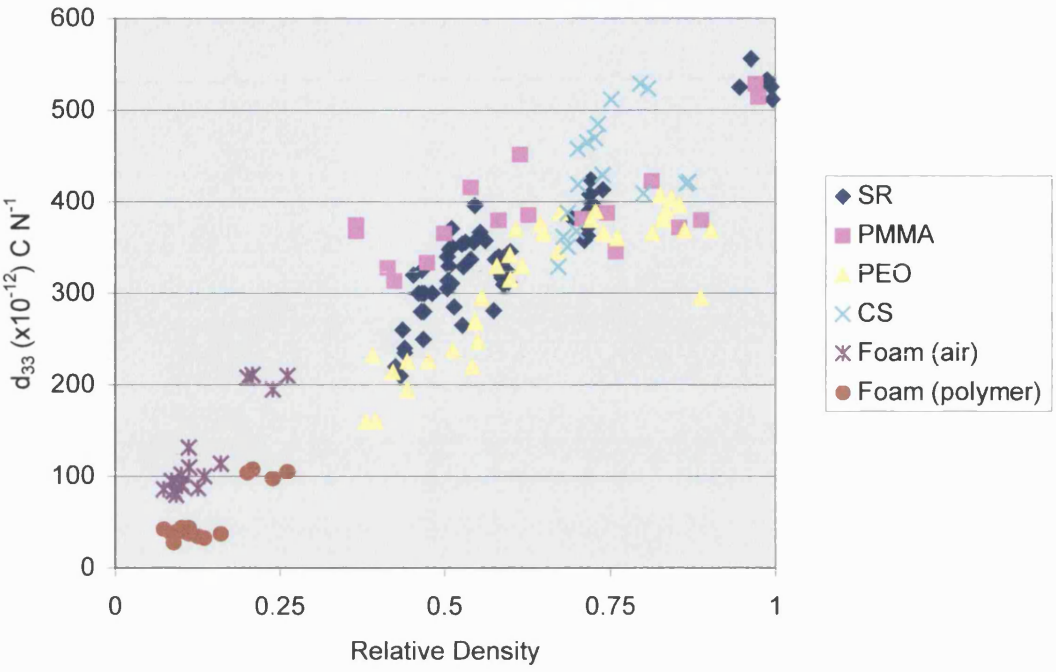

Figure 6-8: Results of d_{33} vs relative density for all samples.

The chart in Figure 6-8 shows the values of d_{33} against relative density for all samples made by the BurPS and foam methods. The different inclusion materials, inclusion sizes are represented by different colours. The general trend of the results is an increase in the value of d_{33} with increasing relative density. The trend shows a higher dependence of d_{33} on porosity at low values of relative density and lower dependence at high relative density.

It can also be seen from the chart that the four different BurPS production methods produce ranges of d_{33} that are in visibly different bands to each other. The PEO samples (polyethylene oxide) can be seen to have a consistently lower value of d_{33} for a given relative density compared to other types of BurPS composite. PMMA can be seen to have the highest value of d_{33} for a given relative density. This is surprising as the PMMA samples produced had many cracks in the microstructure, which were due to pressing a soft ceramic powder with a hard plastic inclusion.

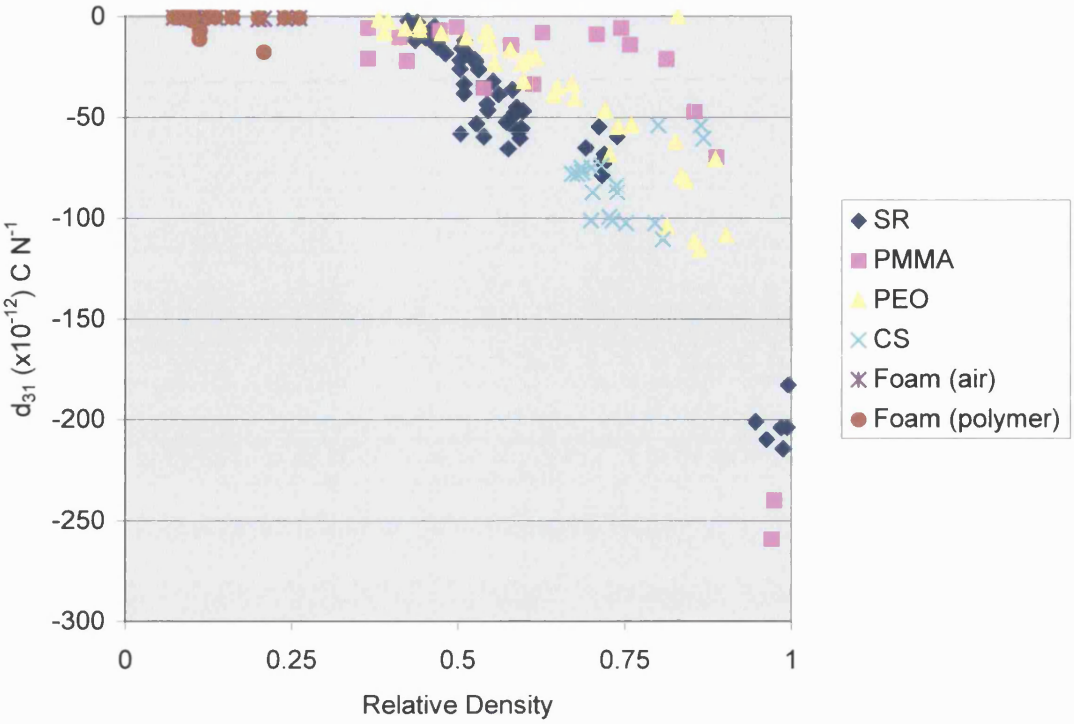

Figure 6-9: Results of d_{31} vs. relative density for all samples.

The chart in Figure 6-9 shows the values of d_{31} of all the BurPS samples. Again the general trend can be clearly seen that the absolute value of d_{31} increases with relative density. This chart also shows the four different BurPS inclusion materials having different values of d_{31} although the density ranges are similar.

The highest absolute value of d_{31} for a given relative density is observed with the SR samples at low density and with the CS samples at high density. A high value of d_{31} is undesirable for high d_h values. The samples with the lowest value of d_{31} for a given range of densities are the samples made with PMMA. The low values of d_{31} are believed to originate from the large amounts of cracking in the samples.

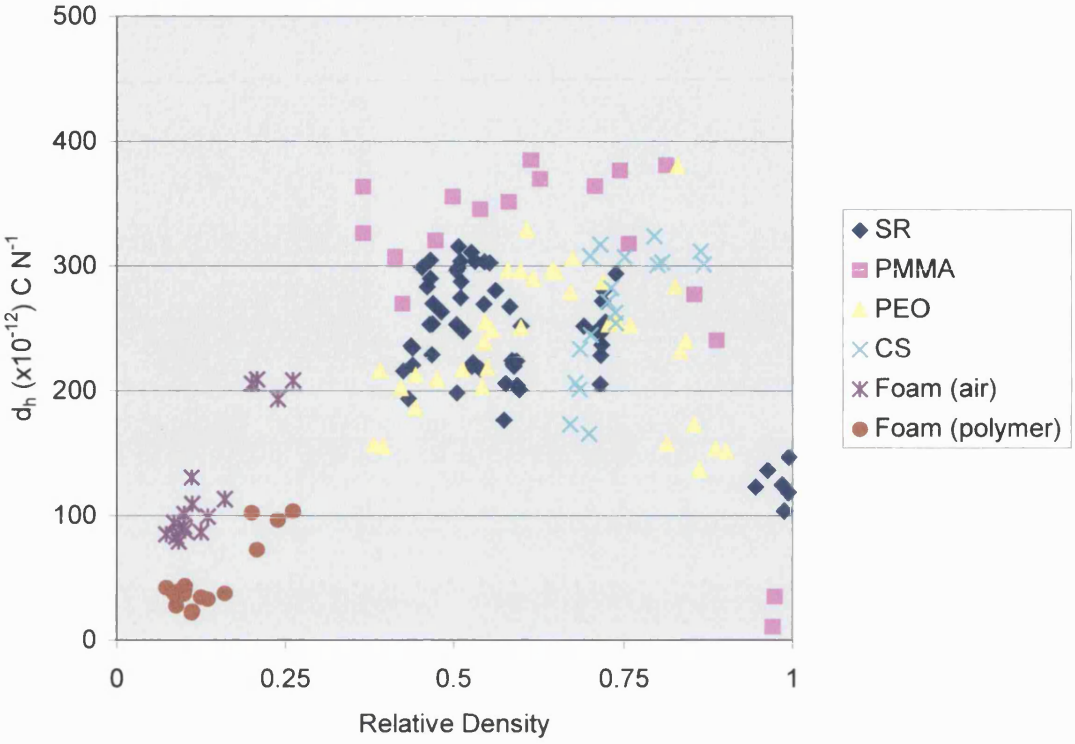

Figure 6-10: Chart showing d_h versus. Relative density for all results.

The chart in Figure 6-10 shows the variation of d_h with respect to relative density for all the BurPS and foam results. This chart is a combination of the charts in Figure 6-8 and Figure 6-9, as $d_h=d_{33}+2d_{31}$.

The value of d_h is important in choosing a material for an active piezoelectric device. A high value of d_h will result in a high strain per unit applied electrical field for a device. Such a property is desirable for an application such as a hydrostatic piezoelectric driver (point source).

A trend can be seen within each series of results, a maximum is present for each set, the position of the maximum changes depending on the inclusion material used to manufacture the composites. The highest values of d_h are obtained using PMMA as the inclusion material. At first thought this is surprising since the PMMA samples showed extensive cracking in the composites normal to the poling direction.

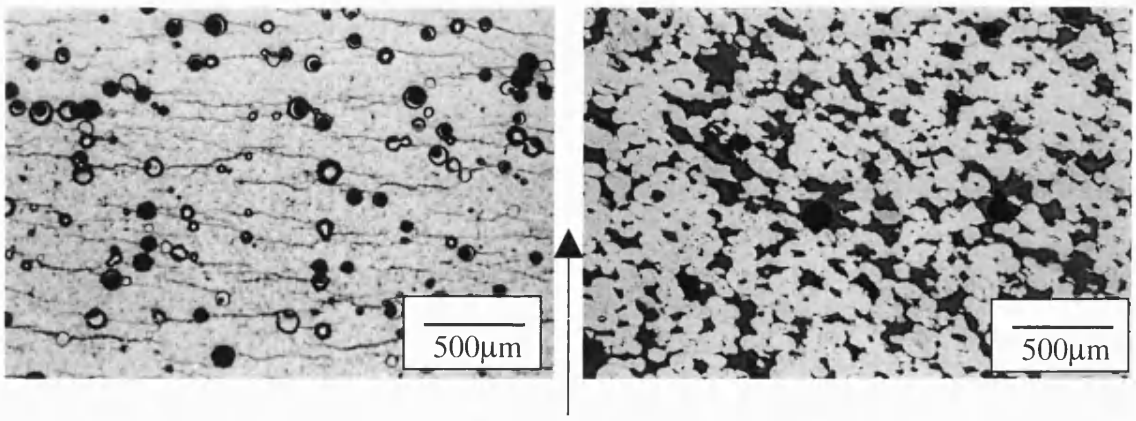

Figure 6-11: Optical micrograph showing a) cracking of samples produced using PMMA spheres and b) no cracks present in structures made with PEO. The arrow indicates pressing, poling and electric field direction during testing.

These cracks are caused by the pressing of the powder and inclusion material during manufacture. A typical sample made by PMMA inclusion is shown in Figure 6-11a. The cracks can be seen clearly in the micrograph. The arrow in the figure indicates the direction of the applied pressure during green body manufacture, the poling direction and the direction of applied electric field during testing. The high d_{33} of the PMMA samples may be due to the force applied perpendicular to the cracks during testing, which may act to close the cracks and reduce the effective porosity. During d_{31} testing the force is applied parallel to the cracks, which may lead to crack opening and a further reduction in d_{31}.

The foam based materials, while resulting in a modest value of d_h (approx. 100 – 200pCN^{-1}), still show a higher value than for dense PZT-5H (approx. 44pCN^{-1}). These foam materials have many other material property advantages, such as low density in their favour.

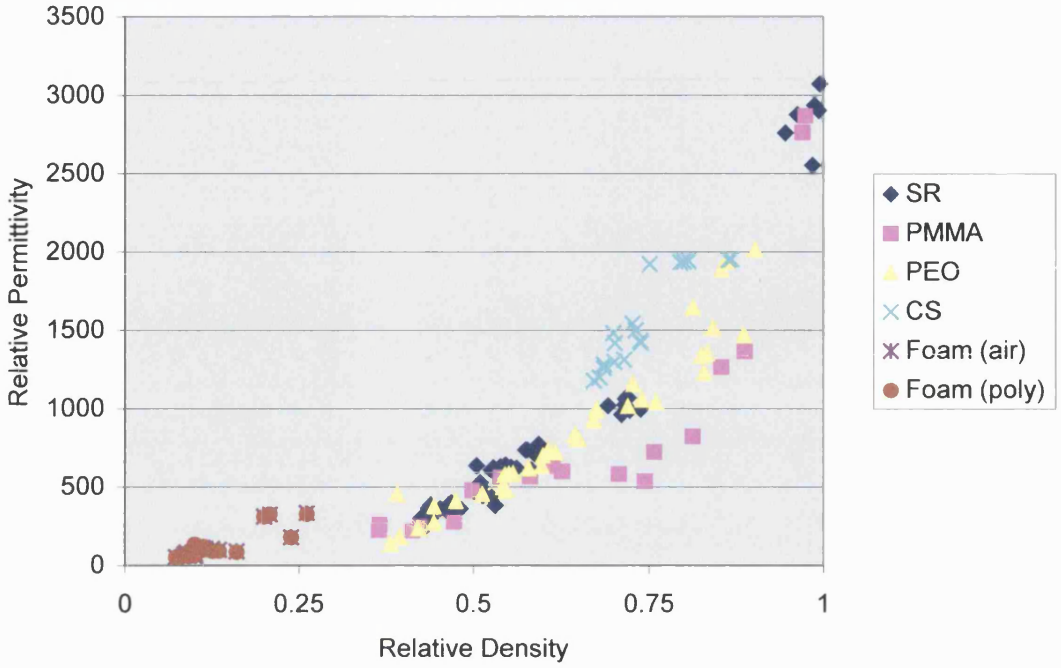

Figure 6-12: Chart showing relative permittivity vs. relative density for all results.

The chart in Figure 6-12 shows the values of relative permittivity against relative density for all the values of the samples made by BurPS and foam method. The graphs illustrate a number of interesting points. The results for the samples made with PEO and SR have similar values as a function of relative density. The samples made with PMMA however have lower values of permittivity than expected. This can be explained by the cracking shown in Figure 6-11a reducing the bulk of material that has an uninterrupted path from the top to the bottom of the sample.

The results obtained from the CS samples appear to be slightly higher than those of the PEO and SF. This is because the CS samples had few very small pores and a large amount of the bulk material is left continuous. This increases the permittivity for a given relative density compared to the PEO and SR, which have larger, better-distributed pores.

The foam-based materials have the lowest permittivity, which is to be expected as they have low relative density, ranging from 0.1 to 0.3. These values for the permittivity are similar irrespective of the passive phase (air or polymer) present. These low values of permittivity give rise to large values of g_h.

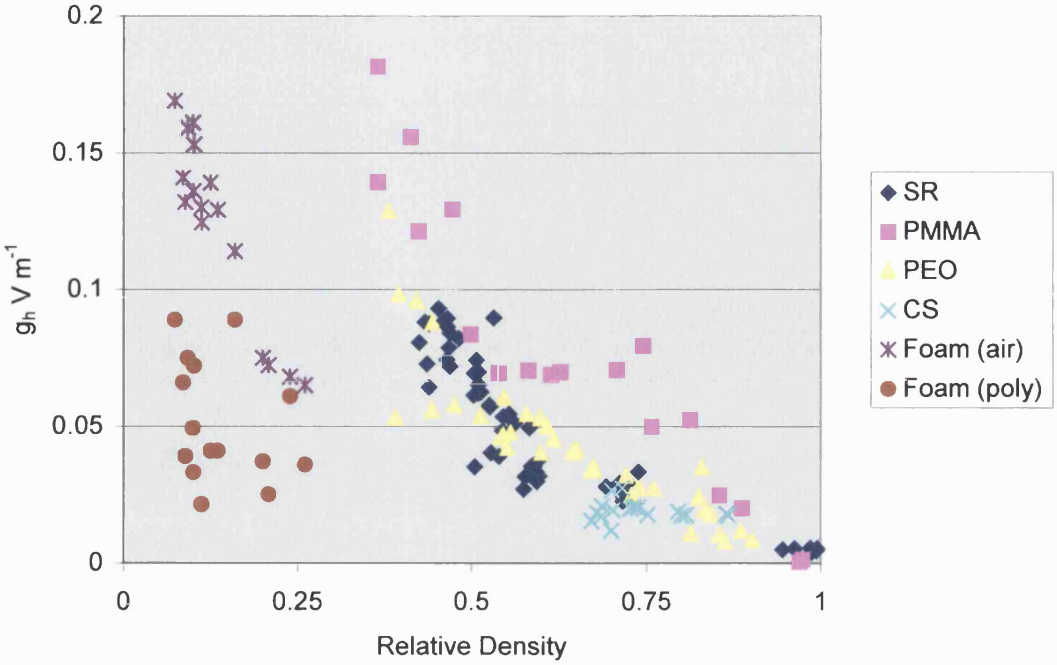

Figure 6-13: Chart showing g_h versus. Relative density for all results.

The chart in Figure 6-13 shows the values of g_h for all the samples made by the BurPS method. This chart is calculated from the values of d_h and permittivity.

The value of g_h is important when choosing a material for a passive piezoelectric device. A high value of g_h will result in a high electric field per unit hydrostatic stress applied. This figure of merit is used for sensing devices, such as hydrophones.

It can be seen that the PMMA samples have an increased value of g_h over PEO and SR samples which arises from their suppressed values of ε_{33} and d_{31} caused by the cracking of samples during manufacture.

It can also be seen that the CS samples have a lower value of g_h than the PEO and SR samples. Again this is due to the high permittivity values of the CS samples.

For the optimal value of g_h a BurPS sample manufactured using PMMA with low relative density would be desirable. However the presence of cracks may be undesirable in terms of mechanical properties, reliability and sensitivity of properties to water depth.

An alternative to the PMMA samples would be the foam-based materials. Unfortunately the PZT-porosity foam based materials are difficult to use, however the PZT-polymer foam based materials, while having a lower value of g_h are robust and well suited to applications such as hydrophones.

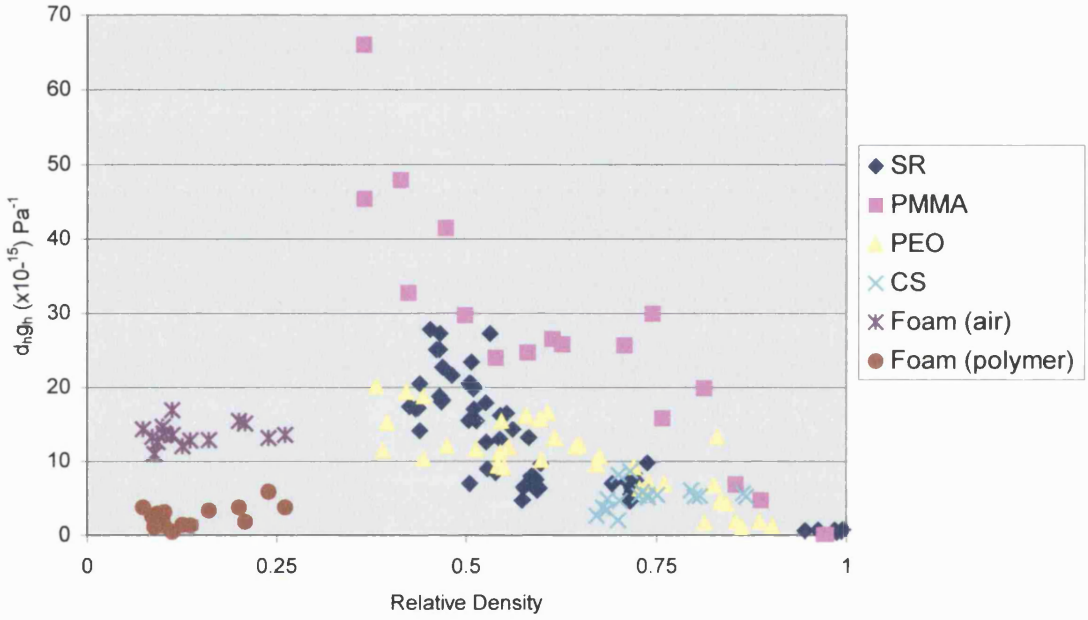

Figure 6-14: Graph showing the hydrostatic figure of merit, $d_h.gh$, for all samples with respect to relative density.

The graph in Figure 6-14 shows the hydrostatic figure of merit $d_h.g_h$ for all samples with respect to relative density. This figure of merit is used for devices, which are used in both passive and active modes. A peak in $d_h.g_h$ can clearly be seen at approximately 30% relative density and the highest values correspond to the PMMA based BurPS samples. This maximum value of $d_h.g_h$ is due to the high values of g_h shown by the PMMA based samples. This was caused by the low permittivity measured, which was in turn a result of extensive cracking in the samples. This extensive cracking may be undesirable in real life conditions, in this case the BurPS samples based on SR material are the most applicable.

6.3 Influence of Unit Cell Geometry on Piezoelectric Properties

It has been discussed that the production of PZT-porosity samples made with only a single phase show the same dependence of d values with respect to relative density to the modelling of the two-phase PZT-polymer composite. For this reason advanced modelling was undertaken to try to more accurately model the single phase PZT-porous samples.

The direct path between electrodes of the simple, square pore model was thought to be responsible for the anomalous results, d_{33} remaining constant as a function of porosity. Removing the direct path by modelling a complete microstructure was not possible, as this would consume vast amounts of computing power, which was not available for this study. Instead the direct path was removed by producing more complex unit cells, which are more representative of the real microstructures. The path between the electrodes was made more tortuous within a single unit cell in order to mimic that of the manufactured samples.

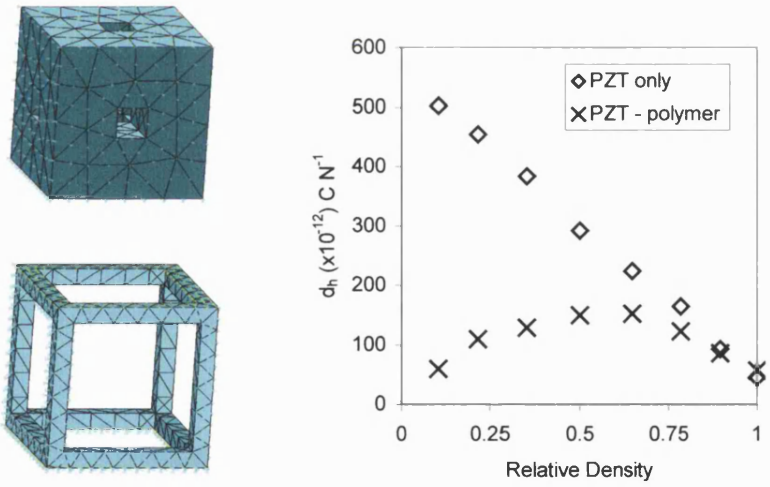

Figure 6-15: Charts showing d_h against relative density for PZT porosity and PZT-polymer models for the square pore model.

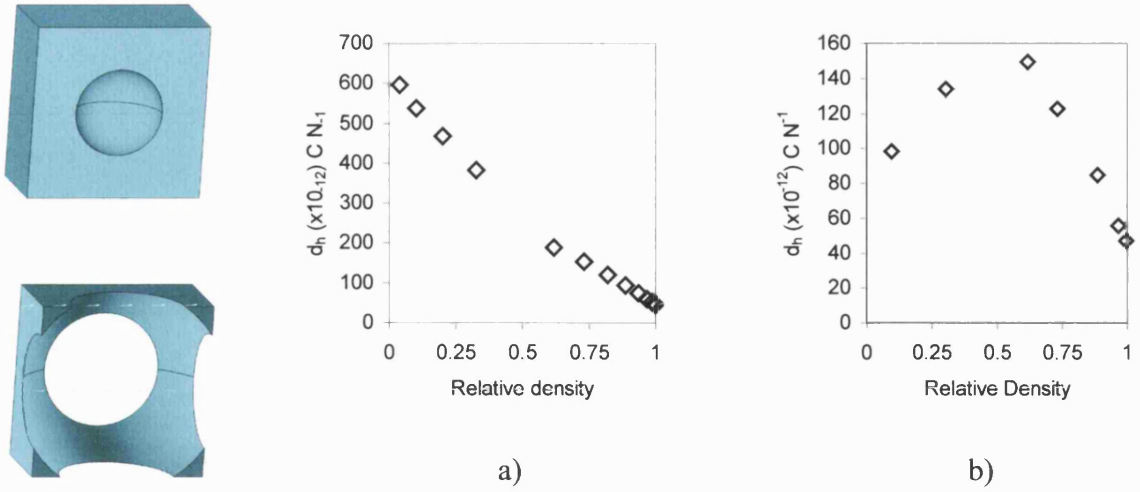

Figure 6-16: Charts showing d_h against relative density for a) PZT only and b) PZT-polymer models. 1D BurPS model.

The charts shown in Figure 6-16 show the values of d_h for both PZT porosity and PZT-polymer models for the single pore, (1D BurPS type) FEA model. Figure 6-17a) shows the chart for the PZT only model.

It can be seen that the approximate values are similar to the square pore model shown in Figure 6-16, but the trend for the single pore, 1D BurPS model can be seen to change gradient approximately 50% relative density. This is when the model changes from an isolated pore model to an interconnecting pore model. This transition can also be seen in Figure 6-17 for the 3D BurPS PZT-porosity model.

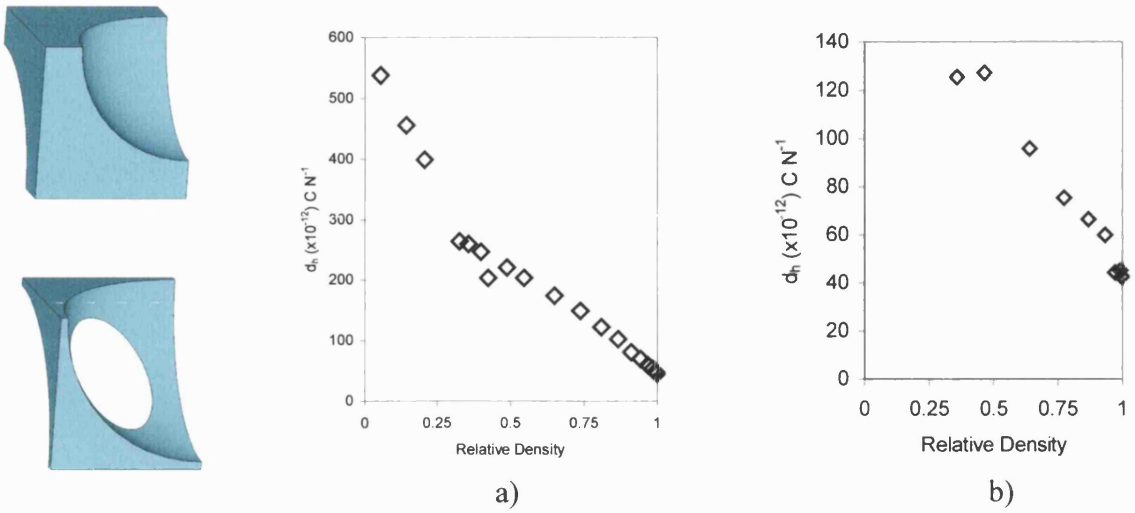

Figure 6-17: Charts showing d_h against relative density for a) PZT only and b) PZT-polymer models. 3D BurPS model.

In the case of the 3D model the change in gradient of the chart in Figure 6-17a is at around 30% relative density. This also corresponds to the transition between a isolated pore and a continuous pore model. This transition is at a lower relative density (higher porosity) than the 1D BurPS model due to the increase in packing density of the spherical pores in this 3D BurPS model.

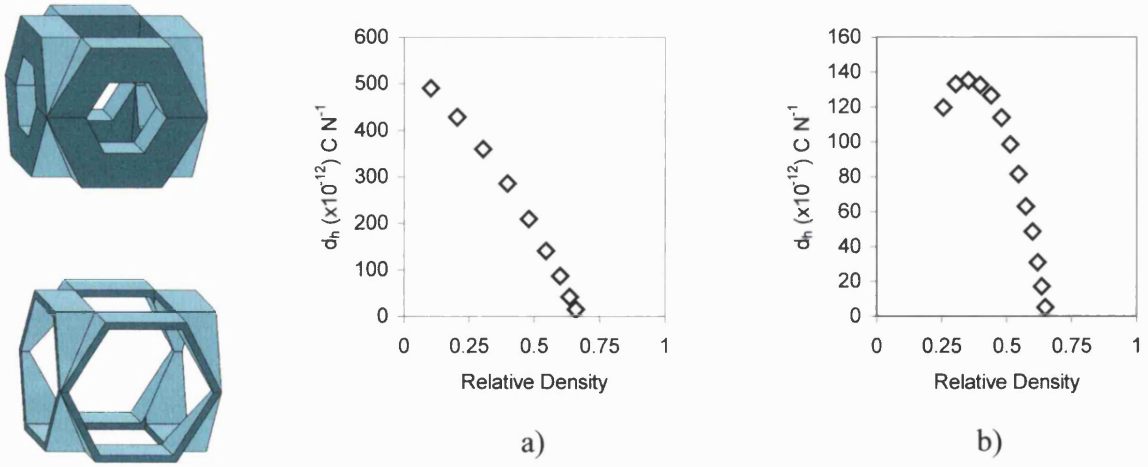

Figure 6-18: Charts showing d_h against relative density for a) PZT-porosity and b) PZT-polymer models for the hexagonal model.

The charts shown in Figure 6-18 are the values of d_h for the hexagonal model Figure 6-18a) shows the PZT only model and Figure 6-18b) shows the PZT polymer model. Since in this model there is always interconnected porosity there is no step change in the gradient of the line in the PZT-porosity d_h results. In addition the gradient of the line in the low relative density range 10 – 30% density is similar to the gradient of the lines in the 1D and 3D BurPS models at similar values of relative density.

It can be seen how with this particular shape of unit cell the results from both the PZT only and PZT –polymer model seem to have the full range of d_h values within a limited range of relative densities below 0.6. This can be attributed to the fact that the top and bottom areas of the unit cell were a constant area and only their thickness was varied. Thus when the relative density is high there is a greatly reduced volume, contributing to d_{33} activity, present oriented normal to the poling and electric field directions.

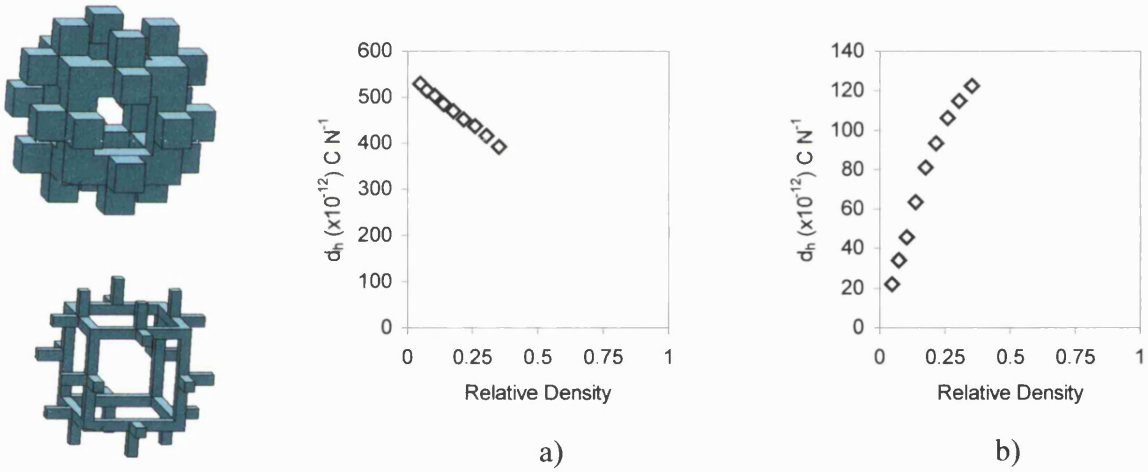

Figure 6-19: Charts showing d_h against relative density for a) PZT only and b) PZT-polymer models. Ashby model.

The charts in Figure 6-19 show the results for the PZT-porosity only and PZT-polymer models for the Ashby-type model. Unfortunately due to the physical nature of the model only low values of relative density could be modelled. The results are similar to those exhibited by the square pore model. A constant gradient is shown for the PZT only model and although only a section of the curve is shown for the PZT-polymer model, comparing this chart to all others shown in this series, a maximum can be assumed.

6.3.1 Summary of Modelling

Accurate modelling of a porous piezoelectric device is very difficult. Ideally the modelled unit would reflect exactly the real life composite and the modelled structure would contain many pores. Unfortunately the computational power required to do this is immense. It is for this reason that simple representative unit cells have to be taken and models based upon them. Results for all models are shown in Figure 6-20.

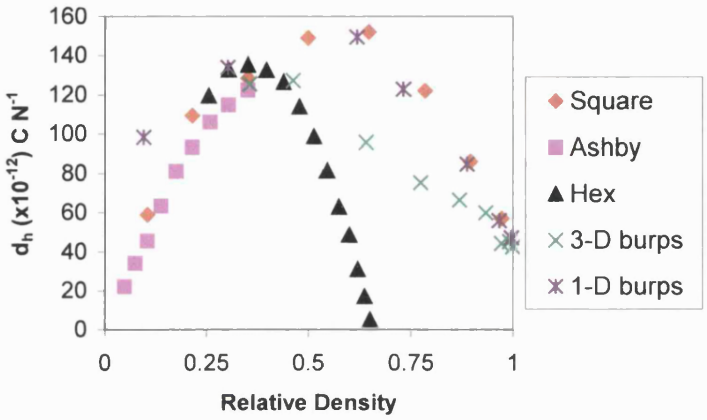

Figure 6-20: dh for all models against relative density.

For reasons described in the relevant sections the modelling of the single phase, PZT-porosity, models has flaws making the d_h increase with increasing porosity. The modelling of the two phase PZT – polymer models shows trends that are shown in the manufactured and tested samples. These trends show an increased value of d_h at around 50% porosity. This d_h peak is situated at different values of relative density for different Young's modulus polymers used as the second phase material.

The optimum value of g_h seems to be a composite with very low ceramic volume fraction where permittivity and therefore device capacitance is at a minimum. Since the hydrostatic voltage constant, g_h, is related to the sensitivity of the composite and is at a maximum at very high levels of porosity or polymer content and not the absolute signal level given off, this can be misleading. However too small a permittivity is not preferred for a device. The device capacitance should be large enough to prevent interference from stray capacitance associated with long hydrophone cables used to attach this device to associated electronics.

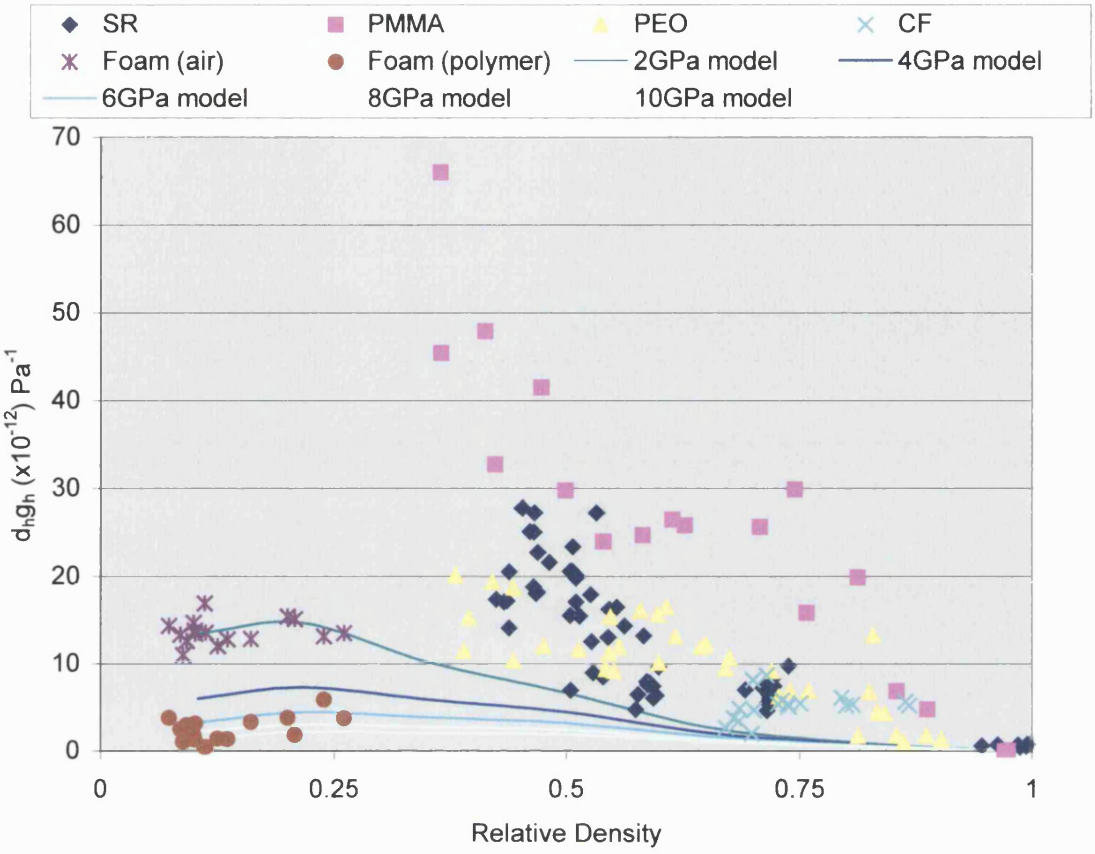

Figure 6-21: Graph showing $d_h.g_h$ for PZT - polymer square pore model including experimental data from all manufacturing methods.

A figure of merit which is commonly used for a device which is to be used both actively and passively is $d_h.g_h$. The maximum value of $d_h.g_h$ is again obtained using a low Young's modulus polymer (2GPa) with the composite containing around 20% ceramic volume fraction, this is shown in Figure 6-21. Absolute values for the $d_h.g_h$ model are in the same order of magnitude as the practical measurements. The trend shown by the finite element modelling is reflected by the experimental results shown.

6.4 Manufactured Samples

Devices for hydrophones come in a number of shapes and sizes depending on the application of the device. This can range from small devices that can fit into the palm of one's hand (Figure 6-22), such as those used for listening to natural underwater noises, such as dolphin calls etc.

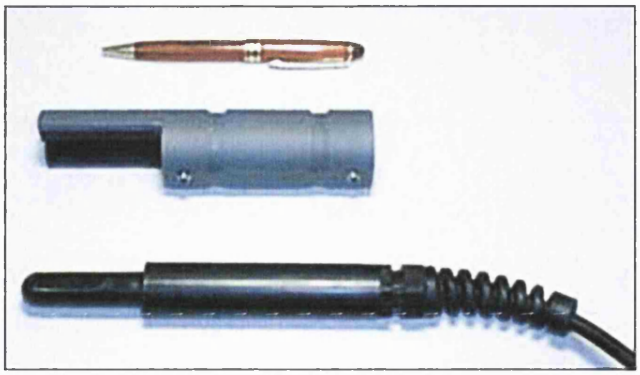

Figure 6-22: Example of small size individual hydrophone. After http://web.ukonline.co.uk/aj.cashmore/index.html

In the case of these small size hydrophones the active material can be around 10mm in diameter and several millimetres thick. This size is similar to the size of samples being produced by the BurPS method for this study.

The BurPS method is ideal for producing small samples of 5 – 30mm in diameter and 1 – 10mm thick. This method would be preferable to produce devices used in small scale hydrophone devices.

The devices can also be scaled up to very large arrays of devices, which are either attached or towed behind a boat or a ship capable of the accurate detection of large objects or vessels at extended distances.

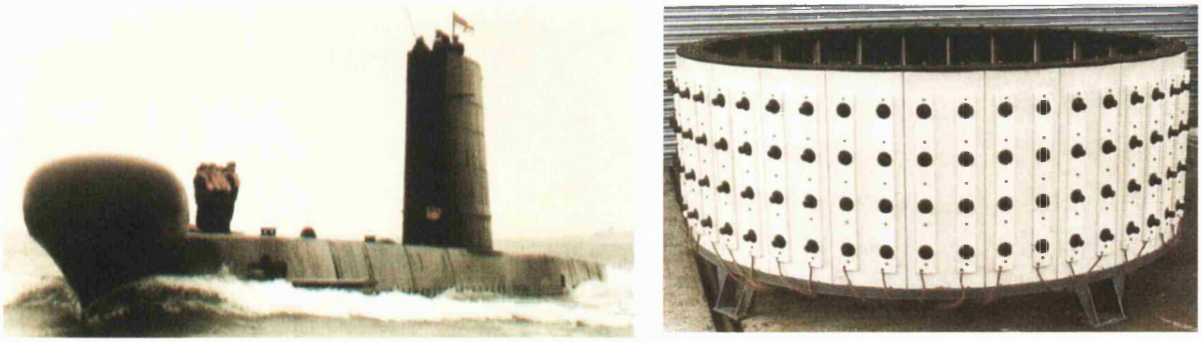

Figure 6-23: example of a large sonar array and positioning on a boat.After http://web.ukonline.co.uk/aj.cashmore/features/electronics/uk-subsonar2.html

Where large arrays are used then a larger device size is advantageous. The samples produced in this study by the foam reticulation method can be made into sizes much larger than can easily be produced by BurPS. The foam reticulation method can produce devices up to 150mm square with thickness up to 50mm. This is more suitable for use in a large array where a great number of large devices are connected together to produce a single large array.

6.4.1 Reduction of Density

Due to the piezocomposites outlined in this study consisting of large amounts of air or polymer, the mass of the devices made from these composites is considerably less than an equivalent device made from a dense ceramic.

The small-scale hydrophone has little to gain in terms of reduced mass from using piezocomposites as the active material only has a mass of a few grams, however large and very large arrays can have a mass of 2000kg. This mass can be substantially reduced by using piezocomposites in place of dense ceramics for the active material. This is further emphasised by the fact that many piezoelectric ceramics for use in hydrophones are lead based. These compounds are of high density, for example the PZT5H used in this study has a theoretical density of 7500kg m^{-3}. Using a 50% dense BurPS sample will reduce the mass of the active parts of the hydrophone by half. Using a 20% ceramic, 80% polymer sample produced by foam reticulation will reduce the mass of the active material to around 35% of the mass of a fully dense ceramic.

The mass comparisons are based on equal performance of the dense and composite based materials. This work has shown that the composite material out-performs dense material in the hydrostatic figures of merit. Further reductions in mass could be achieved by reducing the volume of composite material in order to match the performance of the dense ceramic.

6.4.2 Acoustic Coupling

As stated in Section 1.1.3.3, benefits of reduction in density do not only have an effect on the total mass of the device. The acoustic coupling between the device and the medium in which the device is to receive signals from is dependent on the relative densities of the active piezoelectric and the surrounding medium.

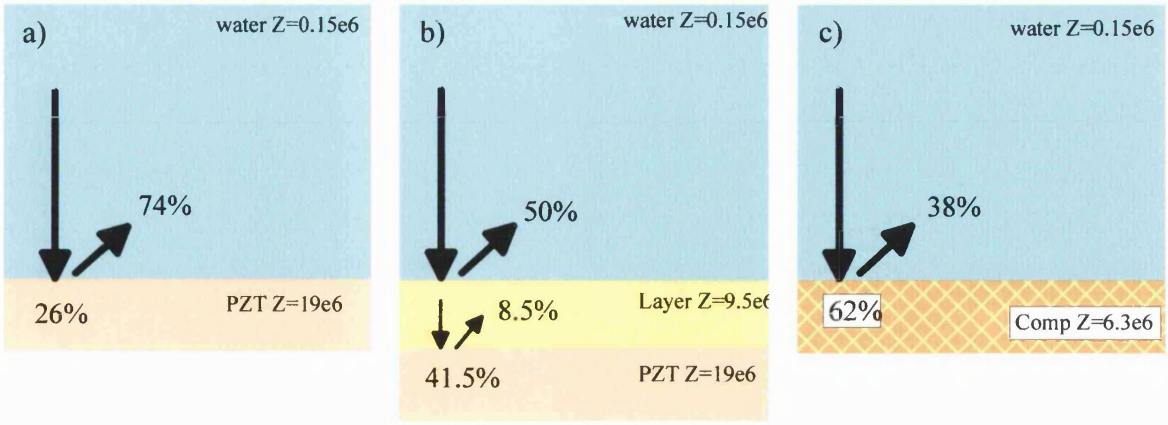

Figure 6-24: Schematic of acoustic energy reflection with and without matching layer and into a piezocomposites. All values of impedance are in kg $s^{-1}m^{-2}$. a) dense PZT, b) dense PZT and matching layer and c) piezocomposite.

Calculations shown in Chapter 1 illustrate that if a matching layer is present between dense PZT and the transmitting medium, more acoustic energy is transmitted from the medium into the PZT.

The efficiency of transfer of acoustic energy can also be increased by changing the density of the active piezoelectric material. If reticulated foam materials such as those detailed in this thesis are used at 80% polymer / 20% ceramic, with a compliant polymer of elastic modulus of 6GPa, then there will be a considerable increase of acoustic energy transferred into the piezoelectric composite (62% - Figure 1-13c) compared to a dense piezoelectric device (26% - Figure 1-13a)

Although this change in the acoustic impedance is mostly beneficial it does mean that any device has to be re-designed with the composites in mind. The new materials are not able to directly replace a dense PZT device in a hydrophone due to different electronic characteristics and the acoustic impedance differences discussed.

6.5 Final Conclusions

A number of final conclusions can be drawn from the research presented in this thesis. These are listed below in two sections, finite element modelling conclusions and experimental data conclusions.

6.5.1 Finite Element Conclusions

i) An interpenetrating finite element model was created and successfully used in a commercial FE package ANSYS version 5.4 through 5.7 which allowed porosity, materials properties (PZT and polymer) and pore shape to be investigated.

ii) A rapid reduction in d_{31} relative to d_{33} was found which gives rise to a high value of d_h.

iii) The d_h maximum was found to be at approximately 50% polymer volume fraction. The location of the maximum is dependent on the polymer Young's modulus of the polymer.

iv) g_h gradually increased with increasing polymer volume fraction due to reduction in permittivity and increasing d_h.

v) A maximum value of $d_h.g_h$ occurred at approximately 80% polymer volume fraction.

vi) A mechanism for the enhancement of d_h and g_h has been proposed based on examining the finite element modelling output.

vii) Increasing the Young's modulus of the polymer decreases d_{33} and g_h due to an increased load being experienced by the inactive polymer material. Polymer stiffness has no effect on d_{31}.

viii) Reducing the Poisson's ratio of the polymer phase gives only limited benefit to d_h and g_h. No benefit is observed by using negative Poisson's ratio polymers.

ix) Piezoelectric materials best suited for enhancement by 3-3 composite manufacture have high bulk values of d_{33} and d_{31}.

6.5.2 Experimental Data Conclusions

i) Manufacturing methods have been developed to produce a range of porous materials.

ii) The BurPS technique is limited to 0.4 to 0.97 relative density due to degassing damaging samples of low density.

iii) PMMA BurPS inclusions cause cracking during pressing and not during poling, as stated in the literature[25].

iv) Self raising flour BurPS inclusions produce a homogeneous microstructure with fine porosity.

v) Experimental data showed a rapid reduction in d_{31} relative to d_{33}, which produced high d_h materials, with a maximum at approximately 50% polymer volume fraction.

vi) Reduction in permittivity and increase in d_h produced an increase in g_h with increasing polymer volume fraction.

vii) A $d_h.g_h$ maximum occurs at 30% ceramic volume fraction.

viii) There was good agreement with the trends predicted by finite element analysis for the experimental results.

ix) Significant increases in figures of merit were achieved compared to the dense material. d_h, ($350pCN^{-1}$ for composite, $45pCN^{-1}$ dense PZT) g_h (0.17 Vm^{-1} for composite, 0.002 for dense PZT) and $d_h.gh$ ($65x10^{-12}$ Pa^{-1} for composite, $90x10^{-15}$ for dense PZT).

x) Although increases in figures of merit were measured, a decrease in coupling coefficient was observed with decreasing ceramic volume fraction.

7 Future Work

Since the completion of this project there has been progress in specific areas, which are a direct consequence from the work reported in this thesis. This work has been carried out at the University of Bath by Dr. H. Kara and Dr. R. Ramesh. This work will be discussed briefly below.

In addition to the progress that has been made, recommendations for future work will be outlined.

7.1 Hydrophone Manufacture

The research carried out by Dr. H. Kara has concentrated on the physical properties of low ceramic volume fraction foam based composites for use in hydrophone applications due to the high g_h figures of merit calculated by modelling, Chapter 2 and measured experimentally, Chapter 4[27,26]. Hydrophones have been manufactured from materials using the reticulated foam technique, outlined in Chapter 3

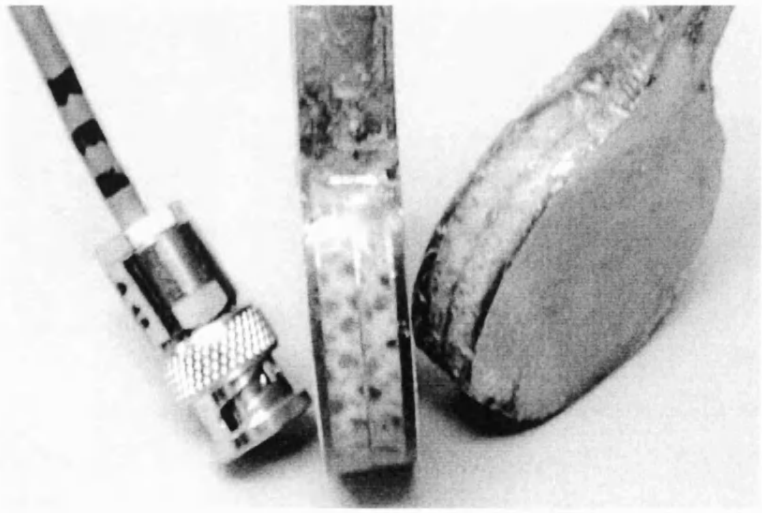

Figure 7-1: Image of two hydrophones manufactured by the reticulated foam process. Picture courtesy of Dr. H. Kara, University of Bath. The BNC connector is shown for scale.

The photograph in Figure 7-1 shows two hydrophones manufactured by using the reticulated foam technique. Each device has been manufactured by using a different pore size starting foam. The device on the right of the image has a small unit cell size, typically below 1mm

and the hydrophone in the centre of the image has a unit cell size of around 2-3mm. An example of the characterisation carried out is shown in Figure 7-2.

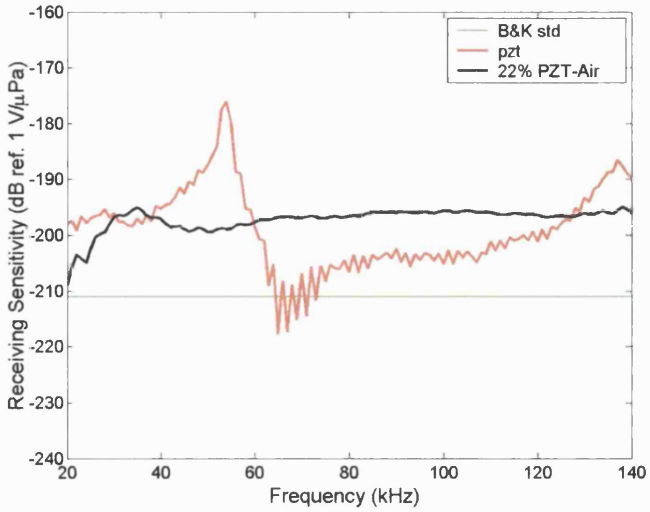

Figure 7-2: Receive sensitivity versus frequency of preliminary hydrophones manufactured from piezocomposite and dense PZT. Note the sharp resonance observed with dense PZT.

The plots shown in Figure 7-2 show the receive sensitivity as a function of frequency for a piezocomposite hydrophone as shown in Figure 7-1. Data for a similar hydrophone is shown manufactured from dense PZT for comparison. It can be seen that the composite hydrophone shows a slightly higher sensitivity and the response is significantly flatter due to the suppression of the radial resonance compared to the dense PZT hydrophone.

Further work is required to test these devices at lower frequencies so that the device is under true hydrostatic conditions. BurPS materials which have high d_h and g_h figures of merit should also be examined so that receive sensitivity can be examined as a function of porosity and related to the figures of merit in this work. The signal to noise ratio (related to $d_h.g_h$) for composite devices should also be measured and compared to dense PZT hydrophones.

Additional work carried out by Dr. Kara highlights some observations made in the reticulated foam based material structures.

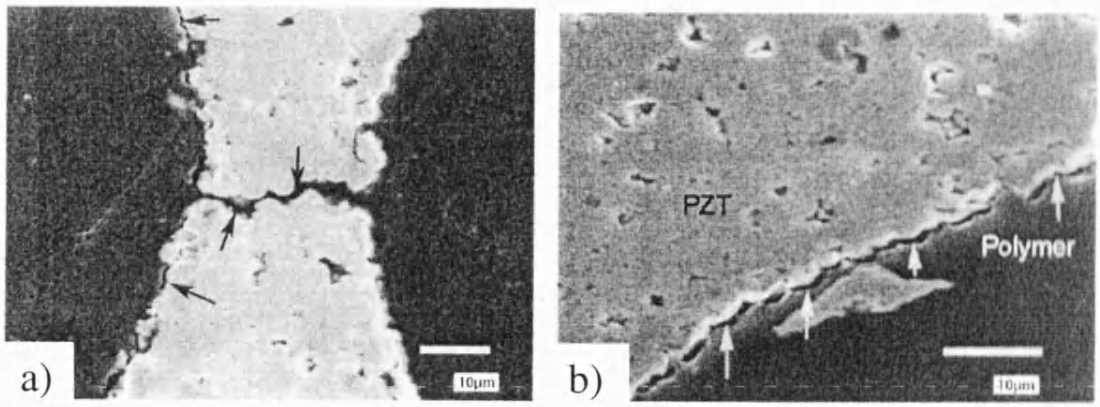

Figure 7-3: Images showing a) strut cracking and b) delamination of the polymer - PZT interface. Pictures courtesy of Dr. Kara, University of Bath.

The images shown in Figure 7-3 indicate manufacturing defects in the foam based PZT-polymer composites. Figure 7-3a shows the cracking in a PZT strut and large pores in the ceramic macrostructure. Further work on reducing these defects would be advisable and would enhance the properties of the PZT-polymer foam based materials. Figure 7-3b shows delamination of the polymer phase from the PZT phase also in the PZT-polymer foam based materials. This type of defect will certainly affect stress transfer between the two phases and therefore values of d_{33} and d_{31}.

7.2 Electrical Characterisation of Piezocomposites

Research carried out by Dr. R. Ramesh, also at the University of Bath, has further characterised piezocomposite materials in terms of coupling coefficient and acoustic impedance. The equations outlined by Ramesh et al.[27] have been used to predict the acoustic impedance whilst experimental data has been compared to the analytical prediction. These can be seen in Figure 7-4.

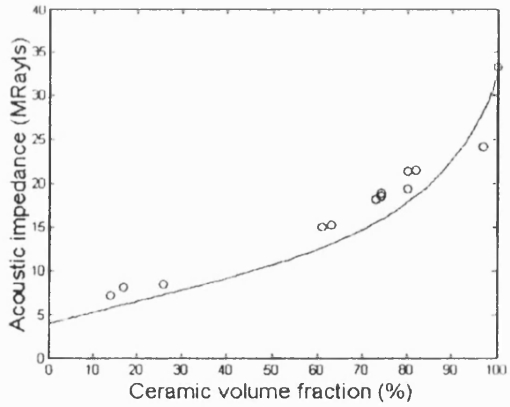

Figure 7-4: Graphs of acoustic impedance as a function of ceramic volume fraction. The solid line represents the predicted values by analytical modelling and the points represent experimental data. Graph from (27).

Figure 7-4 shows the acoustic impedance with respect to the ceramic volume fraction. The solid line represents the analytical prediction and the individual points show experimental data. Here the experimental results show good agreement to the analytical model and as expected the acoustic impedance decreases with decreasing ceramic volume fraction. For reference, the acoustic impedance of water is 0.15 MRayls.

7.3 Future Reticulated Foam Based Structures

As progress has been made to date with reticulated foam based piezocomposites further work in this area would be advantageous. Rudimentary finite element modelling suggests that using a foam with a negative Poisson's ratio would further improve the d_h of piezocomposites. Such negative Poisson's ratio ceramic foams can be manufactured relatively easily by using polymeric negative Poisson's ratio foams, which are commercially available. It can be envisaged that such a material would have a positive d_{33} *and* a positive d_{31} as there would be an *expansion* in the x (1) and y (2) direction associated with the expansion in the z (3) direction. This would lead to extremely large values of d_h.

7.4 Modelling of Large Structures

The modelling of 3-3 piezocomposite structure presented in this thesis has exclusively concentrated on a single representative unit cell for the analysis of a whole foam structure. This was due to restrictions on processing power and storage capabilities of equipment available. The modelling of PZT – porosity conducted in both Chapter 2 and Chapter 5 could be improved if large, multi-pore, structures could be modelled. This would provide

more accurate representations to actual foam materials. Modelling could also be improved by determining all the piezoelectric and stiffness matrices as a function of porosity so that when modelling a 3-3 hydrophone, for example, the actual internal structure does not have to be replicated.

7.5 Materials Development

Further work could also concentrate on improving materials processing, such as producing extremely homogeneous microstructures or improving the bond between the PZT and the polymer phases. The polymer composition could also be examined, for example loading the polymer with a piezoelectric material to create a 0-3 connectivity filler, therefore creating a 3 –(0-3) structure or using a piezoelectric polymer such as PVDF.

8 Concluding Remarks

A full porosity range of interconnecting piezocomposites was modelled, using finite element analysis and properties relevant to hydrostatic device performance were measured. Results showed that at porosities of around 50% significant improvements in hydrostatic figures of merit were observed compared to bulk samples.

Piezoelectric composites were manufactured over the full porosity range using both the foam reticulation and burnt out polymer spheres method. Experimental data here also revealed significant improvements in hydrostatic figures of merit compared to dense samples.

In both modelled and experimental data a maximum in d_h was found at around 50% ceramic volume fraction and g_h was shown to be at a maximum for low values of ceramic volume fraction. The maximum value of $d_h g_h$ was shown to be at around 20% ceramic volume fraction.

The trends present in the finite element modelling were validated by the experimental results.

9 References

1. Electronic Ceramic Materials, J. Notwotny, Trans Tech Publications, UK, 1992

2. S-E. Park, T.R. Shroud, "*Ultra High Stain and Piezoelectric Behaviour in Relaxor Based Ferroelectric Single Crystals*", J. Appl. Phys., 82, 4, 1804-1811, 1997L.

3. D. Waller, A. Safari. "*Corona Poling of PZT ceramics and Flexible Piezoelectric Composites*", Ferroelectrics, 87, 189-195, 1988

4. Y. Xu, "*Ferroelectric Materials and Their Applications*", North-Holland, London, 1991

5. L. Nelson, "*Smart Piezoelectric Fibre Composites*", Materials Science and Technology, accepted for publication, Nov. 2002.

6. S. Marselli, V. Pavia, C. Galassi, E. Roncari, F. Craciun, G. Guildarelli, "*Porous Piezoelectric Ceramic Hydrophone*", J. Accoust. Soc. Am, 106, 2, 733-738, 1999.

7. R.E. Newnham, D.P. Skinner, L.E. Cross, "*Connectivity and Piezoelectric-Pyroelectric Composites*", Mat. Res. Bull. , 13, 525-536, 1978

8. T.R. Shrout, W.A. Schluze, J.V. Biggers, "*Simplified Fabrication of PZT / Polymer Composites*", Mat. Res. Bull., 14, 1553-1559, 1979

9. K. Schwartzwalde & A. V. Somers, "*Methods of Making Porous Ceramic Articles*", US Patent No. 3 090 094, 1963

10. F. Cichocki, K. Trumble, "*Tailored Porosity Gradients via Colloidal Infiltration of Compression Moulded Sponges*", Am. Ceram. Soc. 81, 1661-1664, 1998

11. J.G.P. Binner, "*Production and Properties of Low Density Engineering Ceramic Foams*", British Ceramic Transactions, 96, 6, 247-249, 1997

12. D.P. Skinner, R.E. Newnham and L.E. Cross, "*Flexible Composite Transducers*", Mat. Res. Bull. 13, 599-607, 1978

13. V.F. Janas, A. Safari, "*Overview of Fine-Scale Piezoelectric Ceramic / Polymer Composite Processing*", Jn. Am. Ceram. Society, 11, 78, 2945-2955, 1995

14. X. Zhao, J.R.G. Evans, M.J. Edirisinghe, J.H. Song, "*Ink jet printing of ceramic pillar arrays*", J. Mat. Sci., 37, 10, 1987-1992, 2002

15. A. Bandyopadhyay, R. K. Panda, V.F. Janas, M. K. Agarwala, S.C. Danforth, A Safari, "*Processing of Piezocomposites by Fused Deposition Techniques*", J. Am. Ceram. Soc., 80, 6, 1366-1372, 1997.

16. Cellular Solids Structure & Properties, M. F. Ashby, L.J. Gibson, Cambridge University Press, UK, 1999

17. P. Guillaussier, C-A. Boucher, "*Porous Lead Zirconate Titanate Ceramics For Hydrophones*", Ferroelectrics, 187, 121-128, 1996

18. M. Dunn, M. Taya, "*Electromechanical Properties of Porous Ceramics*", J. Am. Ceram. Soc., 76, 7, 1697-1706, 1993

19. W.A. Smith, "*Optimizing Electromechanical Coupling In Piezocomposites Using Polymers with Negative Poisson's Ratio*", Ultrasonics Symposium, 661-666, 1991

20. A.O.Abatan, J.F. Malluck, Z. Tang, 1998, "*Using Coupleed-field Finite Elements to Characterize Piezoceramic Materials*", http://www.sensorsmag.com/articles/pie0698.htm, (27/10/98)

21. J. Bennett, G. Hayward, "*Design of 1-3 Piezocomposite Hydrophones Using Finite Element Analysis*", IEEE Trans. Ultrasonics, Ferroelectrics and Freq. Control, Vol.44, No.3, 1997

22. L.V. Gibansky, S.Torquato, "*Optinal Design of 1-3 Composite Piezoelectrics*", Structural Optimisation, 13, 23-28, 565-574,

23. H.A. Kunkel, S. Locke, B. Pickeron, *"Finite-element analysis of vibrational modes in piezoelectric ceramic disks"*, IEEE Trans Ultra. Ferro. Freq. Cont. 37, 316-328, 1990.

24. 1997L.V. Gibiansky, S. Torquato, "*On The Use of Homogenization Theory To Design Optimal Piezocomposites For Hydrophone Applications*", Mech. Phys. Solids, 45, 5, 689-708, 1997

25. K. Rittenmyer, T. Shrout, W.A. Schulze, R.E. Newnham, "*Piezoelectric 3-3 Composites*", Ferroelectrics, 4, 189-195, 1982

26. H. Kara, A. Perry, R. Stevens, C.R. Bowen, "*Interpenetrating PZT/Polymer Composites for Hydrophones: Models and Experiments*", Ferroelectrics, 265, 317-332, 2002.

27. R. Ramesh, H. Kara, C.R.Bowen, "*The Dielectric, Mechanical and Piezoelectric Properties of 3-3 Piezoelectric Composites.*" Ferroelectrics, 273, 383-388, 2002.

28. Montanaro, Y. Jorand, G. Fantozzi & A. Negro, "*Ceramic Foams by Powder Processing*", Euro. Ceram. Soc. 18, 1339-1350, 1998

29. K. Mizumura, Y. Kurihara, H. Ohashi, S. Kummamoto, K. Okuno, "*Porous Piezoelectric Ceramic Transducer*", Jpn. J. App. Phys, 30, 9B, 2271-2273, 1991

30. C.Dias, D.K. Das-Gupta, Y. Hinton, R.J. Shuford, "*Polymer / Ceramic Composites for Piezoelectric Sensors*", Sensors and Actuators A, 37-38, 343-347, 1993

31. K. Ina, T. Mano, S. Omura, K. Nagata, "*Hydrophone Sensitivity of Porous $Pb(Zr,Ti)O_3$ Ceramics*", Jpn. J. App. Phys., 33, 5381-5384, 1994

32. T. Hayashi, S. Sugihara, J. Okazaki, "*Processing of Porous 3-3 PZT Ceramics Using Capsule-Free O_2-HIP*", Jpn. J. App. Phys., 30, 2243-2246, 1991

33. R.W. Rice, M. Kahn, D.E. Shadwell, "*Ceramic Body With Ordered Pores*", US Patent No. 4 683 161, 1987

34. M.C. Breslin. B. Starck, L. Xu, G.S. Daehn, H.L. Fraser, "*Deformation of Co-Continuous Alumina -Aluminum Composites*", Forth Euro Ceramics, 3 71-77, 1994

35. H.M. Reuther, M. Weinmann, M. Fischer, W. von Münch, F. Assmus, "*Modelling of Oscillating Quartz Sensors and Related Structures*", Sensors and Actuators, 41-42, 643-653, 1994

36. O. Sigmund, S. Torquato, I.A. Aksay, "*On the Design of 1-3 Piezocomposites Using Topology Optimization*", J. Mat. Res. 13, 4, 1038-1048, 1998

37. F. Levassort, M. Lethiecq, C. Millar, L. Pourcelot, "*Modelling of Highly Loaded 0-3 Piezoelectric Composites Using a Matrix Method*", ", IEEE Trans. Ultrasonics, Ferroelectrics and Freq. Control, 45, 6, 1998

38. H. Jeong, D.K. Hsu, "*Quantitative Estimation of Material Properties of Porous Ceramics by Means of Composite Micromechanics and Ultrasonic Velocity*", NDT&E International, 29, 2, 95-101, 1996

39. A. Perry, C. R. Bowen, S. Mahon, "*Finite Element Modelling of 3-3 Piezocomposites*", Scripta Materialia, 41, 9, 1001 – 1007, 1999

40. H.R. Gallantree, "*Piezoelectric Ceramic / Polymer Composites*", British Ceramic Proceedings, No.41, pp161-169, 1989

41. R.W. Rice, "*Comparison of Physical Property-Porosity Behaviour with Minimum Solid Area Models*", J. Mat. Sci., 31, 1509-1528, 1996

42. J.W. Sliwa, S. Ayter, J.P.Mohr, "*Method for Making Piezoelectric Composite*", U.S. Pat. 5 239 736, 1993

43. C. R. Bowen, A. Perry, R Stevens, "*Analytical and Numerical Modelling of 3-3 Piezoelectric Composites*". Journal of the European Ceramic Society, 21, 1463-1467, 2001

10 Appendices

10.1 Macros for finite element modelling

Macros written to enable the modelling of 3-3 structures in ANSYS commercial finite element modelling software.

Square pore model

```
finish
/cle
RESUME,pzt5a.db
/PREP7
*ASK,X,thickness,0.25
*ASK,Y,thickness other side,0.75
BLOCK,0,1,0,1,0,1
BLOCK,X,Y,X,Y,0,1
BLOCK,0,1,X,Y,X,Y
BLOCK,X,Y,0,1,X,Y
VSBV,1,ALL
BLOCK,X,Y,X,Y,0,1
BLOCK,0,1,X,Y,X,Y
BLOCK,X,Y,0,1,X,Y
VADD,1,2,3
VSEL,S,VOLU,,4
!MPCHG,2,ALL
VATT,2,,1,0
VSEL,,ALL
!VSEL,S,VOLU,,5
!VATT,1,,1,0
ALLSEL
VGLUE,4,5
```

```
VSEL,S,VOLU,,1
VATT,1,,1,0


ASEL,S,LOC,Z,1
CM,TOP,AREA
ALLSEL
ASEL,S,LOC,X,1
CM,SIDE,AREA
ALLSEL


SMRTSIZE,SIZLVL,2
VMESH,ALL
```

```
NSEL,S,LOC,Z,1,1
CP,1,VOLT,ALL
ALLSEL
NSEL,S,LOC,Z,0,0
CP,2,VOLT,ALL
ALLSEL
NSEL,S,LOC,Z,1,1
D,ALL,VOLT,0,
ALLSEL
NSEL,S,LOC,Z,0,0
D,ALL,VOLT,1,
ALLSEL
NSEL,S,LOC,Z,0,0
DSYM,SYMM,Z,,
ALLSEL
NSEL,S,LOC,X,0,0
DSYM,SYMM,X,,
ALLSEL
NSEL,S,LOC,Y,0,0
DSYM,SYMM,Y,,
ALLSEL
CNVTOL,F,,,,1E-6
CNVTOL,AMPS,,,,1E-6
CNVTOL,VOLT,,,,1E-6
```

1D BurPS model

```
finish
/cle
/page,,,999999999
RESUME,material,db,,0

*ask,r,Radius of pore,0.3
*ask,S,Mesh size level,5
/prep7
/PNUM,VOLU,1
ET,1,SOLID98

BOPT,NUMB,OFF

! draw model
block,0,1,0,1,0,1
wpof,0.5,0.5,0.5
SPH4,0,0,r
VSBV,    1,    2

smrtsize,S
vmesh,all
```

```
!electrodes coupled set/ loads
nsel,s,loc,z,0
!cp,1,volt,all
d,all,volt,1
allsel

nsel,s,loc,z,1
!cp,2,volt,all
d,all,volt,0
allsel

asel,s,loc,z,0
allsel,below,area
da,all,uz
allsel
```

```
asel,s,loc,x,0
allsel,below,area
da,all,ux
allsel

asel,s,loc,y,0
allsel,below,area
da,all,uy
allsel
finish
/solu
solve

!/post1
!nsel,s,loc,z,1
!allsel,below,nodes
!prNSOL,U,Z
```

3D BurPS model

```
finish
/cle
/page,,,999999999
RESUME,material,db,,0

*ask,r,Radius of pore,0.3
*ask,S,Mesh size level,5
/prep7
/PNUM,VOLU,1
ET,1,SOLID98

BOPT,NUMB,OFF

! draw model
block,0,1,0,1,0,1
SPH4,0,0,r
wpof,1,1,1
SPH4,0,0,r
VSBV,1,2
vsbv,4,3


smrtsize,S
vmesh,all
```

```
!electrodes coupled set/ loads
nsel,s,loc,z,0
!cp,1,volt,all
d,all,volt,1
allsel

nsel,s,loc,z,1
!cp,2,volt,all
d,all,volt,0
allsel

asel,s,loc,z,0
allsel,below,area
da,all,uz
allsel
```

```
asel,s,loc,x,0
allsel,below,area
da,all,ux
allsel

asel,s,loc,y,0
allsel,below,area
da,all,uy
allsel


finish
/solu
solve

!/post1
!nsel,s,loc,z,1
!allsel,below,nodes
!prNSOL,U,Z
```

Hexagonal Model

```
finish
/cle
/page,,,999999999

!material 1 is PZT and material 2 is poly
resume,material.db


/PREP7
*ASK,R,radius of pore,0.5
*ask,S,Mesh size level,5
```

```
!draw model.
wpro,,90
rpr4,6,0,0,1,0,2
rpr4,6,0,0,R,0,2
wpro,,,90
wpof,,,-1
wpof,-1,,
rpr4,6,0,0,1,0,2
rpr4,6,0,0,R,0,2
vadd,1,3
vadd,2,4
vsbv,5,1
wplane,-1,0,0,0
wpcsys,-1,0
block,-0.5,0.5,-0.5,-1.5,-1,1
vsbv,2,1
vatt,1,,1,0


smrtsize,sizevl,S
vmesh,all
```

```
nsel,s,loc,z,.85,.87
cp,1,volt,all
allsel
nsel,s,loc,z,-.85,-.87
cp,2,volt,all
allsel
nsel,s,loc,z,.85,.87
d,all,volt,0
allsel
nsel,s,loc,z,-.85,-.87
d,all,volt,1
nsel,s,loc,z,-.85,-.87
dsym,symm,z,,
allsel
nsel,s,loc,y,0,0
dsym,symm,y,,
allsel
nsel,s,loc,x,-1,-1
dsym,symm,x,,
allsel
cnvtol,amps,,,,1e-6
cnvtol,volt,,,,1e-6
cnvtol,f,,,,1e-6
```

Ashby Model

```
finish
/cle
/page,,,999999999

!material 1 is PZT and material 2 is poly
RESUME,MATERIAL.DB
/PREP7
*ASK,X,thickness,0.25
*ASK,Y,thickness other side,0.75
BLOCK,0,1,0,1,0,1
BLOCK,X,Y,X,Y,0,1
BLOCK,0,1,X,Y,X,Y
```

```
BLOCK,0.5-(X/2),0.5+(X/2),0,X,-.25,0
BLOCK,0.5-(X/2),0.5+(X/2),1-X,1,-
.25,0
BLOCK,0,X,0.5-(X/2),0.5+(X/2),-.25,0
BLOCK,1-X,1,0.5-(X/2),0.5+(X/2),-
.25,0

BLOCK,-.25,0,0,X,0.5-(X/2),0.5+(X/2)
BLOCK,-.25,0,1-X,1,0.5-
(X/2),0.5+(X/2)
BLOCK,-.25,0,0.5-(X/2),0.5+(X/2),1-
X,1
BLOCK,-.25,0,0.5-(X/2),0.5+(X/2),0,X
```

```
VSEL,S,VOLU,,2
SMRTSIZE,SIZLVL,5
VMESH,ALL
ALLSEL
VSEL,S,VOLU,,26
SMRTSIZE,SIZLVL,5
VMESH,ALL
ALLSEL
NSEL,S,LOC,Z,1.25,1.25
CP,1,VOLT,ALL
ALLSEL
NSEL,S,LOC,Z,-0.25,-0.25
CP,2,VOLT,ALL
```

```
BLOCK,X,Y,0,1,X,Y
VSBV,1,ALL

BLOCK,0.5-(X/2),0.5+(X/2),0,X,1,1.25
BLOCK,0.5-(X/2),0.5+(X/2),1-
X,1,1,1.25
BLOCK,0,X,0.5-(X/2),0.5+(X/2),1,1.25
BLOCK,1-X,1,0.5-
(X/2),0.5+(X/2),1,1.25

BLOCK,1,1.25,0,X,0.5-(X/2),0.5+(X/2)
BLOCK,1,1.25,1-X,1,0.5-
(X/2),0.5+(X/2)
BLOCK,1,1.25,0.5-(X/2),0.5+(X/2),1-
X,1
BLOCK,1,1.25,0.5-(X/2),0.5+(X/2),0,X

BLOCK,0.5-(X/2),0.5+(X/2),0,-.25,0,X
BLOCK,0.5-(X/2),0.5+(X/2),0,-.25,1-
X,1
BLOCK,1-X,1,-.25,0,0.5-
(X/2),0.5+(X/2)
BLOCK,0,X,-.25,0,0.5-(X/2),0.5+(X/2)

BLOCK,0.5-(X/2),0.5+(X/2),1,1.25,0,X
BLOCK,0.5-(X/2),0.5+(X/2),1,1.25,1-
X,1
BLOCK,1-X,1,1,1.25,0.5-
(X/2),0.5+(X/2)
BLOCK,0,X,1,1.25,0.5-(X/2),0.5+(X/2)

VADD,ALL

BLOCK,-.25,1.25,-.25,1.25,-.25,1.25
VOVLAP,ALL
/TRLCY,VOLU,0.75,2
VGLUE,2,26
VSEL,S,VOLU,,2
VATT,2,,1,0
ALLSEL
VSEL,S,VOLU,,26
VATT,1,,1,0
ALLSEL

ALLSEL
NSEL,S,LOC,Z,1.25,1.25
D,ALL,VOLT,0,
ALLSEL
NSEL,S,LOC,Z,-0.25,-0.25
D,ALL,VOLT,1,
ALLSEL
NSEL,S,LOC,Z,-0.25,-0.25
DSYM,SYMM,Z,,
ALLSEL
NSEL,S,LOC,X,-0.25,-0.25
DSYM,SYMM,X,,
ALLSEL
NSEL,S,LOC,Y,-0.25,-0.25
DSYM,SYMM,Y,,
ALLSEL
CNVTOL,F,,,,1E-6
CNVTOL,AMPS,,,,1E-6
CNVTOL,VOLT,,,,1E-6
```

10.2 Published work

A.J. Perry, C.R. Bowen, S.W.Mahon "*Modelling of 3-3 Piezocomposites*" British Ceramic Procedings, No. 60, pp 503 , 1999

A. Perry, C. R. Bowen, S. Mahon, "*Finite Element Modelling of 3-3 Piezocomposites*", Scripta Materialia, Vol 41, No. 9, pp 1001 – 1007, 1999

C.R. Bowen A.Perry, R. Stevens "*Materials Parameters Determining the Performance of Piezoelectric 3-3 Composites*" Presented by C.R. Bowen at 7th Frontier Science Research Conference In Materials Science And Technology Series, La Jolla, California, 24-26th Jan, 2000.

A.Perry, C.R.Bowen, S.Mahon "*Modelling of 3-3 piezocomposites*" Ferroelectrics 2000 UK, pp. 67 – 74

A.Perry, C.R. Bowen, H. Kara, S. Mahon. "*Modelling of 3-3 Piezocomposites*" Software for Electrical Engineering Analysis and Design V,WIT Press, pp67-75, 2001.

C.R.Bowen, A. Perry, H. Kara, S.W. Mahon "Analytical modelling of 3-3 Piezoelectric composites", Journal of the European Ceramic Society, 21, 2001, 1463-1467

H. Kara, A. Perry, R. Stevens, C.R. Bowen. "Interpenetrating PZT/polymer Composites for Hydrophones: Models and Experiments" Ferroelectrics, Vol. 265, pp 317-332, 2002